Many-body theory of laser-induced ultrafast demagnetization and angular momentum transfer in ferromagnetic transition metals

Autor: Waldemar Töws
Betreuer: Prof. Dr. Gustavo M. Pastor

Dissertation zur Erlangung des akademischen Grades eines

Doktors der Naturwissenschaften (Dr. rer. nat.)

am Fachbereich Mathematik und Naturwissenschaften der Universität Kassel

Disputation am 10. Juni 2014

Erklärung

Hiermit versichere ich, dass ich die vorliegende Dissertation selbstständig, ohne unerlaubte Hilfe Dritter angefertigt und andere als die in der Dissertation angegebenen Hilfsmittel nicht benutzt habe. Alle Stellen, die wörtlich oder sinngemäß aus veröffentlichten oder unveröffentlichten Schriften entnommen sind, habe ich als solche kenntlich gemacht. Dritte waren an der inhaltlich-materiellen Erstellung der Dissertation nicht beteiligt; insbesondere habe ich hierfür nicht die Hilfe eines Promotionsberaters in Anspruch genommen. Kein Teil dieser Arbeit ist in einem anderen Promotions- oder Habilitationsverfahren verwendet worden.

Kassel, 24. Februar 2014

Waldemar Töws

To Norma, Jonathan, Jeremiah and Naemi

Abstract

An electronic theory is developed, which describes the ultrafast demagnetization in itinerant ferromagnets following the absorption of a femtosecond laser pulse. The present work intends to elucidate the microscopic physics of this ultrafast phenomenon by identifying its fundamental mechanisms. In particular, it aims to reveal the nature of the involved spin excitations and angular-momentum transfer between spin and lattice, which are still subjects of intensive debate.

In the first preliminary part of the thesis the initial stage of the laser-induced demagnetization process is considered. In this stage the electronic system is highly excited by spin-conserving elementary excitations involved in the laser-pulse absorption, while the spin or magnon degrees of freedom remain very weakly excited. The role of electron-hole excitations on the stability of the magnetic order of one- and two-dimensional $3d$ transition metals (TMs) is investigated by using *ab initio* density-functional theory. The results show that the local magnetic moments are remarkably stable even at very high levels of local energy density and, therefore, indicate that these moments preserve their identity throughout the entire demagnetization process.

In the second main part of the thesis a many-body theory is proposed, which takes into account these local magnetic moments and the local character of the involved spin excitations such as spin fluctuations from the very beginning. In this approach the relevant valence $3d$ and $4p$ electrons are described in terms of a multiband model Hamiltonian which includes Coulomb interactions, interatomic hybridizations, spin-orbit interactions, as well as the coupling to the time-dependent laser field on the same footing. An exact numerical time evolution is performed for small ferromagnetic TM clusters.

The dynamical simulations show that after ultra-short laser pulse absorption the magnetization of these clusters decreases on a time scale of hundred femtoseconds. In particular, the results reproduce the experimentally observed laser-induced demagnetization in ferromagnets and demonstrate that this effect can be explained in terms of the following purely electronic non-adiabatic mechanism: First, on a time scale of 10–100 fs after laser excitation the spin-orbit coupling yields local angular-momentum transfer between the spins and the electron orbits, while subsequently the orbital angular momentum is very rapidly quenched in the lattice on the time scale of one femtosecond due to interatomic electron hoppings. In combination, these two processes result in a demagnetization within hundred or a few hundred femtoseconds after laser-pulse absorption.

Deutsche Übersetzung des Titels und der Zusammenfassung

Titel:

Vielteilchentheorie der laserinduzierten ultraschnellen Demagnetisierung und des Drehimpulstransfers in ferromagnetischen Übergangsmetallen

Zusammenfassung:

Es wird eine elektronische Theorie entwickelt, die die durch Absorption eines Femtosekunden-Laserpulses induzierte ultraschnelle Demagnetisierung in itineranten Ferromagneten beschreibt. Die vorliegende Arbeit beabsichtigt die mikroskopische Physik dieses ultraschnellen Phänomens durch Identifizierung seiner grundlegenden Mechanismen aufzuklären, die nach wie vor Gegenstand intensiver Debatten sind. Insbesondere soll die Natur der beteiligten Spinanregungen und des Drehimpulstransfers zwischen Spin und Gitter aufgedeckt werden.

Im ersten vorbereitenden Abschnitt dieser Doktorarbeit wird das Anfangsstadium des laserinduzierten Demagnetisierungsprozesses betrachtet. In dieser Phase ist das elektronische System hochangeregt durch Spin-erhaltende Anregungen, die bei der Absorption des Laserpulses auftreten, wohingegen die Spin- oder Magnon-Freiheitsgrade sehr schwach angeregt bleiben. Durch Anwendung der *ab initio* Dichtefunktionaltheorie wird der Einfluss der Elektron-Loch-Anregungen auf die Stabilität ein- und zweidimensionaler $3d$-Übergangsmetalle untersucht. Die Resultate zeigen, dass die lokalen

magnetischen Momente außergewöhnlich stabil sind, sogar bei sehr hohen lokalen Energiedichten. Dies deutet darauf hin, dass die lokalen Momente ihre Identität während des ganzen Demagnetisierungsprozesses bewahren.

Im zweiten und zentralen Teil der Dissertation wird eine Vielteilchentheorie vorgeschlagen, die die lokalen magnetischen Momente und den lokalen Charakter der beteiligten Spinanregungen, wie zum Beispiel Spinfluktuationen, von Anfang an mitberücksichtigt. In diesem Ansatz werden die relevanten $3d$ und $4p$ Valenzelektronen mittels eines Mehrband-Modell-Hamiltonoperators beschrieben, der die Coulombwechselwirkungen, interatomare Hybridisierung, Spin-Bahn-Wechselwirkungen und die Kopplung an das zeitabhängige Laserfeld auf gleicher Basis einbezieht. Es wird eine exakte numerische Zeitentwicklung für kleine ferromagnetische Übergangsmetall-Cluster durchgeführt. Die dynamischen Simulationen zeigen, dass die Magnetisierung dieser Cluster nach der Absorption eines ultrakurzen Laserpulses auf einer Zeitskala von 100 Femtosekunden abfällt. Insbesondere reproduzieren die Resultate die experimentell beobachtete laserinduzierte Demagnetisierung in Ferromagneten und beweisen, dass dieser Effekt mittels des folgenden rein elektronischen nicht-adiabatischen Mechanismus erklärt werden kann: Zunächst führt auf einer Zeitskala von 10–100 fs nach Laseranregung die Spin-Bahn-Kopplung zu lokalem Drehimpulstransfer zwischen den Spins und den elektronischen Orbitalen, während anschließend der orbitale Drehimpuls sehr schnell auf der Zeitskala von einer Femtosekunde aufgrund interatomarer Bewegung der Elektronen im Gitter verschwindet. Das Zusammenspiel dieser zwei Prozesse resultiert in einer Demagnetisierung innerhalb Hundert oder einiger Hundert Femtosekunden nach Absorption des Laserpulses.

Acknowledgements

I would like to acknowledge my supervisor Prof. Dr. Gustavo M. Pastor whose guidance and advice have made this work possible. Moreover, I thank the IT Service Center of the University of Kassel for providing computer resources, as well as the Otto-Braun Foundation for financial support.

Finally, I would like to give a special acknowledgement to the LORD Jesus Christ by citing a verse from the Bible:

"The LORD *gives strength to his people; the* LORD *blesses his people with peace."* Psalm 29,11

Contents

List of Figures **xi**

List of Tables **xiii**

Glossary **xv**

1 Introduction **1**

1.1 Ultrafast demagnetization in ferromagnetic transition metals 1

1.2 Underlying physics 4

1.2.1 Laser excitation 5

1.2.2 Nonequilibrium between different degrees of freedom 6

1.2.3 Themalization of excited electrons 6

1.2.4 Relaxation between electronic orbital and electronic spin degrees of freedom 7

1.2.5 Magnetization recovery at the picosecond timescale 9

1.2.6 Some open questions 9

1.3 Comparison with ultrafast magnetization dynamics in other materials . 10

1.4 Theoretical approaches 12

1.4.1 Phenomenological three-temperature model 12

1.4.2 Coherent demagnetization 12

1.4.3 Electron-phonon spin-flip scattering 13

1.4.4 Spin-polarized electron diffusion 15

1.4.5 Further phenomenological models 16

1.4.6 Discussion 16

1.5 Goals of this work 17

2 Spin excitations in the presence of high local energy densities 19

2.1 Role of initial nonequilibrium on the magnetic order 20

2.2 Theoretical description 21

2.2.1 Two-temperature view 22

2.2.2 DFT approach to the electronic free energy 23

2.2.3 Effective exchange interactions 25

2.3 Results 27

2.3.1 Fe chains 27

2.3.2 Co and Ni chains 31

2.3.3 Two-dimensional Ni lattices 33

2.4 Delocalized versus local magnetic excitations during the ultrafast demagnetization process 36

3 Many-body theory of magnetization dynamics 39

3.1 Role of electron correlations in ferromagnetism of transition metals . . . 40

3.2 Electronic many-body model 44

3.2.1 Single-particle electronic structure 45

3.2.2 Electron-electron Coulomb interaction 46

3.2.3 Interaction with external fields 48

3.2.4 Spin-orbit coupling 50

3.3 Discussion in view of the magnetization dynamics 53

3.4 Model simplifications 54

3.5 Laser pulse 57

4 Static magnetism 61

4.1 Specific model parameters 61

4.2 Magnetic properties 66

4.2.1 Identifying ferromagnetic phases 67

4.2.2 Ground-state properties of selected high-spin systems 74

4.2.3 Temperature dependence of magnetization 80

5 Magnetization dynamics **85**
5.1 Parameter choice . . . 85
5.2 Ultrafast demagnetization in the triangular system . . . 87
5.3 Local angular-momentum conservation . . . 93
5.4 Importance of spin-orbit coupling . . . 96
5.5 Spectral analysis of the magnetization dynamics . . . 100
5.6 Discussion about the absorbed energy per atom . . . 105
5.7 Dependence on the absorbed energy . . . 108
5.8 Interband hybridization effects . . . 116
5.9 Different band fillings and geometrical structures . . . 118

6 Conclusions and outlook **121**

A Computational details of DFT calculations **127**

B Interatomic hopping integrals **129**
B.1 Dependence of hopping integrals on the interatomic difference vector . . . 129
B.2 Two-center approximation . . . 131
B.3 Slater-Koster integrals . . . 133

C Electron-electron interaction model **137**

D Dipole matrix elements within the intra-atomic approximation **141**
D.1 Wigner-Eckart theorem . . . 141
D.2 Relations between dipole matrix elements . . . 143

E Numerical methods for static calculations **145**
E.1 Lanczos diagonalization method: Ground-state properties . . . 145
E.2 Finite-temperature properties: thermal equilibrium . . . 149
E.3 Method of spectral analysis . . . 151

F Numerical methods for dynamical calculations **155**
F.1 Time-propagation . . . 155
F.2 Assessing the accuracy of Lanczos propagations . . . 160

References **169**

List of Figures

1.1 Setup of a typical femtosecond time-resolved X-ray magnetic circular dichroism experiment 2
1.2 Time-resolved XMCD signal of a 15 nm Nickel film 3
1.3 Different degrees of freedom 5

2.1 Spin-spiral state 23
2.2 Geometry of the 2D Ni square lattice 26
2.3 Spin-wave spectrum of the relaxed Fe chain 28
2.4 Effective exchange interactions in the relaxed Fe chain 29
2.5 Spin-wave spectrum of Fe chains with bulk NN distance 30
2.6 Magnon dispersion relation of relaxed Co and Ni chains 32
2.7 Magnon dispersion relations in the 2D Ni square lattice 34
2.8 Effective exchange interactions in the Ni square lattice 35
2.9 Illustration of local spin fluctuations during the demagnetization process 37

3.1 Correlations in many-body systems 41
3.2 Temperature-induced spin fluctuations in ferromagnets 43

4.1 Ground-state spin angular momentum of small clusters 69
4.2 Ground-state spin angular momentum of selected systems within the two-band model 72
4.3 Magnetic anisotropy in the triangle system 78
4.4 Magnetization as a function of temperature in the $N_e = 4$ triangle system 81

5.1 Dynamics of the isosceles triangle subsequent to fs laser-pulse absorption 88
5.2 Time-dependent properties of the d electrons 90

5.3 Picosecond dynamics of the isosceles triangle 92
5.4 Time dependence of total spin and orbital angular momenta 94
5.5 Magnetization dynamics as a function of the SOC strength 97
5.6 Demagnetization time τ_{dm} and relative magnetization reduction $\Delta S_z/S_z^0$ as a function of spin-orbit coupling strength 98
5.7 Spin and orbital angular-momentum dynamics for opposite spin-orbit couplings 99
5.8 Spectral distribution after laser-pulse absorption 101
5.9 Spectral analysis of the spin dynamics of the triangle system 104
5.10 Demagnetization from a single-particle perspective 107
5.11 Magnetization dynamics for different laser fluences 109
5.12 Dependence of the relative demagnetization and demagnetization time on the laser fluence 110
5.13 Magnetization dynamics for different laser electric-field polarizations . . 111
5.14 Demagnetization efficiency for various laser wave lengths 114
5.15 Demagnetization efficiency as a function of pulse duration 115
5.16 Dependence of spin relaxation on interband hopping integrals 117
5.17 Spin dynamics for different band fillings and structures 120

List of Tables

3.1 Electronic two-band model approximation 55
3.2 Hopping integrals of the model 56
3.3 Intra-atomic dipole matrix elements of the model 57

4.1 Selected high-spin systems 74
4.2 Ground-state properties of selected structures and band fillings 75
4.3 Thermal energies needed to break the short-range magnetic order in the selected clusters 83

5.1 Laser wave lengths and exchange integrals for selected structures and band fillings 119

B.1 Two-center integrals within the $3d$, $4s$ and $4p$ valence bands 133
B.2 Hopping integrals within the $3d$, $4s$ and $4p$ valence bands in terms of two-center integrals 135

D.1 Intra-atomic dipole matrix elements within the $3d$, $4s$ and $4p$ valence bands 144

Glossary

Abbreviations

1D	one-dimensional
2D	two-dimensional
AF	antiferromagnetic
DFT	density functional theory
Eq.	Equation
EY	Elliott-Yafet
FM	ferromagnetic
fs	femtosecond
NC	noncollinear
NN	nearest neighbor
Ref.	Reference
SDW	spin-density wave
SILP	short-iterative Lanczos propagation
SOC	spin-orbit coupling
SP	spectral part
TM	transition metal
VASP	Vienna *ab initio* simulation package
XMCD	X-ray magnetic circular dichroism

Physical constants

c	speed of light $= 299,792,458$ m/s
e	electron charge $= -1.602176565 \times 10^{-19}$ C
$\hbar$	reduced Planck constant $= 0.658211928$ eV fs
k_B	Boltzmann constant $= 8.617332478 \cdot 10^{-5}$ eV/K
m_e	electron mass $= 9.10938291 \times 10^{-31}$ kg
ε_0	vacuum permittivity $= 8.85418782 \times 10^{-12}$ $\mathrm{s^4A^2m^{-3}kg^{-1}}$
μ_B	Bohr magneton $= 5.7883818066 \cdot 10^{-5}$ eV/T

Latin symbols

a	interatomic distance
$\vec{a}$	nearest-neighbor bond
$\vec{B}$	external magnetic field
$\hat{c}_{j\alpha\sigma}$	annihilation operator of an electron at atom j in orbital α with spin σ
$\hat{c}^\dagger_{j\alpha\sigma}$	creation operator of an electron at atom j in orbital α with spin σ
$\hat{D}$, $\hat{D}(\hat{\nu}, \varphi)$	rotation operator of the total system (angle φ around axis $\hat{\nu}$)
$D_\Psi(E)$	spectral representation of many-body state $\lvert \Psi \rangle$
$\hat{e}$	unit vector
E	electronic energy
ΔE	absorbed laser energy
E_{gs}	ground-state electronic energy
E_{MA}	magnetic-anisotropy energy
ΔE_{SR}	thermal energy needed to break the ground-state short-range magnetic correlations
$\vec{E}(t)$	laser electric field

E_0	maximum of the electric-field amplitude
F	laser fluence
$\hat{H}$	total electronic Hamiltonian
$\hat{H}_0$	single-particle electronic structure Hamiltonian
$\langle H_0^{d,\mathrm{int}} \rangle / n_d$	interatomic hopping energy per d electron
$\hat{H}_C$	electron-electron Coulomb interaction Hamiltonian
$\hat{H}_E$	electron – electric field interaction Hamiltonian
$\hat{H}_{\mathrm{ext}}$	external field Hamiltonian
$\hat{H}_N$, H_N	Hamiltonian / Hamiltonian matrix projected onto the Krylov subspace K^N
$\hat{H}_{\mathrm{SO}}$	spin-orbit Hamiltonian
J	intra-atomic exchange integral
$J_{\vec{R},\vec{R}'}$, $J_{0\delta}$	effective interatomic exchange interactions
$\vec{J}$	total angular momentum
$\vec{k}$	(electron / electric field) wave vector
K^N	Krylov subspace of dimension N
l	orbital angular momentum quantum number
$\vec{L}$	orbital angular momentum
L_{easy}	orbital angular momentum projection along the easy magnetization direction
$(l, l'; m_\zeta)$	Slater-Koster (two-center) integral
$\lvert\, lm \,\rangle$	state having definite angular-momentum quantum numbers l and m
$\lvert\, l_1 l_2; m_1 m_2 \,\rangle$	state of two separated angular momenta l_1 and l_2 having definite z projections m_1 and m_2
m	quantum number of orbital angular momentum projection (on the z axis)
$\vec{M}$	material magnetization
n	radial quantum number
$\lvert\, nlm \,\rangle$	atomic orbital having radial quantum number n and angular-momentum quantum numbers l, m
$\hat{n}$	electron number operator
n_d	number of d electrons
n_{eh}	average number of absorbed photons
n_p	number of p electrons
N_a	number of atoms
N_e	number of electrons
$N_{d\text{-orbitals}}$	number of d orbitals per atom
N_{nnc}	number of nearest-neighbor connections in the lattice
$\vec{q}$	spin-wave vector
$\vec{r}$	electron position
R	rotation matrix
$\vec{R}$	atomic position
$\vec{R}_{jk}$	connection vector between atoms j and k
S	total-spin quantum number
$S^{d,\xi=0}$	spin quantum number in the d-band system excluding the SOC
$\vec{S}$	spin angular momentum
$\vec{S}_d$	spin angular momentum restricted to d electrons
S_{easy}	spin projection along the easy magnetization direction
$\langle\langle \vec{S}_{jd}^2 \rangle\rangle$	average atomic d-electron spin
$\langle\langle \vec{S}_{jd} \cdot \vec{S}_{kd} \rangle\rangle$	averaged nearest-neighbor d-electron spin correlation
$\langle\langle \vec{S}_{jd} \cdot \vec{S}_{kd} \rangle\rangle_{\mathrm{rel}}$	relative nearest-neighbor d-electron spin correlation

$\langle\langle S_{jd}/n_{jd}\rangle\rangle$	average atomic spin quantum number per d electron
$\Delta S_z/S_z^0$	(long-time) laser-induced relative demagnetization
t	time
$t_{jk}^{\alpha\beta}$	hopping integral between orbital α at atom j and orbital β at atom k
T	temperature
T_C	Curie temperature
T_e	temperature of the electron subsystem
T_p	laser pulse duration
T_{SR}	temperature needed to break the ground-state short-range magnetic correlations
$\hat{T}_q^{(k)}$	tensor operator of rank k
$\langle\, nl \,\|\|\hat{T}^{(k)}\|\|\, n'l' \,\rangle$	reduced matrix element of tensor operator $\hat{T}_q^{(k)}$
$\langle\, d \,\|\|\hat{T}^{(1)}\|\|\, p \,\rangle$	reduced matrix element of the spherical tensor operator obtained from $\hat{\vec{r}}$
U	classical direct Coulomb integral
$v_j(\vec{r})$	electrostatic potential of ion j
$v(\vec{r})$	electrostatic potential generated by the ions in the lattice
W_α	spectral weight integrated over spectral part α
$\hat{x}$, $\hat{y}$, $\hat{z}$	unit vector along x, y, z axis

Greek symbols

ε_α^0	on-site energy of atomic orbital α
$\varepsilon_d^{\mathrm{eff}}$	effective d-electron level
$\vec{\varepsilon}$	dimensionless normalized polarization vector of $\vec{E}$
$\hat{\zeta}$	interatomic connection axis
ϑ	number of ($3d$) electrons per atom
λ	laser wave length
λ_x, λ_y, λ_z	x, y, z direction cosine of interatomic connection vector $\vec{R}_{jk}$
$\vec{\mu}$	magnetic moment
ξ	spin-orbit coupling constant
σ	spin index
τ_{dm}	demagnetization time
ϕ_α, ϕ_k	single-particle orbitals
$\|\,\Psi\,\rangle$, $\|\,\Phi\,\rangle$	many-body states
ω	angular frequency
Ω	electronic free energy
Ω_0	electronic free energy for FM configuration
$\Delta\Omega_X$	electronic exchange free energy

1

Introduction

The ultrafast magnetization dynamics in ferromagnetic transition metals (TMs) represents a most interesting and active research field. In the last two decades a large effort has been made in order to explore the demagnetization and even the magnetization reversal on the femtosecond (fs) timescale as well as to understand the underlying physics. The present introduction contains a brief overview of this physical effect and gives the state of the art of theoretical approaches. In particular, several open fundamental questions about the microscopic mechanisms responsible for the experimental observations are discussed, which have motivated the present work.

1.1 Ultrafast demagnetization in ferromagnetic transition metals

In their famous 1996 work Beaurepaire *et al.* have studied the relaxation processes of electrons and spins systems following the absorption of fs optical pulses in ferromagnetic (FM) nickel films (1). They have shown that the Ni magnetization rapidly breaks down during the first picosecond after the excitation. This was a very remarkable experimental finding, since the dynamics of the magnetization proceeds much faster than the shortest magnetic-moment precession periods, which take place on a considerably slower picosecond–to–nanosecond time scale. In this way, the authors pioneered the new interesting research field of laser-induced ultrafast demagnetization. In subsequent years, several groups have performed time-resolved pump and probe experiments on thin films and polycrystalline surfaces of magnetic $3d$ TMs in order to

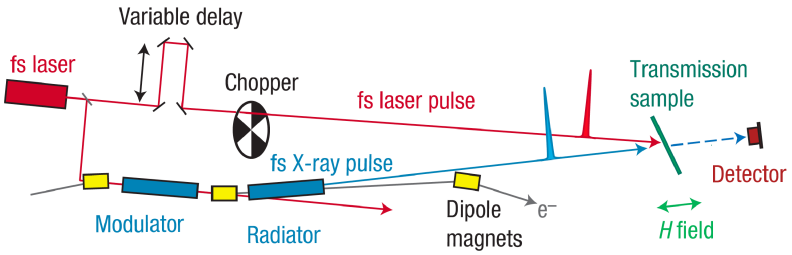

Figure 1.1: Setup of a typical femtosecond time-resolved X-ray magnetic circular dichroism experiment - After Ref. (8).

further investigate this phenomenon. Most of the experiments have been performed on Ni (2, 3, 4, 5, 6, 7, 8, 9, 10), which has the lowest Curie temperature (T_C = 631 K) among the 3*d* TMs. Therefore, only relatively low absorbed energies are required to induce a demagnetization. However, the ultrafast demagnetization has also been observed in other FM metals, for instance in Co (4, 9, 11) and Fe films (12).

A variety of techniques has been applied in these experiments in order to measure the laser-induced magnetization changes as a function of time. Several groups, including Beaurepaire *et al.*, have used the magneto-optical Kerr effect[1] (MOKE). This allows to record hysteresis loops at different time delays between pump and probe pulses and thus to measure the magnetic remanence of the sample as a function of pump-probe delay (1, 11, 12). Moreover, MOKE allows to measure the ellipticity and rotation of the polarization of the reflected light beam (5, 6, 9). Both quantities are directly related to the material magnetization. In addition, a nonlinear magneto-optical method has been applied in Refs. (2, 4), where second-harmonic generation (SHG) has been used to probe the ultrafast magnetization dynamics in Ni and Co. In this case the information about the magnetic response to laser irradiation was obtained from differences of the SHG reflected intensity for opposite magnetization directions. Besides magneto-optical methods, there are other techniques based on photoemission spectroscopy, which have also been used to measure the time-dependent sample magnetization (3, 7, 11). For example, one considers the electrons that are photoemitted by a probe pulse, and sub-

[1]The MOKE describes the changes in polarization and intensity of a light beam after being reflected from a magnetic surface. Two aspects of this effect have actually been used to measure the magnetization dynamics: First, depending on the material magnetization $\vec{M}$, linearly polarized incident light undergoes a rotation of its polarization and/or becomes elliptically polarized. Second, the reflected intensity depends on the magnitude and direction of $\vec{M}$.

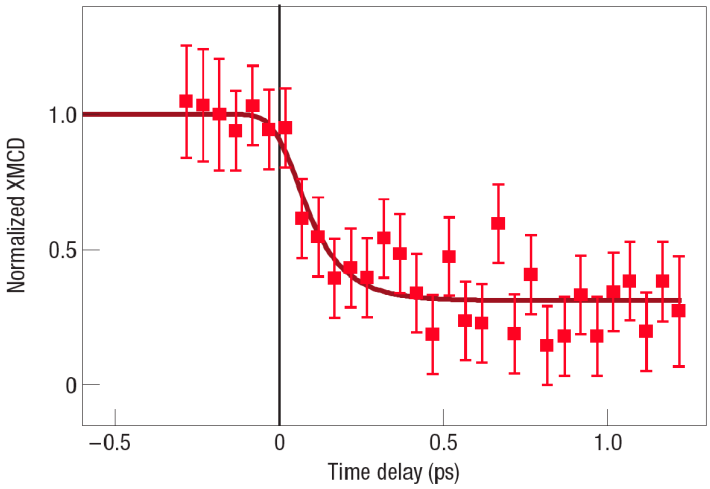

Figure 1.2: Time-resolved XMCD signal of a 15 nm Nickel film - The reference time corresponds to the center of the femtosecond pump pulse which has a 100 fs time width. The decrease of the XMCD signal reflects the decrease in the Ni magnetization within around 120 fs. After Ref. (8).

sequently, one measures the spin polarization of these photoelectrons by using a Mott detector. The corresponding energies can be detected with a time-of-flight technique. Finally, let us mention the X-ray magnetic circular dichroism (XMCD) method, which was used by Stamm *et al.* (8, 10). This method is based on the dependence of the absorption of circularly polarized X-ray pulses in magnetized metals as a function of the photon helicity. In fact, the difference in the absorption spectra for pulses having opposite circular polarizations (i.e., the XMCD signal) gives a measure for the material magnetization. As an example, the setup of the time-resolved XMCD measurements reported in Ref. (8) is illustrated in Figure 1.1. Figure 1.2 shows the corresponding XMCD signal of a 15 nm Ni film, which is excited by a fs laser pulse. The decrease of this signal reflects the ultrafast demagnetization effect (8).

To summarize, there is a lot of evidence that the excitation of a magnetic TM film with an ultrashort laser pulse gives rise to a demagnetization on a time scale τ_{dm} of about hundred or a few hundred femtoseconds. It is clear that the relaxation is so fast that it cannot be explained simply by thermal heating arguments. This ultrafast effect can open the way to new technical applications of controlling and manipulating the magnetization on a subpicosecond time scale. For instance, new faster writing methods in magnetic data storage and memory devices could be developed taking ad-

vantage of this effect. However, in order that this aim becomes possible it is essential to elucidate the microscopic mechanisms responsible for the remarkable demagnetization phenomenon. Unfortunately, the microscopic physics behind this effect is not properly understood yet. Although different physical pictures have been proposed in the literature in order to explain this ultrafast demagnetization, a number of fundamental questions still remain unanswered. These physical pictures and the related open questions are discussed in the following Section.

1.2 Underlying physics

Several explanations have been raised during the discussion of ultrafast magnetization dynamics in itinerant $3d$ TMs. Most of these physical interpretations divide the problem into three components concerning different degrees of freedom: the translational and orbital motion of the electron, the spin variables, and the lattice dynamics (see Figure 1.3). The first of them combines the atomic orbital degrees of freedom and the electron motion throughout the lattice. Second, the spin subsystem describes the spin degrees of freedom including local spin fluctuations and collective spin waves. The third subsystem comprises the motion of the ion cores which form the lattice, usually characterized in terms of phonons (collective lattice vibrations). According to this classification, energy (or temperature assuming thermalization) and angular momentum can be transferred between the components. The laser pulse couples with the electronic degrees of freedom and therefore energy is pumped from the external electric field into the electron bath. The actual demagnetization corresponds mainly to a decrease of spin angular momentum[1], which of course implies an increase of the energy of the spin subsystem. The physical pictures proposed in the literature for different steps of this ultrafast effect are briefly discussed in the following. In particular, we will focus our attention on two central questions: Which microscopic processes govern the energy

[1]The magnetic moment is given by $\vec{\mu} = -\frac{\mu_B}{\hbar}(\vec{L} + 2\vec{S})$, including in general both orbital angular momentum $\vec{L}$ and spin $\vec{S}$. Importantly, in TMs $\vec{L}$ is usually quenched by the crystal field, implying that $\vec{S}$ yields more than 90% of the sample magnetization. Only in small metallic clusters or in systems having reduced dimensions (e.g., wires) the quenching of $\vec{L}$ is significantly weaker than in the bulk. Even if in these cases $\vec{L}$ can contribute appreciably to the total magnetization, it remains in general less important than the spin moments.

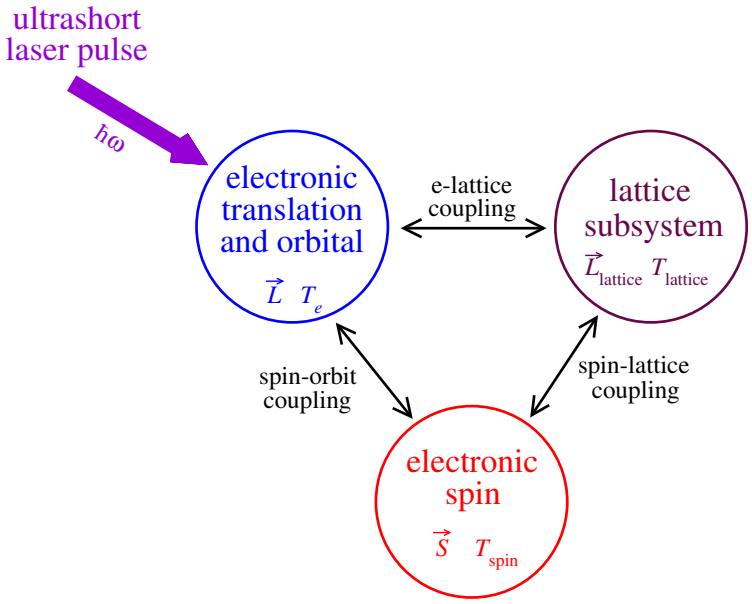

Figure 1.3: Different degrees of freedom - According to literature [for instance, Refs. (1) and (9)], the problem can be schematically divided into the electronic translational, lattice, and electronic spin subsystems. An angular momentum and energy (or temperature assuming thermalization) are assigned to each component. The double-sided arrows denote the couplings allowing exchange of energy and angular momentum between the different subsystems. The bold arrow illustrates the pump laser pulse which couples only with the electronic translational and orbital degrees of freedom.

and angular momentum transfer between the electronic, spin and lattice systems? And, at which time scales do these processes take place?

1.2.1 Laser excitation

Upon laser excitation electron-hole pairs are generated almost instantaneously. It is important to recall that the external laser field cannot directly change by itself the magnetization, since the dominant dipolar transitions preserve the spin projection of the electron involved in the excitation and thus the total spin (13). Consequently, the fast magnetization decrease following the laser excitation reflects intrinsic dynamical properties of the excited magnetic metal. It involves spin angular-momentum transfer, since just after absorption the total spin remains unchanged. A microscopic understanding of this effect seems therefore far from trivial from a conceptual point of view.

1.2.2 Nonequilibrium between different degrees of freedom

The laser pulse initially creates a strong-nonequilibrium situation between excited translational electronic degrees of freedom and nearly non-excited spin and lattice degrees of freedom. The overall dynamics depends on the couplings providing exchange of energy and angular momentum between these three reservoirs, and on the corresponding relaxation times. It is generally accepted that in the considered transition metals the energy relaxation from the electrons to the lattice takes a few picoseconds (1, 6, 13). The process of lattice heating occurs via electron-phonon interaction. Concerning the coupling between spins and lattice, the characteristic times for energy exchange between the magnetic system and the lattice vibrations are about 10–100 ps (1, 2, 13). The corresponding mechanism is the interaction between the spin waves and the phonons, which is mediated by spin-orbit coupling (SOC). These considerations clearly show that the magnetic response (taking place on a timescale of 100 fs) is much faster than the thermalization times with the lattice. One concludes that the fs demagnetization cannot be explained in terms of thermalization effects. In contrast, a strong nonequilibrium, with the lattice on the one side and the electronic degrees of freedom on the other side, seems to prevail during the whole ultrafast phenomenon.

1.2.3 Themalization of excited electrons

Before any significant relaxation between the three different kinds of reservoirs takes place, i.e., subsequently to the laser excitation, the excited electron gas rapidly thermalizes its translational degrees of freedom to a Fermi-like distribution due to electron-electron interactions (1, 2, 6, 13). Since the typical electronic collision time in ordinary metals is of the order of 10 fs (14), one estimates that a few femtoseconds are enough to redistribute the absorbed energy within the electronic-translational degrees of freedom and thus thermalize them. Again, it is important to recall that all electron-electron collision processes preserve the total spin too. Therefore, after internal thermalization of the electronic translation and orbital subsystem the total magnetization should be the same as before absorption. The ultrafast demagnetization seems to be the result of the relaxation between electronic-orbital and spin degrees of freedom.[1]

[1] A demagnetization mechanism within the absorption time of the laser pulse has been proposed in Ref. (15). However, this theory seems not to apply to a number of more recent experiments showing that the demagnetization mainly proceeds after the pump pulse is over (6, 7). See also Section 1.4.2.

1.2.4 Relaxation between electronic orbital and electronic spin degrees of freedom

For the spins and the translational electronic subsystem to equilibrate, a mechanism providing efficient exchange of energy and angular momentum between the corresponding degrees of freedom is essential. This constitutes the key to understanding the ultrafast magnetization dynamics. Already in the early stages of this research field, it has been argued that the electron-phonon interactions are too slow to account for a transfer of spin $\vec{S}$ to lattice angular momentum $\vec{L}_{\text{lattice}}$ at a $\sim$ 10 fs time scale (6). Moreover, it is generally accepted that during the demagnetization ($\tau_{\text{dm}} \sim 100$ fs) the lattice temperature does not yet change significantly (13). Therefore, one concluded that the spin relaxation relies mainly on an electronic mechanism, i.e., without involving the coupling to phonons in a crucial way. In fact, the spin-orbit interaction was regarded as the natural mechanism behind the magnetization dynamics. The idea that the ultrafast demagnetization proceeds on an electronic level was confirmed by Rhie *et al.*, who found a collapse of the magnetic exchange splitting for the Nickel $3d$ valence states with a time constant of $\tau_{\text{dm}} \approx 300$ fs (7). They attributed the quenching of the Ni magnetic moment to energy transfer, mediated by SOC, from hot electrons to low-energy spin excitations such as Stoner excitations (16) or magnons (17).

However, several years later a mechanism based on electron spin-flip scattering with phonons has been proposed. In fact, Koopmans *et al.* explained the demagnetization effect by assigning a spin-flip probability —induced by SOC— to each electron-phonon scattering event (18, 19).[1] In that way not only electronic interactions but also interactions with phonons were considered as relevant contributions to the sub-picosecond magnetic response (11). Since then a controversy has arose concerning the question, whether the ultrafast effect proceeds on a purely electronic level or whether it also involves the excitation of phonons.

In this context it is worth mentioning that the SOC Hamiltonian is essentially given by terms of the form $\vec{L}_j \cdot \vec{S}_j$, where j denotes a single atom. Therefore, the SOC conserves the atomic total angular momenta $\vec{J}_j = \vec{L}_j + \vec{S}_j$. This local angular-momentum conservation has an important consequence: If SOC alone (a mechanism based on a purely electronic level) is responsible for the decrease of the spin magnetization, then

[1] This mechanism is discussed in more detail in Section 1.4.3.

the decrease of $\langle\vec{S}\rangle$ should in principle be accompanied by a corresponding increase of $\langle\vec{L}\rangle$. Stamm *et al.* investigated precisely this issue by performing time-resolved XMCD experiments. In a path-breaking work they demonstrated that the spin and orbital angular momenta are *both* quenched on a time scale of 120 fs after laser excitation (8). Inspired by this work, Stamm *et al.* and many other scientists in this field concluded that electron orbits do not act as a reservoir for angular momentum. In contrast, electron spin-flip scattering with phonons or impurities have been considered to be responsible for the ultrafast demagnetization and the angular-momentum transfer from the spins to the lattice (20, 21, 22). This is the explanation provided by the popular microscopic three-temperature model (23).

On the other side, it can be argued that $\vec{L}$ is very rapidly quenched by the electron motion in the metal and, therefore, the SOC triggered transfer from $\vec{S}$ to $\vec{L}$ cannot be observed in an experiment with a finite time resolution of about 50 fs. One would then just observe the decrease of $\vec{S}$. Assuming this, Carpene *et al.* proposed a physical picture, in which the rapid ($\tau_{\mathrm{dm}} \sim 100$ fs) demagnetization, and in particular the observations of Stamm *et al.* in Ref. (8), can be qualitatively understood on a purely electronic level, i.e., without involving a direct coupling with the lattice (12). According to this picture, electron-magnon interactions mediated by the SOC result in a transfer of spin $\vec{S}$ to orbital angular momentum $\vec{L}$, while $\vec{L}$ is almost instantaneously quenched in the lattice due to interatomic electron hoppings. These considerations show that the combination of these two effects (SOC yielding angular-momentum transfer from $\vec{S}$ to $\vec{L}$, and the subsequent quenching of $\vec{L}$ in the lattice) may be a possible mechanism of the fs demagnetization in TMs.

In summary, the driving mechanism for the ultrafast relaxation between electronic translational and electronic spin subsystems is not yet thoroughly understood. A quantitative prediction of the time dependence of the magnetization is still lacking. In particular, the important question, whether the observed fs magnetization dynamics may proceed on a purely electronic level, or whether it necessarily involves interactions with the phonons, has not been answered. Needless to say that understanding the mechanism behind the ultrafast relaxation would allow us to elucidate the nature of the spin excitations involved in this process. This represents a problem of considerable interest. In fact, it is not clear if the observed demagnetization is the result of vanishing or

strongly reduced local magnetic moments, or if it is the result of the excitation of spin waves and local fluctuations of local moments having almost conserved magnitudes.

1.2.5 Magnetization recovery at the picosecond timescale

For times longer than the demagnetization time ($\tau_{\mathrm{dm}} \sim 100$ fs) the electron temperature associated to the electronic translational and orbital degrees of freedom equilibrates with the lattice due to electron-phonon interactions (1, 2, 6, 13). As discussed above (see Section 1.2.2), this typically takes place within a few picoseconds. Similarly, the spin degrees of freedom come to equilibrium with electronic orbital or translational and lattice degrees of freedom on a long time scale of about 10–100 ps. The final equilibrium state is characterized by a recovery of the magnetization, although to somewhat reduced values due to the additional thermal disorder in the spin system (6).

1.2.6 Some open questions

In conclusion, despite intensive efforts in describing the physics behind the ultrafast laser-induced demagnetization, several fundamental questions remain open:

- Is this phenomenon a purely electronic effect, or does it necessarily require phonon excitations to a significant extent?
- Which are the essential microscopic mechanisms responsible for the spin relaxation, i.e., for the angular-momentum transfer away from the spin subsystem?
- What is the nature of the involved spin excitations?

In order to understand the complex underlying many-body physics, it is clear that one needs —besides enlightening experiments— a theory describing the fundamental microscopic mechanisms. The theoretical approaches proposed so far in the literature are discussed in Section 1.4. However, prior to this, it is worth comparing the ultrafast magnetization dynamics in ferromagnetic TMs, which is the subject of the present thesis, with similar phenomena observed in other materials.

1.3 Comparison with ultrafast magnetization dynamics in other materials

In this Section we briefly review the laser-induced ultrafast magnetization dynamics, which has been observed in materials other than transition metals (24). In addition, the basic physics behind these observations is compared with that described in the previous Section 1.2.

First of all, let us recall that the $3d$ TMs such as Fe, Co and Ni are itinerant ferromagnets. This means that the $3d$ electrons at the Fermi level are at the same time excited by the optical pulse and responsible for the magnetic properties. The situation is quite different in magnetic rare-earth metals such as Gd for which ultrafast demagnetization has been observed in many experiments (25, 26, 27, 28, 29). Gadolinium can be regarded as a prototype system for a Heisenberg or localized-electron ferromagnet in the sense that the half-filled $4f$ shell dominates magnetism. In fact, the large magnetic moment of $7\mu_B$ per atom is carried by the strongly localized $4f$ electrons. The FM coupling of neighboring $4f$ magnetic moments is then mediated by the $5d6sp$ conduction-band electrons. A small spin polarization of $0.55\mu_B$ per atom is induced in the $5d6sp$ valence band by means of intra-atomic $4f$–$5d$ exchange interactions. Therefore, the physics of magnetism in $3d$ TMs and in $4f$ rare-earth metals are fundamentally different: In the former case, the itinerant electrons having a significant band width ($\sim$ 5 eV) dominate magnetism, whereas in the latter case strongly localized $4f$ electrons are responsible for magnetism. This suggests that the physics of magnetization dynamics is also fundamentally different. Indeed, in the case of Gd the optical pump pulses excite the conduction electrons in the $5d6sp$ valence band and not the localized $4f$ electrons. It is commonly assumed that this excitation weakens the exchange interaction of neighboring magnetic moments and thus results in a reduction of magnetic order (25). Therefore, in order to understand the spin-relaxation mechanisms, it is indispensable to take into account energy and angular-momentum transfer processes between the $4f$ and the $5d6sp$ electrons (23). It is worth noting the separation of roles of the relevant electrons in Gd. The $4f$ electrons are responsible for magnetism, while the $5d6sp$ electrons mediate the FM coupling between localized $4f$ electrons. Moreover, only the $5d6s$ electrons interact with the laser field. This contrasts with the situation

in $3d$ TMs, where the same $3d$ electrons play these two roles. This renders the description of ultrafast demagnetization in Gd quite different from the case of itinerant ferromagnets such as Ni.

Let us now briefly discuss some experiments on magnetic alloys. For instance, the ultrafast demagnetization effect has been found in permalloys such as NiFe (30) and FeRh alloys (31). In particular, numerous works have been devoted to study the magnetization reversal in GdFeCo, both in thin films (32, 33, 34, 35, 36) and in small nanostructures (37). The material used in these experiments, GdFeCo, is a rare-earth – $3d$ TM ferrimagnetic alloy having two sublattices with opposite magnetization directions. One of them corresponds to the Gd atoms and the other to the $3d$ TM atoms (Fe and Co). It can be regarded as a Heisenberg ferrimagnet, since the magnetization in the two sublattices has opposite sign and is not compensated. In all these examples, the distinct sublattices are different in their dynamical and magnetic properties, i.e., they have different demagnetization times and magnetic moments. Consequently, the exchange interaction between the sublattices is essential for understanding the local and total magnetization dynamics.

Finally, one should mention the rare-earth orthoferrites, which have a strong temperature-dependent magnetic anisotropy due to their strong spin-orbit interaction. In this case, experiments have shown a somewhat slower picosecond laser-induced spin reorientation (38, 39, 40). Here, the observed magnetization dynamics is usually explained as the result of an ultrafast change of the magnetic anisotropy axis, which follows from the excitation and relaxation of both electron and phonon degrees of freedom.

The present brief and by far not exhaustive description of the experimental situation should already show that the physics of ultrafast magnetization dynamics is very manifold and the details of the observed behaviors depend on the kind of material involved in the experiment. In the following we consider only the fundamental case of ferromagnetic transition metals such as Ni, on which the pioneering experiments have been performed (1). In our views, understanding the microscopic physics in these metals should provide a basis for the explanation of ultrafast magnetization dynamics in other more complex materials.

1.4 Theoretical approaches

Several approaches to the theoretical description of ultrafast demagnetization in $3d$ TMs can be found in the literature. In this Section, we summarize a number of them, as far as we know, the most important ones. In doing so, we mainly focus on theories which aim to describe the microscopic mechanism of the spin-relaxation processes.

1.4.1 Phenomenological three-temperature model

In their pioneering work Beaurepaire *et al.* used a model based on three thermalized baths: electrons, spins and phonons (1). In this approach the time evolution of the electron-, spin-, and phonon-temperature is described by three coupled differential rate equations. It is worth noting that —from a fundamental point of view— the introduction of a temperature for the spin system, which is far from equilibrium on the fs time scale, seems quite questionable. Moreover, the interactions between the three baths are considered in a phenomenological manner. Therefore, this model does not answer the question about the nature of the dominant electron-spin interaction. In fact, it does not aim to provide any insight into the microscopic processes involved. In order to remove this limitation, a number of further theoretical works have been performed on the description of the corresponding microscopic physics.

1.4.2 Coherent demagnetization

At the early stages of the theoretical discussion of the microscopic origin of ultrafast demagnetization, it has been debated whether this phenomenon is a coherent or an incoherent effect. The question is whether the demagnetization occurs coherently with the exciting laser pulse, or whether it sets in independently of it, after the pulse absorption is over. In this context Zhang *et al.* presented a theory which describes the ultrafast spin dynamics as a coherent and cooperative effect of the external laser field and the internal SOC (15). The basic idea is that the SOC smears out the original identity of the triplet and singlet states, while the laser field takes advantage of this quantum-mechanical mixing as an avenue to induce demagnetization. In order to support theoretically this picture, Zhang *et al.* used a quantum-mechanical model including on-site Coulomb interaction, band structure, SOC and the external electric field representing the fs laser pulse. Phonons were neglected. By calculating the coherent time

evolution of the many-electron state and of the magnetic moment, they showed that a very large reduction of the magnetic moment, more than 40%, is accomplished on a time scale shorter than 20 fs.

In a later work, Bigot *et al.* also investigated the coherent ultrafast demagnetization induced by femtosecond laser pulses (9). According to their physical picture, the material polarization induced by the photon field interacts coherently with the spins. The corresponding mechanism has its origin in relativistic quantum electrodynamics.

However, experiments such as those reported in Ref. (7) showed that the quenching of the Ni exchange splitting mainly happens *after* the pump pulse is over. Moreover, it has been argued that the experimental number of photons involved in the laser field is not enough to be responsible for a coherent demagnetization (6). Consequently, a synchronic demagnetization during the absorption of the exciting laser pulse does not seem plausible. In fact, most of the other theoretical approaches consider the demagnetization as an incoherent thermal effect whose time scale is mainly determined by internal equilibration processes (24).

1.4.3 Electron-phonon spin-flip scattering

One of the main open questions in the physics of ultrafast magnetization dynamics is to understand if this phenomenon is a purely electronic effect, or if it involves to an important extent phonon excitations and electron-phonon interactions (see Section 1.2.6). Koopmans *et al.* considered the latter hypothesis and investigated the potential role of phonons in the ultrafast demagnetization process (18, 19). They coined the idea of regarding the lattice vibrations as a sink for angular momentum. The model that they introduced consists of three subsystems which interact with each other: (i) independent spin-less electrons, (ii) the lattice described by an ensemble of harmonic oscillators obeying Bose-Einstein statistics, and (iii) a spin system described by an ensemble of identical two-level systems, which obeys Boltzmann statistics and which is treated using a mean-field Weiss model for ferromagnetism (18). The lattice and spin subsystems are assumed to stay in internal equilibrium during the entire process. The most novel aspect of this work is that a finite spin-flip rate α_{sf} induced by the SOC is assigned to each electron-phonon scattering event. These electron-phonon spin-flip processes have been introduced following the ideas of Elliott and Yafet, which were very successful in the context of spin dynamics in semiconductors (41, 42). By solving the Boltzmann

equation for this simple model, they demonstrated that it is possible to have a demagnetization process with the proper subpicosecond time scale. This is shorter than the electron-phonon equilibration time, even though the demagnetization is mediated by phonon scattering. Consequently, the authors argued that phonon-mediated spin-flip-scattering in the spirit of the Elliott and Yafet model provides a significant contribution to the fs magnetic response (18, 19).

The theoretical foundation for this concept has been laid by the group of M. Fähnle (20, 21, 22). Based on their interpretation of the work of Stamm *et al.* (8), they excluded the direct transfer of spin angular momentum to orbital angular momentum within the electronic degrees of freedom as a fundamental process in the post-excitation dynamics (see Section 1.2.4). Instead, the transfer of electronic spin angular momentum to the angular momentum of the lattice is considered as the central spin-relaxation mechanism. This is achieved through Elliott-Yafet (EY) scattering events, i.e., through single-particle processes between an excited electron and a phonon. The group of Fähnle has extended Elliott-Yafet's theory of spin relaxation, originally formulated for nonmagnetic materials, to ferromagnets (21). In particular, a so-called EY relation has been derived which relates the spin-relaxation time to the spin-mixing parameter b^2, which measures the degree of spin mixing[1] for the involved single-particle states (20). Indeed, *ab initio* calculations of b^2 give quantitative support for the EY mechanism in the discussion of ultrafast demagnetization after fs laser-pulse absorption.

This spin-flip scattering mechanism has been successfully used in the microscopic three-temperature model (M3TM) of Koopmans *et al.* (23), which extends a previous model of Koopmans *et al.* (18). The new model considers the exchange of energy between three subsystems: electrons, lattice and spins, which separately always stay in thermal equilibrium. In this model, the spin relaxation is mediated by EY-like processes with a spin-flip rate α_{sf} for electron-phonon scattering events. The authors derived a compact differential equation for the magnetization, and phenomenologically described the overall dynamics of the three subsystems by a set of three coupled rate equations. In this way, the conservation and transfer of angular momentum was explicitly taken into account. By means of the M3TM Koopmans *et al.* succeeded to explain on the same footing the different demagnetization time scales observed in $3d$ TMs (e.g., Ni, Co) and in $4f$ rare earths like Gd [see Refs. (25, 26)].

[1] Notice that the spin of the electron is not a good quantum number due to spin-orbit interaction.

However, despite successful applications based on phonon-mediated spin-flip scattering, some open questions remain. First, within the performed calculations of the spin-mixing parameter b^2 the occupied and unoccupied single-electron states were determined using the effective density functional of the FM ground state at temperature $T = 0$. Thus, the change in the electronic structure following the fs laser-induced excitation has not been taken into account. Second, it is not clear if the EY theory can be applied to discuss ultrafast demagnetization because in these experiments the system is driven far away from equilibrium. In principle, the EY theory is only valid for a situation close to equilibrium (20). Third, within this approach electron-phonon scattering rates are determined by means of Fermi's golden rule, which considers long transition times. However, the demagnetization time of 100 fs is short in this regard, since it corresponds to less than one oscillation period of a typical phonon in Fe or Ni. Notice that on such short time scales the measurable energy distribution of the excited phonons has a very broad width. In other words, the scattered electron does not precisely know the phonon frequency. Therefore, it is not at all clear that Fermi's golden rule can be applied, since the latter implies energy conservation (22). Moreover, recent *ab initio* investigations indicate that the contribution of EY electron-phonon spin-flip scattering is probably too small to account for fs demagnetization in Nickel (43). To summarize, the applicability of the EY mechanism to the strong-nonequilibrium situation found during the ultrafast demagnetization remains an open question.

1.4.4 Spin-polarized electron diffusion

Recently, a semiclassical model for fs laser-induced demagnetization has been proposed, which involves spin-polarized excited-electron diffusion in the superdiffusive regime (44). This mechanism accounts for the experimentally observed demagnetization within $\tau_{\mathrm{dm}} \approx 200$ fs in Ni, without the need to invoke any angular-momentum dissipation channel. The picture here is that the majority spin electrons are diffused from the thin Ni film toward the Al substrate after laser excitation. However, Schellekens *et al.* have recently tested this mechanism by pumping Ni thin films both on insulating substrates and on conducting buffer layers (45). These experiments have shown that in simple FM films the laser-induced demagnetization is not dominated by this kind of spin transport to the substrate. Rather, the authors consider the ultrafast transfer of angular momentum away from the spin system to be local.

1.4.5 Further phenomenological models

Besides the three-temperature models, other phenomenological approaches have been proposed, which assume a thermalized electron subsystem and therefore consider the latter as a heat bath for the spin system. In this context one should mention the atomistic model developed by Kazantseva *et al.* (46, 47). In their approach the spin dynamics is modeled by using essentially an augmented Landau-Lifshitz-Gilbert (LLG) equation which accounts for precession and transversal relaxation of the magnetization vector $\vec{M}$. An alternative approach along these lines is the micromagnetic Landau-Lifshitz-Bloch (LLB) model (48, 49, 50), in which the magnetization is averaged over smaller atomistic scales. Consequently, the magnitude of $\vec{M}$ is not conserved anymore. In addition to the terms in the LLG equation of the model proposed in Refs. (46, 47), the LLB equation contains a temperature-dependent term describing the longitudinal relaxation of $\vec{M}$, which accounts for intrinsic magnetic fluctuations. Clearly, the longitudinal relaxation term is the key factor describing the subpicosecond magnetization dynamics in this approach. From the perspective of the present thesis it is important to note that these phenomenological models do not intend to explain the origin of the coupling between electrons and spins. No information on the microscopic spin-flip mechanism acting on a fs time scale is thus obtained.

1.4.6 Discussion

The previous brief summary clearly shows that a variety of approaches to laser-induced ultrafast magnetization dynamics has been proposed. Some involve purely electronic degrees of freedom and are driven by SOC, others are based on phonon-mediated EY-like spin-dependent electronic scattering, or even require long-range spin-density diffusion. However, the central microscopic mechanism of angular-momentum transfer responsible for the ultrafast decay or decrease of the total electronic spin is not yet thoroughly understood. In other words, the available theories —despite their success in several applications— cannot answer the fundamental open questions raised in Section 1.2.6 in a satisfactory manner.

One of the main theoretical difficulties of this problem is the complex many-body nature of the correlated spin-polarized *d*-electron system which, to crown it all, is far from equilibrium in a laser-induced dynamical state. The most popular theoretical

approaches in this field are based on the EY spin-flip scattering mechanism (20, 21, 22), which relies on a single-particle band-like or delocalized description of the electronic states. From our point of view, this appears to be a serious conceptual limitation, since magnetism in $3d$ TMs is known to be a true many-body effect, which results from non-trivial electronic correlations favoring localized electronic states and the formation of local magnetic moments.[1] Therefore, it seems urgent and most interesting to develop a many-body theory of laser-induced ultrafast demagnetization which takes into account the important electron correlations.

1.5 Goals of this work

The purpose of this work is to contribute to clarify the very fundamental questions concerning the microscopic mechanisms, which are responsible for the observed laser-induced ultrafast demagnetization in ferromagnetic TMs. To this aim, a many-body theory, which approaches this problem from a local perspective, is developed.

As a first preliminary step, we consider in Chapter 2 the strong-nonequilibrium situation between the electronic degrees of freedom, having a relatively high temperature proportional to the absorbed energy, and the spin or magnon degrees of freedom, which remain essentially in the ground state. This corresponds to the initial stage of the ultrafast demagnetization process subsequent to the absorption of an intense femtosecond laser pulse. The magnetic properties of the metal in this nonequilibrium situation are investigated. The role of the emerging very high local energy densities on the magnon dispersion relation and on the stability of local magnetic moments is quantified. In particular, we aim to understand the nature of the involved spin excitations by answering the following basic questions: Is the FM order still stable in such nonequilibrium situations? And, do the local magnetic moments at the $3d$ atoms remain stable? Do they vanish or not?

The results of Chapter 2 provide some important clues for the development of the theory. After this preliminary work, in Chapter 3 we develop our theory of laser-induced magnetization dynamics in TMs, which constitutes the main part of the thesis. To this

[1] The role of electronic correlations in the physics of ferromagnetism in $3d$ transition metals is discussed in Section 3.1.

aim we consider an electronic many-body Hamiltonian which takes into account interatomic hybridizations, Coulomb interactions and SOC on the same footing. The model is solved numerically by taking explicitly into account the electron correlations and the local magnetic degrees of freedom resulting from them (local magnetic moments). The most common theoretical approaches in this field use a single-particle delocalized description of the electronic states (see Section 1.4.6). Therefore, the development of a many-body theory is expected to fill this conceptual gap. Moreover, the present work complements the more widespread k-space approaches, such as the EY theory (20, 21), since it applies a local perspective to the problem. Within the proposed many-body model, the transfer between spin and orbital angular momenta, as well as its interplay with the electronic motion in the lattice, are treated exactly by respecting all microscopic conservation laws. For simplicity, the phonons are not explicitly taken into account, because we consider that at the fs time scale the electrons can be safely decoupled from the much slower lattice dynamics. The following applications of the model allow us to reveal to what extent a SOC-triggered angular momentum transfer on a purely electronic level —from the spins to the orbitals, i.e., from $\vec{S}$ to $\vec{L}$, and from $\vec{L}$ to the lattice— contributes as central spin-relaxation channel. The ground-state magnetic properties of the proposed many-body model, which are relevant for the laser-induced dynamics, are studied in Chapter 4. Subsequently, in Chapter 5, the time propagation of the excited many-body states is performed, from which the time evolution of the magnetization and other properties of the metal is obtained.

In summary, this work intends to deepen our understanding of the fundamental microscopic mechanisms, which are responsible for the angular-momentum transfer and the laser-induced ultrafast demagnetization. The conclusions drawn from our investigations are summarized in the final Chapter 6.

2

Spin excitations in the presence of high local energy densities

The very first consequence of the femtosecond laser pump pulse is the absorption of energy within the electronic degrees of freedom. As already discussed in the preceding Chapter (see Section 1.2.1), this happens without directly inducing any change in the magnetization of the FM material. After the short-time excitation, the absorbed energy is thermalized very rapidly within the electronic-translation and orbital system during a few femtoseconds, well before any significant thermalization of the spin degrees of freedom can take place. In other words, shortly after the excitation through the fs-laser pulse, we may regard the system as separated in two distinct reservoirs: first, the electronic-translation and orbital degrees of freedom, which are assumed to be thermalized to a temperature T_e proportional to the absorbed energy, and second, the spin or magnon degrees of freedom which remain essentially in the ground state.[1] This nonequilibrium situation, corresponding to the initial stage of the ultrafast demagnetization process, is the subject of this Chapter. We are particularly interested to see if the changes in the electronic structure due to the changes in occupation of the electronic translational degrees of freedom in the metal could change the magnon dispersion relation in a way that would favor the observed decrease of FM order. A further important aim of the present Chapter is to identify the nature of the spin excitations

[1] Phonon degrees of freedom are neglected, because (i) they are too slow to play an important role in the considered time range of a few femtoseconds after laser-pulse excitation, and (ii) in this Chapter we focus on the nature of the spin excitations.

at the various temperatures T_e.

As a first step toward these goals, in Section 2.1 we discuss some possible effects of the initial nonequilibrium situation on the magnetic order. Then, the theoretical background for these studies is described in Section 2.2. The results[1] are given in Section 2.3, followed by a discussion in view of the ultrafast demagnetization effect in Section 2.4.

2.1 Role of initial nonequilibrium on the magnetic order

For our purposes, the possible excitations in magnetic materials can be essentially divided into two categories: the first main source is given by collective spin waves, and the second one is represented by single-particle electronic excitations.[2] The two types of excitations correspond to complementary perspectives. The first one is a real-space coherent arrangement of local atomic moments, while the second one is an electronic excitation in k-space. Within the initial scenario —shortly after the fs laser-pulse absorption— the electronic system can be regarded as highly excited by temperature-induced spin-conserving electronic excitations, while the slower collective spin modes involving the local atomic magnetic moments should remain very weakly excited. The selection rules show that the electric field of the laser does not induce significant spin-flip electronic transitions.

It is interesting to notice that the initial strong-nonequilibrium situation with very high local electronic energy densities has a counterpart in the physics of ultrafast lattice dynamics: the effect of laser-induced nonthermal melting of Si (52, 53). This remarkable effect has been explained to be the result of transversal phonon softening in highly excited Si crystals, which leads to a dramatic change of the potential-energy surface for the ionic translational degrees of freedom and, thus, to ultrafast nonthermal melting of the crystal. A comparison with this phenomenon raises the question if, analogously, a FM metal that is highly excited electronically may suffer a catastrophic change in the shape of the magnon spectrum, e.g., a strong softening of particular spin waves. In this case, the high energy density in the electron subsystem could drive a transition

[1] The work described in this Chapter has been published in Ref. (51).

[2] Notice that in the literature single-quasiparticle spin-flip excitations are referred to as Stoner excitations. However, we do not consider this kind of excitation, since the laser-induced electric-dipole transitions preserve the spin.

from FM toward noncollinear (NC) or antiferromagnetic (AF) order, leading to a rapid decrease of the net magnetization.

In other words, it seems a priori possible that in such a strong-nonequilibrium situation the electronic excitations could have a considerable effect on the stability of magnetic order. It is therefore very interesting to understand the role of electron-hole excitations on the magnon modes, since it should provide very useful hints on the behavior of the spin system under high electronic excitation levels and on the possible mechanisms of the laser-induced magnetization dynamics. In particular, we intend to clarify to what extent the FM order and the local atomic magnetic moments are still stable for different initial nonequilibrium situations between electronic and spin degrees of freedom.

2.2 Theoretical description

The effects of electron-hole excitations on the magnon spectrum of $3d$ TMs are investigated by using *ab initio* density functional theory (DFT). We consider low-dimensional systems such as Fe, Co and Ni monoatomic wires and the two-dimensional square-lattice Ni monolayer. This is motivated by the fact that experiments also concern low-dimensional thin films. In addition, we expect that for lower coordination numbers the stability of magnetic order should be weaker than in the fully coordinated solid. Therefore, the effects of electronic excitations on the magnon spectra should be stronger. Moreover, there are clear indications for spiral magnetic order in $3d$ TM nanowires for some nearest-neighbor (NN) distances (54, 55). Exploring the possibility of a FM-to-spiral transition with increasing T_e is also challenging.

In all these cases, we implicitly consider a two-temperature model, describing the electron-translation and orbital subsystem on the one side and the spin subsystem on the other side. This separation of degrees of freedom is explained in more detail in Subsection 2.2.1. The finite-temperature DFT approach, which is used to compute the relevant electronic free energy, is described in Subsection 2.2.2. Finally, Subsection 2.2.3 provides a local perspective on the magnetic state.

2.2.1 Two-temperature view

A two-temperature model is applied in order to describe the initial nonequilibrium state. The electronic translational and orbital degrees of freedom are thermalized at a finite electronic temperature T_e, while the degrees of freedom associated with the local magnetic moments are taken into account by considering virtual spin-wave or magnon states. The very high energy densities induced by the laser absorption result in relatively high electronic temperatures T_e, which would not be meaningful in an equilibrium situation. For the purpose of calculating the dispersion relation of magnons, we consider NC spin configurations. These are represented by general spin-density wave (SDW) states having a wave vector $\vec{q}$. In this context, let us emphasize that the consideration of fixed T_e and of a single magnon mode $\vec{q}$ implies a separation of spin as well as electronic translational and orbital degrees of freedom. This is an idealization valid only just after the absorption, although the two baths remain afterwards in a nonequilibrium situation.

In the SDW states the local atomic magnetic moments $\vec{\mu}$ show a spiral configuration given by

$$\vec{\mu}(\vec{R}) = \mu_0 \left[\hat{e}_1 \cos(\vec{q}\cdot\vec{R}) + \hat{e}_2 \sin(\vec{q}\cdot\vec{R})\right] \tag{2.1}$$

(see Figure 2.1). Here, $\vec{R}$ denotes the position of the atoms carrying a local magnetic moment of magnitude μ_0, while $\hat{e}_1$ and $\hat{e}_2$ are orthogonal unit polarization vectors.[1] In this way, all the different FM, AF and spiral states can be described on the same footing.[2] It is important to note that the magnitude μ_0 of the local magnetic moments depends, in general, on T_e and $\vec{q}$. It is one of the goals of the present Chapter to quantify these dependences.

The SDW configurations are used to determine the magnetic order and the magnon dispersion relation of the system at a given electronic temperature T_e. The dispersion relations are derived from the electronic free energy Ω as a function of spin-wave vector $\vec{q}$ (56, 57). Special attention is given to the form of the spin-wave spectrum as a function

[1] Notice that all possible orientations of the orthogonal magnetization unit vectors $\hat{e}_1$ and $\hat{e}_2$ are equivalent, since the SOC has not been included neither in the spin model (see Section 2.2.3) nor in the *ab initio* DFT calculations. Therefore, the orientation of the spin $\vec{S}$ is completely decoupled from the orbital degrees of freedom and the geometrical structure of the sample.

[2] The collinear FM and AF states are included as particular limits. The former corresponds to small wave vectors ($q \simeq 0$), while the latter corresponds to wave vectors at the zone boundary ($q \simeq \pi/a$ in one dimension).

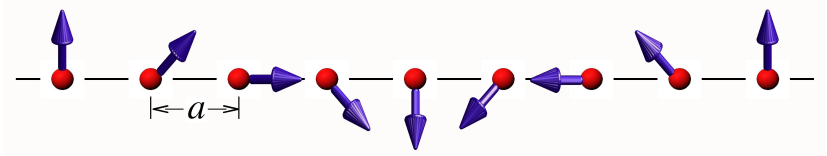

Figure 2.1: Spin-spiral state - Illustration of a spin wave with wave vector $q = 4\pi/a$ for a linear chain having nearest-neighbor distance a. The arrows indicate the local atomic magnetic moments $\vec{\mu}$.

of $\vec{q}$ and T_e, and to the changes in the local magnetic moments and their interatomic exchange couplings due to electronic excitations.

2.2.2 DFT approach to the electronic free energy

We have chosen a DFT based approach for the purpose of investigating the magnon dispersion relations at finite temperatures T_e, since DFT represents an efficient method of determining the electronic properties of matter from first principles. Let us first describe the very basics of this theory. The central point in DFT, as originally formulated by Hohenberg and Kohn, is that the electron density $\rho(\vec{r})$ replaces the wave function as the fundamental unknown of the many-body problem (58). Actually, this is a consequence of the existence of a bijective mapping between ground-state densities $\rho_{\mathrm{gs}}(\vec{r})$ and the corresponding ground-state wave functions. Practical calculations are usually based on the Kohn-Sham (KS) scheme which reduces the interacting N_e-electron problem to a set of self-consistent single-particle equations (59). Within the corresponding KS auxiliary single-particle system, the electron density $\rho(\vec{r})$ is expressed in terms of N_e occupied KS orbitals $\phi_k(\vec{r})$ as

$$\rho(\vec{r}) = \sum_{k=1}^{N_e} |\phi_k(\vec{r})|^2 \quad . \tag{2.2}$$

All contributions of the non-trivial electronic exchange and correlation energy, as well as correlation contributions to the kinetic energy, are included in the so-called exchange-correlation energy functional $E_{\mathrm{xc}}[\rho]$. The ground-state density and other ground-state properties are then obtained by minimizing the total energy functional $E[\rho]$, including $E_{\mathrm{xc}}[\rho]$, with respect to densities $\rho(\vec{r})$ of the form (2.2). The KS transformation is in principle exact, thus allowing one to take into account all electronic correlation effects. Unfortunately, the universal functional $E_{\mathrm{xc}}[\rho]$ is unknown. Consequently, the results

of applications depend on the available approximations. We shall not discuss here the various proposed approximations to $E_{\rm xc}[\rho]$, since this goes beyond the scope of the present thesis. The interested reader is referred to the very good introductions to DFT given in Refs. (60, 61).

DFT has been originally formulated as a ground-state theory, i.e., it is based on the minimization of the total energy E. However, for $T_e > 0$ it is the electronic free energy Ω what becomes minimal in the equilibrium state. For this case, Mermin developed a finite-temperature extension of DFT (62), which we apply in order to calculate Ω and the magnon dispersion relation. Following Janak's fractional-occupation number formulation (63), we express the electronic density as

$$\rho(\vec{r}) = \sum_k \eta_k \ |\phi_k(\vec{r})|^2 \ , \tag{2.3}$$

where $0 \leq \eta_k \leq 1$ are the occupation numbers of the Kohn-Sham orbitals $\phi_k(\vec{r})$. The electronic free energy[1] is given by

$$\Omega[\rho] = E[\rho] - T_e S_e[\rho] - \varepsilon_\mu N_e \ , \tag{2.4}$$

where $E[\rho]$ is the internal electronic-energy functional including the exchange-correlation functional $E_{\rm xc}[\rho]$, ε_μ is the chemical potential, $N_e = \sum_k \eta_k$ is the number of particles, and $S_e[\rho]$ is the electronic entropy, which we approximate by the non-interacting expression

$$S_e[\rho] = -k_B \sum_k \left\{\eta_k \ln \eta_k + (1-\eta_k)\ln(1-\eta_k)\right\} \ . \tag{2.5}$$

In other words, the exchange and correlation contributions to $S_e[\rho]$ are included in $E_{\rm xc}[\rho]$. For each magnetic configuration of the system, which in our case is characterized by the spin-wave vector $\vec{q}$, Ω is minimized with respect to $\rho(\vec{r})$ by varying η_k, $\phi_k(\vec{r})$ and $\phi_k^*(\vec{r})$ independently. Recalling Janak's theorem (63), namely, $\partial E/\partial \eta_k \,|_{\{\phi_k\}} = \varepsilon_k$, where ε_k refers to the KS eigenvalues, and computing $\partial S/\partial \eta_k$ from Eq. (2.5), one obtains

$$\frac{\partial \Omega}{\partial \eta_k} = \varepsilon_k - \varepsilon_\mu - k_B T_e \ln\left(\frac{1-\eta_k}{\eta_k}\right) \ . \tag{2.6}$$

[1]Notice that usually, Ω as given by Eq. (2.4) is called *grand potential* of the grand-canonical ensemble. Instead of that, we use the notation of *free energy* for Ω, since we consider definite numbers of electrons N_e for the DFT calculations. The reference to the grand-canonical ensemble is justified by the equivalence between the canonical and the grand-canonical ensembles in the thermodynamic limit.

This implies that at equilibrium $\eta_k = f(\varepsilon_k)$, where $f(\varepsilon)$ is the Fermi function for the given ε_μ. The variation with respect to $\phi_k^*(\vec{r})$ yields the usual KS equations (59), where $\rho(\vec{r})$ is given by Eq. (2.3) with the Fermi-Dirac occupation numbers $\eta_k = f(\varepsilon_k)$. These equations give the following practical minimization scheme for the free energy Ω. First, for each $\vec{q}$ the KS equations are solved self-consistently by setting the occupations η_k of the KS orbitals according to the Fermi distribution at the given electronic temperature T_e. This step can be solved numerically by using a standard DFT program, e.g., the Vienna *ab initio* simulation package (VASP) (64, 65) or Wien2K (66, 67). The electron density $\rho(\vec{r})$ is thereby given by Eq. (2.3). As discussed above, this procedure is equivalent to a direct minimization of Ω. The internal electronic energy E is obtained in the same way as in a ground-state calculation. The electronic entropy S_e is given by Eq. (2.5) in terms of the self-consistent occupations η_k. Before discussing the *ab initio* results in Section 2.3, it is useful to analyze the $\vec{q}$-dependence of Ω from a local perspective in terms of effective exchange interactions between the local magnetic moments.

2.2.3 Effective exchange interactions

The local magnetic moments $\vec{\mu}(\vec{R})$ are the result of the spin polarization of the $3d$ electrons, and are therefore essentially localized within the atomic Wigner-Seitz spheres. This suggests a local interpretation of the free energy $\Omega(\vec{q})$ by introducing effective temperature-dependent exchange interactions $J_{\vec{R},\vec{R}'}$ between neighboring moments. Consequently, we propose a classical Heisenberg-like spin model for the free energy given by

$$\Omega(\vec{q}) = -\frac{1}{2}\sum_{\vec{R}}\sum_{\delta\vec{R}\neq 0} J_{0,\delta\vec{R}}\,\hat{\mu}_{\vec{R}}\cdot\hat{\mu}_{\vec{R}+\delta\vec{R}}\ , \tag{2.7}$$

where $\delta\vec{R}$ are lattice vectors to neighboring atoms, $\hat{\mu}_{\vec{R}}$ denotes the unit vector along the magnetic moment $\vec{\mu}(\vec{R})$ of atom $\vec{R}$, and $J_{0,\delta\vec{R}}$ are the effective exchange couplings. Notice that any temperature dependence of the magnitude of the local moments is effectively included in the coupling parameters $J_{0,\delta\vec{R}}$.

For a periodic one-dimensional (1D) chain having interatomic distance a, the dispersion relation derived from Eq. (2.7) reads as

$$\frac{\Omega(q)}{N_a} = \frac{\Omega_0}{N_a} + \sum_{\delta=1}^{\nu} J_{0\delta}\left[1-\cos(\delta q a)\right]\ , \tag{2.8}$$

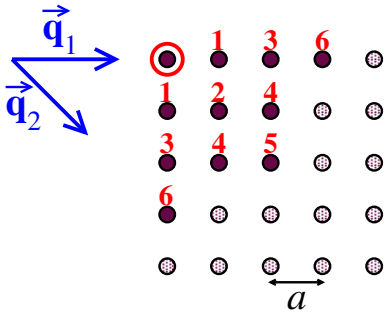

Figure 2.2: Geometry of the 2D Ni square lattice - The numbers indicate the different non-equivalent nearest neighbors δ of the atom 0, and a denotes the lattice constant. The vectors $\vec{q}_1$ and $\vec{q}_2$ illustrate the considered SDW propagation directions along NN and second-NN bonds, respectively.

where N_a stands for the number of atoms in the periodic cell. As we shall see, taking into account the couplings up to fourth NNs ($\nu = 4$) provides a very accurate description of all the *ab initio* dispersion relations. For future reference it is useful to introduce the exchange free energy $\Delta\Omega_X = \Omega(\pi/a) - \Omega_0$, given by the difference in Ω between the AF and FM configurations. A stable FM configuration is obtained when $\Omega(q)$ has a local minimum at $q = 0$, while a stable AF configuration corresponds to a local minimum at $q = \pi/a$.

For the calculations on periodic two-dimensional (2D) square lattices we consider two different SDW propagation directions, namely, $\vec{q}_1$ along a NN bond $\vec{a}$, and $\vec{q}_2$ along a second-NN bond $\vec{a}'$, where $a' = \sqrt{2}a$ (see Figure 2.2). Since the magnetic couplings $J_{0,\delta\vec{R}}$ in Eq. (2.7) vanish for large interatomic distances $\delta\vec{R}$, it is reasonable to restrict the non-zero couplings to sixth NNs $J_{0\delta}$ ($\delta = 1, \ldots 6$). The free energy $\Omega(\vec{q})$ can then be written as

$$\begin{aligned}\frac{\Omega(\vec{q}_1)}{N_a} = \frac{\Omega_0}{N_a} &+ (J_{01} + 2J_{02} + 2J_{04})\,(1 - \cos q_1 a) \\ &+ (J_{03} + 2J_{04} + 2J_{05})\,(1 - \cos 2q_1 a) \\ &+ J_{06}\,(1 - \cos 3q_1 a)\end{aligned} \tag{2.9}$$

for SDWs along $\vec{a}$, and as

$$\begin{aligned}\frac{\Omega(\vec{q_2})}{N_a} = \frac{\Omega_0}{N_a} &+ (2J_{01} + 2J_{04})\left[1 - \cos\left(q_2\frac{a}{\sqrt{2}}\right)\right] \\ &+ (J_{02} + 2J_{03})\left[1 - \cos\left(2q_2\frac{a}{\sqrt{2}}\right)\right] \\ &+ (2J_{04} + 2J_{06})\left[1 - \cos\left(3q_2\frac{a}{\sqrt{2}}\right)\right] \\ &+ J_{05}\left[1 - \cos\left(4q_2\frac{a}{\sqrt{2}}\right)\right]\end{aligned} \tag{2.10}$$

for SDWs along $\vec{a}'$. As we shall see in the following Section, comparison with *ab initio* calculations shows that this model is pertinent and that the effective exchange interactions are indeed short ranged.

2.3 Results

This Section presents the results obtained by using the finite-temperature DFT method (see Section 2.2). The calculations aim to clarify the role of a high electronic energy density or large electronic temperature T_e, which describes electron-hole excitations, on the magnon modes. Results are given for representative low-dimensional $3d$ TMs, namely, for Fe, Co and Ni monoatomic wires, and for the square-lattice Ni monolayer. In the following subsections the magnetic properties are discussed as a function of T_e. Special attention is given to the nature of stable magnetic order, to the spin-wave spectrum, and to the underlying exchange interactions between the local moments. The main computational details on the *ab initio* DFT calculations may be found in Appendix A.

2.3.1 Fe chains

In the case of 1D Fe, two different bond lengths are investigated. First, we consider the relaxed free-standing distance $a = 2.25$ Å. The corresponding ground-state magnetic order is a spin-spiral state. In addition, we consider also the bulk NN distance $a = 2.48$ Å showing a FM ground state, since the systems involved in typical demagnetization experiments also have FM order.

Figure 2.3 shows the spin-wave spectrum for the relaxed distance $a = 2.25$ Å. For different representative electronic temperatures $k_B T_e \leq 500$ meV the free energy Ω

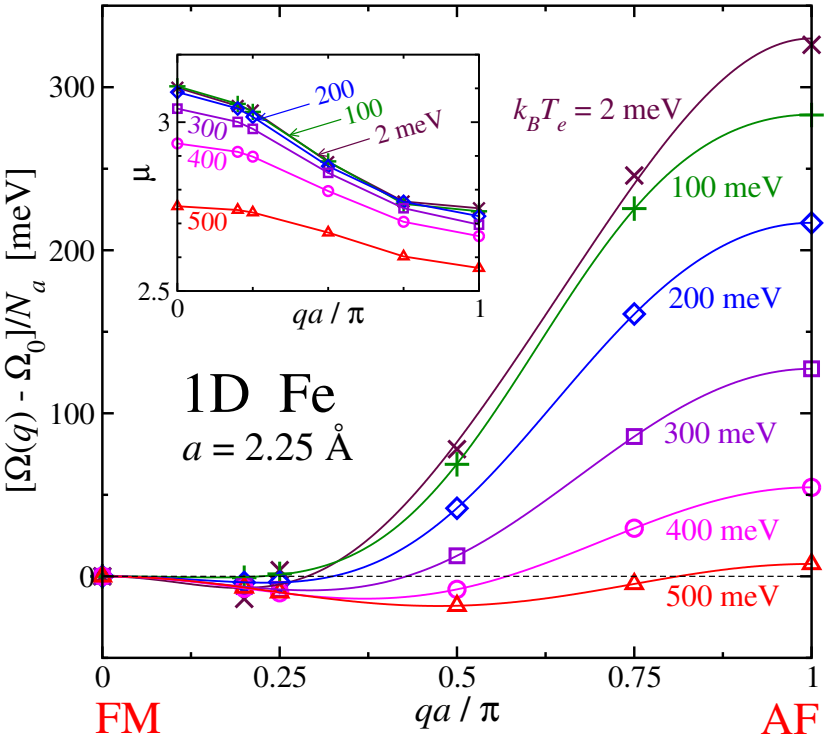

Figure 2.3: Spin-wave spectrum of the relaxed Fe chain - The electronic free energy per atom $\Omega(q)/N_a$ relative to the FM state ($q = 0$) is shown for 1D Fe wires (NN distance $a = 2.25$ Å) as a function of the spin-density wave vector q and electronic temperature T_e. The curves are the fits of *ab initio* results (symbols) to the classical spin model (2.8). The inset figure illustrates the corresponding local magnetic moment μ within the atomic Wigner-Seitz spheres.

relative to the FM case ($q = 0$) is given as a function of the SDW vector q. The symbols indicate the DFT results, while the curves represent the fit to a classical Heisenberg model including up to 4th NN interactions (see Section 2.2.3). The results for $k_BT_e = 2$ meV show that the ground state is a spin-spiral state having a wave vector $q_m \simeq \pi/5a$ and an energy around 14 meV per atom lower than the FM one. The wave vector q_m yielding the lowest Ω increases with increasing T_e and reaches $q_m \simeq \pi/2a$ for $k_BT_e = 500$ meV. Moreover, with increasing electronic temperature T_e, the free energy difference between the AF and FM configurations, also referred to as the exchange free energy, decreases monotonously from $\Delta\Omega_X = 326$ meV for $k_BT_e = 2$ meV to a nearly vanishing value of $\Delta\Omega_X = 8$ meV per atom for $k_BT_e = 500$ meV. Notice that this decrease is not caused by a drastic reduction of the magnitude of the local

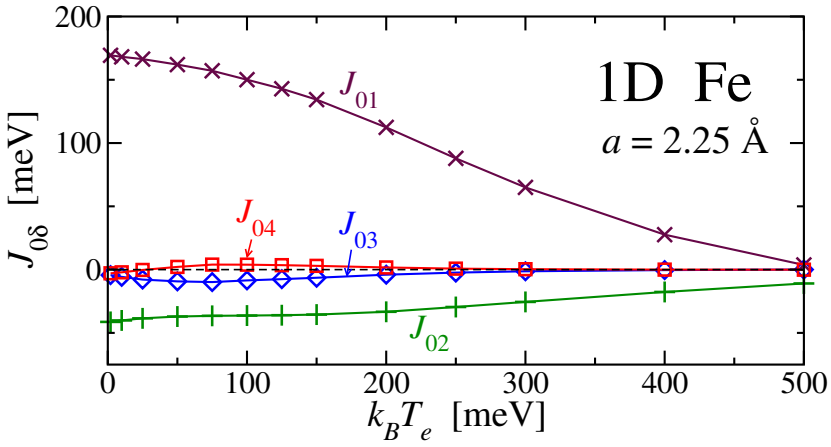

Figure 2.4: Effective exchange interactions in the relaxed Fe chain - The exchange couplings $J_{0\delta}$ between a local magnetic moment and its δth NN are given as a function of the electronic temperature T_e. The results correspond to Fe chains having NN distance $a = 2.25$ Å. See also Figure 2.3.

magnetic moments μ shown in the inset of Figure 2.3.[1] Indeed, μ is only reduced by less than 12% as one increases q from FM to AF order, or as T_e is increased, even for the largest considered electronic temperatures. The local moments thus show a remarkable stability. Moreover, the general form of the spectra remains essentially unchanged for all T_e. Therefore, in all cases the spiral SDW represents the most stable configuration.

A more detailed understanding of the magnetic order and spin-wave dispersion relation is provided by the effective exchange couplings $J_{0\delta}$ between a local moment and its δth nearest neighbor. In Figure 2.4 the temperature dependence of $J_{0\delta}$ in the relaxed Fe chain is shown. One observes that the second NN coupling J_{02} is not only negative (opposite to J_{01}) but also quantitatively important at all T_e. The ratio $|J_{02}|/J_{01}$ ranges from 0.24 at $k_B T_e = 2$ meV to 0.64 for $k_B T_e = 400$ meV. This leads to a competition between the FM and AF states which tends to favor the intermediate NC spiral arrangement. In other words, the spin-spiral configurations are the result of magnetic frustrations between NN and second NN couplings $J_{01} > 0$ and $J_{02} < 0$. The former favor parallel spin alignment between first NNs, while the latter favor antiparallel alignment between second NNs. The most significant temperature dependence of the

[1] The DFT results verify that the magnitudes $|\vec{\mu}(\vec{R})|$ of atomic moments are independent of the atomic site $\vec{R}$. This agrees with the model Equation (2.1), and gives us the motivation to consider in the following μ as the site-independent local-moment magnitude.

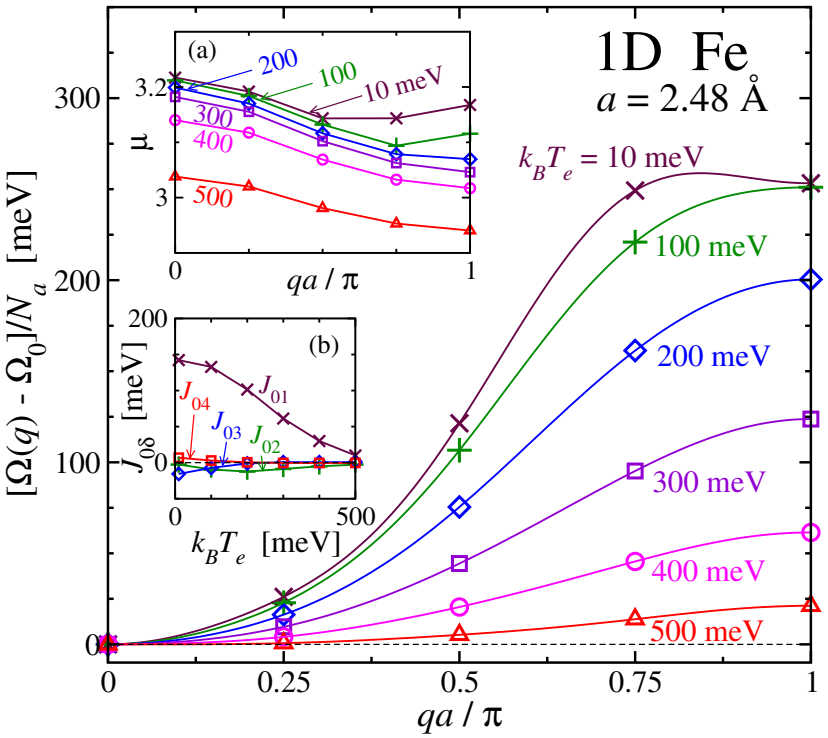

Figure 2.5: Spin-wave spectrum of Fe chains with bulk NN distance - The electronic free energy $\Omega(q)$ is given relative to the FM case ($q = 0$) for 1D Fe chains ($a = 2.48$ Å) as a function of q and T_e. The curves are the fits of *ab initio* results (symbols) by using a classical Heisenberg spin model [see Eq. (2.8)]. The inset (a) shows the local magnetic moment μ, while inset (b) shows the magnetic couplings $J_{0\delta}$ between a local moment and its δth NN.

effective exchange interactions is the rapid decrease of J_{01} with increasing T_e. This reduces the stability of the FM state relative to the AF state, and thus explains the decrease of $\Delta\Omega_X = \Omega(\pi/a) - \Omega_0$ with increasing T_e (see Figure 2.3).

As a second example, we consider Fe chains having a larger bond length $a = 2.48$ Å, which corresponds to the bulk NN distance. This lattice parameter is close to the one expected for epitaxial growth on noble metal surfaces. Figure 2.5 shows the corresponding $\Omega(q)$ for different electronic temperatures T_e. In contrast to the relaxed distance $a = 2.25$ Å, the ground-state is here FM over the whole range of studied temperatures. This can be interpreted in terms of the magnetic couplings $J_{0\delta}$ given in the inset (b) of Figure 2.5. In fact, the AF second NN coupling J_{02}, which is usually at the origin of the stability of spin-spiral waves, is now negligible in comparison to the large FM

coupling J_{01}. As for the relaxed bond length (Figure 2.3), the exchange free energy decreases from $\Delta\Omega_X = 253$ meV, for $k_BT_e = 10$ meV, down to $\Delta\Omega_X = 21$ meV for $k_BT_e = 500$ meV. Again, this decrease is not related to an important reduction of the local magnetic moments μ, since these remain almost constant ($\mu \approx 3\mu_B$) within the considered temperature range [see the inset (a) of Figure 2.5]. Our results confirm therefore the idea that the local magnetic moments in $3d$ TMs preserve their identity, and that spin-wave excitations, or more generally spin fluctuations, remain the relevant magnetic excitations even at very high electronic temperatures.

2.3.2 Co and Ni chains

In contrast to Fe, the Co and Ni chains have FM ground states at their respective relaxed bond lengths $a = 2.15$ Å and $a = 2.17$ Å (54, 55, 68). It is therefore interesting to investigate them in order to quantify to what extent the stability of the FM order can be modified by increasing the electronic temperature. The results presented in Figure 2.6 show that $\Omega(q)$ remains FM-like in Co and Ni chains as long as the local magnetic moments μ are not zero. In Co, this is the case for all considered temperatures, whereas in Ni μ vanishes almost for all q if $k_BT_e \geq 400$ meV [see the insets (a) and (c) of Figure 2.6]. A vanishing μ implies the absence of magnetism, in which case the value of q is irrelevant. One concludes that in these chains no magnetic-phase transitions occur with increasing T_e.

In Co the NN magnetic coupling J_{01} is FM. It dominates clearly over the second NN coupling J_{02}, as well as over the couplings with further neighbors [see inset (b)]. This explains that $\Omega(q)$ increases monotonously with q. In Ni chains J_{02} is not negligible. However, both J_{01} and J_{02} are positive [see inset (d)]. Consequently, there are no frustrations and the dispersion relation is FM-like. It is interesting to note that AF order ($q = \pi/a$) cannot be realized in Ni chains, at least as long as the size of the local moments is determined self-consistently. Indeed, as shown in the inset (c) of Figure 2.6, one obtains $\mu = 0$ for $q = \pi/a$, even at the lowest T_e. One should keep in mind that for vanishing spin moments $\mu \to 0$ within the Wigner-Seitz spheres the notion of effective exchange interactions between local moments breaks down. The electronic free energy Ω would be independent of q and, therefore, the Heisenberg model becomes inappropriate as a means to fit the *ab initio* free energies. This is reflected in the somehow artificial behavior of the Heisenberg fits for low temperatures and large SDW vectors at the AF

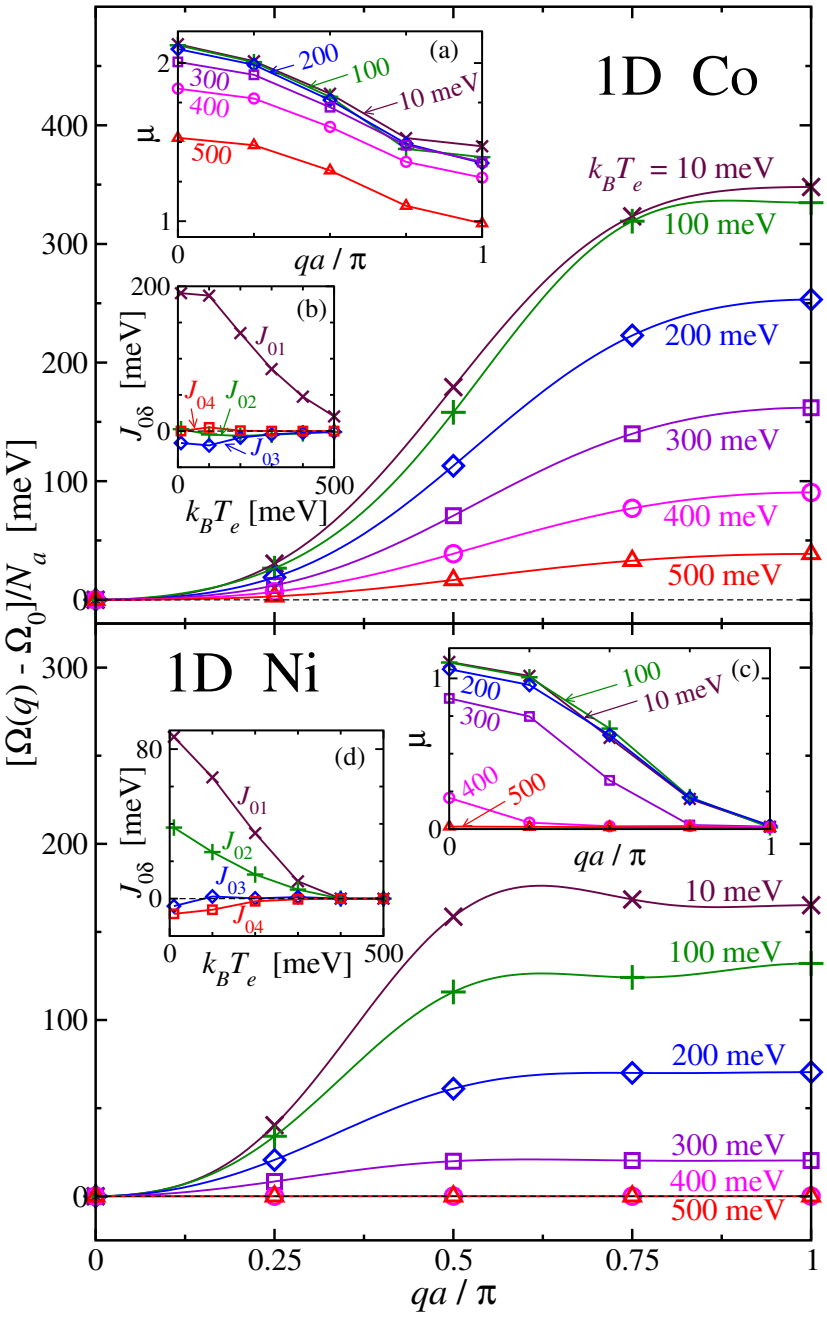

Figure 2.6: Magnon dispersion relation of relaxed Co and Ni chains - The electronic free energy $\Omega(q)$ is given relative to the FM case Ω_0 as a function of q and T_e. The considered bond lenghts of the Co and Ni chains are $a = 2.15$ Å and $a = 2.17$ Å, respectively. The curves represent model fits of *ab initio* results (symbols) according to Eq. (2.8). The insets (a) and (c) show the corresponding local magnetic moments μ, while the insets (b) and (d) show the effective magnetic couplings $J_{0\delta}$ between the different NNs.

zone boundary (see the Ni free-energy curves for $k_B T_e \leq 100$ meV and $q \gtrsim 3\pi/4a$ in Figure 2.6). As T_e increases beyond $k_B T_e \simeq 300$ meV, one observes that μ vanishes above a critical value q_c, which decreases with increasing T_e until $\mu = 0$ for all q. This behavior is a consequence of the relatively large d-band filling and comparatively small exchange splitting of the Ni atoms.

Exception made of Ni for large T_e and $q \simeq \pi/a$, it is important to observe that the local magnetic moments are remarkably stable up to considerably large electronic temperatures. For example in Co (Ni) chains, μ remains almost unaffected by increasing T_e up to $k_B T_e \simeq 300$ meV (200 meV). This corresponds to electronic energy densities which go far beyond those usually involved in the demagnetization experiments (1, 2, 7, 23). Therefore, the temperature-induced decrease of the FM-AF spin-flip energy $\Delta\Omega_X = \Omega(\pi/a) - \Omega_0$ is not a consequence of vanishing μ (e.g., in Co $\Delta\Omega_X$ decreases from 350 meV for $k_B T_e = 10$ meV to 250 meV per atom for $k_B T_e = 200$ meV). A similar behavior has been observed in Fe chains.

2.3.3 Two-dimensional Ni lattices

In the previous Section 2.3.2 we found that in Ni wires the spin excitation energies decrease significantly with increasing electronic temperature by keeping the FM order stable. We would like to investigate if similar trends hold in 2D Ni lattices. For this purpose we consider a free-standing Ni monolayer corresponding to the surface of thin Ni films grown on Ag(100) (3). In this sense, the considered Ni layer aims to model the TM films used in a large number of demagnetization experiments. Since Ag has a fcc structure with lattice constant $d = 4.086$ Å, the resulting epitaxial (100)-monolayer is a square lattice with NN distance $a = d/\sqrt{2} = 2.89$ Å.

In Figure 2.7, the calculated magnon dispersion relation of the Ni monolayer is given for two different propagation directions of the SDWs, namely, $\vec{q}_1$ along a NN bond $\vec{a}$ and $\vec{q}_2$ along a second NN bond $\vec{a}'$. In the latter case the distance of adjacent planes perpendicular to $\vec{q}_2$ is $a/\sqrt{2}$. Analogously to the 1D chains, the *ab initio* results for the electronic free energy $\Omega(\vec{q})$ (symbols) are fitted by using a classical Heisenberg-like spin model described in Section 2.2.3 (curves). Thereby, exchange couplings between local moments up to sixth NNs are taken into account (see Figure 2.2). The main conclusion inferred from Figure 2.7 is that for both propagation directions the spin-wave spectra are qualitatively similar to 1D Ni. The FM order is stable for all electronic

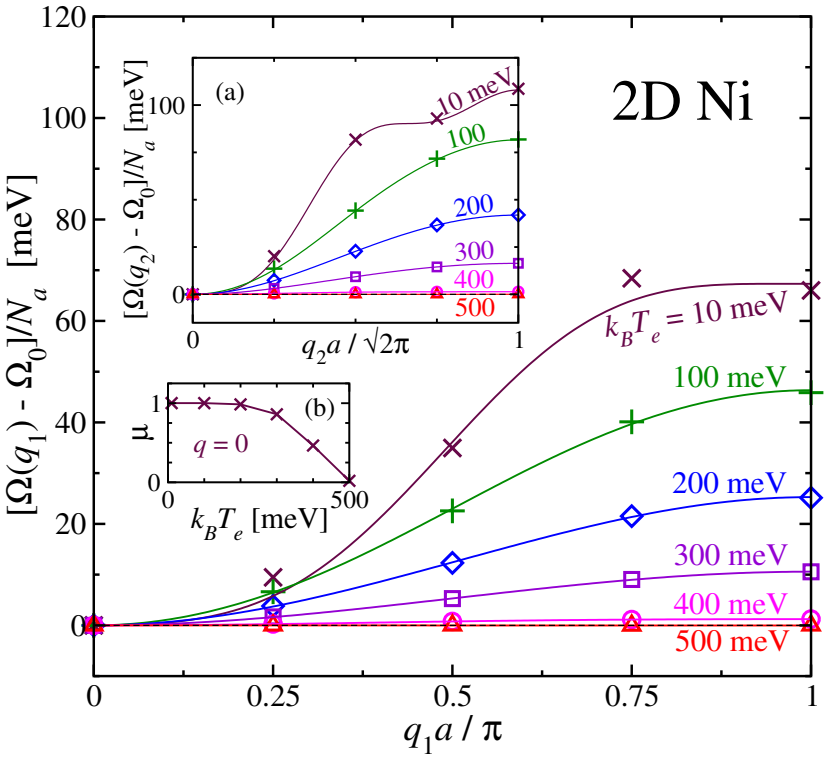

Figure 2.7: Magnon dispersion relations in the 2D Ni square lattice - For different electronic temperatures T_e the electronic free energy $\Omega(\vec{q})$ relative to the FM case is shown as a function of the SDW vector $\vec{q}_1$, which points along a NN connection. The lattice parameter of the Ni square lattice is $a = 2.89$ Å. The curves are fits of *ab initio* results (symbols) by using the classical spin model (2.7). The inset (a) shows the SDW spectrum for $\vec{q}_2$ along second NN connections. In the inset (b) the local magnetic moment μ in the FM configuration is given as a function of T_e.

temperatures T_e, as long as the local magnetic moments μ are not vanishing ($k_B T_e \leq$ 400 meV). See the inset (b) of Figure 2.7, where μ is given for $q = 0$. This means that no magnetic-phase transitions seem to be triggered by increasing the electronic temperature (electron-hole single-particle excitations). Comparison with 1D chains shows a reduction of the exchange free energy $\Delta\Omega_X$. In fact, in the Ni monolayer we find $\Delta\Omega_X = \Omega(q_1 = \pi/a) - \Omega_0 = 66$ meV and $\Delta\Omega_X = \Omega(q_2 = \sqrt{2}\pi/a) - \Omega_0 = 109$ meV per atom for the $\vec{q}_1$ and $\vec{q}_2$ propagation directions, whereas $\Delta\Omega_X = 165$ meV per atom for the linear chain. This is most probably a consequence of the larger NN distance $a = 2.89$ Å of the monolayer corresponding to the Ag(100) substrate, as compared to the relaxed NN distance $a = 2.17$ Å of the linear Ni chain.

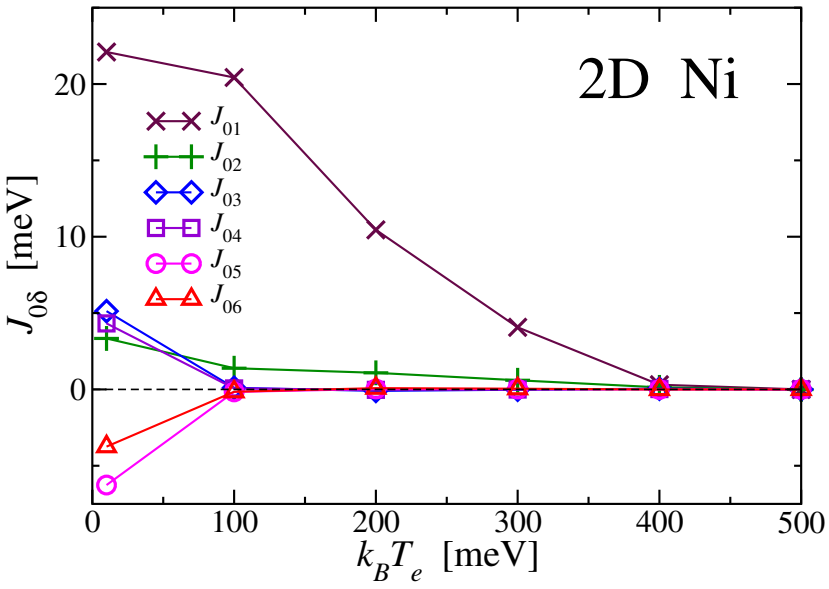

Figure 2.8: Effective exchange interactions in the Ni square lattice - The exchange couplings $J_{0\delta}$ between the NN local moments in a Ni monolayer ($a = 2.89$ Å) are shown as a function of the electronic temperature T_e. See also Figure 2.7.

Figure 2.8 shows the magnetic coupling constants $J_{0\delta}$ obtained by applying Eqs. (2.9) and (2.10) to the spin-wave spectra of Figure 2.7. At low temperatures (e.g., $k_B T_e =$ 10 meV) the $J_{0\delta}$ up to fourth NN are positive, thus adding up constructively to the increase of $\Omega(q)$ with increasing q. Only J_{05} and J_{06} are negative. Notice, moreover, that these couplings almost always contribute to $\Omega(q)$ in combination with other positive couplings, for example as $J_{04} + J_{06}$ for the third row perpendicular to $\vec{q}_2$ (see Figure 2.2). Thus, they do not lead to any significant frustration. One should mention that for large SDW vectors ($q_1 \geq 3\pi/4a$ and $q_2 \geq 3\sqrt{2}\pi/4a$) and low temperatures ($k_B T_e = 10$ meV) the DFT calculations are very difficult to converge quite accurately. This might be at the origin of the oscillations of $\Omega(\vec{q})$ obtained for the Ni monolayer for large q [see inset (a) in Figure 2.7]. Therefore, the values of the exchange couplings $J_{0\delta}$ with $\delta = 3$–6 derived from the Heisenberg fits are for $k_B T_e = 10$ meV not very reliable and might probably be overestimated. For $k_B T_e \geq 100$ meV, only the first and second NN couplings are not zero. These results for $J_{0\delta}$ explain the FM-like dispersion relation of the Ni monolayer from a local perspective.

2.4 Delocalized versus local magnetic excitations during the ultrafast demagnetization process

In this Chapter, the effects of high levels of electronic excitations on the stability of the magnetic order and on the magnon spectrum of low-dimensional TMs have been investigated in the framework of DFT. This physical situation corresponds to the nonequilibrium state typically found just after the absorption of a strong laser pulse, where the electronic degrees of freedom have a finite, potentially large temperature T_e, and the collective modes of the local atomic magnetic moments $\vec{\mu}(\vec{R})$ are non-excited or weakly excited. Some important conclusions can now be drawn from the results given in the previous Section 2.3, in particular concerning the magnetic moments and the nature of spin excitations during the ultrafast demagnetization process.

The T_e dependences of the dispersion relations $\Omega(q)$, which have been determined for Fe, Co and Ni chains, and the Ni monolayer, do not show any signs of a phase transition or breakdown of the magnetic order: In the case of Co and Ni chains, the FM order is stable for all T_e, except in Ni for $k_B T_e \geq 400$ meV where the local magnetic moments μ vanish. Fe chains with relaxed equilibrium distance show a NC spiral ground state already for $T_e = 0$ and for all T_e. In the Ni square monolayer the FM order is stable for all temperatures $k_B T_e \lesssim 400$–500 meV. Since the general shape of the magnon spectrum remains essentially unchanged, one concludes that a high level of thermal excitation of the electronic translational degrees of freedom (electron-hole excitations) does not result in any breakdown or decrease of the FM order. In other words, a transition from FM order toward some other type of AF or NC order, which is triggered simply by an electronic equilibrium state at high energy density or temperature, does not seem to be a plausible explanation for the observed laser-induced ultrafast demagnetization.

Furthermore, one generally observes for all the considered systems, that the exchange free energy $\Delta\Omega_X$, as measured by the difference in Ω between AF and FM configurations, decreases with increasing electronic temperature T_e. This decrease in the spin-excitation energies obviously favors the spin-flip processes subsequent to an ultrafast heating of the electron subsystem. Except for the special case of Ni wires at very high T_e, the decrease in $\Delta\Omega_X$ is not the result of an important reduction of the local magnetic moments μ. In contrast, the local moments remain quite stable, even at very high levels of laser-induced energy density (often up to $k_B T_e \simeq 500$ meV).

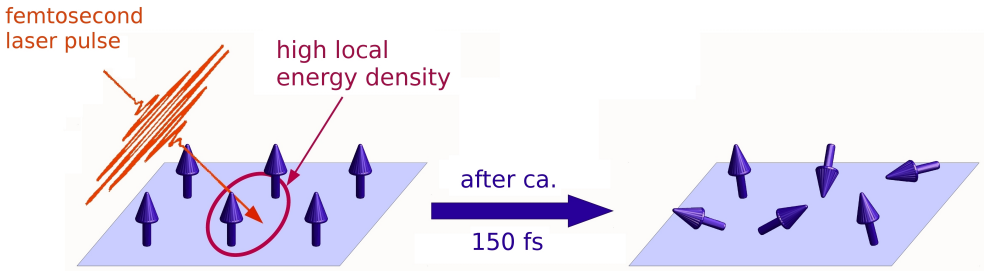

Figure 2.9: Illustration of local spin fluctuations during the demagnetization process - The demagnetized state following laser absorption should be regarded as a disordered configuration of local atomic magnetic moments, whose magnitude remains essentially unchanged.

The large stability of μ indicates that in the experimentally used thin TM films, these local magnetic degrees of freedom should preserve their identity throughout the entire demagnetization process. This means that spin waves, or more generally spin fluctuations, should be regarded as very important processes in the magnetization dynamics. In other words, the ultrafast demagnetization in TMs should be regarded as the result of local spin fluctuations, i.e., disorder in the orientation of the atomic magnetic moments. This physical picture is illustrated in Figure 2.9.

To summarize, we conclude that the dominant magnetic excitations during the demagnetization process should have local character, i.e., they are fluctuations of localized atomic magnetic moments. Consequently, any successful theory of ultrafast magnetization dynamics in TMs should take into account the important local magnetic moments. However, most of the so far available approaches to this effect are based on delocalized electronic states, for instance, the EY spin-flip scattering mechanism (20, 21, 22), which are not designed for describing the local magnetic degrees of freedom. The many-body approach proposed in the following Chapter 3 aims to take into account the electronic correlations responsible for the formation of the atomic magnetic moments from the very beginning.

From a more methodological perspective, we would like to recall that the magnetic properties discussed in this Chapter have been obtained in the framework of finite-temperature DFT by combining a generalized gradient approximation for the ground-state energy functional (see Appendix A) with the single-particle entropy of the auxiliary Kohn-Sham non-interacting system. This approach is probably justified

for weakly correlated systems. However, its application to $3d$ transition metals may not be quite accurate, since the magnetically relevant $3d$ electrons are rather localized and thus experience strong intra-atomic Coulomb interactions. Still, it is our hope that the conclusions drawn in this Chapter will remain qualitatively valid under the light of more sophisticated approaches, thus providing a useful insight on the complex magnetization dynamics of laser excited TMs.

3

Many-body theory of magnetization dynamics

In Chapter 2 the possible magnetic excitations in the initial stage shortly after the laser-pulse absorption have been investigated from a static point of view. The main goal was to identify the nature of these excitations. As an important result it has been found that the atomic magnetic moments remain stable even at extremely high levels of electronic excitation. Therefore, it is reasonable to expect that after the laser-pulse absorption they remain stable and their fluctuations represent most relevant spin excitations in the metal. However, nothing has been said about their dynamics, for instance, about the underlying mechanisms of the spin-flip processes and the corresponding rates. Actually, the microscopic mechanism of spin relaxation and the spin-flip rate are of crucial importance: the former can provide a clue as to the fundamental physics behind ultrafast magnetization dynamics, whereas the latter determines the characteristic time of the spin relaxation.

These aims motivate a theoretical study of the dynamical aspects of the magnetic excitations. For this purpose, we make the transition from *ab initio* DFT calculations to many-body models. Usually, models are used to describe and to solve a given problem by considering only the most essential contributions to its physics. This is also the way how we will proceed in the following: A simple and transparent model will be proposed, which contains only the most essential microscopic contributions to the ultrafast magnetization dynamics, and which do not include any phenomenological terms inducing a spin relaxation. In order to describe the situation of fluctuating

stable local magnetic moments, it is necessary to consider electronic correlations, which are responsible for the formation of these important local moments. The many-body theory developed in this thesis takes into account these correlations from the very beginning. Thus, it is expected to provide new insights into the physics of laser-induced magnetization dynamics.

In the present Chapter, we will first discuss the importance of electron correlations in the magnetism of the considered $3d$ TMs (see Section 3.1). Section 3.2 describes the proposed many-body Hamiltonian. A discussion of this model in view of the magnetization dynamics is given in Section 3.3. Some relevant model simplifications are presented and discussed in Section 3.4. These do not affect the fundamental mechanism of the dynamics, since they do not introduce any bias. They are simply meant to reduce the computational effort involved in the numerical calculations. The simplified model will be used in the subsequent Chapters 4 and 5. Finally, Section 3.5 gives the mathematical description of the electric field in the femtosecond laser pulse.

3.1 Role of electron correlations in ferromagnetism of transition metals

The ferromagnetism in $3d$ transition metals can be regarded as an effect of electronic correlations. In order to elaborate their role in more detail, we begin with a brief very general discussion of correlations in many-body systems.

Let us consider two physical observables $\hat{A}_1$ and $\hat{A}_2$ of a many-body system, for instance, two local properties. If one makes separate measurements of them, one obtains information on their probability distributions p_1 and p_2, and in particular, on their expectation values $\langle \hat{A}_1 \rangle$ and $\langle \hat{A}_2 \rangle$ (see Figure 3.1). In many cases including two-particle interactions, e.g., the present problem of ferromagnetism, the knowledge of these expectation values is not enough to describe the physical state satisfactorily. In addition, expectation values of their product $\langle \hat{A}_1 \hat{A}_2 \rangle$ need to be taken into account, since they give us information about the correlation between measurements A_1 and A_2. If $\hat{A}_1$ and $\hat{A}_2$ are independent observables, then $\langle \hat{A}_1 \hat{A}_2 \rangle = \langle \hat{A}_1 \rangle \langle \hat{A}_2 \rangle$. However, in the most important general case, the expectation value of $\hat{A}_1 \hat{A}_2$ is not given simply in terms of the expectation values $\langle A_1 \rangle$ and $\langle A_2 \rangle$. If

$$\langle \hat{A}_1 \hat{A}_2 \rangle \neq \langle \hat{A}_1 \rangle \langle \hat{A}_2 \rangle \ , \tag{3.1}$$

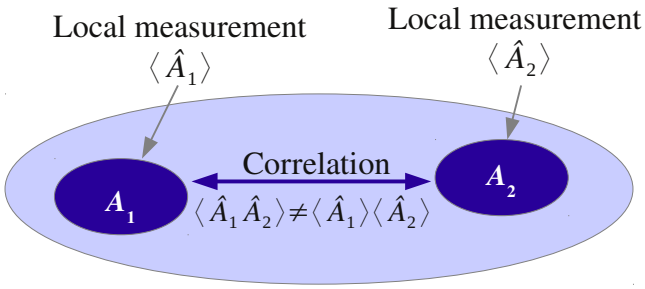

Figure 3.1: Correlations in many-body systems - The local measurements of two observables $\hat{A}_1$ and $\hat{A}_2$, yielding the expectation values $\langle \hat{A}_1 \rangle$ and $\langle \hat{A}_2 \rangle$, don't give any information about the correlation between measurements A_1 and A_2. As a consequence of correlations, the expectation value of the product $\hat{A}_1 \hat{A}_2$ cannot be given simply in terms of $\langle \hat{A}_1 \rangle$ and $\langle \hat{A}_2 \rangle$.

one says that the two observables $\hat{A}_1$ and $\hat{A}_2$ are correlated.[1] The inequality (3.1) implies that correlations preclude us from extracting the complete information on the physical state just from separate measurements of local properties. The origin of correlations in many-body systems is always the interaction between particles. Therefore, they play a crucial role in many-particle systems.

In our work we consider interacting electrons, so that the correlations are driven by the Coulomb interactions. In this case, an evident example of correlation effects resulting from the Coulomb repulsion is given by the tendency to increase the distance between two electrons. This results in a reduced probability of finding the two electrons at the same position $\vec{r}$ in space. Therefore, the two-electron probability $p(\vec{r}_1, \vec{r}_2)$ of finding them at two approaching points $\vec{r}_1$ and $\vec{r}_2$ within the extent of the electronic wave function (i.e., within a region with nonzero single-electron probability $p(\vec{r}) \neq 0$) satisfies

$$p(\vec{r}_1, \vec{r}_2) < p(\vec{r}_1) p(\vec{r}_2) \quad \text{for} \quad \vec{r}_1 \to \vec{r}_2 \ . \tag{3.2}$$

Notice that if the probability distributions were uncorrelated, one would have $p(\vec{r}_1, \vec{r}_2) = p(\vec{r}_1) p(\vec{r}_2)$ for all $\vec{r}_1$, $\vec{r}_2$. This means that in the case of interacting electrons, the prob-

[1] From the point of view of statistics, the relationship between two observables can be described in terms of conditional probabilities for their simultaneous measurement, such as the probability $p(A_1|A_2)$ for an outcome A_1 of observable $\hat{A}_1$ under the condition that the measurement of $\hat{A}_2$ has given the result A_2. If the conditional probabilities and the probability distributions of the corresponding separate measurements p_1 or p_2 are equal [i.e., $p(A_1|A_2) = p_1(A_1)$], then the two observables $\hat{A}_1$ and $\hat{A}_2$ are independent or uncorrelated. Otherwise, they are correlated and the inequality (3.1) holds.

ability density $p(\vec{r}_1, \vec{r}_2)$ of finding one particle at point $\vec{r}_1$ and a second particle at $\vec{r}_2$ is correlated.

Electronic correlations play also an important role in the physics of ferromagnetism as they allow the formation of local magnetic moments even at temperatures above the Curie temperature T_C, where the net magnetization vanishes. First, we would like to emphasize that the stability of the local atomic moments can be traced back to the antisymmetry of the many-electron wave function. This can be already understood by considering the simple example of two electrons in the absence of external magnetic fields. The Hamiltonian of this problem is independent of the spin variables. Therefore, the stationary two-particle states can be written as a product of a spatial and a spin part. Since electrons are fermions, the total wave function must be antisymmetric with respect to a simultaneous interchange of both the spatial and spin coordinates $(\vec{r}, \sigma)$ of the two particles. This implies that the antisymmetric spin part (with respect to interchange of σ) corresponds to a symmetric spatial part (with respect to interchange of $\vec{r}$) of the wave function, and vice versa. The antisymmetric spatial wave function corresponding to the triplet state must have a node at $\vec{r}_1 = \vec{r}_2$, i.e., $\Psi_{\text{triplet}}(\vec{r}, \vec{r}) = 0$. In contrast in the symmetric spatial wave function (corresponding to the singlet) $\Psi_{\text{singlet}}(\vec{r}, \vec{r})$ is enhanced. In general, $|\Psi_{\text{triplet}}(\vec{r}_1, \vec{r}_2)|^2 < |\Psi_{\text{singlet}}(\vec{r}_1, \vec{r}_2)|^2$ within a neighborhood of the hypersurface $\vec{r}_1 - \vec{r}_2 = 0$, i.e., exactly in that region where the Coulomb repulsion $\propto 1/|\vec{r}_1 - \vec{r}_2|$ between the two electrons is strongest. These arguments explain why the Coulomb interaction energy is lower for the triplet than for the singlet. Actually, the energy lowering, which is referred to as the exchange energy, favors parallel alignment of spins (69). In atomic physics, this trend is known as the first Hund's rule: within an atomic shell, the electrons preferentially occupy different spatial orbitals while maximizing the total spin.

In ferromagnetic TMs, this quantum-mechanical exchange interaction results locally, i.e., at each single atomic site, in a parallel spin alignment or, in other words, in the formation of local magnetic moments. The existence of the local moments is incorporated in the physical picture of ferromagnetism. According to this picture, the magnetic moments $\vec{\mu}_j$ at the different atoms j, which are ferromagnetically ordered at low temperatures $T \approx 0$, start to fluctuate in their orientation with increasing T. The important point is that these thermally induced fluctuations keep the magnitude μ_j of the local magnetic moments almost fixed. Even at the Curie temperature T_C,

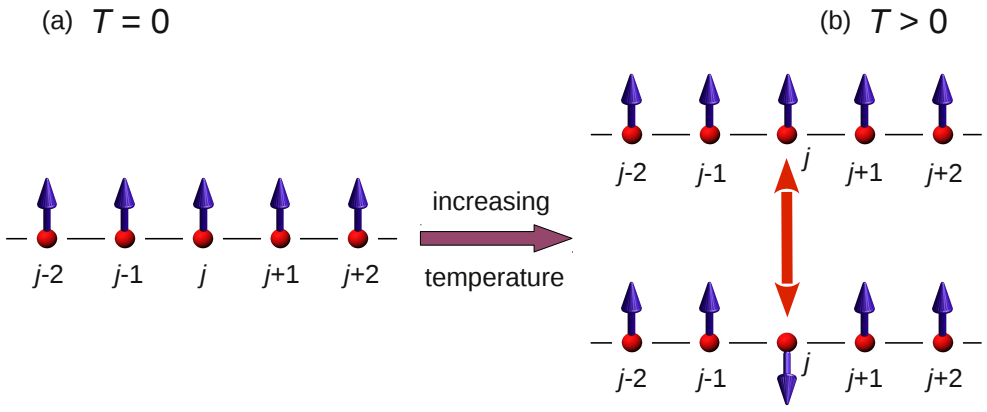

Figure 3.2: Temperature-induced spin fluctuations in ferromagnets - (a) FM order of the local magnetic moments $\vec{\mu}_j$ at $T = 0$. The index j denotes the atomic sites. (b) Illustration of a spin fluctuation with increasing T. The magnetic moments $\vec{\mu}_j$ start to fluctuate in their orientation keeping their magnitudes μ_j almost fixed. This kind of disorder results in the decrease of the magnetization with increasing T.

the local moments μ_j remain stable, although —due to the contribution of entropy to the free energy— their directions are completely disordered. In other words, it is not a reduction of $|\vec{\mu}_j|$ but a disorder in the orientations, what yields the decrease of magnetization with increasing T and the disappearance of magnetization for $T \to T_C$.

This interpretation is illustrated in Figure 3.2. On the right-hand side (b) a spin fluctuation at atom j is depicted. At finite temperatures $T > 0$ the many-body state is built up of such spin fluctuations, whose number increases with increasing temperature. Consequently, with increasing T the spin expectation value $\langle \vec{S}_j \rangle$ decreases due to spin fluctuations, while $\langle \vec{S}_j \cdot \vec{S}_j \rangle$, reflecting the magnitude of the local magnetic moments, remains quite stable. One realizes that these spin fluctuations represent a correlation effect, since in that case $\langle \vec{S}_j \cdot \vec{S}_j \rangle > \langle \vec{S}_j \rangle \langle \vec{S}_j \rangle$. This result of correlations cannot be properly described by mean-field theories. For instance, the mean-field approximation $\langle \vec{S}_j \cdot \vec{S}_j \rangle = \langle \vec{S}_j \rangle \langle \vec{S}_j \rangle$ would fail inasmuch as it yields zero for the local magnetic moments at T_C. As a consequence, such theories fail to reproduce the behavior of the atomic magnetic moments at the Curie point and, in particular, the quantitative value of T_C.

To summarize, correlations play an important role for the formation and stability of the local magnetic moments μ_j. However, a theoretical description of electronic correlations is far from trivial. The following Section shows a possible way to take

them into account.

3.2 Electronic many-body model

In order to understand the fundamental mechanisms behind the laser-induced demagnetization effect, we propose a many-body model, which is expected to contain, in a transparent way, the most relevant physical contributions involved in the response of the magnetic system to an intense ultrashort laser pulse. The aim of transparency implies that the model should be chosen as simple as possible. Therefore, contributions, which are expected to play minor roles in the ultrafast magnetization dynamics, are not considered explicitly. In particular, the lattice degrees of freedom and the coupling to phonons are not taken into account, since at the fs time scale the electrons can be decoupled from the much slower lattice dynamics.[1] The model is based on the purely electronic level by considering the relevant valence electrons in $3d$ TMs. The corresponding Hamiltonian

$$\hat{H} = \hat{H}_0 + \hat{H}_C + \hat{H}_{\text{ext}}(t) + \hat{H}_{\text{SO}} \tag{3.3}$$

takes into account only the most essential electronic contributions on the same footing: $\hat{H}_0$ describes the single-particle electronic structure in the tight-binding approximation. $\hat{H}_C$ models the electron-electron Coulomb interaction. It is this term what introduces the important correlation between the electrons and leads to the formation and stabilization of the local magnetic moments $\vec{\mu}_j$. $\hat{H}_{\text{ext}}$ represents the interaction with time-dependent external fields and describes the initial laser excitation. Finally, $\hat{H}_{\text{SO}}$ is the spin-orbit coupling, which is responsible for the transfer of angular momentum between spin and orbital degrees of freedom. Importantly, phenomenological terms, which may a priori induce a spin relaxation, are not included.

Before discussing the various terms of Eq. (3.3) in the following subsections, let us emphasize that the purpose of the present thesis is to understand the role of purely electronic mechanisms in the ultrafast demagnetization. We aim to elucidate the fundamental physics of this phenomenon. In this sense, in the forthcoming Chapter 5 we will

[1] In this context, it is worth recalling that the coupling to phonons has been proposed as an important demagnetization mechanism (18, 19, 20, 21). Nevertheless, for the reasons given above and for the sake of simplicity we do not consider the electron-phonon coupling within our model. The role of phonon excitations and electron-phonon interactions will be discussed in the concluding Chapter 6.

investigate the dynamical interplay between the electronic contributions in model (3.3), and see to what extent it can explain the experimental results.

3.2.1 Single-particle electronic structure

In transition metals such as Ni, the most relevant $3d$ valence band is known to be relatively narrow. According to the calculations of Wang and Callaway, the $3d$ band width of bulk Ni is in the order of 5 eV (70). A narrow band means that the probability of finding the $3d$ electrons shows clear peaks around the ions in the solid (16). Therefore, it is a well established approach to describe the electronic structure of the considered ferromagnets by means of a tight-binding lattice model, in which the localized character of $3d$ orbitals is incorporated by means of a finite set of discrete atomic orbitals.[1] The single-particle term of the Hamiltonian reads

$$\hat{H}_0 = \sum_{j\alpha\sigma} \varepsilon_\alpha^0 \hat{n}_{j\alpha\sigma} + \sum_{\substack{jk \\ j\neq k}} \sum_{\alpha\beta\sigma} t_{jk}^{\alpha\beta}\, \hat{c}_{j\alpha\sigma}^\dagger \hat{c}_{k\beta\sigma} \ . \tag{3.4}$$

It is responsible for the electron delocalization, band formation and metallic behavior. Here, ε_α^0 denotes the energy of the localized atomic orbital α,[2] and $t_{jk}^{\alpha\beta}$ is the hopping integral between orbital α at atom j and orbital β at atom k ($j \neq k$). Moreover, $\hat{c}_{j\alpha\sigma}^\dagger$ ($\hat{c}_{j\alpha\sigma}$) represent creation (annihilation) operators of an electron at atom j in orbital α with spin σ, and $\hat{n}_{j\alpha\sigma} = \hat{c}_{j\alpha\sigma}^\dagger \hat{c}_{j\alpha\sigma}$ are the corresponding electron number operators.

It is well known that in TMs the $3d$ electrons dominate the magnetic properties. If one is interested in magnetic phenomena, this usually leads to the assumption that considering only the $3d$ electrons as relevant valence electrons provides a reasonable approximation. However, for the description of laser-induced excitations it is not sufficient to include only the $3d$ band in our model, since no optical absorption can occur within a d band. The parity selection rule $\Delta l = \pm 1, \pm 3, ...$ for optical transitions requires the inclusion of bands with different orbital angular momentum quantum numbers l. We

[1] Notice that in bulk Ni the finite width of the $3d$ band ($\sim$ 5 eV) reflects its itinerant character. However, the probability density of the $3d$ electrons still has clear distinct maxima around the Ni ions. The tight-binding ansatz takes into account this atomic structure of the metal in a simple way.

[2] The basis orbitals α can be chosen as atomic orbitals whose radial and angular parts are usually characterized by the radial quantum number n and by the quantum numbers $\{l,m\}$ of orbital angular momentum as well as its projection on the z axis, respectively. In this case, the angular part, also referred to as spherical harmonics, is an eigenstate of $\hat{\vec{L}} \cdot \hat{\vec{L}}$ and $\hat{L}_z$.

are certain that the essential dynamics can be described by considering the $3d$, $4s$ and $4p$ bands within $\hat{H}$.

Let us finally mention that the single-particle electronic structure Hamiltonian does not depend on the spin σ, since it includes neither external nor effective magnetic fields. Only the kinetic energy of the valence electrons and their interaction with the lattice potential are included in $\hat{H}_0$. Consequently, the action of $\hat{H}_0$ cannot induce any spin-flip processes. Nevertheless, the hopping integrals $t_{jk}^{\alpha\beta}$ being of the order of 1 eV play an important role, since they determine the shortest frequency $f \gtrsim (1\text{ fs})^{-1}$ in the dynamics of the system. Moreover, the hopping elements between different atoms,

$$t_{jk}^{\alpha\beta} = \int \mathrm{d}^3 r\, \phi_\alpha^*(\vec{r} - \vec{R}_j) \left(-\frac{\hbar^2 \nabla^2}{2m_e} + v(\vec{r}) \right) \phi_\beta(\vec{r} - \vec{R}_k) \;, \tag{3.5}$$

drive the electron motion in the lattice. Here, $\phi_\alpha(\vec{r} - \vec{R}_j)$ denotes the wave function of single-particle orbital α at atom j, m_e is the electron mass, and $v(\vec{r})$ is the potential generated by the ions in the metal. The valence electrons move within the potential $v(\vec{r})$, which is incorporated in the integrals $t_{jk}^{\alpha\beta}$. Therefore, $v(\vec{r})$ and $t_{jk}^{\alpha\beta}$ reflect the interaction between electrons and the lattice. This demonstrates that it is worth studying the hopping integrals in more detail. To this aim, in Appendix B we discuss some properties of $t_{jk}^{\alpha\beta}$, e.g., symmetry properties, and present the two-center approximation for their determination (71). The two-center approximation has proven extremely successful in the description of the electronic structure of solids (72). For this reason, we expect that its application allows one to accurately model the electron motion in the lattice.

3.2.2 Electron-electron Coulomb interaction

The second term in Eq. (3.3) is the electronic Coulomb interaction energy $\hat{H}_C$. It is responsible for the appearance of ferromagnetism. As discussed in Section 3.1, due to the antisymmetry of the many-electron wave function the effective Coulomb repulsion for a pair of electrons with parallel spins is weaker than for antiparallel spins (69). This is known as the exchange interaction. Therefore, for the purpose of conceiving a model for the electron-electron interaction, it is indispensable to include the important exchange interaction. In the following, a model of $\hat{H}_C$ is presented, which takes into account this exchange energy in a natural way and, thus, is suitable for describing ferromagnetism in transition metals.

Before giving an explicit expression for the Hamiltonian $\hat{H}_C$, let us discuss two further important aspects, which allow us to simplify the form of $\hat{H}_C$. First, in metals the electric field originated from charges at large distances r is very effectively screened by the mobile conduction electrons. Consequently, only the intra-atomic interaction energy needs to be taken explicitly into account. Secondly, it is reasonable to consider only the Coulomb repulsion among the $3d$ electrons to describe the electron interaction, since magnetism in TMs is dominated by the $3d$ electrons and by the interactions between them. Actually, the higher atomic $4s$ and $4p$ orbitals are much less localized than the $3d$ orbitals, so that the Coulomb interactions involving $4s$ and $4p$ electrons do not play a significant role in the magnetic properties. Therefore, they can be regarded as noninteracting due to their more delocalized character.

The above considerations are incorporated in the transparent model

$$\hat{H}_C = \frac{1}{2}\sum_j \left[U\left(\hat{n}_{jd} - \vartheta\right)^2 - 2J\hat{\vec{S}}_{jd}\cdot\hat{\vec{S}}_{jd}\right] \tag{3.6}$$

for the electron-electron interaction, by means of which the main magnetic properties of transition metals can be described. In particular, $\hat{H}_C$ includes the important exchange interaction, and it takes into account only the intra-atomic interaction-energy terms and the dominant interactions among $3d$ electrons. At this point, we will continue with discussing the effects of the two terms in $\hat{H}_C$, while a detailed derivation of this model is given in Appendix C. First of all, the operator $\hat{H}_C$ is responsible for the correlation between the d electrons, as it represents a two-particle operator. The first term in Eq. (3.6) describes the classical Coulomb energy and is specified by the Coulomb parameter U. Here, $\hat{n}_{jd} = \sum_{\alpha\in 3d,\sigma}\hat{n}_{j\alpha\sigma}$ denotes the number of interacting $3d$ electrons at atom j. This term tends to suppress the charge fluctuations associated to electron delocalization throughout the lattice. The second term linear in the effective exchange parameter J provokes the creation and stability of local magnetic moments. The operator $\hat{\vec{S}}_{jd}$ denotes the spin at atom j restricted to the $3d$ electrons. Notice that in Eq. (3.6) the Coulomb repulsion energy of a uniform $3d$-electron density ϑ has been subtracted.[1] Actually, the interaction-energy contribution of ϑ d electrons per atom is

[1] In a system having N_a atoms and n_d electrons in the $3d$ valence band, the uniform $3d$-electron density per atom is given by $\vartheta = n_d/N_a$. However, in order to definitely determine the parameter ϑ prior to numerical simulations (which actually yield n_d), we simply use $\vartheta = N_e/N_a$ in the present thesis. This is equivalent to the assumption that almost all electrons occupy the lowest $3d$ band.

incorporated as an additional constant in the single-particle energies ε_α^0. This leads, as will be shown in Appendix C, to the effective $3d$-electron level

$$\varepsilon_d^{\text{eff}} = \varepsilon_d^0 + \frac{1}{2}\left[U\,(2\vartheta - 1) + \frac{1}{2}J\right] \ . \tag{3.7}$$

The formulations (3.6) and (3.7) will be used in the following Chapters.

Finally, it is important to note that $\hat{H}_C$ does not change the total magnetization of the system, since the total spin $\vec{S}$ commutes with $\hat{H}_C$ ($[\hat{\vec{S}}, \hat{H}_C] = 0$). This means that the action of the electron-electron interaction term alone cannot result in spin relaxation. Actually, spin relaxation is induced exclusively by the spin-orbit coupling Hamiltonian $\hat{H}_{\text{SO}}$, which will be discussed in Section 3.2.4.

3.2.3 Interaction with external fields

The operator $\hat{H}_{\text{ext}}(t)$ in Eq. (3.3) takes into account the interaction with external fields:

$$\hat{H}_{\text{ext}}(t) = \hat{H}_E(t) + \hat{H}_B = -e\hat{\vec{r}}\cdot\vec{E}(t) \ - \ \hat{\vec{\mu}}\cdot\vec{B} \ . \tag{3.8}$$

The first term in this equation, i.e.,

$$\hat{H}_E(t) = -e\vec{E}(t)\cdot\sum_j\sum_{\alpha\beta}\sum_\sigma \langle\,\alpha\,|\hat{\vec{r}}|\,\beta\,\rangle\,\hat{c}^\dagger_{j\alpha\sigma}\hat{c}_{j\beta\sigma} \ , \tag{3.9}$$

describes the interaction with the laser electric field by means of the intra-atomic dipole approximation, which considers a uniform classical field $\vec{E}$. Here, e ($e < 0$) is the electron charge and $\vec{E}(t)$ denotes the time-dependent electric field. The electric-dipole matrix elements $\langle\,\alpha\,|\hat{\vec{r}}|\,\beta\,\rangle$ are very simple if one chooses the eigenstates of $\hat{\vec{L}}\cdot\hat{\vec{L}}$ and $\hat{L}_z$ as the single-particle basis of the atomic orbitals, i.e., $|\,\alpha\,\rangle = |\,nlm\,\rangle$ which are characterized by the radial quantum number n and by the quantum numbers $\{lm\}$ of orbital angular momentum and its projection onto the z axis. The term $\hat{H}_E$ describes the initial laser excitation. Since the direct coupling to the laser light contains only terms diagonal in the spin variable σ, it is clear that $\hat{H}_E$ cannot induce any spin-flip excitations in the metal.

The effect of $\hat{H}_E$ depends in a crucial way on both the time dependence of the electric field $\vec{E}(t)$ (i.e., the shape of the laser pulse) and the matrix elements $\langle\,nlm\,|\hat{\vec{r}}|\,n'l'm'\,\rangle$ between the atomic orbitals at the same lattice sites. Section 3.5 gives a mathematical description of the laser field applied in the present work. Let us now briefly comment

on the dipole matrix elements. In order to determine them, it is useful to consider the symmetry of the angular part $|\, lm \,\rangle$. First of all, notice that the parity selection rule states

$$\langle\, nlm \,|\hat{\vec{r}}|\, n'l'm' \,\rangle = 0 \quad \text{unless} \quad l + l' + 1 \text{ even.} \tag{3.10}$$

Consequently, $\hat{H}_E$ allows only $4s$–$4p$ and $3d$–$4p$ transitions among the considered $3d$, $4s$ and $4p$ orbitals. By further exploiting symmetry properties and the Wigner-Eckart theorem (73), it is possible to derive explicit relations between the non-vanishing matrix elements of $\hat{\vec{r}}$. This is explicated in Appendix D.

Besides coupling to electric fields, we also consider the coupling $\hat{H}_B$ to external magnetic fields $\vec{B}$ [see last term in Eq. (3.8)]. This term is used for the purpose of stabilizing a magnetization direction as in the experiment (see Chapter 4). Actually, the nonzero magnetic moment $\vec{\mu}$ is imposed on $|\, \Psi \,\rangle$ by including a nonzero magnetic field $\vec{B} \neq 0$ and considering the limit $\vec{B} \to 0$.

The description of the coupling to $\vec{B}$ is intra-atomic and Zeeman-like, i.e.,

$$\hat{H}_B = -\hat{\vec{\mu}} \cdot \vec{B} \;, \tag{3.11}$$

where

$$\hat{\vec{\mu}} = -\frac{\mu_B}{\hbar} \left(\hat{\vec{L}} + 2\hat{\vec{S}} \right) \tag{3.12}$$

is the magnetic moment. Using

$$\vec{B} \cdot \hat{\vec{L}} \;=\; \frac{1}{2} \left(B_x + iB_y \right) \hat{L}_- + \frac{1}{2} \left(B_x - iB_y \right) \hat{L}_+ + B_z \hat{L}_z \tag{3.13}$$

and an equivalent relation for $\vec{B} \cdot \hat{\vec{S}}$, one obtains

$$\begin{aligned} \hat{H}_B = {} & \frac{\mu_B}{2\hbar} \left(B_x - iB_y \right) \sum_{jnl} \sum_{m,m'} \sum_{\sigma\sigma'} \left[(L_+)_{nlm,nlm'} \delta_{\sigma\sigma'} + 2(S_+)_{\sigma\sigma'} \delta_{mm'} \right] \hat{c}^\dagger_{jnlm\sigma} \hat{c}_{jnlm'\sigma'} \\ & + \frac{\mu_B}{2\hbar} \left(B_x + iB_y \right) \sum_{jnl} \sum_{m,m'} \sum_{\sigma\sigma'} \left[(L_-)_{nlm,nlm'} \delta_{\sigma\sigma'} + 2(S_-)_{\sigma\sigma'} \delta_{mm'} \right] \hat{c}^\dagger_{jnlm\sigma} \hat{c}_{jnlm'\sigma'} \\ & + \frac{\mu_B}{\hbar} B_z \sum_{jnlm\sigma} \left[(L_z)_{nlm,nlm} + 2(S_z)_{\sigma\sigma} \right] \hat{c}^\dagger_{jnlm\sigma} \hat{c}_{jnlm\sigma} \;. \end{aligned} \tag{3.14}$$

The spin matrix elements are given by

$$(S_z)_{\sigma\sigma'} \;=\; \frac{\hbar}{2} \sigma \, \delta_{\sigma\sigma'} \;, \tag{3.15}$$

$$(S_+)_{\sigma\sigma'} \;=\; \hbar \, \delta_{\sigma,\uparrow} \, \delta_{\sigma',\downarrow} \;, \text{ and} \tag{3.16}$$

$$(S_-)_{\sigma\sigma'} \;=\; \hbar \, \delta_{\sigma,\downarrow} \, \delta_{\sigma',\uparrow} \;, \tag{3.17}$$

where $\sigma = \pm 1$ for spin $\uparrow$ / $\downarrow$. The orbital angular-momentum matrix elements are found by recalling that the operator $\hat{\vec{L}}$ does not act on the radial part of the atomic orbitals $|\, nlm \,\rangle$, but only on their angular part given by the spherical harmonics $|\, l, m \,\rangle$. The action of $\hat{\vec{L}}$ on them can be summarized by

$$\hat{L}_z \,|\, n, l, m \,\rangle \;=\; m\hbar \,|\, n, l, m \,\rangle \quad \text{and} \tag{3.18}$$

$$\hat{L}_\pm \,|\, n, l, m \,\rangle \;=\; \sqrt{l(l+1) - m(m \pm 1)}\, \hbar \,|\, n, l, m \pm 1 \,\rangle \;. \tag{3.19}$$

Using Eqs. (3.18) and (3.19), one obtains

$$(L_z)_{nlm,n'l'm'} \;=\; \delta_{n,n'}\, \delta_{l,l'}\, \delta_{m,m'}\, m\hbar \quad \text{and} \tag{3.20}$$

$$(L_\pm)_{nlm,n'l'm'} \;=\; \delta_{n,n'}\, \delta_{l,l'}\, \delta_{m,m'\pm 1}\, \sqrt{l(l+1) - m'm}\, \hbar \;. \tag{3.21}$$

3.2.4 Spin-orbit coupling

The last term in model (3.3) is the intra-atomic SOC, which arises from relativistic corrections to the Hamiltonian (69). Physically, the spin-orbit interaction describes the coupling between the electronic spin $\vec{S}_a$ and the magnetic field created by its own orbital motion $\vec{L}_a$ around the nucleus. In first quantization the corresponding Hamiltonian for a single atom reads

$$\hat{H}_{\mathrm{SO}}^{\mathrm{atom}} = \sum_a \frac{1}{2m_e^2 c^2} \frac{1}{r} \frac{\partial v(r)}{\partial r}\, \hat{\vec{L}}_a \cdot \hat{\vec{S}}_a \;, \tag{3.22}$$

where the sum is taken over all electrons a, m_e is the electron mass, r denotes the distance to the nucleus, and $v(r)$ is the electrostatic potential created by the nucleus and the remaining core electrons. One can rewrite the atomic spin-orbit Hamiltonian as

$$\hat{H}_{\mathrm{SO}}^{\mathrm{atom}} = \sum_a \frac{\xi_a(r)}{\hbar^2}\, \hat{\vec{L}}_a \cdot \hat{\vec{S}}_a \tag{3.23}$$

in terms of SOC constants $\xi_a(r)$, which are all positive ($\xi_a(r) > 0$ for all r) because of $\partial v(r)/\partial r > 0$ in the direct neighborhood of the nucleus. The concept of spin-orbit coupling is easily extended to the bulk by applying the intra-atomic approximation.[1]

[1] In the bulk, one would in principle obtain matrix elements of the form $\langle\, \phi_{j\alpha} \,|\, \vec{r} \times \vec{p}\, \frac{1}{r}\, \partial v(r)/\partial r \,|\, \phi_{k\beta} \,\rangle$ between orbitals $\phi_{j\alpha}$ and $\phi_{k\beta}$ at different atoms $j \neq k$. However, these interatomic SOC integrals are very small in comparison with intra-atomic matrix elements. Therefore, they can be neglected, and the general spin-orbit Hamiltonian $\hat{H}_{\mathrm{SO}}$ in the bulk becomes a simple sum over atomic contributions.

Using this approximation the general spin-orbit Hamiltonian in second quantization can be written as

$$\hat{H}_{\mathrm{SO}} = \frac{\xi}{\hbar^2} \sum_{j} \sum_{\alpha\beta \in 3d} \sum_{\sigma\sigma'} \left(\vec{L} \cdot \vec{S} \right)_{\alpha\sigma,\beta\sigma'} \hat{c}^{\dagger}_{j\alpha\sigma} \hat{c}_{j\beta\sigma'} \ . \tag{3.24}$$

Here, ξ is the effective spin-orbit constant averaged over the electron-nucleus distance r, $(\vec{L} \cdot \vec{S})_{\alpha\sigma,\beta\sigma'}$ denotes the intra-atomic matrix elements of $\hat{\vec{L}} \cdot \hat{\vec{S}}$ with respect to orbitals α, β and spin σ, σ'. Since the spin-orbit constant $\xi_a(r)$ is proportional to $1/r \cdot \partial v(r)/\partial r$, the SOC plays an essential role only in a small region around the nucleus. This implies that the spin-orbit interaction $\hat{H}_{\mathrm{SO}}$ can be restricted to the most localized orbitals among the considered valence bands. Consequently, it is only necessary to consider the SOC within the $3d$ band ($\alpha\beta \in 3d$), where ξ can surely be assumed to be the same for all d electrons due to their common radial part of the atomic wave function.

Let us now briefly discuss the effects of $\hat{H}_{\mathrm{SO}}$. Because of $\xi > 0$, a single electron would try to align the spin antiparallel to its orbital angular momentum in the ground state. As discussed in Ref. (69), this implies that in atoms having a less than half-filled outermost d shell, the total ground-state $\vec{L}$ is antiparallel to the total ground-state $\vec{S}$. In the opposite case of a more than half-filled d shell, $\vec{L}$ and $\vec{S}$ are parallel aligned in the ground state.[1] This is also known as the third Hund's rule. Notice that the interesting TMs Fe, Co and Ni have a more than half-filled d band. As a consequence, we expect in these metals a parallel alignment of $\vec{L}$ and $\vec{S}$ in the corresponding ground states. Actually, it is the term $\vec{L} \cdot \vec{S}$ what couples the spin $\vec{S}$ and orbital angular momentum $\vec{L}$. Very importantly, this coupling breaks the spin rotational invariance. Moreover, since the orbital motion is directly coupled to the lattice via the electrostatic potential

[1] The ground-state alignment between atomic $\vec{L}$ and $\vec{S}$ can be understood as follows. In the case of a less than half-filled outermost d shell, all electrons have the same spin projection σ according to the first Hund's rule. The spatial orbitals are occupied beginning with the largest projection m of $\vec{L}$ in the direction antiparallel to $\vec{S}$. This yields an antiparallel alignment between $\vec{S}$ and $\vec{L}$. In the opposite case of a more than half-filled d shell, first all spatial orbitals are occupied with one particular spin projection σ. These have zero net orbital angular momentum. Notice that the favored spin-projection direction gives also the projection direction of the total atomic spin $\vec{S}$. Then, the remaining electrons having opposite spin projection $-\sigma$ occupy spatial orbitals beginning with the largest projection of $\vec{L}$ in the direction antiparallel to $-\sigma$, i.e., parallel to σ. Consequently, in this case $\vec{S}$ and $\vec{L}$ are parallel aligned.

of the ions, the SOC results in the magnetic anisotropy (74).[1] From the dynamical point of view, the SOC acts as a channel for the local transfer between $\vec{S}$ and $\vec{L}$. This angular-momentum transfer comes along with a coupling of the up- and down-spin manifolds, which provides equilibration of the spin with the electronic system. In fact, in the absence of SOC (and external magnetic fields) the total spin $\vec{S}$ is conserved, since

$$\left[\hat{\vec{S}}, \hat{H}_0\right] = \left[\hat{\vec{S}}, \hat{H}_C\right] = \left[\hat{\vec{S}}, \hat{H}_E\right] = 0 \,. \tag{3.25}$$

For these reasons the SOC represents a key mechanism in the demagnetization process.

In order to determine the matrix elements of $\hat{\vec{L}} \cdot \hat{\vec{S}}$, it is important to notice that $\hat{\vec{L}}$ acts only on the spatial part $|\,\alpha\,\rangle$ and $\hat{\vec{S}}$ acts only on the spin part $|\,\sigma\,\rangle$ of the single-particle states. Therefore, the matrix elements can be decomposed as

$$(\vec{L} \cdot \vec{S})_{\alpha\sigma,\beta\sigma'} = (\vec{L})_{\alpha\beta} \cdot (\vec{S})_{\sigma\sigma'} = \langle\, \alpha \,|\hat{\vec{L}}|\, \beta \,\rangle \cdot \langle\, \sigma \,|\hat{\vec{S}}|\, \sigma' \,\rangle \,. \tag{3.26}$$

Moreover, using the relation

$$\hat{\vec{L}} \cdot \hat{\vec{S}} = \frac{1}{2}\hat{L}_+\hat{S}_- + \frac{1}{2}\hat{L}_-\hat{S}_+ + \hat{L}_z\hat{S}_z \tag{3.27}$$

and the expressions (3.15)–(3.17) for the spin matrix elements, one can rewrite Eq. (3.24) as

$$\begin{aligned}\hat{H}_{\mathrm{SO}} = \frac{\xi}{\hbar} \sum_j \sum_{\alpha\beta\in 3d} \Bigg[& \frac{1}{2}(L_+)_{\alpha\beta}\, \hat{c}^\dagger_{j\alpha\downarrow}\hat{c}_{j\beta\uparrow} \\ & + \frac{1}{2}(L_-)_{\alpha\beta}\, \hat{c}^\dagger_{j\alpha\uparrow}\hat{c}_{j\beta\downarrow} + \frac{1}{2}\sum_\sigma (L_z)_{\alpha\beta}\, \sigma\, \hat{c}^\dagger_{j\alpha\sigma}\hat{c}_{j\beta\sigma} \Bigg] \,.\end{aligned} \tag{3.28}$$

The orbital angular-momentum matrix elements $(\vec{L})_{\alpha\beta}$ can be simplified by using the atomic orbitals $|\,nlm\,\rangle$ as the single-particle basis, characterized by the radial quantum number n and by the quantum numbers $\{lm\}$ of orbital angular momentum and its projection onto the z axis. This corresponds to the choice of basis states α in the previous Section 3.2.3. Finally, the elements $\langle\, nlm \,|\vec{L}|\, n'l'm' \,\rangle$ are given by Eqs. (3.20) and (3.21).

[1] The magnetic anisotropy originated from the SOC is also referred to as magneto-crystalline anisotropy in order to distinguish it from the shape anisotropy originated from the dipole-dipole interactions.

3.3 Discussion in view of the magnetization dynamics

To summarize, the model Hamiltonian $\hat{H}$ describes the most important microscopic mechanisms within the valence electron system including the spin degrees of freedom. It contains the characteristic features of magnetic TMs: electronic hoppings, which yield the metallic behavior, and Coulomb interactions including the exchange integrals, which are responsible for the formation of localized magnetic moments. However, from the point of view of magnetization dynamics, it is important to note that neither the electron hoppings nor the Coulomb interaction can change the total magnetization of the system. In other words, the total spin is conserved if one considers only the tight-binding term $\hat{H}_0$ and the electron-electron interaction term $\hat{H}_C$. The same holds for the interaction $\hat{H}_E$ with the external laser electric field: coherent optical transitions described by dipole matrix elements are spin conserving. The deficiency of $\hat{H}_0$, $\hat{H}_E$ and $\hat{H}_C$ to induce spin-flip excitations in the metal is reflected by the commutation relations

$$\left[\hat{\vec{S}}, \hat{H}_0\right] = \left[\hat{\vec{S}}, \hat{H}_C\right] = \left[\hat{\vec{S}}, \hat{H}_E\right] = 0 \,. \tag{3.29}$$

Therefore, in the absence of external noncollinear magnetic fields $\vec{B}$ it is only the spin-orbit coupling $\hat{H}_{\mathrm{SO}}$, what couples the two spin manifolds. In this sense, the ultrafast spin dynamics is exclusively triggered by the SOC. This justifies our focus on studying the separated role of $\hat{H}_{\mathrm{SO}}$ in the relaxation between the spin and translational electronic degrees of freedom subsequently to the excitation of electrons by an ultrashort laser pulse.

It is worth noting that the SOC describes the transfer of angular momentum between spin $\vec{S}$ and orbital angular momentum $\vec{L}$. Actually, $\hat{H}_{\mathrm{SO}}$ locally conserves $\vec{J}_j = \vec{L}_j + \vec{S}_j$. The SOC has to be distinguished from the electrostatic spin-conserving interaction between the electrons and the lattice. The latter is taken into account by $\hat{H}_0$, which describes the motion of electrons in the lattice. This role of $\hat{H}_0$ can be understood by recalling that the spin-independent potential $v(\vec{r})$ generated by the ions in the lattice is incorporated in the hopping integrals $t_{jk}^{\alpha\beta}$ [see Eq. (3.5)]. Since $\hat{H}_0$ includes these hoppings, it implicitly takes into account the electrostatic interaction between the electrons and the fixed ions.

Furthermore, it should be noted that effects, such as spin-polarized electron diffusion toward the substrate and other couplings to the environment, are not included in the

present model (3.3). In fact, it has been recently shown that in simple FM films the laser-induced demagnetization is not dominated by spin transport to the substrate but rather by an ultrafast local transfer of angular momentum away from the spin system (45). All further dissipation and relaxation mechanisms, which result from the coupling to the environment, and which occur on the most interesting timescale of ten to hundred femtoseconds, conserve the total magnetization of the sample. The same holds for the valence electron scattering with core electrons. Therefore, we believe that omitting the coupling to the environment is a reasonable assumption for the ultrafast fs magnetization dynamics, since these terms do not lead to any spin relaxation.

3.4 Model simplifications

The electronic Hamiltonian (3.3) can in principle be used straightforwardly to determine the time propagation of any state under the action of external fields. However, an exact solution requires to include a large number of many-electron basis states, which increases exponentially with the number of single-particle orbitals. This fact actually limits the accessible system sizes and the number of orbitals per atom, since the numerical effort needs to remain affordable. For this reason, we propose some model simplifications. The objective in mind is to simplify the model by keeping the minimum number of degrees of freedom, which are inevitable for the description of electron motion in the lattice, Coulomb repulsion, spin-orbit interaction and laser excitation on the same footing.

First, we know that the electronic transitions resulting from light-matter interactions can be described by dipole-transitions between only the $3d$ orbitals characteristic for the magnetic properties and the excited $4p$ orbitals. Since $\hat{H}_E$ does not directly couple the $4s$ electrons to the most important valence $3d$ electrons, the $4s$ band can be ignored without affecting the ability of $\hat{H}_E$ to model the effect of laser-pulse absorption. This motivates the use of only $3d$ and $4p$ orbitals as the restricted single-particle basis set for the relevant valence electrons. However, a complete treatment of the atomic $3d$ and $4p$ orbitals, i.e., 16 orbitals per atom including spin degeneracy, is still numerically too demanding. Therefore, we propose a further simplification, namely to reduce the degree of orbital degeneracy from $N_{d\text{-orbitals}} = 5$ to $N_{d\text{-orbitals}} = 3$ for $3d$ and from $N_{p\text{-orbitals}} = 3$ to $N_{p\text{-orbitals}} = 1$ for $4p$ orbitals. This means that the $3d$ and $4p$ electrons

Notation	Character	Mathem. description	Orbital degeneracy
d	localized	$n = 3, \quad l = 1$	$m = -1, 0, +1$
p	delocalized	$n = 4, \quad l = 0$	$m = 0$

Table 3.1: Electronic two-band model approximation - Only four orbitals per atom are included in the many-body model: the three-fold degenerated localized $3d$ orbitals and the delocalized $4p$ orbitals, which are mathematically described by $l = 1$ and $l = 0$ atomic states, respectively. The electronic Coulomb repulsion and the SOC are considered only within the localized d orbitals.

are mathematically described by orbital shells having quantum numbers $l = 1$ and $l = 0$ respectively. Let us note that by reducing the orbital degeneracy we actually reduce the number of relaxation channels. Therefore, we should get rather a slower magnetization dynamics than a faster one in comparison with non-reduced orbital degeneracies.

The above-mentioned two-band approximation (including four orbitals per atom) yields the minimum number of atomic orbitals, which are necessary for taking into account the selection rules for optical transitions and subsequent SOC-triggered spin relaxation: (i) both d and p orbitals are needed for describing the laser-induced optical transitions, and (ii) three-fold orbital and two-fold spin degeneracies of the localized d orbitals are needed for the SOC inducing spin-flip processes and angular momentum transfer between $\vec{S}$ and $\vec{L}$.[1] Since these essential features of the valence electrons in TMs are included in the above approximation, it is expected to serve as a reliable model for magnetization dynamics in ferromagnets. In particular, this approximation is intended to provide an understanding of the processes involved in the ultrafast demagnetization effect.

Table 3.1 summarizes the model simplification which we apply from now on: Only four orbitals per atom, namely the three-fold degenerated d band and the p band, are included in this approximation. Mathematically, the corresponding atomic orbitals are described by $l = 1$ (representing the localized $3d$ electrons) and $l = 0$ (representing

[1] It is worth noting that a further reduction in the degree of orbital degeneracy from $N_{d\text{-orbitals}} = 3$ to $N_{d\text{-orbitals}} = 2$ for the $3d$ orbitals is not allowed. Although this reduction would significantly simplify the model as well as take into account the SOC-induced spin relaxation, the resulting d-p hopping integrals would not satisfy the 2π-rotation symmetry in space. This is shown in the Appendix B.1, where the angle dependence of the hopping integrals is discussed.

Hopping	Expression in terms of Slater-Koster integrals
$t_{jk}^{p0,p0}$	$(p,p;\sigma)$
$t_{jk}^{p0,d0}$	$\lambda_z\,(p,d;\sigma)$
$t_{jk}^{p0,d\pm1}$	$\mp\frac{1}{\sqrt{2}}(\lambda_x \pm i\lambda_y)\,(p,d;\sigma)$
$t_{jk}^{d0,d0}$	$\lambda_z^2\,(d,d;\sigma) + (1-\lambda_z^2)\,(d,d;\pi)$
$t_{jk}^{d0,d\pm1}$	$\mp\frac{\lambda_z}{\sqrt{2}}(\lambda_x \pm i\lambda_y)\,[(d,d;\sigma) - (d,d;\pi)]$
$t_{jk}^{d\pm1,d\pm1}$	$\frac{1}{2}\,[(1-\lambda_z^2)\,(d,d;\sigma) + (1+\lambda_z^2)\,(d,d;\pi)]$
$t_{jk}^{d+1,d-1}$	$-\frac{1}{2}(\lambda_x - i\lambda_y)^2\,[(d,d;\sigma) - (d,d;\pi)]$

Table 3.2: Hopping integrals of the model - Interatomic hoppings $t_{jk}^{lm,l'm'}$ in terms of two-center integrals, as obtained by applying the two-band model (see Table 3.1). Similarly to Table B.2, the indices λ_x, λ_y and λ_z denote the direction cosines of the connection vector $\vec{R}_{jk}$. Notice that the entries not given in the table can be obtained by applying the relation $t^{\alpha\beta}(\vec{R}_{jk}) = [t^{\beta\alpha}(-\vec{R}_{jk})]^*$.

the delocalized $4p$ electrons) states. The electronic Coulomb interaction and the SOC are considered only within the localized d orbitals (mathematically, $l = 1$ states). It is important to notice that the model parameters need to satisfy the conservation laws resulting from the lattice symmetry, the local conservation of total atomic angular momenta in every spin-orbit coupling transition, and the optical selection rules. For this reason, the interatomic hopping integrals, the orbital angular-momentum matrix elements and the intra-atomic dipole matrix elements are determined by using the mathematical description in terms of $l = 1$ and $l = 0$ atomic orbitals. The resulting expressions for the hopping integrals and the dipole matrix elements are given in Tables 3.2 and 3.3, while the matrix elements of $\vec{L}$ read

$$(L_z)_{p0,p0} = (L_\pm)_{p0,p0} = (L_z)_{p0,dm} = (L_\pm)_{p0,dm} = 0\ , \tag{3.30}$$

$$(L_z)_{dm,dm'} = \delta_{m,m'}\hbar \quad , \text{ and} \tag{3.31}$$

$$(L_\pm)_{dm,dm'} = \delta_{m,m'\pm1}\sqrt{2}\,\hbar\ . \tag{3.32}$$

Dipole element	Expression given by Wigner-Eckart theorem
$\langle\, d, m \,\vert \hat{x} \vert\, p, 0 \,\rangle$	$-\frac{m}{\sqrt{2}} \langle\, d \,\vert\vert \hat{T}^{(1)} \vert\vert\, p \,\rangle$
$\langle\, d, m \,\vert \hat{y} \vert\, p, 0 \,\rangle$	$\frac{i}{\sqrt{2}}(1-\delta_{m,0}) \langle\, d \,\vert\vert \hat{T}^{(1)} \vert\vert\, p \,\rangle$
$\langle\, d, m \,\vert \hat{z} \vert\, p, 0 \,\rangle$	$\delta_{m,0} \langle\, d \,\vert\vert \hat{T}^{(1)} \vert\vert\, p \,\rangle$

Table 3.3: Intra-atomic dipole matrix elements of the model - Interband matrix elements $\langle\, d, m \,\vert \hat{\vec{r}} \vert\, p, 0 \,\rangle$, as obtained by applying the two-band model (see Table 3.1) and the Wigner-Eckart theorem (see Appendix D).

3.5 Laser pulse

In the present Section we want to consider the femtosecond laser pulse in more detail. Actually, the whole spin-relaxation dynamics is stimulated by the laser pulse. Its mathematical description is given in terms of the electric field

$$\vec{E}(t) = E_0\, \vec{\varepsilon}\, \cos(\omega t)\, e^{-\frac{t^2}{T_p^2}} \ . \tag{3.33}$$

Here, $\vec{\varepsilon}$ denotes a dimensionless normalized polarization vector. The term $\cos(\omega t)$ represents the electric-field oscillations at a fixed position in space, where the frequency ω is related to the wave length λ by $\omega = 2\pi c/\lambda$ (c denotes the speed of light in vacuum). The Gauss envelope $\exp\left(-t^2/T_p^2\right)$ is centered around the pump time $t = 0$ fs. The pulse duration T_p is defined such that at times $t = \pm T_p$ the amplitude of $\vec{E}(t)$ is reduced by the factor $1/e$ with respect to $t = 0$ fs. At $t = 0$ the electric-field attains its maximal amplitude E_0. The scalar factor E_0 is a measure for the intensity of the electric field. It is related to the fluence F of the pulse (i.e., energy flow per unit area) by

$$E_0 = \left(\frac{2}{\pi}\right)^{1/4} \sqrt{\frac{2F}{c\varepsilon_0 T_p}} \ , \tag{3.34}$$

where ε_0 is the vacuum permittivity. By integrating the time-dependent intensity (field energy transferred per unit area and time)

$$I(t) = \frac{1}{2}\, c\, \varepsilon_0\, E_0^2\, e^{-\frac{2t^2}{T_p^2}} \ , \tag{3.35}$$

averaged over the rapid oscillations, one obtains

$$\int_{-\infty}^{+\infty} \mathrm{d}t\, I(t) \ = \ \sqrt{\frac{2}{\pi}}\, \frac{F}{T_p} \int_{-\infty}^{+\infty} \mathrm{d}t\, e^{-\frac{2t^2}{T_p^2}} \ = \ F \ . \tag{3.36}$$

In most of the following cases, we will consider linearly polarized laser pulses which are characterized by a real polarization vector $\vec{\varepsilon} \in \mathbb{R}^3$. Then, using Eq. (3.33) the Hamiltonian $\hat{H}_E(t)$ describing the interaction between electrons and laser pulse reads

$$\hat{H}_E(t) = -e\,E_0\,\cos(\omega t)\,e^{-\frac{t^2}{T_p^2}}\,\vec{\varepsilon}\cdot\hat{\vec{r}}\,, \tag{3.37}$$

whose matrix elements are given in terms of matrix elements of $\hat{\vec{r}}$ (see Sections 3.2.3 and 3.4). However, for some purposes it is also interesting to study the effect of circularly polarized light on the magnetic system. To this aim, let us consider $\sigma_\pm$ photons which carry an angular momentum $\pm\hbar$ along the z quantization axis. We model the corresponding dipole transitions between the lower d orbitals and the higher p orbital by means of the modified Hamiltonian

$$\hat{H}_E^{\sigma_\pm}(t) = -e\,E_0\,\cos(\omega t)\,e^{-\frac{t^2}{T_p^2}}\,\left\{\hat{P}_p\,(\vec{\varepsilon}_\pm\cdot\hat{\vec{r}})\,\hat{P}_d\,+\,\hat{P}_d\,(\vec{\varepsilon}_\mp\cdot\hat{\vec{r}})\,\hat{P}_p\right\}\,. \tag{3.38}$$

Here, $\hat{P}_d$ and $\hat{P}_p$ denote projection operators onto the d and p orbitals, respectively, and the polarization vector $\vec{\varepsilon}_\pm$ is now complex. It is given by

$$\vec{\varepsilon}_\pm = \frac{1}{\sqrt{2}}\,(\hat{e}_x \pm i\hat{e}_y)\,, \tag{3.39}$$

where $\hat{e}_x$ ($\hat{e}_y$) is a unit vector along the x (y) axis. In order to understand the roles of the two summands in Eq. (3.38) and the differences to Eq. (3.37), let us give their matrix elements. Assuming the model simplifications of Section 3.4, one obtains

$$\langle\, p,0\,|\hat{P}_p\,(\vec{\varepsilon}_\pm\cdot\hat{\vec{r}})\,\hat{P}_d|\,d,m\,\rangle \;=\; \pm\delta_{\mp1,m}\,\langle\, d\,||\hat{T}^{(1)}||\,p\,\rangle^* \quad\text{and} \tag{3.40}$$

$$\langle\, d,m\,|\hat{P}_p\,(\vec{\varepsilon}_\pm\cdot\hat{\vec{r}})\,\hat{P}_d|\,p,0\,\rangle \;=\; 0 \tag{3.41}$$

for the first summand. Notice that we have used the notation $\langle\, d\,||\hat{T}^{(1)}||\,p\,\rangle$ for the reduced matrix element of the spherical tensor operator obtained from $\hat{\vec{r}}$, as introduced in Appendix D. Since $(\vec{\varepsilon}_\pm\cdot\hat{\vec{r}})^\dagger = \vec{\varepsilon}_\mp\cdot\hat{\vec{r}}$, a simple complex conjugation yields the matrix elements of the second summand, i.e.,

$$\langle\, d,m\,|\hat{P}_d\,(\vec{\varepsilon}_\mp\cdot\hat{\vec{r}})\,\hat{P}_p|\,p,0\,\rangle \;=\; \pm\delta_{\mp1,m}\,\langle\, d\,||\hat{T}^{(1)}||\,p\,\rangle \quad\text{and} \tag{3.42}$$

$$\langle\, p,0\,|\hat{P}_d\,(\vec{\varepsilon}_\mp\cdot\hat{\vec{r}})\,\hat{P}_p|\,d,m\,\rangle \;=\; 0\,. \tag{3.43}$$

Equations (3.40) and (3.41) demonstrate that the first summand in $\hat{H}_E^{\sigma_+}$ [see Eq. (3.38)] describes the absorption of a σ_+ photon, which carries an angular momentum $+\hbar$ to

the electron orbits by inducing an intra-atomic transition from the d-electron local orbitals to the p-electron local orbital. The second summand in Eq. (3.38) is the complex adjoint operator which ensures that the Hamiltonian $\hat{H}_E^{\sigma_+}$ remains hermitian. Physically, it describes the emission of a σ_+ photon which comes along with subtraction of angular momentum $+\hbar$ from the electron orbits and reverse transition from the p orbital back to the d orbitals [see Eqs. (3.42) and (3.43)]. Similarly, the operator $\hat{H}_E^{\sigma_-}$ with the opposite helicity σ_- corresponds to the absorption and emission of angular momentum $-\hbar$ (i.e., $+\hbar$ replaced by $-\hbar$). To summarize, the Hamiltonian $\hat{H}_E^{\sigma_\pm}$ takes into account the absorption and emission of only σ_+ or σ_- circularly-polarized photons, whereas the Hamiltonian $\hat{H}_E(t)$ in Eq. (3.37) considers linear polarizations representing a superposition of both σ_+ and σ_- helicities.

Finally, it is worth noting that we have neglected the magnetic field $\vec{B}(t)$ induced by the time variations of $\vec{E}(t)$. The associated field $\vec{B}(t)$ results from the Maxwell equation in vacuum

$$\vec{\nabla} \times \vec{B} = \frac{1}{c^2} \frac{\partial \vec{E}}{\partial t} \ . \tag{3.44}$$

In the case of continuous electromagnetic waves in the vacuum, the Maxwell equations yield

$$\vec{B} = \frac{1}{\omega} \vec{k} \times \vec{E} \ , \tag{3.45}$$

where $\vec{k}$ is the wave vector of the plane waves. However, since $\omega = kc$, the magnitude of the magnetic field is of the order $|\vec{B}| = \frac{1}{c} |\vec{E}|$. This means that the effect of $\vec{B}$ is considerably smaller (by a factor of $1/c$) than the effect of the electric field $\vec{E}$. These considerations give us the motivation for the neglection of $\vec{B}$. Hence, we consider only the electric field $\vec{E}$, which interacts solely with the electronic orbital degrees of freedom and thus conserves the magnetization.

4

Static magnetism

In the previous Chapter, an electronic model has been introduced which takes into account the electron-electron interaction, the spin-orbit coupling and the electron motion in the lattice on the same footing. Before studying the roles of these different processes on the magnetization dynamics as well as their interplay, it is important to understand the magnetism as described by the model from a static perspective. To this aim, first, the main comments on the model parameters are discussed in Section 4.1. In the subsequent Section 4.2 the parameter regimes of ferromagnetic ground states are identified. Moreover, the stability of the FM order in some representative examples among them is investigated. These FM ground states will be used in Chapter 5 as initial states for the purpose of performing an exact time evolution of the magnetization following the laser-pulse absorption.

4.1 Specific model parameters

The primary aim of the many-electron model proposed in the present thesis is the description of magnetization dynamics in $3d$ transition metals. With this objective in mind, the model parameters must be specified in a way such that they allow us to draw conclusions from the model dynamics on the dynamics of $3d$ ferromagnets (e.g., Nickel films or solids). This implies that, on the one hand, the parameters in Hamiltonian (3.3) need to be set as realistic as possible, in order that the static magnetic model properties are similar to the true ones. On the other hand, it is very worthwhile to reduce the model complexity (for instance, the dimensionality, the system size, etc.) by keeping

the most essential electronic ingredients which are responsible for static magnetism and magnetization dynamics. In the following these two ideas will guide the specification of the model parameters.

First of all, let us mention that the elementary electronic transitions involved in the spin-orbit interaction and laser-pulse absorption, as well as the intra-atomic Coulomb interactions which are crucial for TM magnetism, are of *local* nature. Due to their locality and essentially intra-atomic character we expect that these processes result basically in the same *local* physics both in small clusters and in the bulk. Since this *local* physics is crucial for the spin relaxation,[1] it seems sound to consider small systems, for which *exact* numerical results are achievable. The investigation of the ground-state properties and the laser-induced magnetization dynamics in small systems should allow us to draw useful conclusions on the behavior in the larger systems of experimental interest. In this work we consider clusters of $N_a = 2$–4 atoms as applications. Indeed, the idea of modeling bulk systems by means of solvable small-size clusters has been already used successfully in the past for describing the photoemission spectra of periodic systems [see Ref. (75)].

Let us continue with the hopping integrals $t_{jk}^{\alpha\beta}$. This quite important set of parameters reflects the electron dynamics in the lattice. The hopping elements are taken from tight-binding theory and are expressed in terms of Slater-Koster integrals, where the two-center approximation is applied (for details see Appendix B). We consider only first NN Slater integrals to be nonzero, for which we use $(d, d; \sigma) = 0.412$ eV, $(d, d; \pi) = -0.489$ eV, $(p, p; \sigma) = 1.516$ eV and $(p, d; \sigma) = -0.555$ eV. These parameters imply the following hopping-integral properties: (i) choosing the z axis to be orthogonal to the interatomic connection vector $\vec{R}_{jk}$, the L_z non-conserving hopping elements $t_{jk}^{d+1,d-1}$ dominate within the d band, (ii) the relatively large p–p hopping elements $t_{jk}^{p0,p0}$ yield very mobile p electrons as it is the case for strongly delocalized electrons within the $4p$ band in TMs, and (iii) the interband hopping energy between p and d electrons is considerably large (see Table 3.2). Therefore, the above choice of Slater-Koster integrals yields hopping elements which resemble the ones of localized $3d$ and delocalized $4p$ electrons in metallic Ni (76).

[1] Recall that the nonlocal physics described by the interatomic electron hoppings $t_{jk}^{\alpha\beta}$, i.e., the electron motion in the lattice, does not induce any relaxation of the spins.

The number of electrons N_e is a further important parameter. It is not specified at this stage: various values of N_e will be considered in the following investigations. Nevertheless, it is worth discussing the choice of N_e and its consequences. First, let us recall that in the case of Fe, Co and Ni, the most narrow valence band, the $3d$ band, is more than half-filled. This of course suggests to choose a more than half-filled d band within the electronic model (3.3). Alternatively, it is also possible to consider holes instead of electrons in the d band. From the mathematical perspective the unitary transformation, which transforms all electrons into holes (h) and vice versa, reads

$$\hat{c}^\dagger_{j\alpha\sigma} = \hat{h}_{j\alpha\sigma} \quad \text{and} \tag{4.1}$$

$$\hat{c}_{j\alpha\sigma} = \hat{h}^\dagger_{j\alpha\sigma} \ . \tag{4.2}$$

Then, all single-particle terms in the Hamiltonian transform as

$$\hat{c}^\dagger_{j\alpha\sigma}\hat{c}_{k\beta\sigma'} \ = \ \delta_{jk}\delta_{\alpha\beta}\delta_{\sigma\sigma'} - \hat{h}^\dagger_{k\beta\sigma'}\hat{h}_{j\alpha\sigma} \ . \tag{4.3}$$

One can show that the interaction-energy Hamiltonian $\hat{H}_C$ is invariant under this electron-hole transformation, while the resulting SOC strength ξ^h for the holes and the original electron SOC parameter ξ^e are related by

$$\xi^h = -\xi^e \ . \tag{4.4}$$

This opens the possibility to study the spin relaxation in TMs having a more than half-filled $3d$ band by considering a less than half-filled d band (holes) together with a negative SOC constant ξ.[1] In fact, we will apply this idea in the present work. However, the electron-hole transformation (4.1)–(4.3) alone has no significant practical interest, since it does not reduce the Hilbert-space dimension. In contrast, it is advantageous to simply consider less than half-filled d bands instead of more than half-filled ones, keeping the electronic band structure[2] and the occupation of the higher p band (empty or very weakly occupied) unmodified. In other words, we propose the following two changes:

(i) modeling FM transition metals such as Ni by means of less than half-filled $3d$ bands, and simultaneously

[1] In Section 3.2.4 it has been discussed that $\xi > 0$ for electrons.

[2] This means that the same single-particle Hamiltonian $\hat{H}_0$, the same electronic levels ε^0_α and the same interatomic hopping integrals $t^{\alpha\beta}_{jk}$ are used for both *electron* and *hole* calculations.

(ii) changing the sign of ξ.

Indeed, this can significantly reduce the number of many-body basis states, as demonstrated in the following simple example: Consider $N_a = 3$ atoms, each of them having $\vartheta = 5$ d electrons. Taking into account the (empty) p band, the system contains 12 orbitals (or 24 including the spin degeneracy) occupied by 15 electrons. Consequently, the dimension of the Hilbert space is given by $\binom{2\cdot 12}{15} = 1,307,504$. However, by considering 5 holes instead of 5 electrons per atom within the d band, i.e., $\vartheta = 1$ particle per atom, one obtains a reduced Hilbert-space dimension of $\binom{2\cdot 12}{3} = 2,024$. Hence, the transition from more to less than half-filled d bands largely simplifies the practical diagonalization of the many-body Hamiltonian. Accordingly, in a large part of the present thesis we will model Ni by approximately one hole per atom in the d band, i.e., by approximately one carrier per atom.[1] This simplification is physically legitimate, since the three fundamental electronic processes or terms in the Hamiltonian, namely, spin-orbit coupling $\hat{H}_{\mathrm{SO}}$, electron-electron Coulomb interaction $\hat{H}_C$ including the exchange interaction, and the electronic motion in the lattice $\hat{H}_0$, are not affected by the number of fermions. Therefore, we expect that the present choice of the d-band occupation does not affect the mechanisms involved in the magnetization dynamics and, thus, does not significantly change the qualitative physics of spin relaxation. In order to verify this assumption, in the forthcoming Section 5.9 we have investigated the magnetization dynamics of the model for various d-band occupations. There, it will be shown that the qualitative behaviors are very similar for both more and less than half-filled d bands.

Let us now consider the SOC constant ξ, which describes the strength of the coupling and of the potential angular-momentum transfer between spin and orbital degrees of freedom. According to Ref. (74), for typical $3d$ TMs the SOC strengths are in the range of $\xi = 50$–100 meV. We have chosen its lowest bound of 50 meV. Moreover, as discussed above, the sign of ξ has been changed, finally yielding

$$\xi = -50 \text{ meV} \tag{4.5}$$

for the following studies. Since we will use models having a less than half-filled d band, the negative SOC strength implies a parallel alignment between $\vec{L}$ and $\vec{S}$ (see

[1] In addition, a variation of N_e will also be considered in the following Chapters in order to investigate the dependence of magnetization dynamics on the band filling.

Section 3.2.4). This agrees with the ferromagnets Ni, Co and Fe. However, one could ask oneself about the physical meaning of a negative SOC strength. In order to address this question, let us consider the unitary transformation

$$\hat{c}^{\dagger}_{j,m,\uparrow} \longrightarrow \hat{c}^{\dagger}_{j,-m,\uparrow} \quad \text{and} \tag{4.6}$$

$$\hat{c}^{\dagger}_{j,m,\downarrow} \longrightarrow -\hat{c}^{\dagger}_{j,-m,\downarrow} \,, \tag{4.7}$$

where m denotes the orbital angular momentum z-projection quantum number. These transformations yield a change of sign in the SOC strength, i.e., $\xi \rightarrow -\xi$, and the modifications $\hat{L}_{-}\hat{S}_{+} \rightarrow \hat{L}_{+}\hat{S}_{+}$ and $\hat{L}_{+}\hat{S}_{-} \rightarrow \hat{L}_{-}\hat{S}_{-}$ in the non-diagonal SOC terms. Consequently, the transformed spin-orbit coupling conserves $\vec{L} - \vec{S}$ instead of $\vec{L} + \vec{S}$. This can be interpreted as follows: a change of sign in ξ is equivalent to a spin-orbit interaction which conserves the angular-momentum difference $\vec{L} - \vec{S}$. We believe that this slight difference —i.e., if upon the action of $\hat{H}_{\mathrm{SO}}$ the orbital angular momentum $\vec{L}$ increases or if it decreases with decreasing spin $\vec{S}$— is not relevant, since, as we shall see, $\vec{L}$ is quenched by the electron motion in the lattice anyway. Therefore, we expect that the transformation $\xi \rightarrow -\xi$ does not change the physics of ultrafast angular-momentum transfer and demagnetization. This assumption is indeed confirmed in Section 5.4, where the dependence of spin relaxation on the SOC parameter ξ including both signs is studied in some detail.

Next, we discuss the direct Coulomb integral U, which represents the direct Coulomb repulsion energy of two d electrons at the same atom. Its value can be obtained from the photoemission spectrum. Experiments using photoemission of either core or valence electrons have revealed a satellite peak in the spectrum of Ni approximately 6 eV below the main lines (77, 78, 79). This satellite in the spectrum is attributed to the emission of electrons from atoms having one $3d$ hole (before emission), while the main lines at the Fermi level correspond to the emission from atoms having zero $3d$ holes. Therefore, the satellite position with respect to the Fermi level gives an approximation to the direct Coulomb parameter, i.e., $U \approx 6$ eV for Ni (16). In addition, by solving a four-site d-electron model, Victora and Falicov have proposed a slightly smaller value of $U = 4.3$ eV to provide the proper satellite position (75). In the present thesis we use

a similar value,[1] namely,

$$U = 4.5 \text{ eV} . \tag{4.8}$$

It is important to notice that this direct intra-atomic Coulomb parameter is a little bit larger than the single-particle d-band width in the trimer model ($W_d = 1.9$ eV). This implies that in our model the d electrons must be regarded as strongly correlated.

In order to specify the p-electron level ε_p^0 relative to the effective d-electron level $\varepsilon_d^{\text{eff}}$, let us recall that the p-orbital occupation depends on the ratio between the interband d-p hopping integrals and the difference $\varepsilon_p^0 - \varepsilon_d^{\text{eff}}$ between atomic d and p levels. This argument is of course consistent with perturbation theory. In other words, the choice of ε_p^0 affects the occupancy of the higher p band and is therefore important. Keeping this in mind, we have used

$$\varepsilon_p^0 - \varepsilon_d^{\text{eff}} = 1 \text{ eV} \tag{4.9}$$

in the present thesis. This value is appropriate, since it is in the same order of magnitude as the interatomic hoppings including the d-p integrals [$(p, d; \sigma) = -0.555$ eV]. Therefore, as we shall see in Section 4.2.2 it results in an intermediate (i.e., small but not negligible) p-level occupation already in the ground state. This agrees with the considerable hybridization between the $3d$ band and higher valence bands in transition metals.

The remaining important parameter of the model (3.3) is the intra-atomic exchange Coulomb integral J. It plays an important role, since it determines the stability of the local magnetic moments. The choice of J is discussed in the following Section. There, J will be set so as to yield a stable FM ground state.

4.2 Magnetic properties

As a preliminary step toward the investigation of magnetization dynamics in Chapter 5, it is necessary to identify the parameter regimes of stable ferromagnetic ground states. To this aim, in the present Section the ground-state magnetic order is tested in terms of model parameters which have not been specified so far: geometrical structure, number of atoms N_a, number of electrons N_e, and exchange parameter J. First, in

[1] In addition to the direct Coulomb integral $U = 4.5$ eV, we have also considered the parameters $U = 4$, 5 and 6 eV. However, significant differences in the magnetic properties and in the magnetization dynamics of the model have not been found.

Subsection 4.2.1 we address solely the question if the ground state of a given system is FM or not. This allows us to choose a few representative systems, whose ground states will later be used as initial states for time propagations under the action of external laser pulses. Then, in Subsection 4.2.2 several ground-state properties of these system examples, such as the ground-state spin and orbital angular momenta and the magnetic anisotropy, are investigated. Finally, Subsection 4.2.3 considers the dependence of the static magnetization on the temperature. This allows us to quantify the stability of the FM order in the initial state before the laser-pulse action with respect to energy absorption and subsequent thermalization.

We would like to remark that the present model is applicable to the detailed study of electronic correlations in a variety of magnetic properties. Although this route is certainly very interesting in the context of both ground-state and finite-temperature magnetism, at this point we focus only on such properties which are important for the laser-induced magnetization dynamics. However, a brief outlook on the various possibilities of the model is given in the concluding Chapter 6.

4.2.1 Identifying ferromagnetic phases

In order that the many-body model (3.3) can be used to describe the laser-induced ultrafast demagnetization, it is clear that appropriate band fillings and interaction parameters must be chosen so that the ground state is ferromagnetic. Otherwise, there would be no FM order before laser-pulse absorption. Therefore, it is important to find the FM phases of the model, i.e., the parameter regimes in which the ground state is ferromagnetically ordered.

To this aim, we first consider the ground-state magnetic order within only the d band as the relevant valence band. This single-band restriction simplifies the identification of FM phases. Its physical motivation is that in typical $3d$ TMs the static magnetic properties are determined dominantly by the more localized d valence electrons. Consequently, considering only the d band represents a sound approach if one aims to compute static magnetic properties which do not involve optical transitions to higher bands. Furthermore, let us recall that ferromagnetism in transition metals mainly results from the electron-electron Coulomb interaction, while the spin-orbit coupling has little effect on the ground-state spin magnetization but is responsible —from the static point of view— essentially for orbital magnetism and magnetic anisotropy.

For this reason, in this first step the SOC is not taken into account ($\xi = 0$). Then, the electronic Hamiltonian commutes with the total spin $\hat{\vec{S}}$ and, therefore, all stationary states can be chosen as eigenstates of $\hat{\vec{S}}^2$ having definite spin quantum number S. Since the Hamiltonian also commutes with $\hat{S}_+$ and $\hat{S}_-$, all states having a given quantum number S have the same energy independent of the spin projection (along an arbitrary quantization axis). This means that the ground-state quantum number S determines the maximal spin polarization in the ground state. It is important to notice that the magnetic order is most sensitive to the exchange parameter J, which is responsible for the stability of the atomic magnetic moments. In addition, the magnetic order also depends on the structure and band filling, as it is the case in $3d$ TMs. For these reasons, we have determined the ground states of several small clusters, having $N_a = 2$–4 atoms and different geometries, as a function of J and number of electrons N_e. The corresponding static calculations have been performed by applying a Lanczos diagonalization method (80), whose mathematical description is given in Appendix E. The results are summarized in Figure 4.1. It shows, for the considered structures, the ground-state spin quantum number $S^{d,\xi=0}$ in terms of J and N_e.[1] In our calculations only exchange integrals J smaller than the direct Coulomb integral U have been taken into account, i.e., the parameter J has been varied within the range $0 \leq J \leq U = 4.5$ eV. A ferromagnetic ground state exists if $S^{d,\xi=0} \geq 1$ for N_e even or $S^{d,\xi=0} \geq 3/2$ for N_e odd. First, one observes that for most structures and band fillings the ground state has minimal spin (i.e., $S^{d,\xi=0} = 0$ or $1/2$) for $J = 0$. However, in some cases a degeneracy in the single-particle spectrum of $\hat{H}_0$ leads to $S^{d,\xi=0} = 1$ or $3/2$ already for $J = 0$ (for the dimer having $N_e = 2$ and 10 electrons, the $N_a = 3$ linear chain having $N_e = 2$, 9 and 16 electrons, the triangle having $N_e = 6$ and 14 electrons, the $N_a = 4$ linear chain having $N_e = 2$ and 22 electrons, and the pyramid having $N_e = 4$, 5, 15 and 22 electrons). For those numbers of electrons N_e, for which a FM ground-state order is possible, the total spin quantum number $S^{d,\xi=0}$ tends to increase stepwise with increasing parameter J. In other words, with increasing exchange energy J the tendency toward FM order of the local magnetic moments increases. Furthermore, whether the ground state is ferromagnetic or not strongly depends on the band filling. For instance, Figure 4.1 shows that

[1] The spin quantum number in the d-band system (excluding the SOC) is denoted by $S^{d,\xi=0}$, in order to distinguish it from the corresponding spin quantum number S in the two-band model including both d and p bands and SOC.

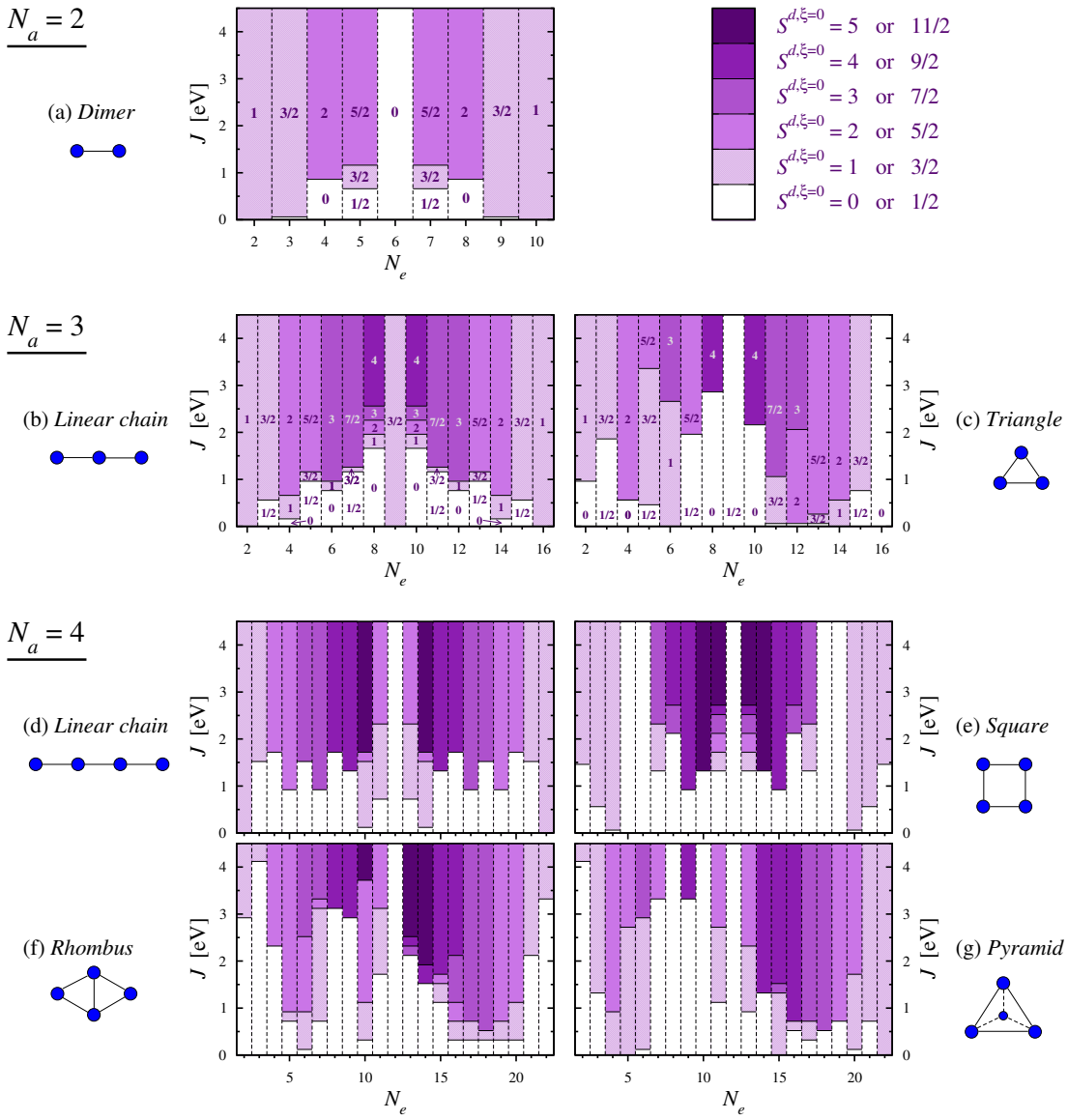

Figure 4.1: Ground-state spin angular momentum of small clusters - The ground-state spin quantum number $S^{d,\xi=0}$ is shown for several small clusters, having $N_a = 2$–4 atoms and different geometries, as a function of exchange energy J and number of electrons N_e. In these calculations, only the d band of localized electrons has been included in the model. Moreover, the spin-orbit coupling has not been taken into account ($\xi = 0$).

for half-band filling ($N_e = 3N_a$) the ground states of most of the considered structures have $S^{d,\xi=0} = 0$ or $S^{d,\xi=0} = 1/2$,[1] whereas one electron below or above half-band filling the ground states are ferromagnetic.

Based on the results given in Figure 4.1 we choose the following structures and band fillings as applications for the dynamical simulations in Chapter 5:

- Dimer ($N_a = 2$) having $N_e = 3$ electrons
- Linear chain ($N_a = 3$) having $N_e = 5$ and 7 electrons
- Triangle ($N_a = 3$) having $N_e = 3$, 4, 5, 7 and 15 electrons
- Rhombus ($N_a = 4$) having $N_e = 5$ electrons

These examples show FM order in the ground state for sufficiently large exchange energies J. They provide a representative selection since band fillings from low to high band filling N_e and different numbers of atoms $N_a = 2$–4 are considered.[2] In the present thesis a particular focus is set on the isosceles triangle having $N_e = 4$ electrons as the main system. This structure represents a two-dimensional geometry similar to the thin films used in the experiments. Its particular occupation by $N_e = 4$ electrons is appropriate for several reasons: it takes into account the important intra-atomic Coulomb repulsion between two electrons due to $\nu = N_e/N_a = 4/3 > 1$, it yields a FM ground state with saturated spin $S^{d,\xi=0}$ already for rather small exchange parameters $J > 0.5$ eV, and it is computationally affordable. The other chosen electron occupations N_e and geometries (dimer, $N_a = 3$ linear chain, and rhombus) serve as a comparison in order to elucidate possible dependences of the magnetization dynamics on the band filling and structure. In fact, we shall see in Section 5.9 that the laser-induced spin dynamics is qualitatively very similar for all considered structures and band fillings. These systems show the same physics as long as the corresponding ground states are ferromagnetic. Therefore, we expect that the detailed choice of the system

[1] The $N_a = 3$ linear chain is an exception. There, a degeneracy in the single-particle spectrum leads to $S^{d,\xi=0} = 3/2$ for half-band filling, i.e., $N_e = 9$, and all considered J.

[2] Actually, in most of the chosen examples the FM ground states are fully spin polarized for sufficiently large exchange parameters J. They have the maximum spin quantum number $S^{d,\xi=0}$ for a given number of electrons N_e, i.e., $S^{d,\xi=0} = N_e/2$ for $N_e \leq 3N_a$ or $S^{d,\xi=0} = (6N_a - N_e)/2$ for $N_e > 3N_a$. The sole exception is given by the triangle occupied by $N_e = 7$ electrons. The corresponding ground states have a non-saturated spin $S^{d,\xi=0} \leq 5/2$ for $J \leq U = 4.5$ eV.

is not critical for the purpose of investigating the mechanisms involved in the ultrafast demagnetization.

So far, the SOC has not been considered and only one band, namely the d band of localized electrons, has been effectively included in the model (3.3). The corresponding ground states can in principle be used as initial states for studying the laser-induced magnetization dynamics. However, for the purpose of describing the electronic response to the laser-pulse absorption, the electron-light interaction and, thus, both the d and p bands need to be taken into account. In addition, the spin-orbit coupling must be taken into account in order to allow for spin relaxation. It is clear that the inclusion of the additional p valence band and spin-orbit interaction represents a change in the Hamiltonian of the system: from the d-band restricted model excluding SOC to the two-band model including d and p bands as well as SOC. This can result in some modifications in the corresponding ground states. Since the most essential magnetic properties are determined dominantly by the d electrons, one expects that the FM phases (i.e., the parameter regimes in terms of structure, N_e and J, for which the ground states are ferromagnetic) of the d-band restricted model should not differ strongly from the FM phases of the two-band model. Nevertheless, this assumption needs to be verified explicitly. Therefore, in the following it is demonstrated that the above chosen structures and band fillings also correspond to high-spin parameter regimes of the two-band model, for which the ground states have relatively large quantum numbers S.

In order to elaborate the modifications introduced by the transition from the d band to the two-band model, let us notice that the addition of the higher p band including finite d-p hopping integrals leads to d-p hybridization. Indeed, in transition metals the $3d$ band considerably hybridizes with higher valence bands. This change of the system may have an effect also on the ground-state spin quantum number S. Moreover, the spin-orbit Hamiltonian $\hat{H}_{\mathrm{SO}}$ does not commute with the total spin square $\hat{\vec{S}}^2$. Hence, by including the spin-orbit interaction, $\vec{S}^2$ is not conserved anymore. In other words, the ground states cannot always be chosen such that they have definite spin quantum numbers S. These considerations show that the inclusion of the p band and SOC results in a modified functional dependence of S on the exchange energy J. In order to investigate it, both the d and p bands as well as the SOC having a strength of $\xi = -50$ meV are now included in the model. The ground states of the above chosen systems are determined as a function of J, and the results are shown in Figure 4.2.

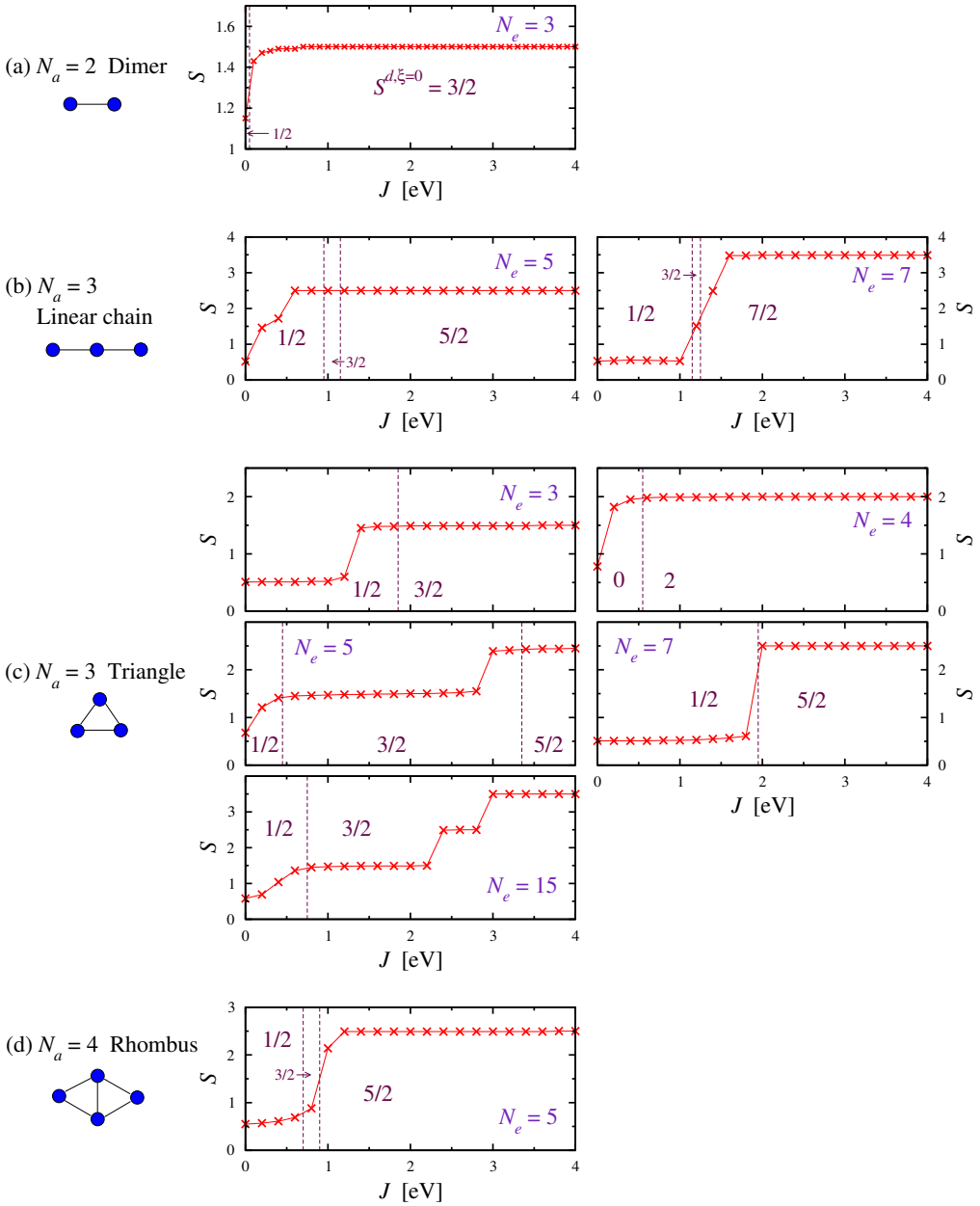

Figure 4.2: Ground-state spin angular momentum of selected systems within the two-band model - The ground-state spin quantum number S is shown as a function of exchange energy J for (a) the dimer having $N_e = 3$ electrons, (b) the $N_a = 3$ linear chain having $N_e = 5$ and 7 electrons, (c) the triangle having $N_e = 3$–5, 7 and 15 electrons, and (d) the rhombus having $N_e = 5$ electrons. Here, the two-band model, including both d and p bands and SOC, has been used. The vertical dotted lines illustrate the parameter ranges of the ground-state spin $S^{d,\xi=0}$ (indicated by numbers) obtained by excluding the p band and SOC (see Figure 4.1).

There, the ground-state spin quantum number S, which is now defined in terms of the expectation value of $\vec{S}^2$, i.e.,

$$S(S+1)\,\hbar^2 \;=\; \left\langle \hat{\vec{S}}^2 \right\rangle \;, \tag{4.10}$$

is compared with the precise spin quantum number $S^{d,\xi=0}$ of the corresponding system which does not include the p band and SOC (see Figure 4.1). One observes that in many of the considered examples (namely, the dimer, $N_a = 3$ linear chain having $N_e = 7$, triangle having $N_e = 7$, and rhombus) the dependence of S on J remains quite unmodified: changes can be seen only within very small intervals around those critical parameters J_c, for which Figure 4.1 has shown a stepwise transition between two different discrete ground-state spin quantum numbers $S^{d,\xi=0}$. In the other examples ($N_a = 3$ linear chain having $N_e = 5$, and triangle having $N_e = 3$–5 and 15) the critical parameters J_c decrease by 0.3–0.7 eV after the inclusion of the p band and SOC. This means that the extent of the high-spin (large quantum number S) parameter regimes in terms of J increases. Let us also mention the case of the triangle having $N_e = 15$ electrons. There, due to the addition of the p band the total number of orbitals increases from 18 to 24 including the two-fold spin degeneracy. Hence, the maximum admissible spin quantum number of $N_e = 15$ electrons increases from 3/2 (within the d band only) to 9/2 (within both d and p bands). This explains why for $J \geq 3$ eV the ground-state spin quantum number within the two-band model $S = 7/2$ exceeds by far the corresponding spin $S^{d,\xi=0} = 3/2$ within the d-band restricted model.

Finally, having revealed the functional dependence of S on the exchange energy J, which is shown in Figure 4.2, we are now able to choose appropriate parameters J. Our choices for the selected structures and band fillings are summarized in Table 4.1. These are set so as to yield stable high-spin ground states. Notice that both saturated and non-saturated spin states are considered among the ground states of the selected systems. Indeed, the ground-state spin quantum number S is almost saturated for the dimer, the $N_a = 3$ linear chain having $N_e = 7$, the triangle having $N_e = 3$–5 and the rhombus, while it is non-saturated for the $N_a = 3$ linear chain having $N_e = 5$ and the triangle having $N_e = 7$ and 15.

In the following the magnetic properties of the chosen examples of structures and band fillings are investigated in more detail. In particular, Section 4.2.2 considers several important ground-state properties of these systems including the magnetic

System size	Structure	Band filling	Exchange integral	Spin
$N_a = 2$	Dimer	$N_e = 3$	$J = 0.4$ eV	$S = 1.49$
$N_a = 3$	Linear chain	$N_e = 5$	$J = 0.3$ eV	$S = 1.52$
		$N_e = 7$	$J = 1.6$ eV	$S = 3.48$
$N_a = 3$	Triangle	$N_e = 3$	$J = 1.6$ eV	$S = 1.48$
		$N_e = 4$	$J = 0.8$ eV	$S = 1.99$
		$N_e = 5$	$J = 3.2$ eV	$S = 2.41$
		$N_e = 7$	$J = 2.4$ eV	$S = 2.50$
		$N_e = 15$	$J = 1.0$ eV	$S = 1.47$
$N_a = 4$	Rhombus	$N_e = 5$	$J = 1.4$ eV	$S = 2.49$

Table 4.1: Selected high-spin systems - A selection of small clusters having $N_a = 2$–4 atoms and different structures, band fillings N_e and exchange energies J is shown. The ground-state spin quantum number S is indicated for each of these systems. Their ground states are used as initial states for the dynamical studies in Chapter 5.

anisotropy, while Section 4.2.3 addresses the stability of ferromagnetism with respect to energy absorption.

4.2.2 Ground-state properties of selected high-spin systems

In the previous Section we have chosen several structures and band fillings as representative examples. Their ground states will be used as initial states for the dynamical studies in Chapter 5. Therefore, the ground-state magnetic properties of these systems are certainly important for the initial stage of the laser-induced magnetization dynamics within the model. For this reason, in the present Section we want to describe the properties of the selected ground states in more detail.

So far the ground states have been characterized only in terms of the total spin quantum number S, which is associated to the eigenvalue $S(S+1)\hbar^2$ of $\hat{\vec{S}}^2$. Actually, the ground states of all the selected systems satisfy $S \gtrsim 1$ for N_e even or $S \gtrsim 3/2$ for N_e odd. Therefore, they are regarded as high-spin states. Now, Table 4.2 shows several further ground-state properties besides S: easy magnetization direction, spin and orbital angular-momentum projections along the easy magnetization axis, d and p-band occupations, local magnetic moments, and magnetic-anisotropy energies.

Structure (N_a)	N_e	J [eV]	S	Easy axis/ plane	S_{easy} [$\hbar$]	L_{easy} [$\hbar$]	n_d	n_p	$\langle\langle \vec{S}^2_{jd} \rangle\rangle$ [$\hbar^2$]	E_{MA} [meV/at]
Dimer ($N_a = 2$)	3	0.4	1.49	z	0.989	0.227	0.022	2.978	1.361	3.3
Lin. chain ($N_a = 3$)	5	0.3	1.52	z	0.987	0.174	0.796	4.204	1.118	7.1
	7	1.6	3.48	z	1.988	0.089	0.087	6.913	2.543	0.8
Triangle ($N_a = 3$)	3	1.6	1.48	z	1.468	0.799	0.059	2.941	0.762	4.8
	4	0.8	1.99	z	1.982	0.268	0.238	3.762	1.086	2.8
	5	3.2	2.41	z	2.334	0.462	0.041	4.959	1.580	1.5
	7	2.4	2.50	xy	1.497	0.070	0.055	6.945	2.544	−0.7
	15	1.0	1.47	z	1.457	−0.043	1.151	13.849	1.199	1.0
Rhombus ($N_a = 4$)	5	1.4	2.49	z	2.436	0.492	0.207	4.793	1.024	2.4

Table 4.2: Ground-state properties of selected structures and band fillings - Results are given for the selected high-spin clusters (N_a = 2–4 atoms) having various electron occupations N_e and exchange integrals J: total-spin quantum number S, easy magnetization direction, spin and orbital angular-momentum projections S_{easy} and L_{easy} along the easy axis, d and p-level occupations n_d and n_p, square of the atomic d-electron spin $\langle\langle \vec{S}^2_{jd} \rangle\rangle$, and magnetic-anisotropy energy E_{MA}. The considered structures lie within the xy plane, which implies that the z axis is orthogonal to all interatomic vectors.

First, let us discuss the properties related to the magnetic anisotropy, which originates from the spin-orbit interaction. Since the SOC breaks the spin-rotational invariance of the model, it leads to an anisotropy with respect to the magnetization direction, i.e., the energy of the state depends on the direction of the vector $\vec{S}$. In order to determine this favored direction (easy magnetization axis or easy plane) we have included external magnetic fields $\vec{B}$ having different orientations in the model. Then, by minimizing the total energy for a given field $\vec{B}$, a nonzero magnetic moment $\vec{\mu}$ parallel to $\vec{B}$ has been imposed on the many-body state. In the next step, we have taken the limit $B \to 0$ keeping the directions of the magnetic fields unchanged. In this way, the resulting states keep their magnetization directions, too, i.e., their magnetization directions are stabilized along the directions of $\vec{B}$. Finally, the easy magnetization axis has been identified as the particular spin direction of that state, which has the lowest energy among the states resulting from the limit $\vec{B} \to 0$ taken in various directions.[1]

[1]In practice, we have used only three orthogonal directions of the magnetic field $\vec{B}$ and compared

The easy magnetization axes for the considered systems are indicated in the fifth row of Table 4.2. They have been found to be perpendicular to the 1D chains (dimer and $N_a = 3$ linear chain) or to the 2D planes (triangle and rhombus planes). The sole exception is given by the triangle having $N_e = 7$ electrons, where the easy magnetization direction is inside the triangle plane.

Besides the magnetic anisotropy, the SOC leads to a mixing of the up and down-spin manifolds. Therefore, in the ground states the maximal spin projection along the easy magnetization axis S_{easy} can be significantly smaller than the quantum number S, or it can even vanish, for example, when $\vec{S}$ and $\vec{L}$ add to yield $\vec{J} = \vec{L} + \vec{S} = 0$, in which case the many-body state is rotationally invariant. This consideration shows that it is necessary to verify that the ground states of the selected systems can be spin polarized along the easy axis. To this aim, the sixth row of Table 4.2 shows the ground-state spin projections S_{easy} for all the selected structures and band fillings.[1] One observes that for the triangle having $N_e = 3$–5 and 15 electrons, and for the rhombus, S_{easy} is almost equal to S. In these examples including the main triangle system having $N_e = 4$ electrons, the ground states are almost fully spin polarized, i.e., essentially all the electrons have the same spin projection. The other selected systems (dimer, $N_a = 3$ linear chain, and triangle having $N_e = 7$ electrons) don't have a saturated spin polarization, since S_{easy} is considerably smaller than S. However, for these structures and band fillings the ground-state spin projection is still finite, i.e., $S_{\text{easy}} \gtrsim \hbar$, which means that the ground states of these systems also have a significant FM order. In conclusion, for all the considered systems ground states having considerable spin polarizations can indeed be stabilized by including magnetic fields $\vec{B}$ along the easy axes and considering the limit $\vec{B} \to 0$. Hence, these ground states can be regarded as typical FM states, and therefore are appropriate to serve as initial states for the investigation of the model magnetization dynamics.

Table 4.2 also shows the orbital angular-momentum projection L_{easy} along the easy magnetization axis (seventh row). One can see that L_{easy} is relatively small with respect to S_{easy}, i.e., $L_{\text{easy}} \leq 0.23\, S_{\text{easy}}$, except for the triangle having $N_e = 3$ electrons. In particular, for the triangle system having $N_e = 4$ electrons, one finds $L_{\text{easy}} = 0.089\hbar$

the ground-state energies of the corresponding models.

[1] In the corresponding calculations, the direction of the total magnetic moment has been stabilized by including a magnetic field $\vec{B}$ along the easy axis and considering the limit $\vec{B} \to 0$.

per atom, while the spin projection is given by $S_{\text{easy}} = 0.661\hbar$ per atom. In other words, the orbital angular momentum $\vec{L}$ is very effectively suppressed by interatomic electron hoppings. Notice that this situation corresponds to the orbital magnetism in ferromagnetic bulk TMs, in which $\vec{L}$ is almost totally quenched ($L_{\text{easy}} \approx 0.05$–$0.15\hbar$ per atom) due to the electron motion in the lattice (81). Furthermore, one observes in Table 4.2 that the crossing from less- to more-than half-band filling in the triangle comes along with a transition from parallel to antiparallel alignment of $\vec{S}$ and $\vec{L}$. This behavior reflects the third Hund's rule.[1]

In the context of magnetic anisotropy, it is insightful to consider rotations of the magnetization direction at temperature $T = 0$. In fact, the differences in energy for different orientations of the spin $\vec{S}$ can be regarded as a measure for the stability of the FM order along the easy axis with respect to rotations of the magnetization direction. Let us recall that for the triangle having $N_e = 4$ electrons we have found an off-plane easy axis. In other words, the FM ground state exhibits a magnetic moment along the off-plane axis (z axis). In the following, the detailed dependence of the energy on the polar angle θ between the z axis (normal vector to the triangle xy plane) and the magnetic-moment direction is investigated for the triangle system. To this aim, Figure 4.3 shows the energy $E(\theta)$ as a function of θ, where $E(\theta)$ is defined as the lowest energy of all the states having a magnetic moment $\vec{\mu}$ with the given polar angle θ and the same magnitude as the easy-axis ground-state moment μ_{gs}.[2] Notice that the dependence of E on the in-plane azimuth angle φ is not considered, since we are only interested in computing the energy required to rotate the magnetization vector from the off-plane to the in-plane direction. One observes that this energy difference, known as the magnetic-anisotropy energy E_{MA}, is given by $E_{\text{MA}} = E(\pi/2) - E(0) = 2.8$ meV per atom. For the other selected systems the magnetic-anisotropy energies have been computed in a similar way. In the considered one- and two-dimensional structures

[1] See also Sections 3.2.4 and 4.1, where the effects of the spin-orbit coupling and the consequences of a negative SOC constant ξ are discussed.

[2] In practice, different orientations of the magnetic moments $\vec{\mu}$ have been stabilized by applying an external magnetic field $\vec{B}$ along different angles θ and φ. For each direction of $\vec{B}$ the magnitude of the magnetic field is such that the projection of the resulting magnetic moment $\vec{\mu}$ on the direction of $\vec{B}$ is the same as the off-plane ground-state magnetic moment μ_z. Defining $E(\theta, \varphi)$ as the energy of the corresponding states, where the field energy $-\vec{\mu} \cdot \vec{B}$ has been subtracted, one ensures that the energies $E(\theta, \varphi)$ for the different moment orientations are comparable. Finally, for a given polar angle θ the energy $E(\theta)$ is given by the minimum in $E(\theta, \varphi)$ with respect to the azimuth angle φ.

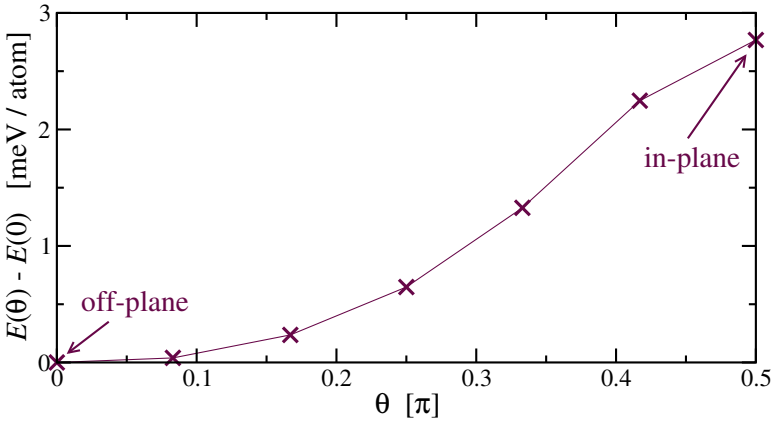

Figure 4.3: Magnetic anisotropy in the triangle system - Energy E of the triangle having $N_e = 4$ electrons is shown as a function of the polar angle θ between the normal vector to the triangle plane and the magnetic-moment direction. The particular energies corresponding to the off-plane and in-plane directions of the magnetization are indicated. The symbols represent numerical results, while the line is a guide to the eyes.

E_{MA} has been determined as the difference in energy between parallel or in-plane spin orientation and perpendicular spin orientation.[1] The results are shown in the last row of Table 4.2. Notice that the negative sign of E_{MA} for the triangle having $N_e = 7$ electrons means that the easy magnetization direction lies within the plane of the triangle. For all the other considered systems the easy axis is in the perpendicular direction.

Next, the eighth and ninth rows of Table 4.2 give the occupation

$$n_d = \sum_{j\sigma} \langle \hat{n}_{jd\sigma} \rangle \tag{4.11}$$

of the narrow d band and the occupation

$$n_p = \sum_{j\sigma} \langle \hat{n}_{jp\sigma} \rangle \tag{4.12}$$

of the higher p valence band. One observes that for all the considered structures and band fillings n_p is much smaller than n_d, but it is nevertheless finite. These non-vanishing p-band occupations are the result of considerable interband d-p hybridizations. We shall discuss in Section 5.8 that the presence of d-p hybridizations in the

[1] The parallel spin orientation in 1D structures means that $\vec{S}$ is aligned parallel to the dimer or chain, while in the case of the in-plane spin orientation in 2D structures $\vec{S}$ is oriented within the triangle or rhombus plane.

initial state facilitates the laser-induced spin relaxation by enhancing the change in the total spin.

Finally, let us consider the local magnetic moments. They are known to play an important role in the ferromagnetism of transition metals. Before in Chapter 5 the dynamics of these moments after laser-pulse absorption will be investigated, it is useful to quantify their ground-state magnitudes. To this aim, the tenth row of Table 4.2 shows the square of the atomic d-electron spin

$$\langle\langle \vec{S}_{jd}^{\,2} \rangle\rangle = \frac{1}{N_a} \sum_{j=1}^{N_a} \left\langle \hat{\vec{S}}_{jd} \cdot \hat{\vec{S}}_{jd} \right\rangle \ , \tag{4.13}$$

which can be regarded as a measure for the magnitude or strength of local magnetic moments. This quantity is defined as the average of squared d-electron spins over N_a atoms.[1] Importantly, the particular values of $\langle\langle \vec{S}_{jd}^{\,2} \rangle\rangle$ can be understood as the result of two main tendencies: first, the d-electron charge fluctuations $\langle (\hat{n}_{jd} - \langle \hat{n}_{jd} \rangle)^2 \rangle$ are minimized for a given number of d electrons n_d, and second, the square $\langle \hat{\vec{S}}_{jd} \cdot \hat{\vec{S}}_{jd} \rangle$ of the d-electron spin is maximized at each atomic site j. We would like to illustrate the application of these criteria for the main triangle system having $n_d = 3.8 \approx 4$ d electrons ($N_e = 4$). In this case, assuming $n_d = 4$, the atomic charge fluctuations $\langle (\hat{n}_{jd} - \langle \hat{n}_{jd} \rangle)^2 \rangle$ are minimized by occupying one atom with two d electrons and the remaining two atoms with only a single d electron. The 2-1-1 charge configurations have maximum atomic spin quantum numbers of $S_{jd} \approx 1$, 1/2 and 1/2, respectively. Thus, the corresponding squares of the local d-electron spins are given by $\langle \hat{\vec{S}}_{jd} \cdot \hat{\vec{S}}_{jd} \rangle \approx 2\,\hbar^2$, $3/4\,\hbar^2$ and $3/4\,\hbar^2$, which yields $\langle\langle \vec{S}_{jd}^{\,2} \rangle\rangle_{\max} \approx 1.167\,\hbar^2$. Remarkably, the exact numerical result $\langle\langle \vec{S}_{jd}^{\,2} \rangle\rangle = 1.086\,\hbar^2$ deviates only slightly from the maximum admissible value. For all the other selected systems one can show analogously that the computed expectation values $\langle\langle \vec{S}_{jd}^{\,2} \rangle\rangle$ imply maximum atomic spins S_{jd} under the constraint of minimum charge fluctuations. This demonstrates that the local magnetic moments in the ground states of all the selected systems are almost saturated.

[1] The numerical calculations have verified that the expectation values $\langle \hat{\vec{S}}_{jd} \cdot \hat{\vec{S}}_{jd} \rangle$ are independent of the lattice site j. Therefore, the magnitude of the local magnetic moments can be regarded as site-independent.

4.2.3 Temperature dependence of magnetization

The ground states of all the considered systems for the dynamic simulations have been shown to be ferromagnetic. However, the spin excitations which measure the stability of the FM order with respect to the level of excitation or temperature have not been considered at all. A quantification of the stability of the ground-state magnetic order is important for the forthcoming discussion of spin dynamics. In particular, we expect that the temperature dependence of the equilibrium magnetization can help to clarify the role of thermalization of absorbed energy in the laser-induced demagnetization process. With this motivation in mind we address in the present Section the temperature dependence of the magnetization and spin-correlation function. The following discussions are restricted to the triangle structure having $N_e = 4$ electrons, since this system serves as the main application for the investigation of magnetization dynamics in Chapter 5. Nevertheless, we expect that the conclusions have general validity.

We have computed two important spin observables of the triangle system as a function of T: (i) the square $\langle\langle \vec{S}_{jd}^2 \rangle\rangle$ of the atomic d-electron spin [see Eq. (4.13)], which gives the magnitude of the local magnetic moments, and (ii) the nearest-neighbor d-electron spin correlation

$$\langle\langle \vec{S}_{jd} \cdot \vec{S}_{kd} \rangle\rangle = \frac{1}{N_{\mathrm{nnc}}} \sum_{\langle j,k \rangle} \langle \vec{S}_{jd} \cdot \vec{S}_{kd} \rangle \ , \tag{4.14}$$

which measures the correlation between neighboring moments.[1] In the above definition N_{nnc} is the number of nearest-neighbor connections in the whole lattice, and $\sum_{\langle j,k \rangle}$ denotes a sum among NNs j and k. The numerical calculations have been performed by using the so-called finite-temperature Lanczos method (82), which is described in Appendix E.2.

Results for these temperature-dependent magnetic properties are shown in Figure 4.4(a). One observes that the local magnetic moments $\langle\langle \vec{S}_{jd}^2 \rangle\rangle$ remain very stable for temperatures up to $T = 2500$ K. This is of course understandable since the local moments are stabilized by the relatively large exchange-energy parameter $J = 0.8$ eV. In contrast, the nearest-neighbor spin correlation $\langle\langle \vec{S}_{jd} \cdot \vec{S}_{kd} \rangle\rangle$ decreases significantly in the temperature range between $T = 500$ and 2000 K. For low temperatures, $T < 500$ K,

[1] Notice that the spin observables $\vec{S}_{jd}$ and $\vec{S}_{kd}$ are restricted to d electrons only, since they dominate the magnetic properties of $3d$ TMs.

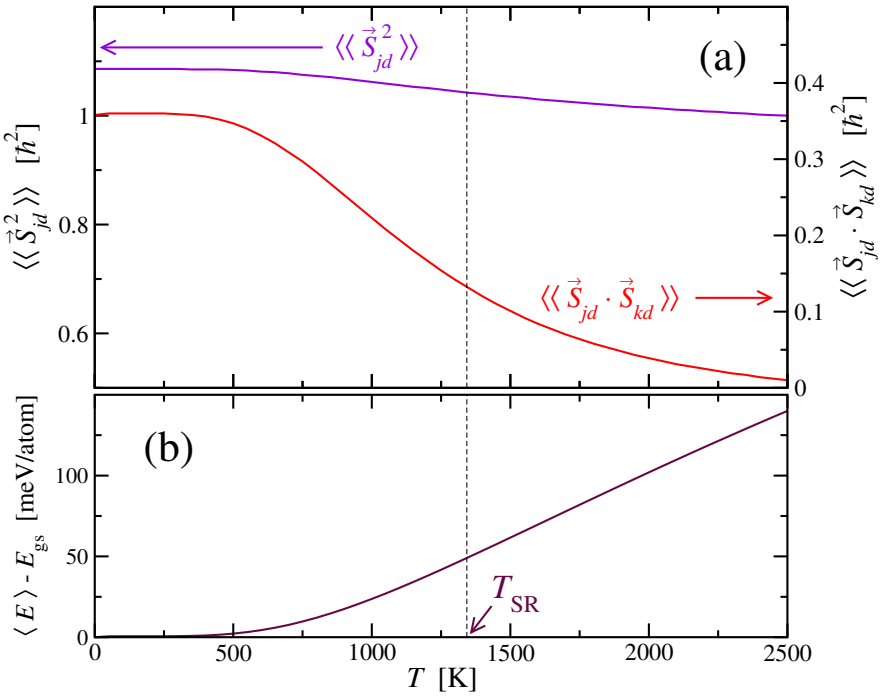

Figure 4.4: Magnetization as a function of temperature in the $N_e = 4$ triangle system - (a) Temperature dependence is shown for two spin observables in the triangle having $N_e = 4$ electrons: the square $\langle\langle \vec{S}_{jd}^2 \rangle\rangle$ of the atomic d-electron spin, and the nearest-neighbor d-electron spin correlation $\langle\langle \vec{S}_{jd} \cdot \vec{S}_{kd} \rangle\rangle$. In addition, (b) the thermal internal energy $\langle E \rangle$ in equilibrium relative to the ground-state energy $E_{\rm gs}$ is given as a function of T. The *short-range* temperature $T_{\rm SR}$ is indicated by a vertical dotted line.

the NN spin correlations are nearly constant and almost equal to the $T = 0$ values, whereas for high temperatures, $T > 2000$ K, they vanish almost completely. This behavior is similar to the situation in the bulk, where the long-range magnetization is finite below and exactly vanishes above the Curie temperature T_C. However, two fundamental differences between the temperature-dependent magnetism in the bulk and in the cluster should be mentioned. First, in the solid it is the long-range magnetic order what vanishes in the paramagnetic phase, while the short-range magnetic order remains finite even for temperatures well above T_C. In small clusters we have no access to the long-range order since long distances do not exist. Therefore, not the long-range but rather the short-range magnetic order described by the NN spin correlations $\langle\langle \vec{S}_{jd} \cdot \vec{S}_{kd} \rangle\rangle$ is appropriate for characterizing the finite-temperature magnetism in the considered clusters. Secondly, a clear transition with increasing temperature T from

the ferromagnetic to the paramagnetic phase, which is typical for FM solids, cannot take place for small-size systems. For this reason, the temperature above which the FM order is destroyed cannot be defined in the same way as the Curie temperature in the bulk. Instead, for the sake of comparison we define the *short-range* temperature $T_{\rm SR}$ as the particular temperature what yields a decrease by a factor $1/e = 0.368$ in the NN spin correlations $\langle\langle \vec{S}_{jd} \cdot \vec{S}_{kd} \rangle\rangle_T$ with respect to $T = 0$. In other words, $T_{\rm SR}$ is defined by

$$\langle\langle \vec{S}_{jd} \cdot \vec{S}_{kd} \rangle\rangle_{T=T_{\rm SR}} \quad = \quad 0.368 \, \langle\langle \vec{S}_{jd} \cdot \vec{S}_{kd} \rangle\rangle_{T=0} \; . \tag{4.15}$$

In the case of the triangle system having $N_e = 4$ electrons we have found a *short-range* temperature of $T_{\rm SR} = 1343$ K.

For the purpose of later discussions it is useful to quantify the stability of the ferromagnetic order with respect to energy absorption. To this aim, we have also computed the thermal internal energy of the electronic system in equilibrium at $T > 0$ relative to the ground-state energy, i.e., $\langle E \rangle - E_{\rm gs}$.[1] Its temperature dependence is illustrated in Figure 4.4(b). The particular thermal energy at $T_{\rm SR}$ is denoted by the energy

$$\Delta E_{\rm SR} = \langle E \rangle_{T_{\rm SR}} - E_{\rm gs} \; . \tag{4.16}$$

We have found $\Delta E_{\rm SR} = 50$ meV per atom for the triangle system. $\Delta E_{\rm SR}$ can be interpreted as the average energy needed —assuming thermalization— in order to break the ground-state short range magnetic correlations and thus to significantly demagnetize the triangle.

A similar analysis of the temperature dependence of magnetic order has been performed for all the selected structures and band fillings. The resulting energies $\Delta E_{\rm SR}$ are summarized in Table 4.3.

[1] The internal energy is given by the expectation value $\langle E \rangle = \langle \hat{H} \rangle$ of the Hamiltonian at the temperature T (canonical ensemble).

System size	Structure	Band filling	Thermal energy at T_{SR}
$N_a = 2$	Dimer	$N_e = 3$	$\Delta E_{\mathrm{SR}} =$ 74 meV/atom
$N_a = 3$	Linear chain	$N_e = 5$	$\Delta E_{\mathrm{SR}} =$ 23 meV/atom
		$N_e = 7$	$\Delta E_{\mathrm{SR}} =$ 30 meV/atom
$N_a = 3$	Triangle	$N_e = 3$	$\Delta E_{\mathrm{SR}} =$ 18 meV/atom
		$N_e = 4$	$\Delta E_{\mathrm{SR}} =$ 50 meV/atom
		$N_e = 5$	$\Delta E_{\mathrm{SR}} =$ 77 meV/atom
		$N_e = 7$	$\Delta E_{\mathrm{SR}} =$ 87 meV/atom
		$N_e = 15$	$\Delta E_{\mathrm{SR}} =$ 118 meV/atom
$N_a = 4$	Rhombus	$N_e = 5$	$\Delta E_{\mathrm{SR}} =$ 58 meV/atom

Table 4.3: Thermal energies needed to break the short-range magnetic order in the selected clusters - The energy ΔE_{SR} describing the thermal energy needed in order to break the short-range magnetic correlations is given for all selected clusters having $N_a = 2$–4 atoms and different structures and band fillings. ΔE_{SR} represents the energy of the electronic system in equilibrium at the *short-range* temperature T_{SR}, which is associated to the disappearance of short-range magnetic order.

5

Magnetization dynamics

In Chapter 4 we have studied the ground-state and finite-temperature magnetic properties of the electronic model (3.3). The purpose of the present Chapter is to go beyond static magnetism and to address the challenging topic of magnetization dynamics. To this aim, we apply the electronic Hamiltonian (3.3) in order to propagate many-body states in time.

In the first Section 5.1 the choice of laser parameters for the numerical time evolutions is presented. Afterwards, the dynamics of the triangle system is studied in the second Section 5.2. The following Sections 5.3 and 5.4 address the fundamental problem of angular-momentum transfer and the central role of the spin-orbit interaction. In Section 5.5 the magnetization dynamics is analyzed from a spectral point of view, followed by a discussion about the role of the absorbed energy per atom in Section 5.6. This will lead, as we shall see, to the conjecture that the ultrafast demagnetization effect primarily depends on the number of absorbed photons. Arguments for this dependence are given in Section 5.7, where the role of laser energy absorption is investigated in more detail. Finally, the last two Sections 5.8 and 5.9 analyze the roles of interband hybridization, band filling and structure.

5.1 Parameter choice

In the following we focus on the isosceles Ni_3 triangle having $N_e = 4$ electrons, hopping integrals as described in Section 4.1, SOC constant $\xi = -50$ meV, Coulomb parameter $U = 4.5$ eV, exchange energy $J = 0.8$ eV and relative p level $\varepsilon_p^0 - \varepsilon_d^{\text{eff}} = 1$ eV. This set

of parameters yields an almost fully spin-polarized FM ground state, which constitutes the initial state for the time evolution following the laser excitation. The magnetization in the ground state is oriented perpendicular to the triangle plane (xy plane), since the magneto-crystalline anisotropy yields an off-plane easy axis (z axis).

The laser excitation is modeled by means of a pump pulse, whose duration is $T_p = 5$ fs corresponding to the limit of very short pulse durations. The main advantage of this choice is that in this limit the pump pulse is so short that the relaxation, which is responsible for the demagnetization effect, sets in not before the laser electric field is switched off. In contrast, the coherent interaction of electrons with the laser field takes place during the absorption time. Therefore, the limit $T_p \to 0$ ensures that these two effects proceed on two different time scales. In particular, it allows us to study the relaxation dynamics after laser-pulse absorption separated from the effect of coherent interaction with the laser field. However, our choice $T_p = 5$ fs is not the exact experimental case. Usually, in typical demagnetization experiments pump pulses of 50–100 fs duration have been applied (1, 5, 7, 8, 9, 10, 11, 12). In order to compare with these experimentally relevant cases, in Section 5.7 we have considered different pulse durations T_p and investigated the role of T_p in the magnetization dynamics. In the following, $t = 0$ refers to the time at which the laser-pulse intensity is maximal. The laser wave length is $\lambda = 800$ nm, which corresponds to the photon energy $\hbar\omega = 1.55$ eV used in several experiments (2, 7, 8, 10, 11, 12). The laser-field polarization vector $\vec{\varepsilon} = \hat{e}_x$ is aligned parallel to the triangle plane (xy plane), along one of the NN bonds. This corresponds to an incident linearly polarized laser pulse having wave vector $\vec{k}$ within the yz plane, i.e., $\vec{\varepsilon} \cdot \vec{k} = 0$.

Let us now discuss the parameters governing the laser-induced electronic dipole transitions, namely (i) the dipole parameter $\langle\, d \,||\hat{T}^{(1)}||\, p \,\rangle$ which determines the matrix elements of $\vec{r}$ (see Table 3.3), and (ii) the laser fluence F or the maximal amplitude of the laser electric field E_0 which are related to each other by Eq. (3.34). In this context, it is important to notice that —as we shall argue in the forthcoming Section 5.6— the maximum admissible demagnetization depends basically on the number of absorbed photons. For this reason, the parameters $\langle\, d \,||\hat{T}^{(1)}||\, p \,\rangle$ and F have been chosen such that they yield a sufficiently large number of absorbed photons. In fact, it is enough to consider just one of these parameters (i.e., $\langle\, d \,||\hat{T}^{(1)}||\, p \,\rangle$, or F which is a function of E_0) as a free parameter, since only the product $\vec{E} \cdot \hat{\vec{r}}$ enters into the electric-dipole

Hamiltonian $\hat{H}_E$. Therefore, in practice we have considered a constant dipole parameter $\langle\, d \,||\hat{T}^{(1)}||\, p \,\rangle = 0.5$ Å, and varied only the fluence F of the laser pulse in order to control the level of excitation.[1] As a result of this variation, we have found that the laser fluence $F = 40$ mJ/cm^2 gives rise to a sufficiently high level of excitation: it yields a maximum admissible demagnetization of around 60 %. For this reason, we have chosen the parameter $F = 40$ mJ/cm^2.

For the purpose of the following investigations, several important model and laser-field parameters are varied separately with respect to the basic ones listed here. This will allow us to draw conclusions on the essential processes responsible for the magnetization decrease. In particular, the hopping integrals, the SOC strength, the laser fluence, the electric-field polarization, the wave length, the pulse duration, the band filling and the structure are varied in order to determine the dependence of the magnetization dynamics on them. In doing so, the Ni_3 triangle having the basic parameters given in the present Section serves as a reference system. Let us remark that in the following dynamical studies, the parameters which are not explicitly mentioned are chosen as described for this reference triangular system.

The time evolution of the initial state $|\,\Psi\,\rangle$ is performed numerically by using the short-time iterative Lanczos propagation method (83), whose details are described in Appendix F. The thus obtained time-dependent many-body wave function $|\,\Psi(t)\,\rangle$ allows us to compute the expectation value $O(t) = \langle\,\Psi(t)\,|\hat{O}|\,\Psi(t)\,\rangle$ of basically any physical observable $\hat{O}$ as a function of time t. Notice that the external magnetic field has been switched off (i.e., $\vec{B} = 0$).

5.2 Ultrafast demagnetization in the triangular system

Let us first investigate the magnetization dynamics of the basic reference isosceles triangle. To this aim, the time evolution of the many-body wave function $|\,\Psi(t)\,\rangle$ during the first picosecond after laser-pulse absorption has been calculated. The most relevant spin observables are shown in Figure 5.1 as a function of time t. One clearly observes

[1] Notice that the discrete spectra of the considered small clusters fundamentally differ from the continuous bulk spectra. Therefore, we expect that, depending on what the laser pulse is acting on (cluster or bulk), it gives rise to very different energy absorptions. For this reason, it seems not sound to take the fluence F from experiments, but rather to adjust F so as to obtain a reasonable level of excitation.

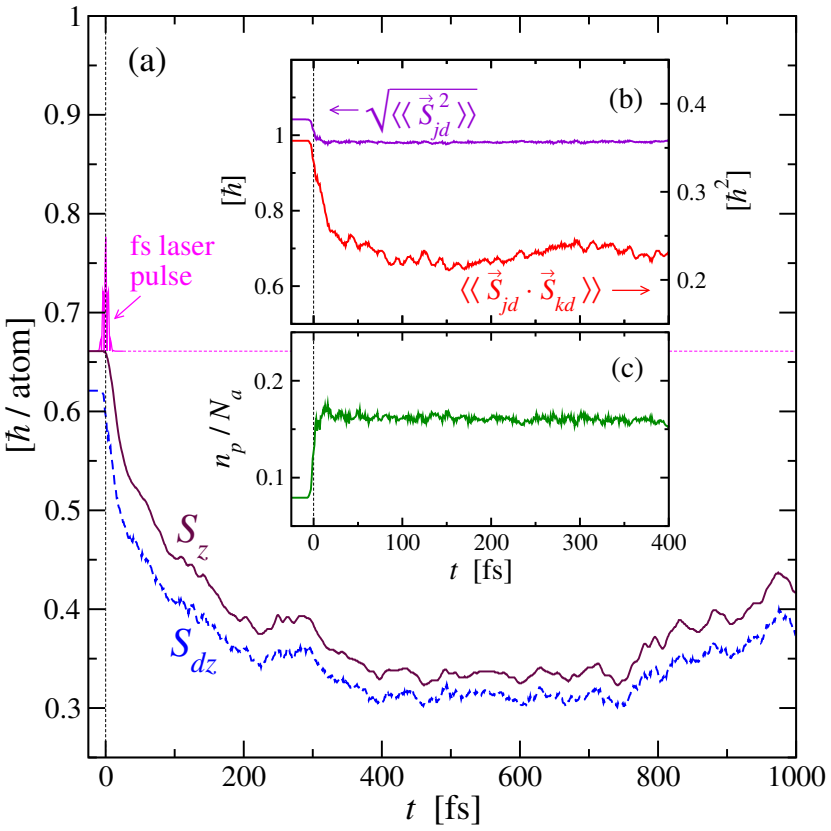

Figure 5.1: Dynamics of the isosceles triangle subsequent to fs laser-pulse absorption - Several time-dependent properties of the basic triangular system ($N_a = 3$ atoms) having $N_e = 4$ electrons are shown subsequent to a $T_p = 5$ fs laser pulse: (a) off-plane total spin and d-electron spin angular momenta S_z and S_{dz}. The rapid oscillations (magenta curve) indicate the laser field $|\vec{E}|$. (b) NN d-electron spin correlation $\langle\langle \vec{S}_{jd} \cdot \vec{S}_{kd} \rangle\rangle$ and d-electron local moment $\sqrt{\langle\langle \vec{S}_{jd}^{\,2} \rangle\rangle}$. (c) p-electron occupation n_p.

that the off-plane spin component S_z along the easy axis decreases from $0.66\,\hbar$ down to $0.32\,\hbar$ per atom during the first hundreds of femtoseconds, i.e., well after the laser pulse.[1] This is very remarkable since it demonstrates the ultrafast demagnetization on a purely electronic level.

In addition, Figure 5.1(a) compares the total spin S_z with the d-electron spin S_{dz}. Their time evolutions are very similar. This shows that the decrease in S_z subsequent to the laser pulse is a d-band intrinsic effect, as of course expected from the fact that magnetism in $3d$ TMs is dominated by the $3d$ electrons. In order to further characterize

[1] The in-plane components (S_x, S_y) and (S_{dx}, S_{dy}) are negligibly small during the simulation time.

the demagnetization process it is important to study the behavior of the local magnetic moments. For this purpose, Figure 5.1(b) shows the average atomic d-electron spin $\sqrt{\langle\langle \vec{S}_{jd}^2 \rangle\rangle}$ [see Eq. (4.13)], which measures the strength of the local moments: $\sqrt{\langle\langle \vec{S}_{jd}^2 \rangle\rangle}$ decreases only slightly from $1.04\,\hbar$ to around $0.98\,\hbar$ simultaneously with the laser pulse. Consequently, the local magnetic moments remain remarkably stable. This stability is a consequence of the strong Coulomb interactions. Figure 5.1(b) also shows the d-electron spin correlation $\langle\langle \vec{S}_{jd} \cdot \vec{S}_{kd} \rangle\rangle$ between nearest neighbors [see Eq. (4.14)], which decreases significantly from $0.36\,\hbar^2$ to $0.22\,\hbar^2$ within the first 80 fs. The results give us a picture of the involved spin excitations: during the first picosecond the local moments barely decrease but fluctuate in their orientations. In other words, local spin fluctuations seem to be responsible for the demagnetization. Notice that the laser induces electric-dipole transitions from the d band to the higher p band. Therefore, it is interesting to analyze these electronic d-p transitions during the interaction time with the laser field. To this aim, in Figure 5.1(c) the p-electron number n_p is shown as a function of t. One observes a small increase from $n_p = 0.08$ to $n_p \approx 0.17$ per atom, which is accompanied by laser-energy absorption. This charge transfer from the d to the p electrons induces the small decrease in $\sqrt{\langle\langle \vec{S}_{jd}^2 \rangle\rangle}$ illustrated in Figure 5.1(b).[1]

Since the spin relaxation takes place basically within the band of localized d electrons, we focus on the d band. Figure 5.2 shows the time dependence of three relevant observables. First, it shows the average atomic spin quantum number per d electron

$$\langle\langle S_{jd}/n_{jd} \rangle\rangle \;=\; \frac{1}{N_a} \sum_{j=1}^{N_a} \frac{S_{jd}}{n_{jd}} \;. \tag{5.1}$$

Here, $n_{jd} = \langle \hat{n}_{jd} \rangle$ denotes the number of d electrons at atom j, and the atomic d-electron spin quantum number S_{jd} is related to the corresponding squared spin $\langle \vec{S}_{jd}^2 \rangle$ by

$$S_{jd}(S_{jd}+1)\,\hbar^2 \;=\; \left\langle \vec{S}_{jd}^2 \right\rangle \;. \tag{5.2}$$

Second, the relative NN d-electron spin correlation

$$\langle\langle \vec{S}_{jd} \cdot \vec{S}_{kd} \rangle\rangle_{\rm rel} \;=\; \frac{1}{N_{\rm nnc}} \sum_{\langle j,k \rangle} \frac{\langle \vec{S}_{jd} \cdot \vec{S}_{kd} \rangle}{\sqrt{\langle \vec{S}_{jd}^2 \rangle \, \langle \vec{S}_{kd}^2 \rangle}} \tag{5.3}$$

[1] See also the discussion of Figure 5.2, where the atomic spin quantum number per d electron, $\langle\langle S_{jd}/n_{jd} \rangle\rangle$, is shown as a function of time.

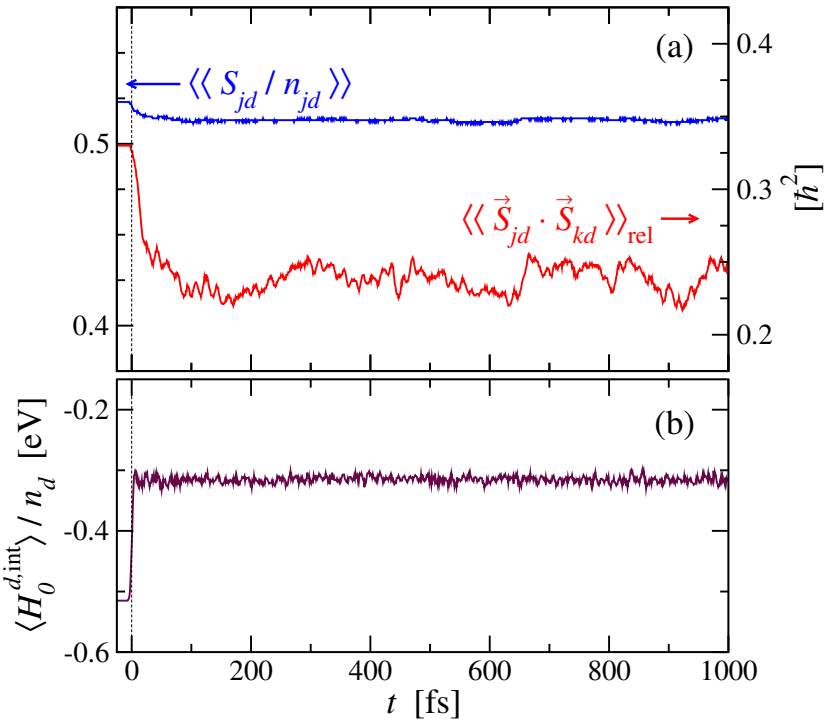

Figure 5.2: Time-dependent properties of the d electrons - The laser-induced dynamics of several d-electron properties in the isosceles triangle model are shown: (a) average atomic spin quantum number $\langle\langle S_{jd}/n_{jd}\rangle\rangle$ per d electron and relative NN d-electron spin correlation $\langle\langle \vec{S}_{jd}\cdot\vec{S}_{kd}\rangle\rangle_{\rm rel}$, (b) interatomic hopping energy $\langle H_0^{d,\rm int}\rangle/n_d$ per d electron. The vertical dotted lines indicate the time at which the exciting laser pulse has its maximum ($T_p = 5$ fs).

is shown, where $\sum_{\langle j,k\rangle}$ denotes a sum among NNs j and k. Third, we consider the interatomic hopping energy per d electron

$$\langle H_0^{d,\rm int}\rangle/n_d \;=\; \frac{1}{n_d}\sum_{\substack{jk\\ j\neq k}}\sum_{\alpha\beta\in d}\sum_{\sigma} t_{jk}^{\alpha\beta}\,\langle \hat{c}^{\dagger}_{j\alpha\sigma}\hat{c}_{k\beta\sigma}\rangle \;. \tag{5.4}$$

Here, n_d is the total occupation of the d band, i.e., $n_d = \sum_{j=1}^{N_a}\langle\hat{n}_{jd}\rangle$. Notice that the quantities $\langle\langle S_{jd}/n_{jd}\rangle\rangle$ and $\langle H_0^{d,\rm int}\rangle/n_d$ are given relative to the number of d electrons, and $\langle\langle \vec{S}_{jd}\cdot\vec{S}_{kd}\rangle\rangle_{\rm rel}$ describes the average angle between NN d-electron spins. In this way, they measure intrinsic properties of d electrons. The time evolutions of $\langle\langle S_{jd}/n_{jd}\rangle\rangle$ and $\langle\langle \vec{S}_{jd}\cdot\vec{S}_{kd}\rangle\rangle_{\rm rel}$ during the first picosecond are shown in Figure 5.2(a). First, one observes that the local moment per d electron $\langle\langle S_{jd}/n_{jd}\rangle\rangle$ remains essentially unaffected by the laser-pulse absorption: it decreases by less than 2%, while at the same

time $\sqrt{\langle\langle \vec{S}_{jd}^2 \rangle\rangle}$ decreases by around 6% (see Figure 5.1). This means that the small decrease in $\sqrt{\langle\langle \vec{S}_{jd}^2 \rangle\rangle}$ results mainly from the laser-induced charge transfer from the d to the p electrons. Thus, the magnetic moment per carrier is even more stable (independent of the laser excitation) than what the results for $\sqrt{\langle\langle \vec{S}_{jd}^2 \rangle\rangle}$ (Figure 5.1) let us a priori expect.[1] Second, the relative NN d-electron spin correlation $\langle\langle \vec{S}_{jd} \cdot \vec{S}_{kd} \rangle\rangle_{\rm rel}$ significantly decreases by more than 30%, which is in the same order of magnitude as the decrease in $\langle\langle \vec{S}_{jd} \cdot \vec{S}_{kd} \rangle\rangle$ shown in Figure 5.1. These results show that the ultrafast demagnetization can be understood in terms of fluctuations of local d-electron magnetic moments. During the whole demagnetization process the local moments, whose magnitude is measured by $\langle\langle S_{jd}/n_{jd} \rangle\rangle$, remain remarkably stable.

It is interesting to compare the laser-induced changes in the spin observables with their thermal averages in equilibrium at finite temperatures $T > 0$.[2] We have found that the equilibrium temperatures, yielding the same expectation values $\langle\langle S_{jd}/n_{jd} \rangle\rangle$ and $\langle\langle \vec{S}_{jd} \cdot \vec{S}_{kd} \rangle\rangle_{\rm rel}$ as obtained in the time-dependent evolution shortly after the laser-pulse absorption (i.e., for $t \gtrsim 100$ fs), are 1230 K and 955 K, respectively. Notice that these temperatures are below the short-range temperature of the basic triangle system, $T_{\rm SR} = 1343$ K, which denotes the temperature needed to break the NN magnetic correlations $\langle\langle \vec{S}_{jd} \cdot \vec{S}_{kd} \rangle\rangle$. In order to discuss the role of thermalization it is useful to quantify the thermal internal energy in equilibrium at temperatures between $T = 955$ and 1230 K. This thermal energy is given by $\langle E \rangle - E_{\rm gs} = 20$–$40$ meV per atom relative to the ground-state energy (see Figure 4.4). On the other side, for the time-propagated state we have found a total absorbed laser energy of $\Delta E = 302$ meV per atom, which is one order of magnitude larger. Figure 5.2(b) shows that the largest portion of this energy is transferred to the degrees of freedom of the electron motion within the d band: one observes that the interatomic hopping energy $\langle H_0^{d,\rm int} \rangle / n_d$ increases by about 200 meV per d electron. This demonstrates that the spin degrees of freedom can be regarded to be in a nonequilibrium situation with respect to the highly excited electronic orbital and translational degrees of freedom, even after a few hundreds of femtoseconds (i.e., after the demagnetization is completed). Therefore, one concludes that the femtosecond

[1] Let us recall that for the basic triangle system we have considered for simplicity a d band filling below half-band filling. However, we have also done calculations for above half-band filling. There, we have observed that the $d \to p$ charge transfer induces a slight enhancement of $\langle\langle S_{jd}/n_{jd} \rangle\rangle$.

[2] In this context, we consider the canonical ensemble describing thermal equilibrium. The temperature-dependent calculations have been performed as explained in Appendix E.2.

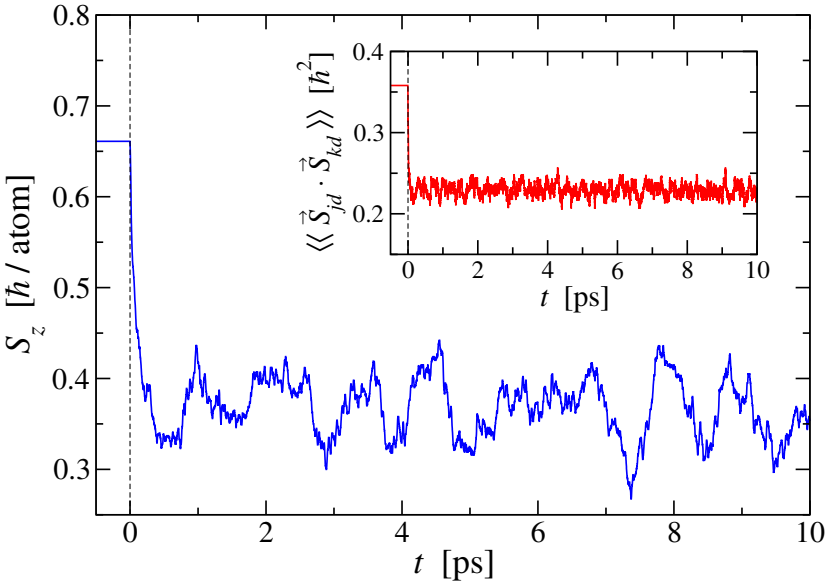

Figure 5.3: Picosecond dynamics of the isosceles triangle - Laser-induced dynamics of the off-plane spin S_z and NN d-electron spin correlation $\langle\langle \vec{S}_{jd} \cdot \vec{S}_{kd} \rangle\rangle$ is shown for the first 10 picoseconds after laser-pulse absorption. The triangle system and the pump-laser field have been modeled as in the calculations reported in Figure 5.1.

laser-induced demagnetization does not originate from the thermalization of absorbed laser energy.

Finally, let us discuss the electronic-model dynamics on the picosecond time scale. To this aim, Figure 5.3 shows the time dependence of two important spin observables during the first 10 picoseconds after laser-pulse absorption, i.e., on a time scale which has been considerably extended in comparison with the one in Figure 5.1. One observes that both the off-plane spin S_z and NN d-electron spin correlation $\langle\langle \vec{S}_{jd} \cdot \vec{S}_{kd} \rangle\rangle$ do not significantly change after a relaxation time of around 200-300 fs,[1] except for oscillations around a quite constant mean value. This means that even on the longer picosecond time scale the thermal equilibrium between on the one side spin and on the other side electronic orbital and translational degrees of freedom is not achieved. The origin of this nonequilibrium can be explained by the fact that the model (3.3) does not take into account any interaction with the environment. Thus, dissipation of energy into the environment is not considered neither, implying that the many-body state

[1] We shall see in Section 5.4 that this relaxation time is essentially determined by the spin-orbit interaction strength.

$|\,\Psi(t)\,\rangle$ propagates only within a subspace of the whole Hilbert space, namely within the subspace of constant mean energy $\langle E \rangle$. Therefore, a thermal equilibrium which results from the thermal contact with the environment (or bath) cannot be achieved within our model. This explains why the model remains demagnetized on the 10-ps time scale, and shows again that the demagnetization is not a heat-driven effect, i.e., it is not the result of thermalization of absorbed laser energy. Rather, the thermalization between the electrons and the environment is important essentially for explaining the magnetization recovery, which has been observed in experiments on $3d$ TMs a few picoseconds after the laser-pulse absorption (see also Section 1.2.5). Notice that we are interested only in the first hundreds of femtoseconds in which the ultrafast demagnetization takes place. For this purpose, it is not necessary to take into account interactions with the environment. Therefore, the present model, which does not consider the environment at all, represents a sound approach which allows us to focus on the electronic response to the ultrafast laser excitation.

5.3 Local angular-momentum conservation

Let us now address the problem of angular-momentum transfer. In this context it is important to recall that the spin-orbit coupling, which is the sole direct channel for the spin relaxation within the present many-body model, acts locally at atomic sites. Therefore, the total angular momentum $\vec{J}_j = \vec{L}_j + \vec{S}_j$ at each atom j is conserved upon the action of the SOC Hamiltonian $\hat{H}_{SO}$, since $\hat{H}_{SO}$ commutes with $\hat{\vec{J}}_j$ for all j. Consequently, on each electronic transition induced by $\hat{H}_{SO}$ the spin S_{jz} can decrease only if angular momentum is transferred locally —by means of $\hat{H}_{SO}$— from S_{jz} to L_{jz}. However, one can see in Figure 5.4(a) that L_z does not increase as S_z decreases. Over the considered period of 200 fs after laser excitation the orbital angular momentum L_z oscillates between 0 and $0.1\,\hbar$ per atom.[1] The fact that L_z remains very small can be understood by considering the problem from the lattice perspective. Indeed, the orbital angular-momentum conservation does not hold for the dynamics in the extended metal or cluster, since the Hamiltonian $\hat{H}$ and in particular $\hat{H}_0$ do not commute with $\hat{\vec{L}}_j$ and $\hat{L}_{jz}$. Then, the question "Where is $\vec{S}$ going to?" may arise.

[1] The in-plane components (S_x, S_y) and (L_x, L_y) are not shown since they have been found to be almost zero during all the considered simulation time.

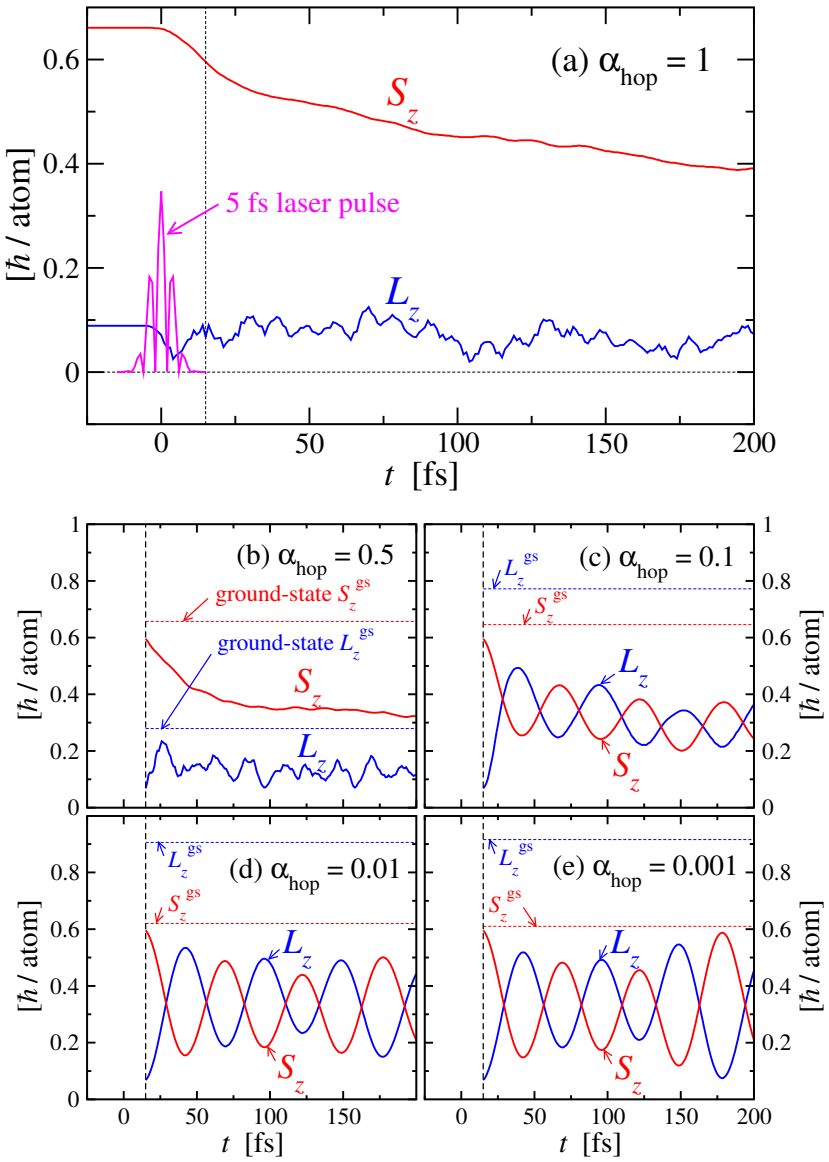

Figure 5.4: Time dependence of total spin and orbital angular momenta - The time dependences of S_z and L_z are shown for triangles having various hopping integrals: (a) Relaxation driven by the fs laser pulse, where realistic two-center integrals $(d, d; \sigma)$, $(d, d; \pi)$, $(p, p; \sigma)$ and $(p, d; \sigma)$ derived from the Ni bulk band structure (as given in Section 4.1) have been used. The magenta oscillating curve indicates the shape of the laser electric field $|\vec{E}|$. (b)–(e) Two-center integrals multiplied by $\alpha_{\rm hop}$. Here, the excited state of the original $\alpha_{\rm hop} = 1$ system at $t = 15$ fs after laser-pulse absorption has been used as the initial state for the time propagation. The time evolutions start at $t = 15$ fs as indicated by vertical dotted lines. For each $\alpha_{\rm hop}$ the corresponding ground-state values of the spin $S_z^{\rm gs}$ and orbital angular momentum $L_z^{\rm gs}$ are illustrated by horizontal dotted lines.

In order to find the answer, Figures 5.4(a)–(e) show the angular-momentum transfer between $\vec{L}$ and $\vec{S}$ for triangles having various hopping integrals $t_{jk}^{\alpha\beta}$. In these examples the two-center integrals $(d,d;\sigma) = 0.412$ eV, $(d,d;\pi) = -0.489$ eV, $(p,p;\sigma) = 1.516$ eV and $(p,d;\sigma) = -0.555$ eV, as given in Section 4.1, have been multiplied by a factor $\alpha_{\mathrm{hop}} = 0.001$–$1.0$. Of course, the resulting ground-state angular momenta L_z^{gs} and S_z^{gs} are also modified by this scaling: L_z^{gs} significantly increases from $0.09\,\hbar$ per atom for $\alpha_{\mathrm{hop}} = 1$ to $0.92\,\hbar$ per atom for $\alpha_{\mathrm{hop}} = 0.001$, while at the same time S_z^{gs} only slightly decreases from $0.66\,\hbar$ to $0.61\,\hbar$ per atom. These ground-state values are illustrated by horizontal dotted lines. In fact, as we reduce the hopping integrals we approach the atomic limit, where Hund's rules, in particular the second rule (maximal L), hold. In all cases, $\vec{L}^{\mathrm{gs}}$ and $\vec{S}^{\mathrm{gs}}$ align parallel to each other in the ground state. The initial state used for the time propagations in parts (b)–(e) has been chosen as the excited state of the original $\alpha_{\mathrm{hop}} = 1$ system shortly after the laser excitation, at $t = 15$ fs.[1] This state is almost fully spin polarized ($S_z = 0.6\,\hbar$), and has an orbital angular momentum $L_z = 0.07\,\hbar$ which is relatively small in comparison with the ground-state values L_z^{gs} corresponding to $\alpha_{\mathrm{hop}} \leq 0.5$. Since the (initial) many-body state $\Psi(t{=}15\mathrm{fs})$ at $t = 15$ fs is the same for all considered factors α_{hop}, i.e., for different magnitudes of $t_{jk}^{\alpha\beta}$, a comparison of the subsequent relaxations of $\vec{L}$ and $\vec{S}$ allows us to identify the role of the hopping integrals in the laser-induced angular-momentum dynamics. In the case of small hopping integrals, i.e., $\alpha_{\mathrm{hop}} = 0.001$ and $\alpha_{\mathrm{hop}} = 0.01$ in Figures 5.4(d) and (e), the transfer between S_z and L_z is visible: S_z and L_z oscillate in time keeping their sum almost unchanged. The oscillations look very similar to undamped harmonic oscillations. Importantly, in this case the hopping integrals are one to two orders of magnitude smaller than the strength $\xi = -50$ meV of the spin-orbit interaction, whose action locally conserves $\vec{L}_j + \vec{S}_j$. For $\alpha_{\mathrm{hop}} = 0.1$ the hopping elements and the SOC strength are of the same order of magnitude. In this case, the oscillations of S_z and L_z are still correlated due to the spin-orbit interaction. However, they are damped and their sum $S_z + L_z$ is not conserved anymore. Finally, for $\alpha_{\mathrm{hop}} = 0.5$ and 1.0 the hopping integrals $t_{jk}^{\alpha\beta}$ are much larger than the parameter ξ. Thus, the interatomic electron motion is more dominant than the spin-orbit interaction. In this case one observes that

[1] Notice that in Figures 5.4(b)–(e) the time evolutions start at $t = 15$ fs using the same laser-excited state, namely the propagated state in the original $\alpha_{\mathrm{hop}} = 1$ triangle at $t = 15$ fs after laser excitation, as the initial state for all $\alpha = 0.001$–0.5.

the time dependences of S_z and L_z are not correlated anymore. In fact, L_z fluctuates very rapidly around a relatively small constant mean value, while S_z decreases without any significant oscillations on a time scale of 100–200 fs. In particular, the sum $\vec{L} + \vec{S}$ is not conserved during the relaxation.

One concludes that during the laser-induced relaxation shown in Figure 5.4(a) the interatomic electron hoppings are responsible for the disappearance of angular momentum. In other words, subsequently to the SOC-driven local transfer of angular momentum from $\vec{S}$ to $\vec{L}$, the latter is rapidly quenched by the electron motion in the metal, i.e., spread through the nearest neighbors. In this sense, the interatomic electron motion tends very effectively to damp the oscillations between $\vec{S}$ and $\vec{L}$, which are mediated by the SOC, and acts as a sink for the electronic angular momentum. As a result, the intra-atomic transfer between $\vec{S}$ and $\vec{L}$, which triggers the relaxation of the spin magnetization, cannot be observed experimentally as an increasing L_z. From a more fundamental point of view, this can be understood by noticing that $\vec{L}$ is not conserved in a lattice ($[\hat{H}_0, \hat{\vec{L}}] \neq 0$) due to the lack of rotational symmetry. The relatively large value of the electron hopping integrals of the order of 1 eV implies that L_z is quenched at a very short time scale of the order of $\hbar/1\text{eV}$, i.e., within a few femtoseconds. This also explains the very rapid oscillations in L_z which are noticeable in Figure 5.4(a). In summary, Figure 5.4 allows us to identify in more detail the main demagnetization mechanism within the present model: (i) the SOC yields local angular-momentum transfer between $\vec{S}$ and $\vec{L}$, and subsequently, (ii) $\vec{L}$ is very rapidly quenched by the electron motion in the lattice, such that the electronic orbits do not have enough time to accumulate the angular momentum which is transferred from $\vec{S}$. The combination of these two purely electronic effects results in a decrease of the magnetization within the time scale of a few femtoseconds.

5.4 Importance of spin-orbit coupling

Since the spin-orbit coupling is responsible for the local angular-momentum transfer between $\vec{S}$ and $\vec{L}$, it is interesting to investigate the dependence of the magnetization dynamics on the SOC strength ξ. Indeed, in the same way as reducing the hopping integrals removes the quenching of orbital angular momentum and yields a back and forth transfer of angular momentum between orbital and spin degrees of freedom, we

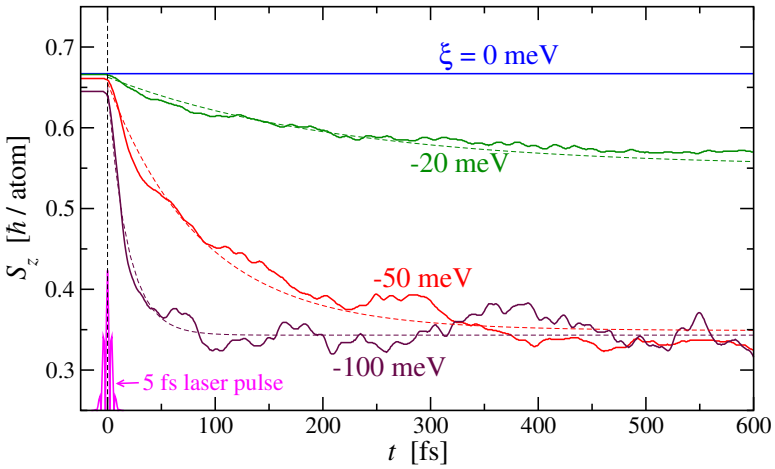

Figure 5.5: Magnetization dynamics as a function of the SOC strength - The time dependence of S_z in an isosceles triangle following a fs laser pulse (full curves) is shown for different SOC parameters from $\xi = 0$ to $\xi = -100$ meV. The dotted curves represent exponential fits to $S_z(t)$ for each ξ. The oscillating function around $t = 0$ (magenta curve) illustrates the exciting laser electric field $|\vec{E}|$.

expect that reducing ξ would allow us to clarify to what extent the SOC is important for defining the magnetization relaxation time. To this aim, Figure 5.5 shows the spin relaxation following the fs laser-pulse absorption for $\xi = 0$, -20, -50 and -100 meV. As expected, the initial ground-state spin magnetization $S_z^0 \approx 0.65$–$0.67\,\hbar$ is quite independent of ξ, since the stability of S_z^0 is the result of Coulomb interactions which concern a much larger energy scale. In contrast, the SOC strongly affects the rate of demagnetization: The larger the SOC constant $|\xi|$, the faster the spin-to-orbit angular momentum transfer proceeds. Moreover, in the limit $\xi = 0$ the total spin is perfectly conserved, since in this case the SOC providing spin-flip processes is turned off. This is not only a very clear indication of the fact that the spin-orbit interaction triggers the magnetization dynamics but it is also a demonstration of the accuracy of the spin-rotational invariance in our numerical implementation.

In order to quantify the demagnetization time τ_{dm}, the time dependence of S_z has been fitted for each considered parameter ξ to an exponential function of the form

$$\tilde{S}_z(t) = \Delta\tilde{S}_z\, \mathrm{e}^{-t/\tau_{\mathrm{dm}}} + \left(\tilde{S}_z^0 - \Delta\tilde{S}_z\right) . \tag{5.5}$$

Here, $\tilde{S}_z^0$ denotes the *fitted* spin at time $t = 0$, and $\Delta\tilde{S}_z$ is the total decrease in $\tilde{S}_z$, i.e., $\Delta\tilde{S}_z = \tilde{S}_z^0 - \tilde{S}_z(t = \infty)$. The demagnetization time τ_{dm} is then defined by the fact that

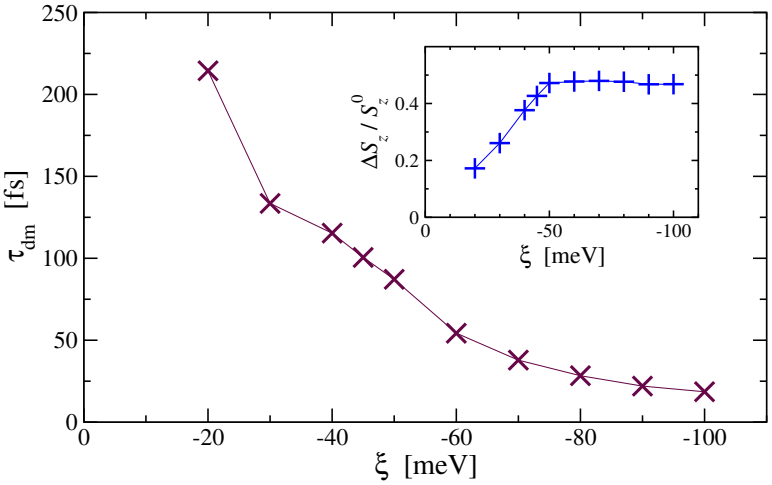

Figure 5.6: Demagnetization time $\tau_{\mathbf{dm}}$ and relative magnetization reduction $\Delta S_z/S_z^0$ as a function of spin-orbit coupling strength - Characteristic time τ_{dm} of the demagnetization, which follows a fs laser-pulse absorption, is shown for various SOC strengths ξ. The numerical results (crosses) are obtained by fitting the exact calculated $S_z(t)$ using the exponential ansatz given by Eq. (5.5) for each ξ. The lines connecting the points are a guide to the eyes. The inset illustrates the corresponding relative demagnetization $\Delta S_z/S_z^0$.

at $t = \tau_{\mathrm{dm}}$ the difference between $\tilde{S}_z(\tau_{\mathrm{dm}})$ and the $t \to \infty$ limit of $\tilde{S}_z$ is $1/e$ times the total magnetization decrease $\Delta\tilde{S}_z$. The exponential fits are shown for each ξ by means of dotted curves in Figure 5.5. The demagnetization times τ_{dm} obtained by this fitting procedure are shown in Figure 5.6 as a function of ξ. One can see how τ_{dm} decreases with increasing SOC strength, from $\tau_{\mathrm{dm}} = 214$ fs for $\xi = -20$ meV, over $\tau_{\mathrm{dm}} = 87$ fs for $\xi = -50$ meV, to $\tau_{\mathrm{dm}} = 19$ fs for $\xi = -100$ meV. These results demonstrate the importance of the SOC as driving mechanism for the ultrafast demagnetization. In other words, the SOC strength ξ controls the rate of the ultrafast spin relaxation.

It is also interesting to take a look at the total (long-time) laser-induced demagnetization $\Delta S_z/S_z^0$ relative to the initial spin expectation value S_z^0, which gives us a measure for the efficiency of demagnetization. Here, ΔS_z denotes the difference between S_z^0 and the fitted $t \to \infty$ limit of the spin moment, i.e.,

$$\Delta S_z \;=\; S_z^0 \;-\; \tilde{S}_z(t = \infty)\;. \tag{5.6}$$

The inset in Figure 5.6 shows that $\Delta S_z/S_z^0$ monotonously increases with increasing $|\xi|$ for $|\xi| \leq 50$ meV, and that it then remains almost constant, at the value $\Delta S_z/S_z^0 \approx 0.5$,

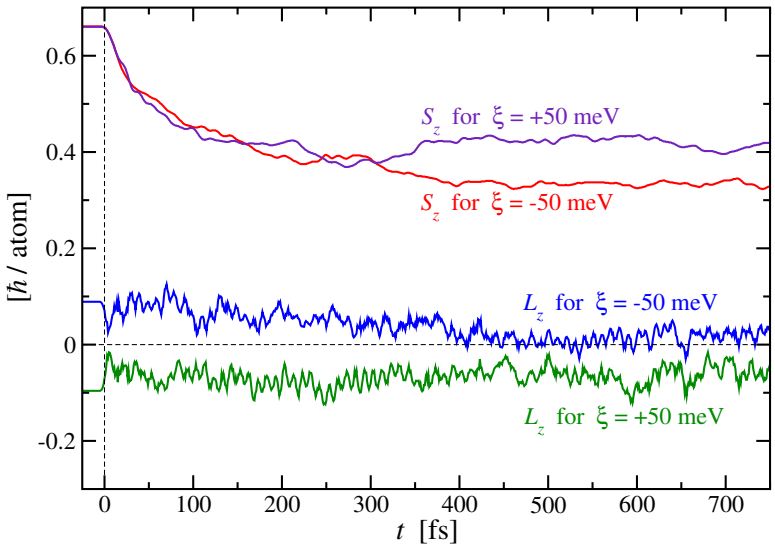

Figure 5.7: Spin and orbital angular-momentum dynamics for opposite spin-orbit couplings - The laser-induced relaxations of S_z and L_z in an isosceles triangle are shown for two opposite values of the SOC strength $\xi = -50$ and $\xi = +50$ meV. The time $t = 0$ (vertical dotted line) indicates the time of the fs laser-pulse excitation.

up to the largest considered $|\xi| = 100$ meV. One concludes that the larger the SOC strength, the more efficient the demagnetization but only up to a certain value, in the present case $\xi \approx -50$ meV. Further enhancement of ξ does not improve the total reduction of S_z as if the maximum attainable demagnetization for the given level of excitation had been reached. However, further increase of ξ does speed up the process. Roughly speaking τ_{dm} is proportional to $1/\xi$, and of the order of $\hbar/\xi$ as one could expect on the basis of an energy uncertainty relation [see Ref. (69)].

In the context of spin-orbit interaction it is worth noting that in all previous model calculations the spin $\vec{S}$ couples parallel to the orbital angular momentum $\vec{L}$. However, the question arises if the orientation of $\vec{S}$ relative to $\vec{L}$ (parallel or antiparallel) has a significant effect on the magnetization dynamics. Parallel LS coupling corresponds to the FM transition metals like Fe, Co and Ni, whose $3d$ bands are more than half-filled, while the antiparallel LS coupling is found in TMs having a less-than half-filled d band.[1] In fact, the answer to this question would give us some hints about the

[1] In Section 3.2.4 it has been discussed that for realistic SOC strengths $\xi > 0$ the angular momenta $\vec{S}$ and $\vec{L}$ align parallel (antiparallel) for more than (less than) half-filled $3d$ bands. However, in the previous model calculations we considered negative SOC parameters $\xi < 0$, in order to invert the

dependence of the laser-induced spin relaxation on band filling.[1] In order to address this problem, Figure 5.7 compares the dynamics for two opposite values of the SOC strength $\xi = -50$ meV and $\xi = +50$ meV, which yield parallel and antiparallel coupling between $\vec{S}$ and $\vec{L}$, respectively. One can see that during the first 300 fs after laser-pulse absorption the time dependences of the spin $S_z(t)$ are almost identical for both signs of ξ. Even on longer time scales $t \gtrsim 300$ fs the calculated $S_z(t)$ do not differ significantly from each other. The qualitative behavior of $L_z(t)$ is also not modified by changing the sign of ξ, except of course for the direction of $\vec{L}$ with respect to $\vec{S}$. Moreover, it has been found that the total absorbed laser energy $\Delta E = 302$ meV per atom is the same for both values of ξ. One concludes that the laser-induced magnetization dynamics is quite independent of the sign of ξ and of the alignment between $\vec{S}$ and $\vec{L}$.[2] The irrelevance of the orientation of $\vec{L}$ can be understood by recalling that $\vec{L}$ is anyway quenched by the electron motion in the lattice, both before and after the laser-pulse absorption. Moreover, it is interesting to note that these results imply that it should be in principle possible to observe the laser-induced demagnetization also in FM metals having a less-than half-filled valence band, i.e., for systems showing an antiparallel coupling of $\vec{L}$ and $\vec{S}$.

5.5 Spectral analysis of the magnetization dynamics

By pumping energy into the electron system the ultrashort laser pulse induces a broad spectral distribution. It is therefore most interesting to separate the total many-body state $|\,\Psi(t)\,\rangle$ into its spectral parts (SPs) and to analyze their role in the dynamics. This approach also provides us with useful hints on the properties of the laser-excited state as a function of absorbed energy.

For this purpose, let us first consider the spectral distribution of $|\,\Psi(t)\,\rangle$

$$D_\Psi(E) \;=\; \sum_k \delta(E - E_k)\;|\langle\,\Phi_k\,|\,\Psi(t)\,\rangle|^2 \tag{5.7}$$

dependence of the alignment between $\vec{S}$ and $\vec{L}$ on band filling. This has been done in order to mimic the parallel alignment between $\vec{S}$ and $\vec{L}$ for $\vartheta = N_e/N_a = 4/3$ electrons per atom (i.e., less than half-band filling) within the electronic model.

[1] The dependence of the magnetization dynamics on band filling is discussed in Section 5.9, where spin relaxations for different numbers of electrons N_e are compared.

[2] This justifies the transformation $\xi \to -\xi$, which has been introduced in Section 4.1.

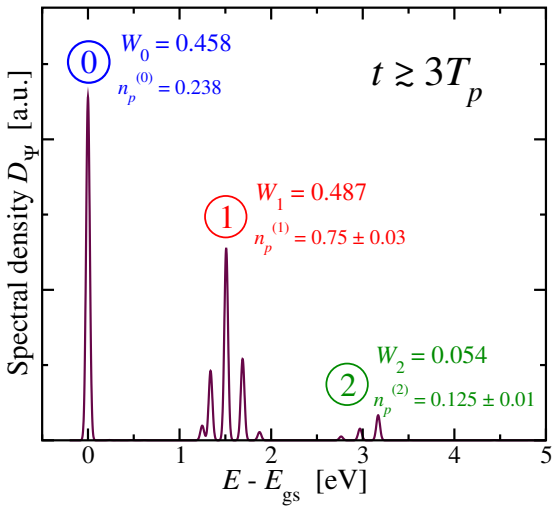

Figure 5.8: Spectral distribution after laser-pulse absorption - Spectral density $D_\Psi(E)$ of the propagated many-body state $|\,\Psi(t)\,\rangle$ is shown as a function of energy E relative to the ground-state energy $E_{\rm gs}$ for times well after the laser-pulse action ($t \gtrsim 3T_p$). The three main spectral parts (SPs) $\alpha = 0, 1, 2$ correspond to the absorption of zero, one and two photon energies, respectively ($\hbar\omega = 1.55$ eV). For each group of peaks α, integrated spectral weights W_α and numbers of p electrons $n_p^{(\alpha)}$ are indicated. The inaccuracy of $n_p^{(\alpha)}$ for $\alpha \geq 1$ reflects the fluctuations of $n_p^{(\alpha)}$ in time.

after the laser-pulse action ($t \gtrsim 3T_p$). Notice that for $t \gtrsim 3T_p$ the Hamiltonian $\hat{H}$ given by Eq. (3.3) is time independent, since the laser field $\vec{E}$ is zero. Consequently, the distribution $D_\Psi(E)$ is conserved after pulse absorption. In Eq. (5.7) the states $|\,\Phi_k\,\rangle$ denote stationary states of the Hamiltonian $\hat{H}$ with $\vec{E} = 0$, and E_k are the corresponding eigenenergies. A Krylov-expansion method described in Appendix E.3 has been used in order to compute the spectral density $D_\Psi(E)$ and the other spectral properties to be considered in the following.

Before the pump pulse, all spectral weight is of course on the ground state having energy $E_{\rm gs}$. As the laser field interacts with the electrons, energy is absorbed and spectral weight is shifted toward some excited many-body states. Well after the pulse absorption the spectral distribution $D_\Psi(E)$ takes the form shown in Figure 5.8: three main peaks or groups of nearby peaks (SPs) are observed which we denote by $\alpha = 0$, 1 and 2. They are centered around the excitation energies $E - E_{\rm gs} \approx 0$, $\hbar\omega$ and $2\hbar\omega$, where $\hbar\omega = 1.55$ eV is the photon energy. This implies that the SPs $\alpha = 0$, 1 and 2 can be associated to the net absorption of zero, one and two photons, respectively. For

each peak α, the spectral weights

$$W_\alpha \;=\; \int_\alpha \mathrm{d}E\, D_\Psi(E) \;=\; \sum_{k\in \mathrm{SP}\alpha} |\langle\, \Phi_k \,|\, \Psi(t)\,\rangle|^2 \tag{5.8}$$

are given as numbers in the Figure. W_α represents the spectrum of $|\,\Psi(t)\,\rangle$ integrated over the energy interval containing the peak or group of peaks α. One can see that the probability of remaining in the initial ground state is $W_0 = 0.46$. The second important part of the spectral distribution of $|\,\Psi(t)\,\rangle$ after pulse absorption is $W_1 = 0.49$, which corresponds to the absorption of energy $\hbar\omega$. From a single-particle perspective one can interpret this part as a linear combination of one-photon electron-hole excitations, although the processes leading to W_1 are of course far more complex many-body processes. Finally, a small weight $W_2 = 0.05$ can be related to the absorption of two photons. This yields the average number

$$\frac{n_{\mathrm{eh}}}{N_a} \;\simeq\; \frac{1}{N_a}\,(W_1 + 2W_2) \;=\; 0.2 \tag{5.9}$$

of laser-induced electron-hole excitations per atom. This quantity corresponds to the ratio between the absorbed energy per atom and the photon energy, i.e.,

$$\frac{n_{\mathrm{eh}}}{N_a} \;=\; \frac{\Delta E}{N_a \hbar\omega}\;. \tag{5.10}$$

It is remarkable that such a small number of electron-hole excitations is sufficient to induce a decrease of around 50% in the magnetization.

In order to get an insight into the nature of the excited many-body states belonging to SPs $\alpha = 1$ and $\alpha = 2$, we have calculated the average number of p electrons $n_p^{(\alpha)}$ corresponding to each SP α.[1] Results are given as numbers in Figure 5.8. There, the inaccuracies of $n_p^{(\alpha)}$ for $\alpha \geq 1$ reflect the fluctuations of $n_p^{(\alpha)}$ in time.[2] Only the p-band occupation $n_p^{(0)}$ (for $\alpha = 0$) is perfectly conserved for $t \gtrsim 3T_p$, since the SP $\alpha = 0$ represents a single state, namely the ground state of the system. It is clear that for this SP one finds $n_p^{(0)} = 0.24$, which coincides with the number of p electrons in the

[1] $n_p^{(\alpha)}$ is obtained by representing the operator $\hat{n}_p$ in the basis of stationary states $|\,\Phi_k\,\rangle$ as described below for $S_z^{(\alpha)}$. See Eq. (5.11) and the related discussion below.

[2] Notice that the excited spectral parts $\alpha \geq 1$ represent distributions having a *finite width* over many stationary states within a narrow energy range. Therefore, the observables within these SPs are not conserved during the time propagation as it would certainly be the case if one would consider *only one* stationary state.

initial ground state. For the first excited SP $\alpha = 1$ the p-band occupation increases up to $n_p^{(1)} \approx 0.75$. Roughly speaking, in these states the p band is occupied by around one electron, whereas the ground-state SP has an almost unoccupied p band ($n_p^{(0)} = 0.24$). This sheds some light on the excitations within SP $\alpha = 1$. They can be interpreted —to a large part— as linear combinations of single $d \to p$ electronic-dipole transitions, which are induced by the absorption of one photon (of energy $\hbar\omega$). For the second excited spectral part $\alpha = 2$ associated to the absorption of energy $2\hbar\omega$, one finds again a relatively small value $n_p^{(2)} \approx 0.13$. This can be explained by two photon absorption processes: The first photon excites a many-body state within SP $\alpha = 1$ basically by inducing a transition from the d to the p band. Then, the second photon excites a state within SP $\alpha = 2$ basically by inducing a transition from the p band to some antibonding d orbital.

Having a physical interpretation of the three main contributions in the spectral density $D_\Psi(E)$, it is very instructive to consider the properties of each spectral part separately. In particular, we would like to investigate the spin relaxation within the excited SPs $\alpha = 1$ and 2. This analysis may help us to understand the role of electron-hole excitations in the ultrafast demagnetization. To this aim, Figure 5.9 shows several magnetic relevant expectation values for the three main SPs of the many-body state $|\,\Psi(t)\,\rangle$ as a function of time. The off-plane projection of the spin magnetization

$$S_z^{(\alpha)}(t) \;=\; \frac{1}{W_\alpha} \int_\alpha \mathrm{d}E\, s_z(E) \tag{5.11}$$

deserves special attention. $S_z^{(\alpha)}(t)$ is given by an integral over each SP α, where in the integrand $s_z(E)$ represents the spin-S_z contribution of weights of $|\,\Psi(t)\,\rangle$ having an average energy E. The spectral density $s_z(E)$ of the spin S_z is given by

$$s_z(E) \;=\; \sum_{j,k} \delta\left(E - \frac{E_j + E_k}{2}\right) \langle\,\Psi(t)\,|\,\Phi_j\,\rangle\,\langle\,\Phi_j\,|\hat{S}_z|\,\Phi_k\,\rangle\,\langle\,\Phi_k\,|\,\Psi(t)\,\rangle \tag{5.12}$$

and therefore gives us a measure for the magnetization originating from different spectral weights. The upper panel (a) of Figure 5.9 shows that shortly after the excitation all SPs have roughly the same magnetization as the ground state. As time evolves the magnetization of the most relevant excited states ($\alpha = 1$) decreases significantly to almost zero, while the magnetization in the lowest SP (ground state, $\alpha = 0$) remains unchanged. The average atomic d-electron squared spin $\langle\langle \vec{S}_{jd}^{\,2} \rangle\rangle$, which measures the

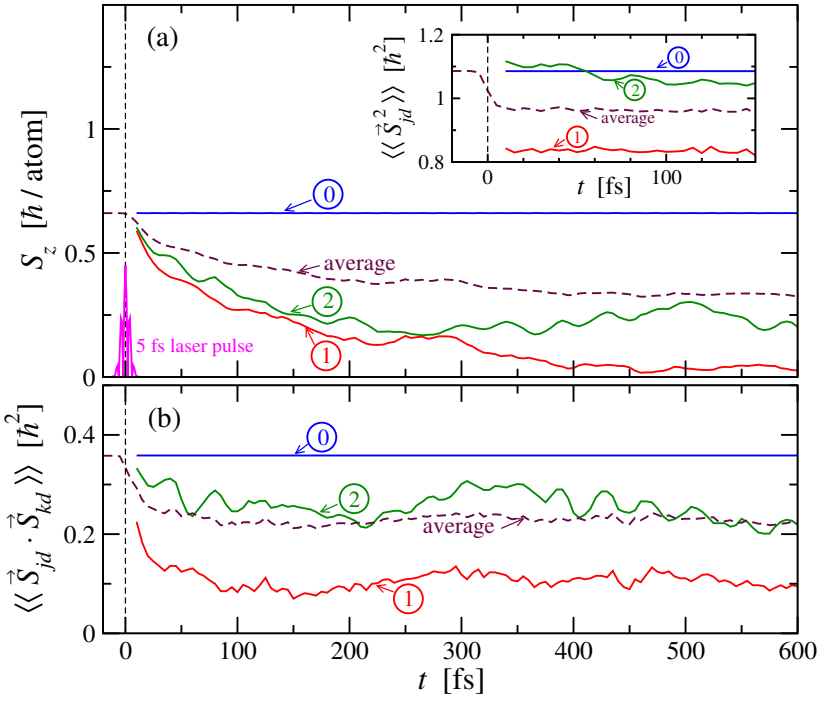

Figure 5.9: Spectral analysis of the spin dynamics of the triangle system - (a) The off-plane spin S_z is shown for the dominant SPs $\alpha = 0$–2 of the many-body state $|\,\Psi(t)\,\rangle$. The different parts α correspond to the three main groups of peaks in the spectral distribution given in Figure 5.8. Results are shown for $t > 10$ fs, i.e., after the passage of the laser pulse, since the SPs are not physically meaningful while the electric field is active. The shape of the laser pulse is illustrated by the magenta oscillating curve. The dotted line coincides with the averaged total magnetization given in Figure 5.1(a). The inset shows the corresponding spectral separation of the atomic d-electron spin $\langle\langle \vec{S}_{jd}^2 \rangle\rangle$, which measures the magnitude of the local magnetic moments. (b) The NN d-electron spin correlations $\langle\langle \vec{S}_{jd} \cdot \vec{S}_{kd} \rangle\rangle$ in the different SPs $\alpha = 0$–2 as a function of t.

magnitude of the atomic magnetic moments, is given in the inset of Figure 5.9(a) for the main SPs $\alpha = 0$–2. The results show that the local magnetic moments of the excited SPs $\alpha = 1$ and 2 are very little modified with respect to the ground state, and that after the passage of the laser pulse they remain very stable as a function of time. The largest change in $\langle\langle \vec{S}_{jd}^2 \rangle\rangle$ is observed for SP $\alpha = 1$, where the expectation value $\langle\langle \vec{S}_{jd}^2 \rangle\rangle$ is reduced by 23% with respect to the ground-state value. Let us recall that in this spectral part ($\alpha = 1$), which corresponds to single-photon absorptions, the decrease in $\langle\langle \vec{S}_{jd}^2 \rangle\rangle$ results mainly from the significant $d \rightarrow p$ charge transitions. See also the p-electron occupation numbers $n_p^{(\alpha)}$ shown in Figure 5.8. Therefore, also in this case the local mo-

ments remain almost saturated. Consequently, the stability of local magnetic moments implies that the observed laser-induced demagnetization must be intimately related to important spin fluctuations. Indeed, Figure 5.9(b) shows that in the most important excited SP $\alpha = 1$, the NN d-electron spin correlation $\langle\langle \vec{S}_{jd} \cdot \vec{S}_{kd} \rangle\rangle$ decreases by 75–80% with respect to its initial ground-state value. These results confirm the conclusions drawn in Section 5.2: The ultrafast demagnetization effect is the result of disorder in the orientation of local magnetic moments, which have very stable magnitudes. In addition, the present analysis reveals the demagnetization process from a spectral point of view: Only weights corresponding to excited many-body states ($\alpha \geq 1$) relax their magnetization by means of decreasing the NN spin correlation. In other words, only when the laser excitation energy is absorbed (within electronic-orbital and interatomic electron-hopping degrees of freedom) it is possible that the SOC acts as an extremely efficient angular-momentum transfer channel from the electronic-orbital toward spin degrees of freedom.

5.6 Discussion about the absorbed energy per atom

Since characterizing the nature of the excitation of electrons is essential for understanding the magnetization dynamics, it is worth discussing the laser-energy absorption in more detail. As we know, the photon energy is quantized so that the smallest absorbed energy is $\hbar\omega$. Consequently, by means of laser-energy absorption spectral weight can be shifted only toward those excited states which have excitation energies of around $1\hbar\omega$, $2\hbar\omega$, ... (see Figure 5.8 in the previous Section). These groups of excited states correspond to one, two, ... photon absorption processes, respectively. In a macroscopic system, the smallest amount of excitation energy per atom $\hbar\omega/N_a$ can be arbitrarily small. However, in our numerical simulations we considered systems having a small number of atoms N_a and a discrete spectrum. In this case, the smallest excitation energy per atom $\hbar\omega/N_a$ is finite, and thus the absorption of only a *single* photon in the whole system is enough to excite a significant part of the finite-system many-body wave function $|\,\Psi\,\rangle$. This suggests that in small systems, for instance in the $N_a = 3$ triangle, absorbing a *single* photon is sufficient to cause a significant spin relaxation, too. In the following we will state this qualitative suggestion more precisely by showing that the maximum admissible demagnetization depends on the number of absorbed photons.

To this aim, let us consider the spectral distribution of the many-body wave function $|\,\Psi(t)\,\rangle$ after the laser-pulse absorption. First, recall that the magnetization in the ground-state SP ($\alpha = 0$) of the many-body wave function $|\,\Psi(t)\,\rangle$ remains unchanged. Only spectral parts $\alpha \geq 1$ associated to groups of excited states within the spectral representation of $|\,\Psi(t)\,\rangle$ contribute to the spin relaxation. For the purpose of assessing the maximum admissible demagnetization $(\Delta S_z/S_z^0)_{\max}$, let us assume these excited states within SPs $\alpha \geq 1$ to be totally demagnetized after the spin relaxation has finished. Therefore, $(\Delta S_z/S_z^0)_{\max}$ must depend on the amount of spectral weight, which the laser pulse has removed from the ground state toward excited SPs. This dependence can also be expressed in terms of the average number of absorbed photons n_{eh}. Considering only the most dominant one-photon absorption processes,[1] the spectral density $D_\Psi(E)$ of the state $|\,\Psi(t)\,\rangle$ consists of only two spectral parts: the ground-state SP ($\alpha = 0$), and the excited SP $\alpha = 1$ corresponding to the excitation energy of around $1\,\hbar\omega$. Then, the weight W_1 of the excited SP is given simply by the average number of absorbed photons, i.e., $W_1 = \frac{\Delta E}{\hbar\omega} = n_{\text{eh}}$. Therefore, by assuming a total demagnetization for states within SP $\alpha = 1$ the maximum admissible demagnetization can be estimated as $(\Delta S_z/S_z^0)_{\max} = W_1 = n_{\text{eh}}$, i.e., it depends linearly on n_{eh}. In the case of the basic isosceles triangle, we have used the photon energy $\hbar\omega = 1.55$ eV and found an average absorbed laser energy of $\Delta E = 906$ meV (see Section 5.2). This yields the average number of absorbed photons $n_{\text{eh}} = \frac{0.906\ \text{eV}}{1.55\ \text{eV}} = 0.58$, i.e., $n_{\text{eh}}/N_a = 0.185$ per atom, and therefore implies that at the most a relative demagnetization of $(\Delta S_z/S_z^0)_{\max} = 0.58$ would be achievable. Notice that in our simulations we have computed numerically $\Delta S_z/S_z^0 = 0.47$, which is only slightly below the maximum value. This demonstrates the high efficiency of the purely electronic spin-relaxation mechanism revealed in the present work.

In larger systems having a continuous spectrum the absorption of a *single* photon does not lead to any significant excitation. In fact, since in this case the corresponding excitation energy per atom would be infinitesimal ($\hbar\omega/N_a \to 0$), the absorption of a *single* photon within the whole system is certainly too little to account for relaxation of the total spin. Rather, in order to excite significantly the many-body wave function, the excitation energy per atom must be finite and not negligibly small. Importantly,

[1] In the previous Section 5.5 we have seen that for the basic triangular system the most dominant laser excitations are given by linear combinations of single-photon absorption processes.

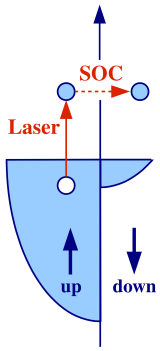

Figure 5.10: Demagnetization from a single-particle perspective - Scheme of majority (spin-up) and minority (spin-down) electronic density of states. The spin-relaxation process is indicated: First, the laser creates a majority electron-hole pair, and second, the electron above the Fermi level flips its spin by means of the spin-orbit coupling.

because of $\hbar\omega/N_a \to 0$ in large systems the spectrum of excited many-body states, which are attainable by laser-pulse absorption, is a quasi continuous function of energy per atom. This implies that a significant level of excitation can be achieved by shifting spectral weight toward SPs having a relatively low energy per atom with respect to the photon energy $\hbar\omega$. In other words, in this case the excitation energies per atom of the relevant laser-excited states in the many-body spectrum are finite but much lower than $\hbar\omega$. In contrast, in small clusters the energy per atom of already the lowest laser-excited states in the spectral representation of $|\,\Psi(t)\,\rangle$ is of the order of $\hbar\omega$, i.e., much higher than the energies per atom of the relevant laser excitations in the bulk. For these reasons, in comparison with our model calculations on small clusters we expect in realistic systems (for instance, in the bulk or thin films) lower absorbed energies $\Delta E/N_a$ and smaller numbers of photon absorption n_{eh}/N_a per atom to yield the same relative demagnetization $\Delta S_z/S_z^0$ as in the considered clusters. Indeed, this expectation agrees with the experiment of Rhie *et al.* on thin Ni films, in which spin dynamics after the absorption of only $n_{\mathrm{eh}}/N_a = \frac{\Delta E}{N_a\,\hbar\omega} = 0.06$ photons per atom (using the same photon energy $\hbar\omega = 1.5$ eV as in our simulations) has been observed (7). In contrast, in our Ni_3 model calculations we have found $n_{\mathrm{eh}}/N_a = 0.19$.

Finally, we would like to present an interpretation of the demagnetization effect from a single-particle perspective. Since only excited states are involved in the magnetization relaxation, we propose the certainly oversimplified picture shown in Figure 5.10:

After the laser-induced creation of electron-hole pairs only the excited majority electrons take advantage of the SOC and flip their spins into the minority band. The fact that in the present small cluster simulations the excitation energy per atom required for the demagnetization is larger than in realistic extended systems can now be explained in terms of the nature of the single-particle spectrum. While in macroscopic systems the spectrum is continuous, the excitation spectrum of small systems is discrete. In comparison with a discrete spectrum, in the solid the density of many-body states is very large. Consequently, there are endless possibilities (much more than in small clusters) for a single electron-hole excitation of finite energy (e.g., $\hbar\omega = 1.5$ eV) to decay into electron-hole pairs around the Fermi level. As a result, for a given number of absorbed photons per atom n_{eh}/N_a, one expects more electron-hole pairs and, subsequently, more spin-flip processes involving these excited electrons. This comparison between discrete and continuous spectra demonstrates that in realistic extended systems a smaller amount of absorbed photons per atom and absorbed laser energy per atom would suffice in order to induce a comparable demagnetization effect. The present qualitative discussion about the absorbed energy per atom shows that the absorption of photon energy plays a central role in the magnetization dynamics. Therefore, in the following Section we present a quantitative detailed investigation of the dependence of the magnetization dynamics on the absorbed energy.

5.7 Dependence on the absorbed energy

In Section 5.5 it has been shown that only weights corresponding to excited many-body states contribute to the ultrafast spin relaxation. This implies that the absorption of photon energy plays a central role in the demagnetization effect, in particular since the absorbed energy gives a measure of the spectral weight transfer from the ground state toward the excited states following the laser pulse. For this reason, it is very interesting to investigate the dependence of the magnetic response on the absorbed laser energy.

For this purpose, simulations for different laser fluences $F = 10$–80 mJ/cm^2 have been performed. Figure 5.11 shows the time dependence of S_z following the absorption of the corresponding laser pulses. As expected, the larger F is, the larger becomes the total (long-time) demagnetization. This behavior can be of course traced back to the absorbed energy ΔE, which is indicated in brackets: With increasing fluence the

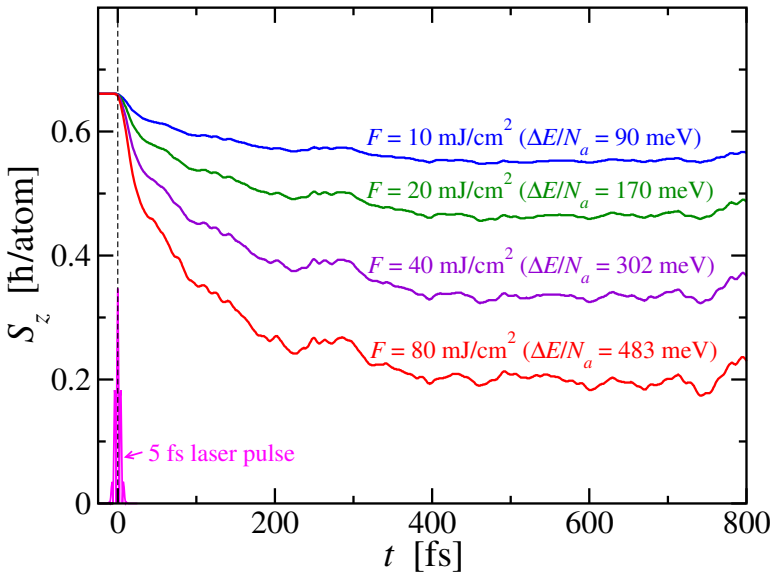

Figure 5.11: Magnetization dynamics for different laser fluences - The total spin S_z relaxation in the Ni_3 triangle following a fs laser pulse is shown for different laser fluences F = 10–80 mJ/cm^2. The corresponding absorbed pump energy ΔE per atom is indicated in brackets. The magenta curve around $t = 0$ illustrates the shape of the laser pulse (electric field $|\vec{E}|$).

amount of absorbed energy also increases. A remarkable result is that the demagnetization time seems to be almost independent of the laser fluence. Actually, only the decrease in magnetization ΔS_z increases with increasing F. In order to quantify this statement, we have fitted the $S_z(t)$ curves to exponential functions of the form (5.5). The derived relative demagnetizations $\Delta S_z/S_z^0$ and demagnetization times $\tau_{\rm dm}$ are shown in Figure 5.12 as a function of the average number of absorbed photons per atom $n_{\rm eh}/N_a = \Delta E/(N_a\hbar\omega)$. While $\tau_{\rm dm}$ is almost independent of $n_{\rm eh}/N_a$, the relative demagnetization scales linearly with the number of photon absorptions.

At this stage of discussion, let us note that so far we have used only one particular set of laser parameters (i.e., laser-pulse polarization, wave length and duration) for describing the initial excitation. It is clearly important to quantify if the laser parameters have an important direct effect on the subsequent magnetization dynamics. To this aim, different laser-pulse polarizations $\vec{\varepsilon}$, wave lengths λ (or frequencies ω) and pulse durations T_p are considered in the following. Varying the laser parameters allows us to control separately the total absorbed energy ΔE, the number of absorbed pho-

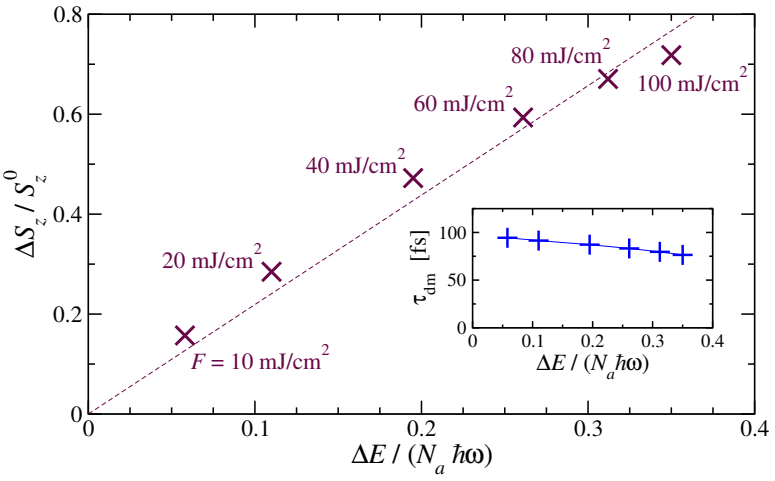

Figure 5.12: Dependence of the relative demagnetization and demagnetization time on the laser fluence - The relative demagnetization $\Delta S_z/S_z^0$ after the fs laser-pulse absorption ($t \gg \tau_{\rm dm}$) is shown as a function of $\Delta E/(N_a\,\hbar\omega)$. The quantity $\Delta E/(N_a\,\hbar\omega)$ can be interpreted as the number of absorbed photons per atom $n_{\rm eh}/N_a = \Delta E/(N_a\,\hbar\omega)$ resulting from laser-pulse absorption. The crosses are obtained by fitting $S_z(t)$ to an exponential decay for each fluence F. The dotted line is a linear fit to the discrete points. The inset shows the corresponding demagnetization times $\tau_{\rm dm}$.

tons or initial electron-hole excitations $n_{\rm eh}$, and many-body density of excited states at energy $E_{\rm gs} + n\hbar\omega$ with $n = 1, 2, \ldots$. In particular, we would like to reveal the roles of ΔE and $n_{\rm eh}$ in the magnetization dynamics. For instance, if the dynamics would be dominantly controlled by the absorbed energy, one would expect $\Delta S_z/S_z^0$ and $\tau_{\rm dm}$ to depend only on $\Delta E = n_{\rm eh}\hbar\omega$ and not on the specific fluence, laser frequency and number of absorbed photons. In contrast, if the average number of absorbed photons is the crucial parameter, the different total absorbed energies ΔE should yield similar $\Delta S_z/S_z^0$ and $\tau_{\rm dm}$ provided that $n_{\rm eh} = \Delta E/\hbar\omega$ is the same. In addition, it is also very interesting to see if maybe other laser parameters can be used to control the subsequent spin relaxation by keeping ΔE and $n_{\rm eh}$ fixed.

In order to investigate the role of the polarization $\vec{\varepsilon}$ of the incident laser pulse, we have considered different electric-field polarizations. Figure 5.13 shows the spin- and orbital angular-momentum dynamics for linear (in-plane) as well as circular σ_+ and σ_- polarizations of $\vec{E}$. Here, the linear polarization corresponds to the reference set of parameters, which yields the magnetization dynamics reported in Section 5.2. Let us recall that the linear pulse can be regarded as the superposition of the two

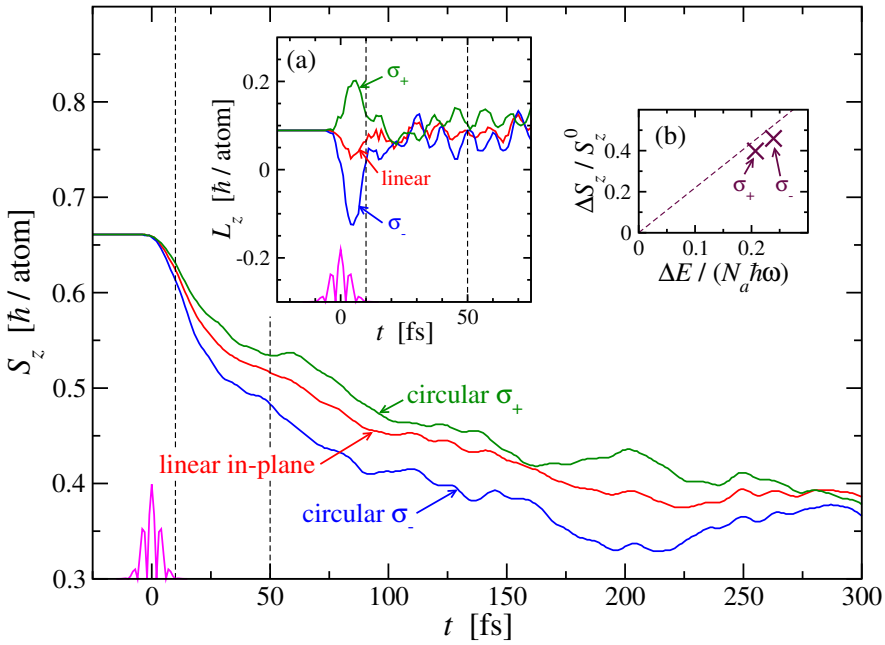

Figure 5.13: Magnetization dynamics for different laser electric-field polarizations - Laser-induced spin relaxation S_z in the triangle system is shown for linear in-plane as well as circular σ_+ and σ_- polarizations of the incident pulse. The vertical dotted lines represent the times $t = 10$ fs and $t = 50$ fs after the passage of the center of the $T_p = 5$ fs laser pulse, whose shape is illustrated by the magenta curve around $t = 0$. Inset (a) shows the corresponding dynamics of the orbital angular momentum L_z within the first 75 fs after pulse absorption, while inset (b) shows the relative demagnetization $\Delta S_z/S_z^0$ for the circularly polarized pulses as a function of $\Delta E/(N_a\,\hbar\omega)$. There, the straight dotted line gives the linear approximation taken from Figure 5.12, and the quantity $\Delta E/(N_a\,\hbar\omega)$ is interpreted as the number of absorbed photons per atom $n_{\rm eh}/N_a$.

circularly polarized σ_+ and σ_- light pulses, where the σ_+ and σ_- photons carry and angular momentum of $+\hbar$ and $-\hbar$ along the out-of plane direction (z quantization axis), respectively.[1] The main Figure shows that the time dependence of S_z is slightly different for the three considered polarizations. After absorption of the σ_- (σ_+) pulse the spin projection decreases faster (slower) than after absorption of the linearly polarized pulse. Moreover, the demagnetization is largest after excitation with σ_- light: At $t = 10$ fs after absorption of the $T_p = 5$ fs pulse, i.e., roughly at the end of the laser-pulse passage,

[1]Exception made for the polarization of $\vec{E}$, all other parameters, which have been used for computing the dynamics following the excitation by means of circularly polarized pulses, correspond to the basic triangle system. In particular, a fluence of $F = 40$ mJ/cm^2 has been used.

the difference in S_z is given by $S_z^{\text{linear}} - S_z^{\sigma-} = 0.011\,\hbar$ per atom ($S_z^{\sigma+} - S_z^{\text{linear}} = 0.007\,\hbar$ per atom). Subsequently, this difference even increases so that at $t = 50$ fs after pulse absorption $S_z^{\text{linear}} - S_z^{\sigma-} = 0.033\,\hbar$ per atom ($S_z^{\sigma+} - S_z^{\text{linear}} = 0.018\,\hbar$ per atom).

Let us now discuss the origin of this polarization effect. To this aim, first we focus our attention on the inset (a) in Figure 5.13, which shows the time dependence of the orbital angular momentum L_z. One can see that the initially strongly quenched positive L_z ($L_z \simeq 0.09\,\hbar$ per atom parallel to S_z) decreases (increases) by around 0.1–$0.2\,\hbar$ per atom during the action of the σ_- (σ_+) circularly polarized pulses, i.e., on a time scale of a few femtoseconds. This behavior of L_z can be understood as the result of transfer of photon angular momentum into electronic orbital angular momentum $\vec{L}$ by means of the electric-dipole interaction. This is consistent with the fact that σ_- (σ_+) light induces $m \to m-1$ ($m \to m+1$) transitions. Moreover, inset (b) shows that in the case of both σ_- and σ_+ polarized pulses an average number of $n_{\text{eh}} \approx 0.2$ photons per atom has been absorbed. Since each of these photons carry an angular momentum of $-\hbar$ or $+\hbar$ respectively, their absorption leads to the observed changes in L_z of around $\pm$0.1–$0.2\,\hbar$ per atom. Therefore, the pulse absorption already causes a small reduction of the total angular momentum $L_z + S_z$. In an atom, the photon angular momentum $\pm\hbar$ initially absorbed within $\vec{L}$ would be —subsequently to the laser-pulse action— partially transferred to $\vec{S}$ by means of the local SOC, which conserves the total angular momentum $\vec{L} + \vec{S}$. In this sense, one could expect that the σ_- (σ_+) circular polarization of the laser field $\vec{E}$ might be the origin of the enhancement (reduction) of the demagnetization effect in the considered triangular system. However, in the lattice this effect is suppressed by the interatomic electron motion. In fact, the inset (a) shows that L_z is very rapidly quenched, and that already $t = 10$ fs after the pulse absorption the differences in L_z for the considered σ_-, σ_+ and linear polarizations are smeared out, while the corresponding differences in S_z evolve on a longer time scale of around 50 fs (see main Figure 5.13). This means that the laser-induced gain or loss in the orbital angular momentum L_z is very rapidly quenched by the electron motion in the lattice so that the SOC does not have enough time to transfer this gain or loss in L_z toward the spin S_z. In other words, the direct transfer of angular momentum from the photons to $\vec{L}$ induced by circularly polarized light has very little effect on the magnetization dynamics following the pulse absorption.

This conclusion is confirmed by the inset (b) in Figure 5.13 as we shall discuss in the following. This inset shows the relative demagnetization $\Delta S_z/S_z^0$, obtained by fitting the $S_z(t)$ curves to Eq. (5.5), as a function of the number of absorbed photons per atom $n_{\rm eh}/N_a = \Delta E/(N_a\,\hbar\omega)$. One can see that excitation using σ_- pulses yields a larger number $n_{\rm eh}$ than excitation using σ_+ pulses. The preference of absorbing σ_- photons can be understood as follows: Since the initial state has a small positive projection $L_z \simeq 0.09\,\hbar$ per atom, the number of occupied orbitals having $m > 0$ is larger than for $m < 0$. This implies that absorption of σ_- photons, which induces $m \to m-1$ electronic transitions, is more probable than absorption of σ_+ photons inducing $m \to m+1$ transitions. However, the long-time demagnetizations $\Delta S_z/S_z^0$ for σ_+ and σ_- circularly polarized light are very close to the straight dotted line, which represents the linear approximation taken from Figure 5.12. Consequently, the small differences in the spin dynamics and, in particular, in $\Delta S_z/S_z^0$ for σ_+ and σ_- polarizations of $\vec{E}$ can be explained to a large extent by means of the corresponding numbers of photon absorption. Hence, the demagnetization effect depends on the photon helicity basically through the absorbed laser energy. This means that it is not the spin relaxation itself but the ability of absorbing laser energy what is found to be a direct function of laser electric-field polarization.

A further important characteristic of the laser field $\vec{E}$ is given by its wave length λ or the associated frequency $\omega = 2\pi c/\lambda$. Therefore, we have calculated the time evolution of the total spin S_z by considering various wave lengths λ of the pump laser. It is clear that the ability of absorbing photons strongly depends on the many-body density of states at energy $E_{\rm gs} + \hbar\omega$. It also depends on the electric-dipole matrix elements between the ground state and the excited states. However, we are mainly interested in elucidating if the ultrafast demagnetization effect can be explained in terms of the absorbed energy per atom $\Delta E/N_a$ alone. Figure 5.14 shows for a few examples of λ the efficiency of demagnetization, i.e., the relative demagnetization $\Delta S_z/S_z^0$, (a) as a function of $\Delta E/N_a$ and (b) as a function of the number of absorbed photons per atom $n_{\rm eh}/N_a = \Delta E/(N_a\,\hbar\omega)$.[1] In panel (a) a systematic dependence of $\Delta S_z/S_z^0$ on $\Delta E/N_a$ cannot be read out clearly. For instance, the simulations for $\lambda = 416$ and 1779 nm yield very similar relative demagnetizations $\Delta S_z/S_z^0$, although the corresponding absorbed

[1] Besides the wave length λ all other parameters are kept fixed. Notice for comparison that in all previous simulations we have used $\lambda = 800$ nm.

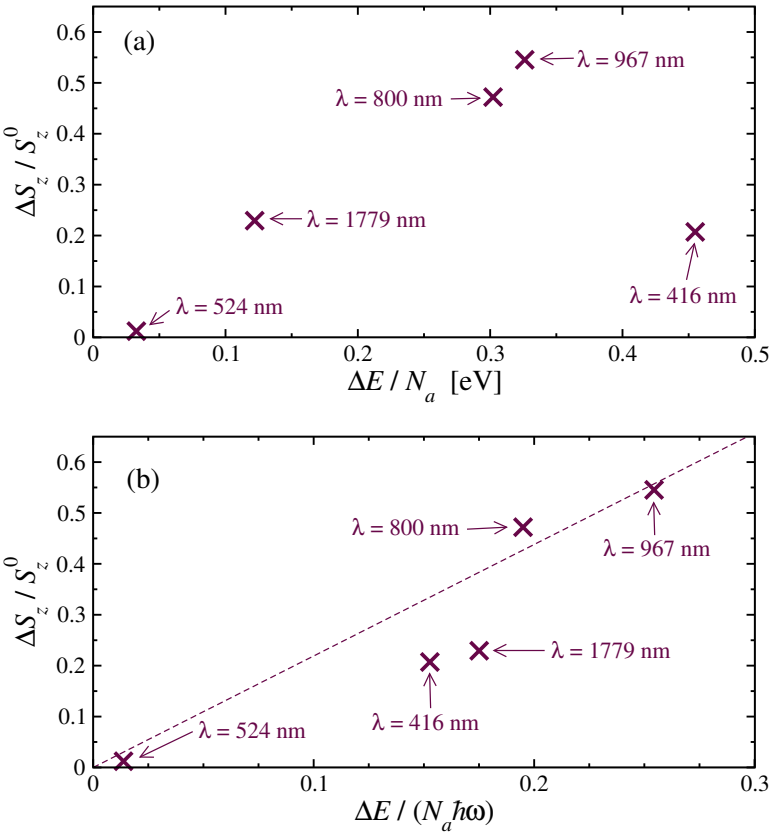

Figure 5.14: Demagnetization efficiency for various laser wave lengths - The relative demagnetization $\Delta S_z/S_z^0$ in the Ni_3 triangle is shown (a) as a function of the absorbed energy per atom $\Delta E/N_a$ and (b) as a function of $\Delta E/(N_a\,\hbar\omega)$ which can be interpreted as the number of absorbed photons per atom $n_{\rm eh}/N_a$. Results (crosses) are given for wave lengths λ = 416, 524, 800, 967 and 1779 nm. The straight dotted line in panel (b) is the linear approximation derived from the results shown in Figure 5.12.

energies $\Delta E/N_a$ differ from each other by a factor of 4. In contrast, in panel (b) one observes that the results for $\Delta S_z/S_z^0$ are roughly consistent with the linear dependence on $n_{\rm eh}/N_a$ (dotted line), which has been previously found by varying the laser fluence (see Figure 5.12). In particular, the numbers of absorbed photons $n_{\rm eh}$ are similar for the λ = 416 and 1779 nm calculations. Consequently, these results provide evidence that the ultrafast demagnetization is not directly related to the absorbed energy. Rather, it can be explained in terms of the number of absorbed photons. This dependence reflects the fact that the ultrafast spin relaxation is not a heat-driven effect.

Let us close this Section by studying the dependence of spin relaxation on the

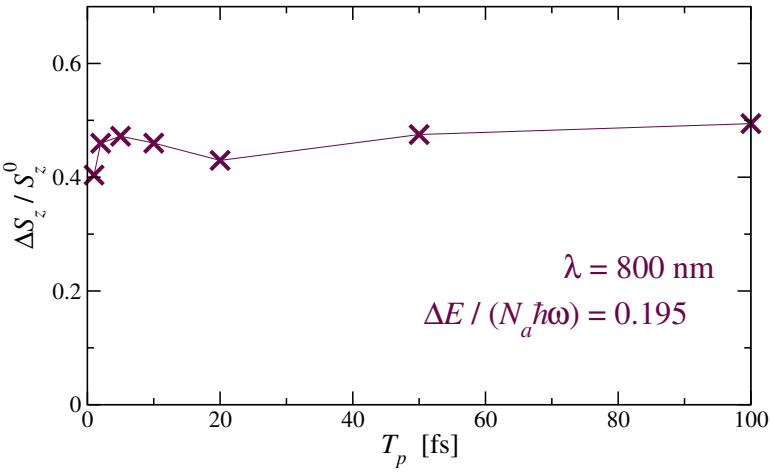

Figure 5.15: Demagnetization efficiency as a function of pulse duration - The relative demagnetization $\Delta S_z/S_z^0$ induced by $\lambda = 800$ nm laser pulses is shown as a function of pulse duration T_p. The laser fluences F have been chosen such that for each considered T_p the Ni_3 triangle always absorbs the same average number of photons $n_{\mathrm{eh}} = \Delta E/(\hbar\omega) = 0.195$ per atom.

pulse duration T_p representing a further characteristic of the laser field. To this aim, simulations have been performed for the laser wave length $\lambda = 800$ nm and various T_p in the range $T_p = 1$–100 fs.[1] Notice that for $\lambda = 800$ nm one femtosecond corresponds to 0.37 of a single electric-field oscillation. This means that such short pulses have a very broad distribution of frequencies ω. Thus, varying T_p from 1 to 100 fs corresponds to changes from very broad to very narrow spectral widths in the frequency domain. In these calculations the laser fluence F has been varied together with T_p such that for each T_p one obtains the same number of absorbed photons $n_{\mathrm{eh}} = 0.195$ per atom.[2] This procedure allows us to suppress the dependence on the average number of absorbed photons and to identify potential direct effects of the pulse duration on the laser-induced spin relaxation. Figure 5.15 shows the relative demagnetization $\Delta S_z/S_z^0$ as a function of T_p. One finds that $\Delta S_z/S_z^0$ depends only weakly on T_p as long as $n_{\mathrm{eh}} = \Delta E/(\hbar\omega)$ is kept constant. This result again confirms that the ultrafast demagnetization depends primarily on the number of absorbed photons. Let us finally mention that this renders

[1] The width T_p is defined such that at the time $t = \pm T_p$ the Gauss envelope of the pulse is reduced by the factor $1/e$ with respect to its maximum at $t = 0$.

[2] Besides T_p and F, all other parameters have been chosen as in the reference Ni_3 triangle studied in Section 5.2.

the mechanism of photon absorption very central. In the following Section we will discuss the role of the *d*-*p* interband hybridization which, as we shall see, facilitates the laser-pulse absorption.

5.8 Interband hybridization effects

We have seen that in the present model the demagnetization appears as the result of photon absorption during fs laser irradiation. Importantly, the absorption of photons is induced by the electric-dipole interaction with the laser field by means of electronic transitions between the lower d and the higher p band. This implies that the elementary electronic $d \to p$ transitions resulting from the pulse absorption play a crucial role in the initial stage of the laser-induced spin relaxation. In other words, they represent a necessary ingredient of this effect.

One can show that the initial rate of the important laser-induced interband $d \to p$ electronic transitions is proportional to the *d*-*p* hybridization quantified by the interband hopping integrals $t_{jk}^{p0,dm}$. To this aim, let us write the time derivative of the p-band occupation n_p as

$$\frac{\mathrm{d}}{\mathrm{d}t}\langle \hat{n}_p \rangle \;=\; \frac{i}{\hbar}\left\langle \left[\hat{H}\,,\,\hat{n}_p\right]\right\rangle \;=\; \frac{i}{\hbar}\left\langle \left[\hat{H}_0\,,\,\hat{n}_p\right]\right\rangle \;+\; \frac{i}{\hbar}\left\langle \left[\hat{H}_E\,,\,\hat{n}_p\right]\right\rangle \;. \tag{5.13}$$

On the right-hand side, the first term describes the contribution of electronic interband hoppings,[1] while the second term represents the contribution of the laser pulse. Actually, only the latter contribution $\langle[\hat{H}_E\,,\,\hat{n}_p]\rangle$ determines the laser-induced rate $\mathrm{d}\,\langle\hat{n}_p\rangle_{\mathrm{Laser}}/\mathrm{d}t$ of the charge transfer from the d to the p electrons (enhancement of the p-band occupation). Using Eq. (3.9) one obtains

$$\begin{aligned}\frac{\mathrm{d}}{\mathrm{d}t}\langle \hat{n}_p \rangle_{\mathrm{Laser}} \;&=\; \frac{i}{\hbar}\left\langle \left[\hat{H}_E\,,\,\hat{n}_p\right]\right\rangle \\ &=\; -\frac{i}{\hbar}e\vec{E}(t)\cdot\sum_{jm\sigma}\left\{\langle\, dm\,|\hat{\vec{r}}|\,p0\,\rangle\,\left\langle \hat{c}^{\dagger}_{jdm\sigma}\hat{c}_{jp0\sigma}\right\rangle \;-\; \langle\, p0\,|\hat{\vec{r}}|\,dm\,\rangle\,\left\langle \hat{c}^{\dagger}_{jp0\sigma}\hat{c}_{jdm\sigma}\right\rangle\right\}\;,\end{aligned} \tag{5.14}$$

demonstrating that the enhancement of the p-band occupation depends linearly on the *d*-*p* matrix elements $\langle\hat{c}^{\dagger}_{jdm\sigma}\hat{c}_{jp0\sigma}\rangle$ and $\langle\hat{c}^{\dagger}_{jp0\sigma}\hat{c}_{jdm\sigma}\rangle$. In the FM ground state these matrix elements are proportional to the interband hybridization (or hopping integrals $t_{jk}^{p0,dm}$).

[1] This term is zero for the initial FM ground state before the laser pump pulse.

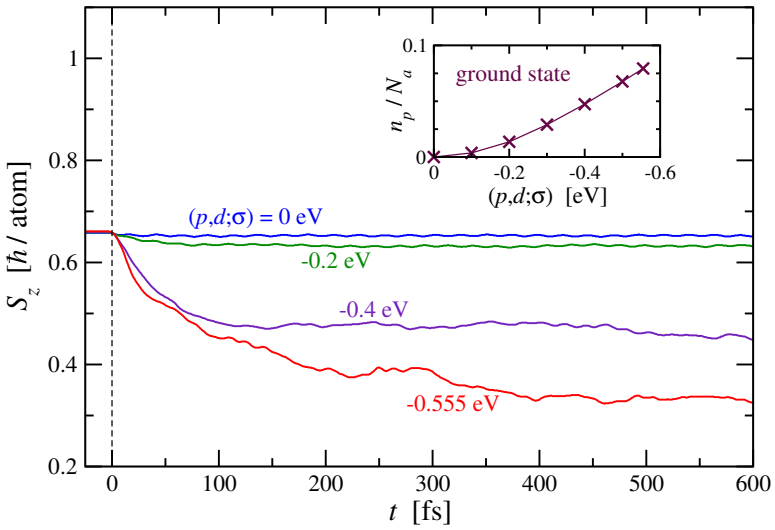

Figure 5.16: Dependence of spin relaxation on interband hopping integrals - Spin relaxation of the isosceles Ni_3 triangle subsequent to a 5 fs laser-pulse absorption is shown for various values of the p-d two-center integral $(p, d; \sigma)$. The time of laser excitation $(t = 0)$ is indicated by a vertical dotted line. The inset illustrates the relation between $(p, d; \sigma)$ and the ground-state p-electron occupation per atom n_p/N_a.

Notice that at the initial time or moment of laser-pulse absorption the many-body state is given by the ground state. Consequently, Eq. (5.14) implies that at this initial time the rate $\frac{\mathrm{d}}{\mathrm{d}t}\langle\hat{n}_p\rangle$ depends linearly on $t_{jk}^{p0,dm}$. In this way, the d-p hybridization determines the strength of the initial push (i.e., the number of photon absorptions by means of $d \rightarrow p$ electronic transitions) during the fs laser excitation. If $t_{jk}^{p0,dm} = 0$, which is the case for instance in isolated atoms, only the second time derivative $\frac{\mathrm{d}^2}{\mathrm{d}t^2}\langle\hat{n}_p\rangle$ would contribute to the enhancement of the p-band occupation $\langle\hat{n}_p\rangle$. Thus, the photon-absorption process would be an effect of second order in time.

In order to numerically verify the important role of interband hybridization in the laser-induced spin relaxation, Figure 5.16 shows the time evolution of the spin S_z for various p-d two-center integrals $(p, d; \sigma) = 0$ eV, -0.2 eV, -0.4 eV and -0.555 eV. Here, the latter value corresponds to the parameter of the reference triangle system. One clearly observes that the larger $|(p, d; \sigma)|$, the larger the demagnetization effect. Notice that the two-center integrals are directly related to the interband hopping elements $t_{jk}^{p0,dm}$ (see Table 3.2), i.e., the magnitude of the integrals $(p, d; \sigma)$ determines the d-p hybridization and thus the d-p matrix elements $\langle\hat{c}_{jdm\sigma}^{\dagger}\hat{c}_{jp0\sigma}\rangle$ within the initial state.

The inset shows the ground-state number of p electrons n_p as a function of $(p, d; \sigma)$. Obviously, the p-band occupation n_p within the ground state increases with increasing hybridization $|(p, d; \sigma)|$. In fact, in this case n_p can be regarded as a measure for the d-p matrix elements $\langle \hat{c}^{\dagger}_{jdm\sigma} \hat{c}_{jp0\sigma} \rangle$ within the initial state before the laser irradiation. Finally, the main Figure 5.16 can be understood as follows: According to Eq. (5.14) d-p hybridization, which is accompanied by a non-vanishing p-band occupation, accelerates the absorption of photons in the ground state by means of electric-dipole transitions. In other words, d-p hybridization increases the initial laser-induced push leading to the enhancement of n_p. In this way, it facilitates the demagnetization effect.

5.9 Different band fillings and geometrical structures

In the previous Sections we have extensively studied the laser-induced spin relaxation in the isosceles triangle having $N_e = 3$ electrons. Now, the question arises if a similar magnetization dynamics also appears in the case of different band fillings and in different geometrical structures.

In order to address this question, we consider first the triangle having various numbers of electrons $N_e = 3$, 4, 5, 7 and 15, and, secondly, various structures: one-dimensional dimer having $N_e = 3$ electrons, $N_a = 3$ linear chain ($N_e = 5$, 7), and two-dimensional rhombus ($N_a = 4$) having $N_e = 5$ electrons. For each of these systems, the exchange-energy parameter J and the laser wave length λ have been chosen such that the ground state is ferromagnetic and the many-body density of states allows the absorption of the photon energy $\hbar\omega$. The choices of the exchange integrals J and the associated wave lengths λ are specified in Table 5.1. All other parameters are the same as in previous calculations of the spin relaxation in the basic triangle system (see, e.g. Figure 5.1). In particular, we have used $\xi = -50$ meV, $T_p = 5$ fs, $F = 40$ mJ/cm^2, and electric-field polarization along the dimer/chain or within the triangle/rhombus plane, respectively. The resulting time dependence of the total spin projection S_{easy} along the easy magnetization axis is shown in Figure 5.17.[1] Panel (a) of this Figure shows that a qualitatively similar spin dynamics is induced by fs laser pulses for all considered band fillings. Moreover, a comparison between the spin relaxations for $N_e = 3$ and $N_e = 15$ demonstrates that the essential behavior of magnetization dynamics does not depend

[1] For each system the easy magnetization axis (or plane) is given in Table 4.2.

System size	Structure	Band filling	Exchange integral	Laser wave length
$N_a = 2$	Dimer	$N_e = 3$	$J = 0.4$ eV	$\lambda = 1240$ nm
$N_a = 3$	Linear chain	$N_e = 5$	$J = 0.3$ eV	$\lambda = 428$ nm
		$N_e = 7$	$J = 1.6$ eV	$\lambda = 652$ nm
$N_a = 3$	Triangle	$N_e = 3$	$J = 1.6$ eV	$\lambda = 463$ nm
		$N_e = 4$	$J = 0.8$ eV	$\lambda = 800$ nm
		$N_e = 5$	$J = 3.2$ eV	$\lambda = 242$ nm
		$N_e = 7$	$J = 2.4$ eV	$\lambda = 320$ nm
		$N_e = 15$	$J = 1.0$ eV	$\lambda = 1934$ nm
$N_a = 4$	Rhombus	$N_e = 5$	$J = 1.4$ eV	$\lambda = 314$ nm

Table 5.1: Laser wave lengths and exchange integrals for selected structures and band fillings - Wave lengths λ of the laser pump pulse, which have been used for the spin-dynamics simulations for various structures and band fillings, are listed. In addition, the choice of the exchange integral J is given for each considered system.

on whether the d band is more than half-filled or it is less than half-filled. This gives us the legitimation to model Ni by less than half-filled d bands as discussed in Section 4.1. Furthermore, panel (b) of Figure 5.17 shows that also in different structures the magnetization decreases after laser-pulse absorption. Let us notice the oscillations in S_{easy}, observed for the dimer and for the $N_a = 3$ chain having $N_e = 7$ electrons. We have found that in these cases the spectral representation of the the wave function $|\,\Psi\,\rangle$ well after laser-pulse absorption, i.e., the many-body spectral density $D_\Psi(E)$, is basically composed of two states whose energies differ from each other by only 10–20 meV. This gives rise to Rabi-like oscillations of the spin S_z having a period of around 200–400 fs. It is clear that this effect can take place only in systems having a discrete spectrum, and thus represents a finite-size effect. Therefore, these oscillations are not relevant for the purpose of drawing conclusions on the physics of magnetization dynamics in realistic thin films or solids. Notice also that in all the other considered simulations the laser-excited states $|\,\Psi\,\rangle$ consist of much more than two states and, thus, oscillations of the spin projection do not occur.

One concludes that demagnetization is possible for different band fillings, geometries and dimensions. This can be explained by the local character of the intra-atomic Coulomb interactions and the elementary electronic transitions involved in the laser excitation and spin-orbit coupling. Since these mechanisms are local, they yield a qualitatively similar magnetization dynamics in all considered cases.

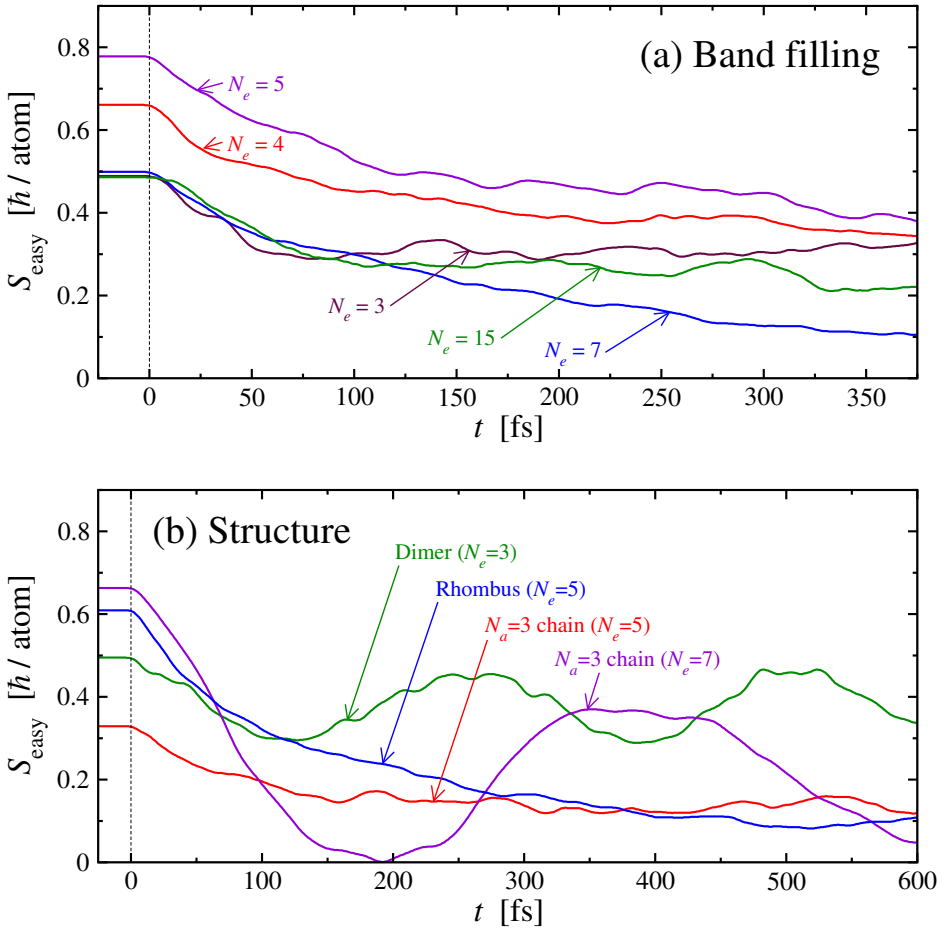

Figure 5.17: Spin dynamics for different band fillings and structures - (a) The laser-induced spin relaxation along the easy magnetization direction is shown for the isosceles triangle having various numbers of electrons N_e. (b) Spin dynamics for different geometrical structures: one-dimensional dimer having $N_e = 3$ electrons, $N_a = 3$ linear chain ($N_e = 5$, 7), and two-dimensional rhombus ($N_a = 4$) having $N_e = 5$ electrons. Notice that for each system the easy magnetization axis (or plane) is specified in Table 4.2. The laser excitation time $t = 0$ is indicated by vertical dotted lines.

6

Conclusions and outlook

In conclusion, a microscopic explanation of the laser-induced ultrafast demagnetization effect in ferromagnetic metals has been given. For the purpose of elucidating the physics of this phenomenon, in a preliminary step the nature of spin excitations has been studied. The results have shown that shortly after the laser-pulse absorption the most relevant spin excitations are given by local spin fluctuations, which represent a disorder of atomic magnetic moments in their orientations. This implies that for a proper description of ultrafast magnetization dynamics, it is very important to take into account local magnetic moments. In the present thesis we have addressed this challenging problem by developing a many-body theory. Its main advantage is that it includes from the very beginning electronic correlations, which favor the formation of the local moments. Our primary ansatz was to consider exclusively the electronic system, which dominates the physics of magnetization dynamics on the femtosecond time scale since it gives the fastest response to laser excitation. The couplings to the slower phonons and the environment have not been considered. In order to investigate the purely electronic processes in the ultrafast demagnetization, we have introduced an electronic many-body lattice model. The underlying Hamiltonian considers electron hoppings in the lattice, Coulomb interaction, light-matter interaction and SOC on the same footing. In this framework the spin relaxation is exclusively triggered by the SOC.

Exact time evolutions of both the initial excitation, i.e., the interaction between electrons and the fs laser pulse, and the subsequent relaxation dynamics in small Ni clusters having up to $N_{\mathrm{a}} = 4$ atoms demonstrate that the ultrafast demagnetization can indeed be explained in terms of a purely electronic mechanism. The results provide

a novel insight into the microscopic mechanism of this effect: First, the laser pulse pumps energy into the electronic system and creates a number of excited electrons. Then, in the excited state the SOC yields a significant spin-to-orbital relaxation, by means of which angular momentum is transferred locally from the spins to the electron orbits on a time scale of several tens to hundreds of femtoseconds. The elementary local transitions involved in the SOC conserve the total angular momentum $\vec{L}+\vec{S}$. However, the electron orbits do not accumulate the angular momentum which is transferred from $\vec{S}$, since on a time scale of only a few femtoseconds $\vec{L}$ is quenched by the electron motion in the lattice. In this way, the interatomic electron motion acts as a very effective sink for the electronic angular momentum. We have found that the combination of these purely electronic effects, i.e., SOC-triggered angular-momentum transfer from $\vec{S}$ to $\vec{L}$ and subsequent quenching of $\vec{L}$ in the lattice, results in a demagnetization within a few hundred femtoseconds. Moreover, we have identified the spin-orbit interaction as the key factor for the demagnetization rate: the stronger the SOC, the faster the spin-to-orbit angular momentum transfer proceeds. A further crucial finding is that the laser-induced decrease in magnetization can be traced back to a decrease in the nearest-neighbor spin correlations, while the magnitudes of the local magnetic moments remain very stable. Actually, this confirms the previous conjecture that the ultrafast demagnetization effect is the result of fluctuations of local moments in their orientations.

In addition to the understanding of the very fundamental mechanisms, the present studies reveal several further characteristics of the ultrafast process. For instance, it has been found that after the femtosecond laser excitation the absorbed energy is stored mainly within the degrees of freedom of the interatomic electron motion. Even after the entire spin relaxation of the model has been completed, the electronic orbital and translational degrees of freedom are far from being in thermal equilibrium with spin degrees of freedom. This implies that the laser-induced demagnetization does not represent a thermalization effect. In contrast, it is the result of non-adiabatic dynamical relaxation processes. The same conclusion can be drawn from our small-cluster findings that the relative demagnetization strength $\Delta S_z/S_z^0$ depends almost exclusively on the number of absorbed photons, rather than on the absorbed laser energy. This dependence clearly indicates that the ultrafast spin relaxation is not a heat-driven effect. It is also important to note that we have not found any direct dependences of $\Delta S_z/S_z^0$ on laser-pulse parameters such as electric-field polarization,

wave length or pulse duration. For instance, even in the case of circularly polarized pulses carrying angular momentum $\pm\hbar$ toward electronic orbital momentum $\vec{L}$, the demagnetization efficiency does not considerably depend on the photon helicity since $\vec{L}$ is very rapidly quenched in the lattice. The essential dependence of the relative demagnetization strength is the dependence on the ability of the electron system to absorb photons.

Let us now discuss the impact of our results obtained for small clusters on the debate about the fundamental microscopic physics of ultrafast magnetization dynamics in ferromagnetic TM solids or thin films. In this context, let us recall that in both the model and realistic TM samples the essential processes involved in the Coulomb interaction, SOC and laser excitation, are local. In fact, the angular-momentum transfer between $\vec{S}$ and $\vec{L}$ is triggered locally by the SOC at atomic sites. Moreover, the most dominant intra-atomic Coulomb interactions and the electric-dipole transitions induced by the laser-pulse absorption have also a local character. For these reasons, we expect that the same electronic microscopic processes dominate the ultrafast magnetization dynamics in different system sizes and dimensions: in small ferromagnetic clusters, in thin films and also in bulk ferromagnets. Good evidence for this expectation is provided by applications to various structures, namely, to the dimer, the linear chain, the triangle and the rhombus. The corresponding results have shown a qualitatively similar spin relaxation in all these cases. Therefore, our model approach allows us to compare the results of exact time evolution, which is restricted to small system sizes ($N_\mathrm{a} \lesssim 4$ atoms), with experimental results. Based on this reasoning, the purely electronic mechanism revealed by the model results explains the ultrafast demagnetization not only in small clusters but also in realistic metals. In other words, we conclude that also in realistic FM transition metals it is the combination of (i) SOC-triggered transfer from $\vec{S}$ to $\vec{L}$ and (ii) quenching of $\vec{L}$ by the electron motion in the metal, what is responsible for the ultrafast demagnetization.

However, several differences between the considered small clusters and the TM samples used in experiments deserve a special attention. First, let us mention the single-particle spectra. In a small cluster the spectrum is discrete, while large systems have a continuous spectrum. Consequently, the probability for a single laser-induced electron-hole excitation of finite energy to decay into electron-hole pairs around the Fermi level is much larger for large systems than for small clusters. This implies that

in macroscopic systems there would be more excited electrons per atom for a given number of absorbed photons per atom, than in our model calculations. Since these excited electrons above the Fermi level take advantage of the SOC and flip their spins into the minority band, we expect that for the same level of excitation (i.e., number of absorbed photons per atom) the relative demagnetization $\Delta S_z/S_z^0$ is also larger in macroscopic systems than in small clusters. In other words, we expect that if one increases the system size, one needs less laser energy absorption per atom in order to induce a comparable demagnetization. A further difference is given by the d-band widths W_d. For the basic Ni_3 triangular system we have found $W_d = 1.9$ eV, which is considerably smaller than the bulk d-band width $W_d^b \approx 5$ eV. The relatively small width W_d for the triangle can be explained by its low dimensionality with respect to the solid. It implies that in the bulk the process of quenching of $\vec{L}$ is expected to take place even faster than in our model simulations. Importantly, these differences between small clusters and realistic large systems do not concern the essential spin relaxation processes and, therefore, do not damage our central conclusions about the fundamental mechanisms responsible for the magnetization dynamics in ferromagnetic metals.

In the context of quenching of angular momentum, let us notice that it has been argued that the total angular momentum $\vec{L} + \vec{S}$ of an isolated sample is a constant of motion. Our findings do not contradict this elemental conservation law, since the present model does not describe an isolated system. In fact, the quenching of $\vec{L}$ by the interatomic electron motion can be interpreted as an angular momentum transfer (on a time scale of ~ 1 fs) from the electron orbits to the lattice motion via the Coulomb interaction between valence electrons and ions. In other words, the hopping integrals $t_{jk}^{m,m'}$ with $m \neq m'$ implicitly allow the transfer of angular momentum between orbital degrees of freedom and the lattice. However, we are not interested in describing the lattice rotation, since this would be physically unreasonable as the lattice is of course fixed within the experimental setup, i.e., coupled to the much larger environment.

Notice that the interactions with the environment and phonons were not considered in the present work, since they do not lead to any significant spin relaxation on the femtosecond time scale. However, on the picosecond or even longer time scale the processes of electron-phonon scattering, spin-polarized electron diffusion toward the substrate, and energy dissipation to the environment are expected to become important for describing the time dependence of the magnetization. In particular, they most

probably lead to the recovery of the sample magnetization. It would be interesting to investigate in more detail the roles of these processes for the dynamics of the system. To this aim, our lattice model could be extended by including mean-field like interactions with the environment and phonons.

Besides extending the electronic many-body model, it can be applied to periodic boundary conditions. Although in this thesis we have considered exclusively systems having open boundary conditions, the model is certainly not restricted to them. In fact, periodic boundary conditions are of particular interest, since they can be used to model realistic periodic systems such as thin films. However, the important elementary electronic transitions involved in the spin-orbit interaction and laser excitation, as well as the most dominant intra-atomic Coulomb repulsion, are local. Therefore, the choice of boundary conditions is expected to play a minor role in the magnetization dynamics. Nevertheless, it is worth verifying this expectation. In this sense, applying our model to systems having periodic boundary conditions would be an interesting route for future studies.

A further very interesting application of the introduced many-body model is the detailed investigation of static magnetic properties. For instance, the model opens the possibility to study the role of the electron correlation in SOC-effects such as the magnetic anisotropy and orbital magnetism. Future work in this direction could lead to an important contribution to the understanding of SOC-effects both in ground-state and finite-temperature magnetism.

Finally, we believe that the electronic explanation of the laser-induced demagnetization in ferromagnetic TMs, which is presented in the present thesis, will enlighten the microscopic physics behind this effect. Moreover, it is our hope that the present work will contribute to the future development of theoretical methods for the description of ultrafast magnetization dynamics. In this context, one could apply the unrestricted Hartree-Fock approximation to the present model Hamiltonian, which basically includes the modifications $\hat{\vec{S}}_{jd} \cdot \hat{\vec{S}}_{jd} \rightarrow 2\langle \hat{\vec{S}}_{jd} \rangle \cdot \hat{\vec{S}}_{jd} - \langle \hat{\vec{S}}_{jd} \rangle^2$ and $\hat{n}_{jd}\hat{n}_{jd} \rightarrow 2\langle \hat{n}_{jd} \rangle \hat{n}_{jd} - \langle \hat{n}_{jd} \rangle^2$. We expect that this would not correctly reproduce the stability of the important local magnetic moments. However, this approximation does not concern the terms describing the laser excitation and the relaxation processes related to the electron motion in the lattice and spin-orbit interaction. Therefore, it would be interesting to apply the

time-dependent unrestricted Hartree-Fock method in order to see if it accounts for the experimentally observed spin relaxation after laser-pulse absorption.

Appendix A

Computational details of DFT calculations

In the present Appendix the main details of the numerical calculations presented in Chapter 2 are briefly described. These calculations have been performed in the framework of Hohenberg-Kohn-Sham's DFT (58, 59), as implemented in the VASP (64, 65). A spin-polarized generalized gradient approximation to the exchange and correlation energy functional (84, 85, 86) is used together with a frozen-core all-electron approach, treating the $3d$, $4s$ and $4p$ electrons as valence states. The spin-polarized Kohn-Sham equations are solved in an augmented plane-wave basis set and the interaction between valence electrons and ionic cores is described by means of the projector-augmented wave method (87).

For the 1D calculations reported in Sec. 2.3 we consider supercells of length $N_a a$ along the z-direction, where $N_a \leq 16$ is the number of atoms in the supercell and a is the NN distance. The corresponding compatible wave vectors are given by $\vec{q} = 2\pi\nu/(N_a a) \cdot \hat{e}_z$ with $\nu \in \mathbb{Z}$.[1] In general, $N_a \leq 8$ is enough to get a good picture of the magnon dispersion relation. However, in some special cases (e.g., Fe) larger cells have been used in order to explore the behavior for small q in more detail. The width of the supercell along the x and y directions is $6a$, which ensures that the interaction between the wire images can be neglected. Analogously to the 1D case, for 2D lattices we consider supercells of length $N_a a$ and $N_a a/\sqrt{2}$ with $N_a = 2, 4, 8$ along the directions of a NN bond $\vec{a}$ and a second-NN bond $\vec{a}'$, respectively. The corresponding SDW

[1] Translational and inversion symmetries allow the restriction $0 \leq \nu \leq N_a/2$.

vectors are given by $\vec{q}_1 = 2\pi\nu/(N_a a) \cdot \hat{e}_{\vec{a}}$ and $\vec{q}_2 = 2\sqrt{2}\pi\nu/(N_a a) \cdot \hat{e}_{\vec{a}'}$. The widths of the supercells in the direction perpendicular to the monolayer plane are $6a$ and $3\sqrt{2}a$, respectively.

The spin-spiral structures are modeled by using a noncollinear spin-polarized formalism, as implemented in VASP by Hobbs *et al.*, where the fundamental variable is the spin-dependent density matrix (88). The direction and magnitude of the local magnetic moments are obtained by integrating the magnetization density within the corresponding Wigner-Seitz sphere. Moreover, in order to consider SDWs with a fixed wave vector $\vec{q}$, it is necessary to impose constraints on the magnetic moments at each atom. For this purpose, a penalty function, which forces the atomic moments to align along the given fixed direction, is added to the energy functional (89, 90). A detailed description of the penalty-functional method is given in the VASP manual.[1] Alternatively, a technique using Lagrange multipliers has also been proposed (91).

The integrations in the Brillouin zone are performed by using the Monkhorst-Pack scheme (92). The actual number of $\vec{k}$ points and the plane-wave cutoff energy $E_{\max}$ depend on the geometry and chemical element. For the linear-chain calculations in Sec. 2.3, a $\vec{k}$-mesh of $1 \times 1 \times 30$ points and $E_{\max} = 450$ eV are in general used. However, in some cases, more demanding values were necessary. For example, in Fe chains having relaxed bond length we used $E_{\max} = 500$ eV and a $\vec{k}$-mesh of $1 \times 1 \times \nu$ with ν at least $140/N_a$. The 2D calculations in Sec. 2.3 are performed with a $\vec{k}$-mesh of $15 \times 15 \times 1$ points and $E_{\max} = 450$ eV. It has been verified that a further increase of the number of $\vec{k}$ points and $E_{\max}$ would modify the resulting energies by less than 1 meV per atom. This value can be regarded as the numerical accuracy of our results, which is good enough for our conclusions (see Section 2.3). It should be noted, however, that for large spin-wave vectors $\vec{q}$ (in particular in the AF case) some calculations do not converge quite well if one considers materials such as Ni, which are intrinsically FM. In these specific cases the accuracy is estimated to be about 10 meV per atom.

[1] http://www.vasp.at/

Appendix B

Interatomic hopping integrals

The form of the single-particle electronic structure Hamiltonian $\hat{H}_0$ in Eq. (3.4) shows that the integrals $t_{jk}^{\alpha\beta}$ drive the electrons to hop from one atom j to another atom k. These hopping integrals $t_{jk}^{\alpha\beta}$ determine the period of the electron motion in the lattice. Therefore, they are of crucial importance for the electron dynamics. In the following, we discuss some properties of $t_{jk}^{\alpha\beta}$ and recall the two-center approximation for their determination.

B.1 Dependence of hopping integrals on the interatomic difference vector

Equation (3.5) shows that the parameters $t_{jk}^{\alpha\beta}$ are the matrix elements of electronic kinetic energy and lattice potential between different atoms ($j \neq k$). As a consequence, keeping the basis orbitals α fixed the hopping integrals in periodic lattices depend exclusively on the difference vector $\vec{R}_{jk} = \vec{R}_j - \vec{R}_k$ between the atoms j and k, both on its magnitude and on its orientation, i.e., $t_{jk}^{\alpha\beta} = t^{\alpha\beta}(\vec{R}_{jk})$.

Let us first consider the angle dependence. We would like to elaborate the consequences of the 2π-rotation symmetry on our model. For this purpose, suppose the total system is rotated by the angle φ around axis $\hat{\nu}$, which is denoted by the rotation operator $\hat{D} = \hat{D}(\hat{\nu}, \varphi)$. Notice that $\hat{D}$ is composed of two contributions: first, the rotation of atomic positions $\hat{D}_a$, described by a rotation matrix R, and second, the rotation of electron orbitals $\hat{D}_e$ around fixed atomic sites. Therefore, $\hat{D} = \hat{D}_a \hat{D}_e$. The rotation $\hat{D}_a$ implies that all atomic positions and interatomic difference vectors are

rotated according to $\vec{R}_j \to R\,\vec{R}_j$ and $\vec{R}_{jk} \to R\,\vec{R}_{jk}$, respectively. Now, we want to find out the relation between the hopping integrals for the rotated interatomic difference vectors $R\,\vec{R}_{jk}$ and the original ones for $\vec{R}_{jk}$, i.e., between $t^{\alpha\beta}(R\,\vec{R}_{jk})$ and $t^{\alpha\beta}(\vec{R}_{jk})$. To this aim, we recall that the electron-orbital part of the rotation $\hat{D}$ is given by

$$\hat{D}_e = \hat{D}_e(\hat{\nu}, \varphi) = e^{-\frac{i}{\hbar}\hat{L}_\nu \varphi} \;, \tag{B.1}$$

where $\hat{L}_\nu = \hat{\vec{L}} \cdot \hat{\nu}$ is the projection of orbital angular momentum $\vec{L}$ on the rotation axis. The operator $\hat{D}_e$ acts on atomic wave functions $\phi(\vec{r})$ as

$$\hat{D}_e \phi(R\,\vec{r}) = \phi(\vec{r}) \;. \tag{B.2}$$

For our purposes, it is sufficient to consider orbitals α, β, which are eigenstates of $\hat{L}_\nu$ having eigenvalues $m_\alpha\hbar$ and $m_\beta\hbar$. In this case, the relation between $t^{\alpha\beta}(R\,\vec{R}_{jk})$ and $t^{\alpha\beta}(\vec{R}_{jk})$ is quite simple. Using the definition for the hopping parameters in Eq. (3.5), one obtains

$$\begin{aligned}
t^{\alpha\beta}(R\,\vec{R}_{jk}) \;&=\; \int \mathrm{d}^3 r'\, \phi_\alpha^*\left(\vec{r'} - R\,\vec{R}_j\right) \left\{ -\frac{\hbar^2 \nabla_{r'}^2}{2m_e} + \underbrace{[\hat{D}_e v(\vec{r'})]}_{= v(R^{-1}\,\vec{r'})} \right\} \phi_\beta\left(\vec{r'} - R\,\vec{R}_k\right) \\
&=\; \int \mathrm{d}^3 r\, \phi_\alpha^*\left(R\,[\vec{r} - \vec{R}_j]\right) \left\{ -\frac{\hbar^2 \nabla_r^2}{2m_e} + v(\vec{r}) \right\} \underbrace{\phi_\beta\left(R\,[\vec{r} - \vec{R}_k]\right)}_{\hat{D}_e^{-1}\phi_\beta(\vec{r} - \vec{R}_k)} \\
&=\; e^{-i(m_\alpha - m_\beta)\varphi} \int \mathrm{d}^3 r\, \phi_\alpha^*\left(\vec{r} - \vec{R}_j\right) \left\{ -\frac{\hbar^2 \nabla_r^2}{2m_e} + v(\vec{r}) \right\} \phi_\beta\left(\vec{r} - \vec{R}_k\right) \\
&=\; e^{-i(m_\alpha - m_\beta)\varphi}\, t^{\alpha\beta}(\vec{R}_{jk}) \;.
\end{aligned} \tag{B.3}$$

The resulting relation

$$t^{\alpha\beta}(R\,\vec{R}_{jk}) \;=\; t^{\alpha\beta}(\vec{R}_{jk})\, e^{-i(m_\alpha - m_\beta)\varphi} \tag{B.4}$$

gives us the angle dependence of the hopping integrals. It is worth noticing that the 2π-rotation symmetry is satisfied only for integer steps $\Delta m = m_\alpha - m_\beta$. In other words, non-vanishing hopping integrals between model orbitals having on the one hand integer and on the other hand noninteger quantum numbers of $\hat{L}_\nu$ violate the rotational symmetry. In the context of the model simplifications discussed in Section 3.4, this means that it is not allowed to further reduce the degree of orbital degeneracy of the $3d$ electrons from $N_{d\text{-orbitals}} = 3$ to $N_{d\text{-orbitals}} = 2$, since in that case the model would

contain both $3d$ orbitals mathematically described by the noninteger quantum number $l = 1/2$ and $4p$ orbitals described by the integer quantum number $l = 0$.

Concerning the dependence of $t_{jk}^{\alpha\beta}$ on the distance $R_{jk} = |\vec{R}_{jk}|$, it has been shown that $t_{jk}^{\alpha\beta} \propto R_{jk}^{-5}$ represents a sound approximation, i.e., the hopping integrals vary as the inverse fifth power of the interatomic distance (93, 94). Since in the present thesis we do not consider atomic motion, we will not further discuss this distance dependence.

B.2 Two-center approximation

In this work, we apply the two-center approximation, in which for the purpose of determining $t_{jk}^{\alpha\beta}$ the lattice potential $v(\vec{r})$ is assumed to be symmetric around the interatomic connection axis $\hat{\zeta}$ between the lattice sites j and k (71).[1] In other words, in Eq. (3.5) we make the assumption

$$v(\vec{r}) \approx v_{jk}(\vec{r}) \ , \tag{B.5}$$

where the two-center potential $v_{jk}(\vec{r})$ is symmetric with respect to rotations around $\hat{\zeta}$.[2]

Let us now discuss several important properties resulting from the symmetry of $v_{jk}(\vec{r})$. First, the symmetry of $v_{jk}(\vec{r})$ with respect to rotations around $\hat{\zeta}$ implies conservation of $\vec{L}$ along $\vec{R}_{jk}$, i.e., conservation of m_ζ. Choosing basis states α as spherical harmonics with definite orbital angular-momentum quantum number l and definite projection m_ζ, this conservation law reads

$$t_{jk}^{nlm_\zeta\,;\,n'l'm'_\zeta} = 0 \quad \text{unless } m_\zeta = m'_\zeta \ . \tag{B.6}$$

A second symmetry to take into account is the mirror symmetry with respect to planes including $\vec{R}_{jk}$: The two-center potential $v_{jk}(\vec{r})$ created by the two atoms at $\vec{R}_j$ and $\vec{R}_k$

[1] The connection axis $\hat{\zeta}$ is given by the unit vector in the direction of $\vec{R}_{jk}$, i.e., $\vec{R}_{jk} = R_{jk}\,\hat{\zeta}$.

[2] The two-center approximation (B.5) can be motivated by considering Eq. (3.5) for $t_{jk}^{\alpha\beta}$. The largest contributions to these matrix elements originate from small spheres around the lattice sites j and k. There, the potential $v(\vec{r})$ is dominated by the local potentials $v_j(r)$ and $v_k(r)$ generated by the two ions j and k, respectively. These potentials $v_j(r)$ and $v_k(r)$ are by themselves symmetric with respect to rotations around the corresponding atomic nuclei. Other ions in the lattice give a contribution to $v(\vec{r})$, which in first approximation is symmetric within the relevant spheres and thus does not affect the symmetry of the potential significantly. Consequently, $v(\vec{r})$ can be assumed to be symmetric around the interatomic connection axis.

is conserved under such a mirror operation $\hat{M}$. Consequently, the operator equality $\hat{M}^\dagger v_{jk}(\vec{r})\hat{M} = v_{jk}(\vec{r})$ holds. The mirror operator acts as

$$\hat{M}\phi_{n,l,m_\zeta}(\vec{r}-\vec{R}_j) \;=\; \phi_{n,l,-m_\zeta}(\vec{r}-\vec{R}_j) \;, \tag{B.7}$$

where $\phi_{n,l,m_\zeta}(\vec{r}-\vec{R}_j)$ is a single-electron state at atom j having radial quantum number n as well as angular-momentum quantum numbers l and m_ζ. Therefore, one obtains

$$\begin{aligned} t_{jk}^{n,l,-m_\zeta\,;\,n',l',-m_\zeta} &= \int \mathrm{d}^3 r\, \phi^*_{n,l,-m_\zeta}(\vec{r}-\vec{R}_j) \left(-\frac{\hbar^2\nabla^2}{2m_e} + v_{jk}(\vec{r})\right) \phi_{n',l',-m_\zeta}(\vec{r}-\vec{R}_k) \\ &= \int \mathrm{d}^3 r\, \phi^*_{nlm_\zeta}(\vec{r}-\vec{R}_j)\, \hat{M}^\dagger \left(-\frac{\hbar^2\nabla^2}{2m_e} + v_{jk}(\vec{r})\right) \hat{M}\, \phi_{n'l'm_\zeta}(\vec{r}-\vec{R}_k) \\ &= \int \mathrm{d}^3 r\, \phi^*_{nlm_\zeta}(\vec{r}-\vec{R}_j) \left(-\frac{\hbar^2\nabla^2}{2m_e} + v_{jk}(\vec{r})\right) \phi_{n'l'm_\zeta}(\vec{r}-\vec{R}_k) \\ &= t_{jk}^{nlm_\zeta\,;\,n'l'm_\zeta} \;. \end{aligned} \tag{B.8}$$

The combination of Eqs. (B.6) and (B.8) implies, first, that the hopping integrals $t_{jk}^{nlm_\zeta\,;\,n'l'm'_\zeta}$ between two atoms j and k are diagonal in the angular-momentum projection m_ζ along the interatomic connection axis, and, second, that they depend on the absolute value $|m_\zeta|$ and not on its sign. Let us finally mention that for homogeneous systems, i.e., for homonuclear bonds jk, the potential $v_{jk}(\vec{r})$ is symmetric with respect to inversion $\hat{I}_{jk}$ around the center between $\vec{R}_j$ and $\vec{R}_k$. This means $\hat{I}^\dagger_{jk} v_{jk}(\vec{r})\hat{I}_{jk} = v_{jk}(\vec{r})$. Since the inversion operator acts as

$$\hat{I}_{jk}\phi_{nlm_\zeta}(\vec{r}-\vec{R}_j) \;=\; (-1)^l \phi_{nlm_\zeta}(\vec{r}-\vec{R}_k) \;, \tag{B.9}$$

one obtains the relation

$$\begin{aligned} t_{jk}^{nlm_\zeta\,;\,n'l'm_\zeta} &= \int \mathrm{d}^3 r\, \phi^*_{nlm_\zeta}(\vec{r}-\vec{R}_j) \underbrace{\left(-\frac{\hbar^2\nabla^2}{2m_e} + v_{jk}(\vec{r})\right)}_{\hat{I}^\dagger_{jk}\left(-\frac{\hbar^2\nabla^2}{2m_e}+v_{jk}(\vec{r})\right)\hat{I}_{jk}} \phi_{n'l'm_\zeta}(\vec{r}-\vec{R}_k) \\ &= (-1)^{l+l'} \int \mathrm{d}^3 r\, \phi^*_{nlm_\zeta}(\vec{r}-\vec{R}_k) \left(-\frac{\hbar^2\nabla^2}{2m_e} + v_{jk}(\vec{r})\right) \phi_{n'l'm_\zeta}(\vec{r}-\vec{R}_j) \\ &= (-1)^{l+l'}\, t_{kj}^{nlm_\zeta\,;\,n'l'm_\zeta} \\ &= (-1)^{l+l'}\, t_{jk}^{n'l'm_\zeta\,;\,nlm_\zeta} \;. \end{aligned} \tag{B.10}$$

Slater-Koster integral $(l, l'; m_\zeta)$	**Matrix element** $t_{jk}^{nlm_\zeta\,;\,n'l'm_\zeta}$
$(s, s; \sigma)$	$t_{jk}^{4s0\,;\,4s0}$
$(s, p; \sigma)$	$t_{jk}^{4s0\,;\,4p0}$
$(s, d; \sigma)$	$t_{jk}^{4s0\,;\,3d0}$
$(p, p; \sigma)$	$t_{jk}^{4p0\,;\,4p0}$
$(p, p; \pi)$	$t_{jk}^{4p1\,;\,4p1}$
$(p, d; \sigma)$	$t_{jk}^{4p0\,;\,3d0}$
$(p, d; \pi)$	$t_{jk}^{4p1\,;\,3d1}$
$(d, d; \sigma)$	$t_{jk}^{3d0\,;\,3d0}$
$(d, d; \pi)$	$t_{jk}^{3d1\,;\,3d1}$
$(d, d; \delta)$	$t_{jk}^{3d2\,;\,3d2}$

Table B.1: Two-center integrals - Minimum set of Slater-Koster integrals of the two-center approximation for the description of electron hoppings within the $3d$, $4s$ and $4p$ valence bands. The greek letters σ, π and δ stand for the angular-momentum projection along the interatomic connection axis $m_\zeta = 0$, 1 and 2, respectively.

In the last step we have used that the matrix element $t_{kj}^{nlm_\zeta\,;\,n'l'm_\zeta}$ is real if the involved orbitals (spherical harmonics) have the same orbital angular-momentum projection m_ζ on the interatomic connection axis. One concludes that for homogeneous bonds interchanging the order of orbital indices nl and $n'l'$ has no effect on $t_{jk}^{nlm_\zeta\,;\,n'l'm_\zeta}$ if the sum of the parities $l + l'$ of the two orbitals is even, but changes the sign if the sum of the parities is odd.

B.3 Slater-Koster integrals

It has been shown above that within the two-center approximation, the hopping integrals $t_{jk}^{nlm_\zeta\,;\,n'l'm'_\zeta}$ between two atoms j and k are diagonal in the angular-momentum projection m_ζ along the interatomic connection axis $\hat{\zeta}$ and do not depend on the sign of m_ζ [see Eqs. (B.6) and (B.8)]. These relations demonstrate that —for the purpose of determining $t_{jk}^{\alpha\beta}$ with respect to arbitrary sets of basis atomic orbitals α, β— it is possible te reduce the number of independent integrals to the set of matrix elements

$$\Big\{(l, l'; m_\zeta) \;=\; t^{nl|m_\zeta|\,;\,n'l'|m_\zeta|}(R_{jk})\Big\}\;, \tag{B.11}$$

which are evaluated for orbitals having definite quantum number l as well as definite projection m_ζ of $\vec{L}$ on the interatomic connection axis.[1] For example, if one considers the $3d$, $4s$ and $4p$ valence bands in transition metals, then there are only 10 independent integrals (see Table B.1), from which all other hopping elements $t_{jk}^{\alpha\beta}$ can be derived.

The integrals $(l, l'; m_\zeta)$ are called Slater-Koster or two-center integrals. Notice that they do not depend on the orientation of $\vec{R}_{jk}$.[2] However, $(l, l'; m_\zeta)$ is a function of the radial part of the involved orbitals and, of course, of the distance R_{jk} between the neighboring atoms. The explicit relations between $t_{jk}^{nlm,n'l'm'}$, where $\hat{z}$ is chosen as the m-quantization axis, and the Slater-Koster integrals are obtained by reformulating the relations given in Ref. (71). The results are summarized in Table B.2. There, the indices λ_x, λ_y and λ_z on the right-hand side denote the direction cosines of the connection vector $\vec{R}_{jk} = \vec{R}_j - \vec{R}_k$, i.e.,

$$\lambda_x = \frac{\vec{R}_{jk} \cdot \hat{x}}{R_{jk}} , \quad \lambda_y = \frac{\vec{R}_{jk} \cdot \hat{y}}{R_{jk}} , \text{ and } \quad \lambda_z = \frac{\vec{R}_{jk} \cdot \hat{z}}{R_{jk}} . \tag{B.12}$$

Notice that the expressions for $t_{jk}^{nlm,n'l'm'}$ in Table B.2, derived by using the two-center approximation, correctly satisfy the angle dependence given in Eq. (B.4).

---

[1] It is to be realized that for homonuclear bonds the fundamental integrals $(l, l'; m_\zeta)$ and $(l', l; m_\zeta)$ are directly related to each other. According to Eq. (B.10), $(l, l'; m_\zeta) = (-1)^{l+l'}(l', l; m_\zeta)$.

[2] This can be seen as follows: A rotation $\hat{D}$ of the interatomic connection axis $\hat{\zeta} \to R\hat{\zeta}$, where R is the rotation matrix, acts as $\hat{D}\phi_{nlm_\zeta}(R\vec{r} - R\vec{R}_j) = \phi_{nlm_\zeta}(\vec{r} - \vec{R}_j)$. Let us notice that the rotated orbital $\hat{D}\phi_{nlm_\zeta}$ is the basis orbital $\phi_{nlm_{R\zeta}}$ with respect to the rotated quantization axis $R\hat{\zeta}$. Then, one obtains

$$\begin{aligned}
t^{nlm_{R\zeta}\,;\,n'l'm_{R\zeta}}(R\,\vec{R}_{jk}) &= \int \mathrm{d}^3r'\,\phi^*_{nlm_{R\zeta}}\left(\vec{r'} - R\,\vec{R}_j\right)\left\{-\frac{\hbar^2\nabla^2_{r'}}{2m_e} + \underbrace{[\hat{D}v(\vec{r'})]}_{=\,v(R^{-1}\,\vec{r'})}\right\}\phi_{n'l'm_{R\zeta}}\left(\vec{r'} - R\,\vec{R}_k\right) \\
&= \int \mathrm{d}^3r\,\phi^*_{nlm_{R\zeta}}\left(R\,[\vec{r} - \vec{R}_j]\right)\left\{-\frac{\hbar^2\nabla^2_{r}}{2m_e} + v(\vec{r})\right\}\underbrace{\phi_{n'l'm_{R\zeta}}\left(R\,[\vec{r} - \vec{R}_k]\right)}_{\phi_{n'l'm_\zeta}(\vec{r} - \vec{R}_k)} \\
&= \int \mathrm{d}^3r\,\phi^*_{nlm_\zeta}\left(\vec{r} - \vec{R}_j\right)\left\{-\frac{\hbar^2\nabla^2_{r}}{2m_e} + v(\vec{r})\right\}\phi_{n'l'm_\zeta}\left(\vec{r} - \vec{R}_k\right) \\
&= t^{nlm_\zeta\,;\,n'l'm_\zeta}(\vec{R}_{jk}) \ .
\end{aligned}$$

This demonstrates that the Slater-Koster integrals $(l, l'; m_\zeta)$ are independent of the orientation of the interatomic connection vector $\vec{R}_{jk}$.

Hopping	Expression in terms of Slater-Koster two-center integrals
$t_{jk}^{4s0,4s0}$	$(s,s;\sigma)$
$t_{jk}^{4s0,4p0}$	$\lambda_z\,(s,p;\sigma)$
$t_{jk}^{4s0,4p\pm1}$	$\mp\frac{1}{\sqrt{2}}(\lambda_x \pm i\lambda_y)\,(s,p;\sigma)$
$t_{jk}^{4s0,3d0}$	$\frac{1}{2}(3\lambda_z^2-1)\,(s,d;\sigma)$
$t_{jk}^{4s0,3d\pm1}$	$\mp\sqrt{\frac{3}{2}}\,\lambda_z\,(\lambda_x \pm i\lambda_y)\,(s,d;\sigma)$
$t_{jk}^{4s0,3d\pm2}$	$\frac{1}{2}\sqrt{\frac{3}{2}}\,(\lambda_x \pm i\lambda_y)^2\,(s,d;\sigma)$
$t_{jk}^{4p0,4p0}$	$\lambda_z^2\,(p,p;\sigma)\,+\,(1-\lambda_z^2)\,(p,p;\pi)$
$t_{jk}^{4p0,4p\pm1}$	$\mp\frac{\lambda_z}{\sqrt{2}}(\lambda_x \pm i\lambda_y)\,[(p,p;\sigma)-(p,p;\pi)]$
$t_{jk}^{4p\pm1,4p\pm1}$	$\frac{1}{2}\,[(1-\lambda_z^2)\,(p,p;\sigma)\,+\,(1+\lambda_z^2)\,(p,p;\pi)]$
$t_{jk}^{4p+1,4p-1}$	$-\frac{1}{2}(\lambda_x - i\lambda_y)^2\,[(p,p;\sigma)\,-\,(p,p;\pi)]$
$t_{jk}^{4p0,3d0}$	$\frac{\lambda_z}{2}\,[(3\lambda_z^2-1)\,(p,d;\sigma)\,+\,2\sqrt{3}\,(1-\lambda_z^2)\,(p,d;\pi)]$
$t_{jk}^{4p0,3d\pm1}$	$\mp\frac{1}{\sqrt{2}}(\lambda_x \pm i\lambda_y)\,[\sqrt{3}\,\lambda_z^2\,(p,d;\sigma)\,+\,(1-2\lambda_z^2)\,(p,d;\pi)]$
$t_{jk}^{4p0,3d\pm2}$	$\frac{\lambda_z}{2\sqrt{2}}(\lambda_x \pm i\lambda_y)^2\,[\sqrt{3}\,(p,d;\sigma)\,-\,2\,(p,d;\pi)]$
$t_{jk}^{4p\pm1,3d0}$	$\mp\frac{1}{2\sqrt{2}}(\lambda_x \mp i\lambda_y)\,[(3\lambda_z^2-1)\,(p,d;\sigma)\,-\,2\sqrt{3}\,\lambda_z^2\,(p,d;\pi)]$
$t_{jk}^{4p\pm1,3d\pm1}$	$\frac{\lambda_z}{2}\,[\sqrt{3}\,(1-\lambda_z^2)\,(p,d;\sigma)\,+\,2\lambda_z^2\,(p,d;\pi)]$
$t_{jk}^{4p\pm1,3d\pm2}$	$\mp\frac{1}{4}(\lambda_x \pm i\lambda_y)\,[\sqrt{3}\,(1-\lambda_z^2)\,(p,d;\sigma)\,+\,2(1+\lambda_z^2)\,(p,d;\pi)]$
$t_{jk}^{4p\pm1,3d\mp1}$	$-\frac{\lambda_z}{2}(\lambda_x \mp i\lambda_y)^2\,[\sqrt{3}\,(p,d;\sigma)\,-\,2\,(p,d;\pi)]$
$t_{jk}^{4p\pm1,3d\mp2}$	$\mp\frac{1}{4}(\lambda_x \mp i\lambda_y)^3\,[\sqrt{3}\,(p,d;\sigma)\,-\,2\,(p,d;\pi)]$
$t_{jk}^{3d0,3d0}$	$\frac{1}{4}(3\lambda_z^2-1)^2\,(d,d;\sigma)\,+\,3\lambda_z^2(1-\lambda_z^2)\,(d,d;\pi)\,+\,\frac{3}{4}(1-\lambda_z^2)^2\,(d,d;\delta)$
$t_{jk}^{3d0,3d\pm1}$	$\mp\frac{\lambda_z}{2}\sqrt{\frac{3}{2}}\,(\lambda_x \pm i\lambda_y)\,[(3\lambda_z^2-1)\,(d,d;\sigma)\,+\,2(1-2\lambda_z^2)\,(d,d;\pi)\,-\,(1-\lambda_z^2)\,(d,d;\delta)]$
$t_{jk}^{3d0,3d\pm2}$	$\frac{1}{4}\sqrt{\frac{3}{2}}\,(\lambda_x \pm i\lambda_y)^2\,[(3\lambda_z^2-1)\,(d,d;\sigma)\,-\,4\lambda_z^2\,(d,d;\pi)\,+\,(1+\lambda_z^2)\,(d,d;\delta)]$
$t_{jk}^{3d\pm1,3d\pm1}$	$\frac{3}{2}\lambda_z^2(1-\lambda_z^2)\,(d,d;\sigma)\,+\,\frac{1}{2}(4\lambda_z^4-3\lambda_z^2+1)\,(d,d;\pi)\,+\,\frac{1}{2}(1-\lambda_z^4)\,(d,d;\delta)$
$t_{jk}^{3d\pm1,3d\pm2}$	$\mp\frac{\lambda_z}{4}(\lambda_x \pm i\lambda_y)\,[3(1-\lambda_z^2)\,(d,d;\sigma)\,+\,4\lambda_z^2\,(d,d;\pi)\,-\,(3+\lambda_z^2)\,(d,d;\delta)]$
$t_{jk}^{3d+1,3d-1}$	$-\frac{1}{2}(\lambda_x - i\lambda_y)^2\,[3\lambda_z^2\,(d,d;\sigma)\,+\,(1-4\lambda_z^2)\,(d,d;\pi)\,+\,(\lambda_z^2-1)\,(d,d;\delta)]$
$t_{jk}^{3d\pm1,3d\mp2}$	$\mp\frac{\lambda_z}{4}(\lambda_x \mp i\lambda_y)^3\,[3\,(d,d;\sigma)\,-\,4\,(d,d;\pi)\,+\,(d,d;\delta)]$
$t_{jk}^{3d\pm2,3d\pm2}$	$\frac{3}{8}(1-\lambda_z^2)^2\,(d,d;\sigma)\,+\,\frac{1}{2}(1-\lambda_z^4)\,(d,d;\pi)\,+\,\frac{1}{8}(\lambda_z^4+6\lambda_z^2+1)\,(d,d;\delta)$
$t_{jk}^{3d+2,3d-2}$	$\frac{1}{8}(\lambda_x - i\lambda_y)^4\,[3\,(d,d;\sigma)\,-\,4\,(d,d;\pi)\,+\,(d,d;\delta)]$

Table B.2: Hopping integrals in terms of two-center integrals - Interatomic hoppings $t_{jk}^{nlm,n'l'm'}$ within the $3d$, $4s$ and $4p$ valence bands are derived by using the two-center approximation. The Slater-Koster integrals $(l,l';m_\zeta)$ and their definitions are listed in Table B.1 The indices λ_x, λ_y and λ_z denote the direction cosines of the connection vector $\vec{R}_{jk}$. Notice that the entries not given in the table can be obtained by applying the relation $t^{\alpha\beta}(\vec{R}_{jk}) = [t^{\beta\alpha}(-\vec{R}_{jk})]^*$.

Appendix C

Electron-electron interaction model

The electron-electron interaction Hamiltonian $\hat{H}_C$ has been introduced in Section 3.2.2. There, we have used physical intuition in order to motivate its explicit form given by Eq. (3.6). Now, in the present Appendix, we would like to present a mathematical derivation for $\hat{H}_C$.

The starting point is the general expression of a two-particle operator

$$\hat{H}_C = \frac{1}{2} \sum_j \sum_{\alpha\beta\gamma\delta \in 3d} \sum_{\sigma\sigma'} U_{\alpha\beta\gamma\delta}\, \hat{c}^\dagger_{j\alpha\sigma} \hat{c}^\dagger_{j\beta\sigma'} \hat{c}_{j\delta\sigma'} \hat{c}_{j\gamma\sigma} \ . \tag{C.1}$$

Here, we already apply the intra-atomic approximation ($\hat{H}_C$ splits in a sum over all the atoms j in the lattice) and consider only the dominant Coulomb repulsion of the most localized $3d$ electrons ($\alpha\beta\gamma\delta \in 3d$). In Section 3.2.2 we have given reasons for these two simplifications. $\hat{H}_C$ is written in terms of Coulomb integrals

$$U_{\alpha\beta\gamma\delta} \ = \ \int \mathrm{d}^3 r \int \mathrm{d}^3 r' \, \phi^*_\alpha(\vec{r}) \phi^*_\beta(\vec{r'}) \, w(|\vec{r} - \vec{r'}|) \, \phi_\gamma(\vec{r}) \phi_\delta(\vec{r'}) \ , \tag{C.2}$$

where $w(r) = e^2/(4\pi\varepsilon_0 r)$ denotes the Coulomb repulsion energy of two electrons of distance r. In the following, the Coulomb interaction Hamiltonian is simplified into a more demonstrative and compact form, so that it contains only the most essential contributions in the context of ferromagnetism. To this aim, let us focus only on direct terms ($\alpha = \gamma$, $\beta = \delta$) and on exchange terms ($\alpha = \delta$, $\beta = \gamma$) of the $3d$ electrons, i.e., only on $U_{\alpha\beta} = U_{\alpha\beta\alpha\beta}$ and on $J_{\alpha\beta} = U_{\alpha\beta\beta\alpha}$ ($\alpha \neq \beta$) for $\alpha, \beta \in 3d$. In this way, the

total orbital angular momentum $\vec{L}$ of the two involved electrons is conserved in each interaction process.[1] As we shall see in Chapter 4, these terms already yield the most important magnetic properties and, in particular, ferromagnetic ground states in some parameter regimes. After a straightforward calculation, the interaction Hamiltonian $\hat{H}_C$ takes the form

$$\begin{aligned}\hat{H}_C &= \frac{1}{2}\sum_j \sum_{\alpha\beta\in 3d} \sum_{\sigma\sigma'} \left[U_{\alpha\beta}\, \hat{c}^\dagger_{j\alpha\sigma}\hat{c}^\dagger_{j\beta\sigma'}\hat{c}_{j\beta\sigma'}\hat{c}_{j\alpha\sigma} \,+\, J_{\alpha\beta}(1-\delta_{\alpha\beta})\, \hat{c}^\dagger_{j\alpha\sigma}\hat{c}^\dagger_{j\beta\sigma'}\hat{c}_{j\alpha\sigma'}\hat{c}_{j\beta\sigma} \right] \\ &= \frac{1}{4}\sum_j \sum_{\alpha\beta\in 3d} \left[2U_{\alpha\beta}\, \hat{n}_{j\alpha}\,(\hat{n}_{j\beta}-\delta_{\alpha\beta}) \,-\, J_{\alpha\beta}(1-\delta_{\alpha\beta}) \left\{ \hat{n}_{j\alpha}\hat{n}_{j\beta} + 4\hat{\vec{S}}_{j\alpha}\cdot\hat{\vec{S}}_{j\beta} \right\} \right] \,,\end{aligned} \tag{C.3}$$

where $\hat{n}_{j\alpha} = \sum_\sigma \hat{n}_{j\alpha\sigma}$, and $\vec{S}_{j\alpha}$ denotes the spin in a single orbital α at atom j.

In the next step we consider the dependence of the integrals $U_{\alpha\beta}$ and $J_{\alpha\beta}$ on the orbitals α and β. It is known to be important for a quantitative description of the orbital polarization of the electronic density. However, this dependence is not essential for describing the total spin polarization within the $3d$ band. Therefore, we neglect the orbital dependence of $U_{\alpha\beta}$ and $J_{\alpha\beta}$, i.e., we set for all α and β

$$\begin{aligned} U_{\alpha\beta} &= \tilde{U} \,, \text{ and} \\ J_{\alpha\beta} &= J \;(\alpha \neq \beta) \,. \end{aligned} \tag{C.4}$$

This yields

$$\hat{H}_C \,=\, \frac{1}{2}\sum_j \left\{ \left(\tilde{U} - \frac{J}{2}\right) \hat{n}_{jd}\hat{n}_{jd} \,-\, \left(\tilde{U} - J\right) \hat{n}_{jd} \,-\, 2J\hat{\vec{S}}_{jd}\cdot\hat{\vec{S}}_{jd} \,+\, \frac{4}{3}J \sum_{\alpha\in 3d} \hat{\vec{S}}_{j\alpha}\cdot\hat{\vec{S}}_{j\alpha} \right\} \,. \tag{C.5}$$

Here, $\hat{n}_{jd} = \sum_{\alpha\in 3d,\sigma} \hat{n}_{j\alpha\sigma}$ denotes the number of interacting $3d$ electrons at atom j. Moreover, we have introduced the total $3d$-electron spin at atom j, $\vec{S}_{jd}$. It is worth discussing the last two terms in the above equation, which are proportional to $\vec{S}_{jd}\cdot\vec{S}_{jd}$ and $\vec{S}_{j\alpha}\cdot\vec{S}_{j\alpha}$, respectively. Both do not affect the spin polarization as they commute with the total spin $\vec{S}$. The first of them favors parallel spin alignment of

[1] The orbital angular-momentum conservation law implies that $U_{\alpha\beta\gamma\delta} = 0$ unless

$$\langle\, \alpha\,|\hat{\vec{L}}|\,\alpha\,\rangle + \langle\, \beta\,|\hat{\vec{L}}|\,\beta\,\rangle \,=\, \langle\, \gamma\,|\hat{\vec{L}}|\,\gamma\,\rangle + \langle\, \delta\,|\hat{\vec{L}}|\,\delta\,\rangle \,,$$

where the basis orbitals $|\,\alpha\,\rangle$, $|\,\beta\,\rangle$, $|\,\gamma\,\rangle$ and $|\,\delta\,\rangle$ are localized at atomic sites. The considered direct and exchange terms $U_{\alpha\beta\alpha\beta}$ and $U_{\alpha\beta\beta\alpha}$ satisfy this conservation law.

all $3d$ electrons in an atom. Therefore, it leads to the creation of atomic magnetic moments and determines their stability. In contrast, the latter term tends to favor a low-spin configuration at each single orbital (empty or doubly occupied orbitals).[1] Consequently, it reduces the stability of ferromagnetism. By comparing these two spin terms, $-J\hat{\vec{S}}_{jd}\cdot\hat{\vec{S}}_{jd}$ and $+\frac{2}{3}J\hat{\vec{S}}_{j\alpha}\cdot\hat{\vec{S}}_{j\alpha}$, one finds that the former tendency toward ferromagnetism is stronger than the latter tendency toward nonmagnetic states. For this reason, we do not explicitly take into account the latter term. Its effect can possibly be incorporated in a reduced exchange-interaction parameter J. Then, defining the effective Coulomb parameter

$$U = \tilde{U} - \frac{J}{2} \ , \tag{C.6}$$

the operator $\hat{H}_C$ can be simplified into the transparent and simple form

$$\hat{H}_C = \frac{1}{2}\sum_j \left(U\hat{n}_{jd}\hat{n}_{jd} - 2J\hat{\vec{S}}_{jd}\cdot\hat{\vec{S}}_{jd}\right) - \frac{1}{2}\sum_j \left(U - \frac{1}{2}J\right)\hat{n}_{jd} \ . \tag{C.7}$$

The first term in this equation, $\frac{1}{2}U\hat{n}_{jd}\hat{n}_{jd}$, represents the classical Coulomb repulsion of electrons at the same atomic site. In some cases, it is useful to substract the Coulomb energy of a uniform $3d$-electron density ϑ from it. Then, Eq. (C.7) can be rewritten as

$$\begin{aligned}\hat{H}_C = & \frac{1}{2}\sum_j \left[U\left(\hat{n}_{jd}-\vartheta\right)^2 - 2J\hat{\vec{S}}_{jd}\cdot\hat{\vec{S}}_{jd}\right] \\ & + \frac{1}{2}\sum_j \left[U(2\vartheta-1)+\frac{1}{2}J\right]\hat{n}_{jd} - \frac{1}{2}\sum_j U\vartheta^2 \ .\end{aligned} \tag{C.8}$$

Notice that the second sum in this equation is an unimportant double-counting correction and gives an additional constant in the single-particle energies ε_α^0. Therefore, this interaction-energy contribution can be incorporated by means of an effective $3d$-electron level

$$\varepsilon_d^{\text{eff}} = \varepsilon_d^0 + \frac{1}{2}\sum_j \left[U\left(2\vartheta-1\right)+\frac{1}{2}J\right] \ . \tag{C.9}$$

In other words, $\varepsilon_d^{\text{eff}}$ includes the Coulomb repulsion energy of ϑ d electrons per atom. Then, the effective electron-electron interaction Hamiltonian reads

$$\hat{H}_C = \frac{1}{2}\sum_j \left[U\left(\hat{n}_{jd}-\vartheta\right)^2 - 2J\hat{\vec{S}}_{jd}\cdot\hat{\vec{S}}_{jd}\right] \ . \tag{C.10}$$

[1]The operator $\hat{\vec{S}}_{j\alpha}\cdot\hat{\vec{S}}_{j\alpha}$ yields zero when the orbital α is empty or doubly occupied and 3/4 otherwise.

Importantly, the model Hamiltonian $\hat{H}_C$ preserves the spin-rotational symmetry of the electron-electron interaction. The above formulations for $\hat{H}_C$ and the effective $3d$-electron level $\varepsilon_d^{\text{eff}}$ are used in the present thesis. They coincide with Eqs. (3.6) and (3.7) in Section 3.2.2.

Appendix D

Dipole matrix elements within the intra-atomic approximation

The purpose of the present Appendix is to derive explicit relations between the intra-atomic dipole matrix elements $\langle\, nlm\,|\hat{\vec{r}}|\,n'l'm'\,\rangle$, in terms of which the interaction between the electron subsystem and the laser pulse is described (see Section 3.2.3). To this aim, we exploit the Wigner-Eckart theorem (73).

D.1 Wigner-Eckart theorem

The calculation of matrix elements of the cartesian operator $\hat{\vec{r}}$ can be traced back to matrix elements of the irreducible spherical tensor operator $\hat{T}^{(k)}_q$ of rank $k = 1$, which is obtained from $\hat{\vec{r}}$ as

$$\begin{aligned} \hat{T}^{(1)}_{+1} &= -\frac{1}{\sqrt{2}}(\hat{x} + i\hat{y}) \;, \\ \hat{T}^{(1)}_{-1} &= \frac{1}{\sqrt{2}}(\hat{x} - i\hat{y}) \;, \\ \hat{T}^{(1)}_{0} &= \hat{z} \;. \end{aligned} \tag{D.1}$$

The matrix elements of $\hat{T}^{(1)}_q$ between eigenstates $|\,nlm\,\rangle$ of the orbital angular momentum $\hat{\vec{L}}^2$ and $\hat{L}_z$ having eigenvalues $\hbar^2\, l(l+1)$ and $\hbar m$ take a particularly simple form. Actually, the Wigner-Eckart theorem relates the various matrix elements $\langle\, nlm\,|\hat{T}^{(k)}_q|\,n'l'm'\,\rangle$ of such tensor operators, and states that

$$\langle\, nlm\,|\hat{T}^{(k)}_q|\,n'l'm'\,\rangle \;=\; \langle\, l'k; m'q\,|\,lm\,\rangle\, \frac{\langle\, nl\,||\hat{T}^{(k)}||\,n'l'\,\rangle}{\sqrt{2l'+1}} \;. \tag{D.2}$$

Here, $\langle\, nl \,||\hat{T}^{(k)}||\, n'l' \,\rangle$ is the so-called reduced matrix element, and the scalar products $\langle\, l'k; m'q \,|\, lm \,\rangle$ are the Clebsch-Gordan coefficients. The latter are related to the addition of two angular momenta $\vec{L}_1$ and $\vec{L}_2$ having given quantum numbers l_1 and l_2. The Clebsch-Gordan coefficients are defined by the representation

$$|\, l_1 l_2; lm \,\rangle \;=\; \sum_{m_1 m_2} |\, l_1 l_2; m_1 m_2 \,\rangle \langle\, l_1 l_2; m_1 m_2 \,|\, lm \,\rangle \tag{D.3}$$

of the state $|\, lm \,\rangle \;=\; |\, l_1 l_2; lm \,\rangle$, in which the sum $\vec{L} \;=\; \vec{L}_1 \oplus \vec{L}_2$ of the two angular momenta $\vec{L}_1$ and $\vec{L}_2$ has definite quantum numbers l and m. Therefore, the state $|\, lm \,\rangle$ satisfies

$$\begin{aligned} \hat{\vec{L}}^2 \,|\, lm \,\rangle \;&=\; l(l+1)\,\hbar^2 \,|\, lm \,\rangle \;\; \text{and} \\ \hat{L}_z \,|\, lm \,\rangle \;&=\; m\hbar \,|\, lm \,\rangle \;. \end{aligned} \tag{D.4}$$

In contrast, in the states $|\, l_1 l_2; m_1 m_2 \,\rangle \;=\; |\, l_1 m_1 \,\rangle |\, l_2 m_2 \,\rangle$ the two angular momenta $\vec{L}_1$ and $\vec{L}_2$ separately have definite z projections m_1 and m_2, i.e.,

$$\begin{aligned} \hat{\vec{L}}_j^2 \,|\, l_1 l_2; m_1 m_2 \,\rangle \;&=\; l_j(l_j+1)\,\hbar^2 \,|\, l_1 l_2; m_1 m_2 \,\rangle \;\; \text{and} \\ \hat{L}_{jz} \,|\, l_1 l_2; m_1 m_2 \,\rangle \;&=\; m_j \hbar \,|\, l_1 l_2; m_1 m_2 \,\rangle \end{aligned} \tag{D.5}$$

for $j = 1, 2$. The definition (D.3) means that the coefficient $\langle\, l_1 l_2; m_1 m_2 \,|\, lm \,\rangle$ represents the projection of the state $|\, lm \,\rangle$ on the state $|\, l_1 l_2; m_1 m_2 \,\rangle$. Of course, these Clebsch-Gordan coefficients satisfy

$$\langle\, l_1 l_2; m_1 m_2 \,|\, lm \,\rangle = 0 \;, \;\; \text{if } m \neq m_1 + m_2 \;. \tag{D.6}$$

Let us now notice two further properties of them. First, they satisfy the recursion relation

$$\begin{aligned} \langle\, l_1 l_2; m_1 m_2 \,|\hat{L}_\pm|\, lm \,\rangle &= \sqrt{(l \mp m)(l \pm m + 1)}\;\hbar \;\langle\, l_1 l_2; m_1 m_2 \,|\, l, m \pm 1 \,\rangle \\ &= \sqrt{(l_1 \pm m_1)(l_1 \mp m_1 + 1)}\;\hbar \;\langle\, l_1 l_2; m_1 \mp 1, m_2 \,|\, lm \,\rangle \\ &+ \sqrt{(l_2 \pm m_2)(l_2 \mp m_2 + 1)}\;\hbar \;\langle\, l_1 l_2; m_1, m_2 \mp 1 \,|\, lm \,\rangle \end{aligned} \tag{D.7}$$

and, second, the normalization condition reads

$$\sum_{m_1 m_2} |\langle\, l_1 l_2; m_1 m_2 \,|\, lm \,\rangle|^2 = 1 \;. \tag{D.8}$$

These two properties can be used for the determination of the Clebsch-Gordan coefficients. The resulting coefficients are given in many books on quantum mechanics, for instance in Ref. (73).

The above considerations imply that the coefficient $\langle\, l'k; m'q \,|\, lm \,\rangle$ in Eq. (D.2) can be interpreted as a projection coefficient resulting from the addition of the two angular momenta $\vec{L}'$ and $\vec{k}$ to $\vec{L}$ ($\vec{L}' \oplus \vec{k} = \vec{L}$). In particular, Eq. (D.6) yields the m-selection rule

$$\langle\, nlm \,|\hat{T}^{(k)}_q|\, n'l'm' \,\rangle = 0 \quad \text{unless } m = m' + q \;. \tag{D.9}$$

This shows that the tensor operator $\hat{T}^{(k)}_q$ carries an orbital momentum q around the z axis. Importantly, the Clebsch-Gordan coefficient $\langle\, l'k; m'q \,|\, lm \,\rangle$ takes into account all the angular dependence of the matrix element $\langle\, nlm \,|\hat{T}^{(k)}_q|\, n'l'm' \,\rangle$ on m', q and m. In contrast, the reduced matrix element $\langle\, nl \,||\hat{T}^{(k)}||\, n'l' \,\rangle$ is independent of m', q and m.

D.2 Relations between dipole matrix elements

The Wigner-Eckart theorem (D.2) is a powerful tool for determining the matrix elements $\langle\, nlm \,|\hat{T}^{(k)}_q|\, n'l'm' \,\rangle$ of the tensor operator $\hat{T}^{(k)}_q$. The required Clebsch-Gordan coefficients can be easily obtained by starting with the "maximal m" state. For example, in the case of $4p$–$4s$ transitions ($l = 1$ and $l' = 0$), this is the angular-momentum state

$$|\, l = 1, m = 1 \,\rangle \;=\; |\, l' = 0, k = 1 \,;\, m' = 0, q = 1 \,\rangle \;, \tag{D.10}$$

where the phase $+1$ has been used by convention. Consequently, the first coefficients read

$$\langle\, l' = 0, k = 1 \,;\, m' = 0, q \,|\, l = 1, m = 1 \,\rangle \;=\; \delta_{q,1} \;. \tag{D.11}$$

Then, by applying the recursion relation (D.7), all other coefficients can be obtained without any ambiguity. The Clebsch-Gordan coefficients for $3d$–$4p$ transitions are determined analogously.

In the next step, the relation between $\hat{T}^{(k)}_q$ and $\hat{\vec{r}}$, see Eq. (D.1), is used for the purpose of computing the dipole matrix elements $\langle\, nlm \,|\hat{\vec{r}}|\, n'l'm' \,\rangle$. The results are summarized in Table D.1. Notice that the two reduced matrix elements $\langle\, 4p \,||\hat{T}^{(1)}||\, 4s \,\rangle$ and $\langle\, 3d \,||\hat{T}^{(1)}||\, 4p \,\rangle$ depend only on the radial part of the $3d$, $4s$ and $4p$ wave functions. They are the same for all m and m'. Since the Hamiltonian $\hat{H}_E$ is given by a product

Appendix D. *Dipole matrix elements within the intra-atomic approximation*

Dipole element	Expression given by Wigner-Eckart theorem
$\langle\, 4p, m \,\vert\hat{x}\vert\, 4s, 0 \,\rangle$	$-\frac{m}{\sqrt{2}} \langle\, 4p \,\vert\vert \hat{T}^{(1)} \vert\vert\, 4s \,\rangle$
$\langle\, 4p, m \,\vert\hat{y}\vert\, 4s, 0 \,\rangle$	$\frac{i}{\sqrt{2}}(1-\delta_{m,0}) \langle\, 4p \,\vert\vert \hat{T}^{(1)} \vert\vert\, 4s \,\rangle$
$\langle\, 4p, m \,\vert\hat{z}\vert\, 4s, 0 \,\rangle$	$\delta_{m,0} \langle\, 4p \,\vert\vert \hat{T}^{(1)} \vert\vert\, 4s \,\rangle$
$\langle\, 3d, m=\pm 2 \,\vert\hat{x}\vert\, 4p, m' \,\rangle$	$\mp\frac{1}{\sqrt{6}}\delta_{m',\pm 1} \langle\, 3d \,\vert\vert \hat{T}^{(1)} \vert\vert\, 4p \,\rangle$
$\langle\, 3d, m=\pm 1 \,\vert\hat{x}\vert\, 4p, m' \,\rangle$	$\mp\frac{1}{\sqrt{12}}\delta_{m',0} \langle\, 3d \,\vert\vert \hat{T}^{(1)} \vert\vert\, 4p \,\rangle$
$\langle\, 3d, m=0 \,\vert\hat{x}\vert\, 4p, m' \,\rangle$	$\frac{1}{6}\left(\delta_{m',1}-\delta_{m',-1}\right) \langle\, 3d \,\vert\vert \hat{T}^{(1)} \vert\vert\, 4p \,\rangle$
$\langle\, 3d, m=\pm 2 \,\vert\hat{y}\vert\, 4p, m' \,\rangle$	$\frac{i}{\sqrt{6}}\delta_{m',\pm 1} \langle\, 3d \,\vert\vert \hat{T}^{(1)} \vert\vert\, 4p \,\rangle$
$\langle\, 3d, m=\pm 1 \,\vert\hat{y}\vert\, 4p, m' \,\rangle$	$\frac{i}{\sqrt{12}}\delta_{m',0} \langle\, 3d \,\vert\vert \hat{T}^{(1)} \vert\vert\, 4p \,\rangle$
$\langle\, 3d, m=0 \,\vert\hat{y}\vert\, 4p, m' \,\rangle$	$\frac{i}{6}\left(\delta_{m',1}+\delta_{m',-1}\right) \langle\, 3d \,\vert\vert \hat{T}^{(1)} \vert\vert\, 4p \,\rangle$
$\langle\, 3d, m=\pm 2 \,\vert\hat{z}\vert\, 4p, m' \,\rangle$	0
$\langle\, 3d, m=\pm 1 \,\vert\hat{z}\vert\, 4p, m' \,\rangle$	$\frac{1}{\sqrt{6}}\delta_{m',\pm 1} \langle\, 3d \,\vert\vert \hat{T}^{(1)} \vert\vert\, 4p \,\rangle$
$\langle\, 3d, m=0 \,\vert\hat{z}\vert\, 4p, m' \,\rangle$	$\sqrt{\frac{2}{9}}\delta_{m',0} \langle\, 3d \,\vert\vert \hat{T}^{(1)} \vert\vert\, 4p \,\rangle$

Table D.1: Intra-atomic dipole matrix elements - Matrix elements $\langle\, nlm \,\vert\hat{\vec{r}}\vert\, n'l'm' \,\rangle$ within the $3d$, $4s$ and $4p$ valence bands as given by the Wigner-Eckart theorem.

of the dipole operator $\hat{\vec{r}}$ and the external field $\vec{E}$ [see Eq. (3.9)], the matrix elements $\langle\, 4p \,\vert\vert \hat{T}^{(1)} \vert\vert\, 4s \,\rangle$ and $\langle\, 3d \,\vert\vert \hat{T}^{(1)} \vert\vert\, 4p \,\rangle$ determine the strength of the coupling between the electronic degrees of freedom and the electric field. In the context of the present model they are regarded as parameters.

Appendix E

Numerical methods for static calculations

The present Appendix describes the numerical procedure for static calculations. These calculations can be divided into three types depending on their objectives: ground-state calculations, finite-temperature calculations, and spectral analysis. In Section E.1 we consider the Lanczos diagonalization method, which has been applied for the purpose of computing the many-body ground state of the electronic model (3.3). In Section E.2, a finite-temperature extension of the Lanczos method is presented. This allows us to determine important properties of systems in thermal equilibrium. Finally, Section E.3 presents a method for determining the spectral representation of a many-body state and the properties of the projections of the state on different energy or frequency ranges.

E.1 Lanczos diagonalization method: Ground-state properties

In many applications, one is primarily interested in properties of the system at very low temperatures T or even at $T = 0$. These properties can be directly derived from the ground state $|\,\Psi_{\mathrm{gs}}\,\rangle$ which denotes the lowest-energy eigenstate of the Hamiltonian $\hat{H}$. The straightforward method to obtain $|\,\Psi_{\mathrm{gs}}\,\rangle$ is given by the complete diagonalization of the Hamiltonian yielding not only the ground state but also all other eigenstates of $\hat{H}$. However, the dimension of a many-body Hilbert space grows exponentially with the number of sites. For N_o orbitals and N_e electrons, the number of many-body states

is given by $N_{\text{states}} = \binom{N_o}{N_e}$, i.e., there are $\binom{N_o}{N_e}$ possibilities to occupy N_o orbitals by N_e electrons. Approximately, matrices of dimension up to 8000×8000 are presently diagonalizable with normal computer facilities. This corresponds to a two-band model having only $N_a = 3$ atoms and $N_e = 3$ electrons. Consequently, in large systems a diagonalization of the full Hamiltonian $\hat{H}$ is out of reach. Instead, for the purpose of computing the ground state, we project $\hat{H}$ onto an optimally chosen subspace of the Hilbert space. Subsequently, we diagonalize the projected Hamiltonian having a greatly reduced dimension.

The particular subspace, called Krylov space K^N, is associated to a given initial vector $|\,\Psi_1\,\rangle$. This space K^N is obtained by acting with the (time-independent) Hamiltonian $\hat{H}$ on the state $|\,\Psi_1\,\rangle$ $N-1$ times, i.e., the Krylov space K^N is of order N and is spanned by the states $\{|\,\Psi_1\,\rangle, \hat{H}|\,\Psi_1\,\rangle, \ldots, \hat{H}^{N-1}|\,\Psi_1\,\rangle\}$:

$$K^N = \text{span}\left\{|\,\Psi_1\,\rangle, \hat{H}|\,\Psi_1\,\rangle, \ldots, \hat{H}^{N-1}|\,\Psi_1\,\rangle\right\} \ . \tag{E.1}$$

However, the set of states $\{\hat{H}^j|\,\Psi_1\,\rangle\}$ is generally not orthogonal. Therefore, we apply the so-called Gram-Schmidt orthogonalization method, in which, as each new Krylov state $|\,\Psi_j\,\rangle$ is constructed it is also orthogonalized to the previous Krylov states (80, 95). The first basis state is just the arbitrary chosen initial state $|\,\Psi_1\,\rangle$ itself. The second basis state, $|\,\Psi_2\,\rangle$, is determined by acting with $\hat{H}$ on $|\,\Psi_1\,\rangle$, and projecting out the component along $|\,\Psi_1\,\rangle$ from $\hat{H}|\,\Psi_1\,\rangle$ so that $\langle\,\Psi_1\,|\,\Psi_2\,\rangle = 0$:

$$\hat{H}|\,\Psi_1\,\rangle = \alpha_1|\,\Psi_1\,\rangle + \beta_1|\,\Psi_2\,\rangle \ . \tag{E.2}$$

Employing $\langle\,\Psi_1\,|\,\Psi_2\,\rangle = 0$, $\langle\,\Psi_1\,|\,\Psi_1\,\rangle = 1$ and $\langle\,\Psi_2\,|\,\Psi_2\,\rangle = 1$, we have

$$\alpha_1 = \langle\,\Psi_1\,|\hat{H}|\,\Psi_1\,\rangle \in \mathbb{R} \ , \tag{E.3}$$

and

$$|\beta_1|^2 = \|(\hat{H} - \alpha_1)|\,\Psi_1\,\rangle\|_2^2 \geq 0 \ . \tag{E.4}$$

For simplicity we assume $\beta_1 > 0$ and attach the phase in the state $(\hat{H} - \alpha_1)|\,\Psi_1\,\rangle = \beta_1|\,\Psi_2\,\rangle$ to $|\,\Psi_2\,\rangle$. Thus, we have

$$\beta_1 = \langle\,\Psi_2\,|\hat{H}|\,\Psi_1\,\rangle = \sqrt{\|(\hat{H} - \alpha_1)|\,\Psi_1\,\rangle\|_2^2}. \tag{E.5}$$

The third basis state, $|\,\Psi_3\,\rangle$, is determined by acting with $\hat{H}$ on $|\,\Psi_2\,\rangle$, and projecting out the components along $|\,\Psi_1\,\rangle$ and $|\,\Psi_2\,\rangle$ from $\hat{H}|\,\Psi_2\,\rangle$ so that $\langle\,\Psi_1\,|\,\Psi_3\,\rangle = \langle\,\Psi_2\,|\,\Psi_3\,\rangle = 0$:

$$\hat{H}|\,\Psi_2\,\rangle = \beta_1|\,\Psi_1\,\rangle + \alpha_2|\,\Psi_2\,\rangle + \beta_2|\,\Psi_3\,\rangle\ , \tag{E.6}$$

where

$$\alpha_2 = \langle\,\Psi_2\,|\hat{H}|\,\Psi_2\,\rangle \in \mathbb{R} \tag{E.7}$$

and

$$\beta_2 = \langle\,\Psi_3\,|\hat{H}|\,\Psi_2\,\rangle = \sqrt{\|(\hat{H}-\alpha_2)|\,\Psi_2\,\rangle - \beta_1|\,\Psi_1\,\rangle\|_2^2} \geq 0\ . \tag{E.8}$$

For general $j \geq 3$ the equation for determining the basis state $|\,\Psi_j\,\rangle$ reads

$$\hat{H}|\,\Psi_{j-1}\,\rangle = \beta_{j-2}|\,\Psi_{j-2}\,\rangle + \alpha_{j-1}|\,\Psi_{j-1}\,\rangle + \beta_{j-1}|\,\Psi_j\,\rangle\ , \tag{E.9}$$

with coefficients

$$\alpha_{j-1} = \langle\,\Psi_{j-1}\,|\hat{H}|\,\Psi_{j-1}\,\rangle \in \mathbb{R} \tag{E.10}$$

and

$$\beta_{j-1} = \langle\,\Psi_j\,|\hat{H}|\,\Psi_{j-1}\,\rangle = \sqrt{\|(\hat{H}-\alpha_{j-1})|\,\Psi_{j-1}\,\rangle - \beta_{j-2}|\,\Psi_{j-2}\,\rangle\|_2^2} \geq 0\ . \tag{E.11}$$

By applying this method for $j = 2, ..., N$, one obtains an orthonormal Lanczos basis $\{|\,\Psi_1\,\rangle, |\,\Psi_2\,\rangle, \ldots, |\,\Psi_N\,\rangle\}$, in which the projected Hamiltonian matrix H_N is symmetric and tridiagonal:

$$H_N = \begin{pmatrix} \alpha_1 & \beta_1 & 0 & \cdots & \cdots & \cdots & 0 \\ \beta_1 & \alpha_2 & \beta_2 & 0 & \cdots & \cdots & 0 \\ 0 & \beta_2 & \alpha_3 & \beta_3 & 0 & \cdots & 0 \\ 0 & 0 & \beta_3 & \alpha_4 & \beta_4 & 0 & 0 \\ \vdots & \vdots & \ddots & \ddots & \ddots & \ddots & 0 \\ 0 & \cdots & \cdots & 0 & \beta_{N-2} & \alpha_{N-1} & \beta_{N-1} \\ 0 & \cdots & \cdots & \cdots & 0 & \beta_{N-1} & \alpha_N \end{pmatrix}\ . \tag{E.12}$$

The diagonalization of H_N can be easily performed numerically. Moreover, with increasing N the lowest eigenvalue E_1^N of H_N converges to the ground-state energy E_{gs}

of the full system.[1] In the present work we have used the condition

$$|E_1^N - E_1^{N-1}| \leq \varepsilon = 10^{-12} \text{ eV} \tag{E.13}$$

as the convergence criterion. The quantity $E_1^N - E_1^{N-1}$ describes the difference in the lowest eigenenergies obtained in two successive steps of the Lanczos algorithm. Notice that energy differences in the order of ε (10^{-12} eV) are above the arithmetic accuracy of the computer. In order to test the convergence of the Lanczos calculations, we have varied the convergence parameter ε and compared the results obtained by starting with different initial vectors $|\,\Psi_1\,\rangle$. The convergence has been found to be very good for all practical purposes.[2] Once the Lanczos algorithm has converged, the ground state $|\,\Psi_{\rm gs}\,\rangle$ of the many-body problem can be approximated by the lowest eigenvector $(v_1, v_2, ..., v_N)^T$ of the N-step Lanczos representation H_N of $\hat{H}$ for a sufficiently large Krylov-space dimension N.[3] In other words, the approximation to the many-body ground state reads

$$|\,\Psi_{\rm gs}\,\rangle = \sum_{j=1}^{N} v_j |\,\Psi_j\,\rangle \ . \tag{E.14}$$

Then, all ground-state observables $\hat{O}$ can be obtained by computing the expectation values

$$\langle \hat{O} \rangle = \langle\,\Psi_{\rm gs}\,|\hat{O}|\,\Psi_{\rm gs}\,\rangle \ . \tag{E.15}$$

A large number of details on the Lanczos method including the reason for convergence, numerical stability of the method and risk of loss of orthogonality in the Lanczos basis can be found in Ref. (80).

[1] Notice that arithmetic rounding errors can result in loss of orthogonality of the numerically obtained Lanczos basis states $|\,\Psi_j\,\rangle$. In this case, difficulties in the convergence, especially for eigenstates having the smallest absolute values of their eigenenergies, appear. See Ref. (80) for the detailed reason. Consequently, the best convergence is given for the eigenstate corresponding to the eigenvalue with largest absolute value. A shift in the single-particle energies ε_α^0 can be used in order to ensure that this is the ground state. We have verified that the Lanczos calculations for the systems considered in the present work converge very well even without such a spectral shift.

[2] Moreover, for system sizes as those which are considered in the present work, we know from applications to the Hubbard and Anderson models that the Lanczos method gives very accurate results for the ground state and its properties.

[3] The eigenvector $(v_1, v_2, ..., v_N)^T$ is assumed to be normalized, i.e., $\sum_{j=1}^{N} v_j^2 = 1$.

E.2 Finite-temperature properties: thermal equilibrium

The Lanczos diagonalization method described in the previous Section E.1 has been conceived for the purpose of determining the ground-state properties (corresponding to $T = 0$). However, if one needs to go beyond $T = 0$ it is necessary to consider a thermal distribution of many-body states, which is of course more demanding than to compute one single ground state. In this work we apply the so-called finite-temperature Lanczos method as proposed in Ref. (82) in order to approach the interesting case $T > 0$ and, in particular, to determine properties of systems in thermal equilibrium.

In the canonical ensemble the thermal average of some observable $\hat{O}$ in thermal equilibrium at temperature $T > 0$ is given by

$$\left\langle \hat{O} \right\rangle_T = \frac{1}{Z} \sum_{\nu=1}^{N_{\text{states}}} \langle\, \nu \,| e^{-\beta \hat{H}} \hat{O} |\, \nu \,\rangle = \frac{1}{Z} \sum_{\nu=1}^{N_{\text{states}}} \langle\, \nu \,| e^{-\frac{1}{2}\beta \hat{H}} \hat{O} e^{-\frac{1}{2}\beta \hat{H}} |\, \nu \,\rangle \;, \tag{E.16}$$

where $\beta = (k_{\text{B}} T)^{-1}$, k_{B} is the Boltzman constant, $\{|\, \nu \,\rangle\}$ is some orthonormal basis of the Hilbert space, and

$$Z = \sum_{\nu=1}^{N_{\text{states}}} \langle\, \nu \,| e^{-\beta \hat{H}} |\, \nu \,\rangle \tag{E.17}$$

is the partition function. Usually, one uses energy eigenstates as the particular basis states $|\, \nu \,\rangle$. However, similarly to the ground-state minimization problem, a full diagonalization is impossible in practice. In order to overcome this limitation one performs a random sampling of the Hilbert space by R random states $|\, r \,\rangle$, as it is described in Ref. (82). The states $|\, r \,\rangle$ are assumed to be normalized, but we do not require them to be orthogonal to each other. Then, thermal averages can be approximated as

$$\left\langle \hat{O} \right\rangle_T \approx \frac{1}{Z} \sum_{r=1}^{R} \langle\, r \,| e^{-\frac{1}{2}\beta \hat{H}} \hat{O} e^{-\frac{1}{2}\beta \hat{H}} |\, r \,\rangle \;, \tag{E.18}$$

and

$$Z \approx \sum_{r=1}^{R} \langle\, r \,| e^{-\beta \hat{H}} |\, r \,\rangle \;. \tag{E.19}$$

In a second step the matrix elements $\langle\, r \,| e^{-\frac{1}{2}\beta \hat{H}} \hat{O} e^{-\frac{1}{2}\beta \hat{H}} |\, r \,\rangle$ and $\langle\, r \,| e^{-\beta \hat{H}} |\, r \,\rangle$ are evaluated by projection onto Krylov subspaces. For each random vector $|\, r \,\rangle$, an N-dimensional Krylov subspace

$$K_{(r)}^{N} = \text{span} \left\{ |\, r \,\rangle, \hat{H} |\, r \,\rangle, \hat{H}^2 |\, r \,\rangle, \, \ldots, \hat{H}^{N-1} |\, r \,\rangle \right\} \tag{E.20}$$

is considered. The Lanczos basis $\{|\,\Psi_j^{(r)}\,\rangle\}$ of the subspace $K_{(r)}^N$ is generated in the same way as in the ground-state Lanczos diagonalization method described in the previous Section E.1. For this particular choice of basis states, the Hamiltonian projected onto $K_{(r)}^N$, denoted by the matrix $H_N^{(r)}$, becomes tridiagonal. Then, $H_N^{(r)}$ is diagonalized, yielding eigenstates $|\,\Phi_j^{(r)}\,\rangle$ satisfying $\langle\,\Phi_i^{(r)}\,|\,\Phi_j^{(r)}\,\rangle = \delta_{ij}$ and corresponding eigenenergies $E_j^{(r)}$ $(j = 1, \ldots, N)$. It is important to note that the initial random state $|\,r\,\rangle$ is the first element of the Lanczos basis that it is generating, i.e.,

$$|\,r\,\rangle \,\in\, K_{(r)}^N = \mathrm{span}\left\{|\,\Phi_j^{(r)}\,\rangle\,;\, j = 1, \ldots, N\right\}\,. \tag{E.21}$$

Moreover, since $K_{(r)}^N$ contains the states $\{|\,r\,\rangle, \hat{H}|\,r\,\rangle, \hat{H}^2|\,r\,\rangle, \ldots, \hat{H}^{N-1}|\,r\,\rangle\}$, the state $e^{-\frac{1}{2}\beta\hat{H}}|\,r\,\rangle$ is *almost* contained within this subspace (in particular, for high temperatures for which k_BT is much larger than the spectral width of the energy distribution in the state $|\,r\,\rangle$). This leads to the idea of projecting the states $e^{-\frac{1}{2}\beta\hat{H}}|\,r\,\rangle$ onto their corresponding Krylov spaces $K_{(r)}^N$ and, therefore, to the approximation

$$\begin{aligned}\left\langle\hat{O}\right\rangle_T \,&\approx\, \frac{1}{Z}\sum_{r=1}^{R}\sum_{j,k=1}^{N}\langle\,r\,|e^{-\frac{1}{2}\beta\hat{H}}|\,\Phi_j^{(r)}\,\rangle\langle\,\Phi_j^{(r)}\,|\hat{O}|\,\Phi_k^{(r)}\,\rangle\langle\,\Phi_k^{(r)}\,|e^{-\frac{1}{2}\beta\hat{H}}|\,r\,\rangle \\ &= \frac{1}{Z}\sum_{r=1}^{R}\sum_{j,k=1}^{N} e^{-\frac{\beta}{2}\left(E_j^{(r)}+E_k^{(r)}\right)}\,\langle\,r\,|\,\Phi_j^{(r)}\,\rangle\langle\,\Phi_j^{(r)}\,|\hat{O}|\,\Phi_k^{(r)}\,\rangle\langle\,\Phi_k^{(r)}\,|\,r\,\rangle\,,\end{aligned} \tag{E.22}$$

while the partition function can be written as

$$\begin{aligned}Z \,&\approx\, \sum_{r=1}^{R}\sum_{j=1}^{N}\langle\,r\,|\,\Phi_j^{(r)}\,\rangle\langle\,\Phi_j^{(r)}\,|e^{-\beta\hat{H}}|\,r\,\rangle \\ &= \sum_{r=1}^{R}\sum_{j=1}^{N} e^{-\beta E_j^{(r)}}|\langle\,r\,|\,\Phi_j^{(r)}\,\rangle|^2\,.\end{aligned} \tag{E.23}$$

Let us now discuss the two opposite limits of high and low temperatures. First, in the case of $T \to \infty$ the thermal equilibrium is a mixed state consisting of a large number of excited many-body states $|\,\nu\,\rangle$. Therefore, a large number R of random states $|\,r\,\rangle$ is required to give accurate results. On the other hand, since $\beta \to 0$, only a few powers $j = 0, \ldots, N-1$ of $\hat{H}^j|\,r\,\rangle$ are necessary for the state $e^{-\frac{1}{2}\beta\hat{H}}|\,r\,\rangle$ to be totally included in $K_{(r)}^N = \mathrm{span}\left\{|\,r\,\rangle, \hat{H}|\,r\,\rangle, \hat{H}^2|\,r\,\rangle, \ldots, \hat{H}^{N-1}|\,r\,\rangle\right\}$. Therefore, in this limit a relatively small Lanczos basis size N is enough for accurate calculations. In the opposite limit of $T \to 0$ or $\beta \to \infty$, the contribution of the ground state $|\,\Psi_{\mathrm{gs}}\,\rangle$ to $\langle\hat{O}\rangle$ and Z dominate.

This implies that for each random vector $|\,r\,\rangle$ the described Lanczos procedure must yield the ground state (having ground-state energy $E_{\rm gs}$) as the lowest eigenstate within $K^N_{(r)}$. Indeed, in this case one obtains

$$\left\langle \hat{O} \right\rangle_{T\to 0} \to \frac{\sum_{r=1}^{R} e^{-\beta E_{\rm gs}} \langle\, r \,|\, \Psi_{\rm gs} \,\rangle \langle\, \Psi_{\rm gs} \,|\hat{O}|\, \Psi_{\rm gs} \,\rangle \langle\, \Psi_{\rm gs} \,|\, r \,\rangle}{\sum_{r=1}^{R} e^{-\beta E_{\rm gs}} |\langle\, r \,|\, \Psi_{\rm gs} \,\rangle|^2} \;=\; \langle\, \Psi_{\rm gs} \,|\hat{O}|\, \Psi_{\rm gs} \,\rangle \;, \quad \text{(E.24)}$$

where the statistical fluctuations are canceled out. This means that the $T = 0$ limit is correctly reproduced by the present approximation, provided that the Lanczos basis size N is sufficiently large in order that the ground states of $H_N^{(r)}$ give a good approximation to the ground state $|\,\Psi_{\rm gs}\,\rangle$ of the full Hamiltonian $\hat{H}$. Consequently, a large Lanczos basis size N is necessary in this limit, whereas small numbers R of random states $|\,r\,\rangle$ are enough.

In the present work, we have applied the finite-temperature Lanczos method in order to determine the dependence of magnetic order on temperature. This dependence has been used in Chapter 5 for *qualitatively* revealing the role of energy absorption and subsequent thermalization in the laser-induced demagnetization process. To this aim, a high accuracy of the temperature-dependent results is not crucial. Having this in mind, numerical parameters of $N = 50$ and only $R = 50$ have been chosen. We have verified that this is accurate enough for our purposes and for the considered small clusters by quantifying the fluctuations in the results for the strength of the local magnetic moments $\langle\langle \vec{S}_{jd}^{\,2} \rangle\rangle$ and the nearest-neighbor magnetic order $\langle\langle \vec{S}_{jd} \cdot \vec{S}_{kd} \rangle\rangle$ [see Eqs. (4.13) and (4.14)] both at relatively low and high temperatures $T = 50$ and 2000 K. The relative discrepancies in these results have been found to be less than 19 %.

E.3 Method of spectral analysis

In this Section we want to present a numerical method to compute the spectral distribution of a given many-body state $|\,\Psi\,\rangle$. Formally, the spectral density of $|\,\Psi\,\rangle$ as a function of many-body energy E is defined by

$$D_\Psi(E) \;=\; \sum_\nu \delta(E - E_\nu)\; |\langle\, \nu \,|\, \Psi \,\rangle|^2 \;, \quad \text{(E.25)}$$

where $\{|\,\nu\,\rangle\}$ is an orthonormal set of eigenstates of the Hamiltonian $\hat{H}$ having eigenenergies E_ν. $D_\Psi(E)$ represents the weight of states $|\,\nu\,\rangle$ having energy $E_\nu = E$ in the

expansion of $|\,\Psi\,\rangle$.[1] This formulation is analog to the definition of the local density of states in a single-particle problem. However, here we replace the local orbital by the many-body state $|\,\Psi\,\rangle$. For its numerical computation we consider the Krylov subspace

$$K_\Psi^N \;=\; \mathrm{span}\left\{|\,\Psi\,\rangle, \hat{H}|\,\Psi\,\rangle, \hat{H}^2|\,\Psi\,\rangle, \,...\,, \hat{H}^{N-1}|\,\Psi\,\rangle\right\}\;, \tag{E.26}$$

which $|\,\Psi\,\rangle$ will explore in the next future, instead of the full Hilbert space. Notice that K_Ψ^N corresponds to the subspace K^N given by Eq. (E.1), whose generation starts with the initial state $|\,\Psi\,\rangle$. As in Section E.2, let

$$\{|\,\Phi_k\,\rangle\,;\, k = 1,\,...\,,N\} \tag{E.27}$$

be the orthonormal basis of K_Ψ^N, which is built up of eigenstates of the Hamiltonian $\hat{H}$ projected onto K_Ψ^N with eigenenergies E_k. These states are the result of the Lanczos algorithm described in Section E.1 and a subsequent diagonalization of a symmetric tridiagonal matrix. This yields the approximation

$$\tilde{D}_\Psi(E) \;=\; \sum_{k=1}^{N} \delta(E - E_k)\;|\langle\,\Phi_k\,|\,\Psi\,\rangle|^2 \tag{E.28}$$

to the exact spectral distribution $D_\Psi(E)$ of $|\,\Psi\,\rangle$ as given by Eq. (E.25). Since $|\,\Psi\,\rangle \in K_\Psi^N$, one obtains

$$\sum_{k=1}^{N} |\,\Phi_k\,\rangle\langle\,\Phi_k\,|\,\Psi\,\rangle \;=\; |\,\Psi\,\rangle \tag{E.29}$$

and, therefore, the normalization condition

$$\int_{-\infty}^{+\infty} \mathrm{d}E\,\tilde{D}_\Psi(E) \;=\; 1\;. \tag{E.30}$$

In order to choose a sufficiently large dimension N of the subspace K_Ψ^N, we have computed the spectral distribution $\tilde{D}_\Psi(E)$ of the propagated state $|\,\Psi(t)\,\rangle$ for different N (at times well after the laser-pulse absorption). It has been found that increasing the Krylov subspace dimension beyond $N = 50$ does not improve the spectral distribution

[1] The meaning of $D_\Psi(E)$ can be illustrated by considering the expansion $|\,\Psi\,\rangle = \sum_\nu a_\nu|\,\nu\,\rangle$ of the many-body state $|\,\Psi\,\rangle$ in terms of stationary states $|\,\nu\,\rangle$. Then, the average energy of $|\,\Psi\,\rangle$ is given by

$$\langle\,\Psi\,|\hat{H}|\,\Psi\,\rangle = \sum_\nu |a_\nu|^2 E_\nu = \int \mathrm{d}E\,\sum_\nu\,\delta(E - E_\nu)|a_\nu|^2 E = \int \mathrm{d}E\,D_\Psi(E)\,E\;.$$

This demonstrates that $D_\Psi(E)$ is the spectral density in the energy distribution for the state $|\,\Psi\,\rangle$.

within a resolution of 100 meV. This width is one order of magnitude smaller than the energy $\hbar\omega = 1.55$ eV, which is added to the electron system by absorbing a single photon. Therefore, the resolution of 100 meV allows us to definitely distinguish between the different spectral parts in $D_\Psi(E)$ associated to the absorption of zero, one and multiple photons (see Section 5.5). For this reason, we have chosen $N = 50$ in the present thesis. This subspace size gives sufficiently accurate results for the spectral densities.

Besides the spectral density of the many-body state $|\,\Psi\,\rangle$, we are also interested in quantifying the *contribution* of the states $|\,\nu\,\rangle$ expanding $|\,\Psi\,\rangle$ and having energy $E_\nu = E$ to the expectation $\langle\,\Psi\,|\hat{O}|\,\Psi\,\rangle$ of some observable $\hat{O}$. Notice that if $[\hat{O},\,\hat{H}] \neq 0$, the usual definition $\langle\,\Psi\,|\,\hat{O}\,\delta(\hat{H}-E)\,|\,\Psi\,\rangle$ for the spectral density of $\langle\hat{O}\rangle$ is not real. Therefore, we use a different definition for the spectral contribution to $\langle\hat{O}\rangle$ as a function of E, namely

$$o_\Psi(E) \;=\; \sum_{\nu\nu'} \delta\left(E - \frac{E_\nu + E_{\nu'}}{2}\right) \langle\,\Psi\,|\,\nu\,\rangle\,\langle\,\nu\,|\hat{O}|\,\nu'\,\rangle\,\langle\,\nu'\,|\,\Psi\,\rangle\;. \tag{E.31}$$

Then, similarly to Eq. (E.28), one can use the approximation

$$\tilde{o}_\Psi(E) \;=\; \sum_{j,k=1}^{N} \delta\left(E - \frac{E_j + E_k}{2}\right) \langle\,\Psi\,|\,\Phi_j\,\rangle\,\langle\,\Phi_j\,|\hat{O}|\,\Phi_k\,\rangle\,\langle\,\Phi_k\,|\,\Psi\,\rangle \tag{E.32}$$

for the purpose of computing such spectral densities. The definition (E.31) has several advantages. First, it is real. Second, it satisfies the sum rule

$$\int_{-\infty}^{+\infty} \mathrm{d}E\, o_\Psi(E) \;=\; \langle\,\Psi\,|\hat{O}|\,\Psi\,\rangle \;=\; \langle\hat{O}\rangle\;. \tag{E.33}$$

Third, for a given energy E, it allows us to identify the spectral parts (accumulation of spectral weight) in the spectrum D_Ψ from which the pairs of states $|\,\nu\,\rangle$ and $|\,\nu\,\rangle'$ contributing to $o_\Psi(E)$ originate:[1] If E lies within an accumulation of spectral weight, then $o_\Psi(E)$ results from the coupling $\langle\,\nu\,|\hat{O}|\,\nu'\,\rangle$ of two states within the *same* spectral part, i.e., from states $|\,\nu\,\rangle$ and $|\,\nu\,\rangle'$ having very nearby energies E_ν and $E_{\nu'}$, such that $E \approx E_\nu \approx E_{\nu'}$. Otherwise, one can conclude that $o_\Psi(E)$ results from the coupling of states belonging to two *different* spectral parts. An important example for spectral

[1] See Section 5.5 and, in particular, Figure 5.8. There, three spectral parts, which are associated to the absorption of zero, one and two photons, are shown. The energy gaps between these spectral parts, i.e., between two successive accumulations of spectral weight, are given by the photon energy $\hbar\omega = 1.55$ eV.

densities of observables is given by the spin density $s_{z,\Psi}(E)$ (in z direction), which tells us how much magnetization $S_z = \langle \Psi | \hat{S}_z | \Psi \rangle$ of the state $| \Psi \rangle$ comes from the pairs of eigenstates $| \nu \rangle$ having an average energy E. We have found that for $s_{z,\Psi}(E)$ the mixing $\langle \nu | \hat{O} | \nu' \rangle$ of states $| \nu \rangle$, $| \nu \rangle'$ originating from different spectral parts is very weak.

Finally, let us mention that in a continuous spectrum $D_\Psi(E)$ and $o_\Psi(E)$ are smooth functions of E. However, in the present case of a discrete spectrum, they are given by a discrete sum of delta functions $\delta(E-\varepsilon)$. In order to visualize $\tilde{D}_\Psi(E)$ and $\tilde{o}_\Psi(E)$, the delta functions are approximated by Gaussians of the form

$$\delta(E-\varepsilon) \;=\; \frac{1}{\sqrt{2\pi\sigma^2}}\, e^{-\frac{(E-\varepsilon)^2}{2\sigma^2}} \;, \tag{E.34}$$

where σ^2 is the variance of the Gauss distribution. In this work we have used $\sigma = 20$ meV, since this broadening of the delta peaks facilitates the analysis of spectral densities such as those shown in Figure 5.8.

Appendix F

Numerical methods for dynamical calculations

The time propagation of many-body states represents a true theoretical and numerical challenge. The purpose of this Appendix is to describe the general concept of the time-evolution operator as well as the so-called short-iterative Lanczos propagation (SILP) method which in the present work has been chosen for the numerical calculations (83). Moreover, the accuracy of the corresponding approximated Lanczos time-evolution operator $\hat{U}^{\mathrm{L}}$ is assessed.

F.1 Time-propagation

Let us suppose that the time-dependent Hamiltonian can be separated as

$$\hat{H}(t) = \hat{H}_0 + v(t)\,\hat{V}\ , \tag{F.1}$$

where $\hat{H}_0$ is time-independent and $v(t)$ is the time-dependent amplitude of some external field $\hat{V}$ (for instance, the laser electric field). A state $|\,\Psi(t_0)\,\rangle$ given at the initial time t_0 propagates as

$$|\,\Psi(t)\,\rangle = \hat{U}(t,t_0)\,|\,\Psi(t_0)\,\rangle \tag{F.2}$$

upon the action of the Hamiltonian $\hat{H}$, where the time-evolution operator $\hat{U}$ is related to $\hat{H}$ by means of the differential equation

$$i\hbar\frac{\partial}{\partial t}\,\hat{U}(t,t_0) = \hat{H}(t)\,\hat{U}(t,t_0)\ . \tag{F.3}$$

Its integration yields the integral equation

$$\hat{U}(t,t_0) = 1 - \frac{i}{\hbar}\int_{t_0}^{t} \mathrm{d}s\, \hat{H}(s)\, \hat{U}(s,t_0)\ . \tag{F.4}$$

The solution of the differential equation (F.3) or the integral equation (F.4) is not trivial in general. However, in the above integral equation one can iteratively substitute $\hat{U}(t,t_0)$ into $\hat{U}(s,t_0)$ to obtain an alternative representation in terms of the Dyson series[1]

$$\hat{U}(t,t_0) = 1 + \sum_{\nu=1}^{\infty} \left(-\frac{i}{\hbar}\right)^{\nu} \int_{t_0}^{t} \mathrm{d}s_1 \int_{t_0}^{s_1} \mathrm{d}s_2 \ldots \int_{t_0}^{s_{\nu-1}} \mathrm{d}s_\nu\, \hat{H}(s_1)\, \hat{H}(s_2) \ldots \hat{H}(s_\nu)\ . \tag{F.5}$$

Here, the integrand is time ordered, i.e., $t \geq s_1 \geq s_2 \geq \ldots \geq s_\nu \geq t_0$. This time order cannot be changed unless $\hat{H}(s)$ commutes with itself at different times s.[2]

In the present Section, starting from the Dyson series (F.5) the short-iterative Lanczos approximation $\hat{U}^{\mathrm{L}}$ to the time-evolution operator is derived. Its very first idea is to divide the total time evolution $\hat{U}(t,t_0)$ in successive propagations over short time intervals Δt. The detailed mathematical justification of considering short Δt is given in the forthcoming Section F.2, where the accuracy of the method is assessed for the limit $\Delta t \to 0$. In the following the derivation of the approximation $\hat{U}^{\mathrm{L}}$ is divided into three steps. As we shall see, this will be useful for estimating the error introduced by $\hat{U}^{\mathrm{L}}$.

As a first step, the time-evolution operator $\hat{U}(t_0+\Delta t, t_0)$ is expanded into its different orders in Δt. At this stage, let us take explicitly into account only the zeroth and first orders. Then, the Dyson series (F.5) can be rewritten as

$$\begin{aligned} \hat{U}(t_0+\Delta t, t_0) \ &= \ 1 \ - \ \frac{i}{\hbar}\int_{t_0}^{t_0+\Delta t} \mathrm{d}s\, \hat{H}(s) \ + \ O(\Delta t^2) \\ &= \ \exp\left(-\frac{i}{\hbar}\int_{t_0}^{t_0+\Delta t} \mathrm{d}s\, \hat{H}(s)\right) \ + \ O(\Delta t^2)\ . \end{aligned} \tag{F.6}$$

This shows that at least up to first order in Δt the approximation in terms of the exponential,

$$\begin{aligned} \hat{U}_e(t_0+\Delta t, t_0) \ &= \ \exp\left(-\frac{i}{\hbar}\int_{t_0}^{t_0+\Delta t} \mathrm{d}s\, \hat{H}(s)\right) \\ &= \ \exp\left(-\frac{i}{\hbar}\Delta t\, \left[\hat{H}_0 + \hat{V}\int_0^1 \mathrm{d}z\, v(t_0+z\Delta t)\right]\right)\ , \end{aligned} \tag{F.7}$$

[1] We assume that the iterative process converges such that the Dyson series (F.5) exists.

[2] In our applications, we have in general $[\hat{H}(s),\, \hat{H}(s')] \neq 0$ for different times $s \neq s'$. This results from the fact that the field-free Hamilton $\hat{H}_0$ does not commute with the external-field operator $\hat{V}$.

is exact.[1] In fact, it is for this reason why it is sound to consider successive propagations over very short time steps Δt and apply the approximation $\hat{U}_e$ to the time-evolution operator.[2] It is interesting to mention that the above approximation $\hat{U}_e(t_0+\Delta t, t_0)$ is also obtained by replacing the time-dependent field amplitude $v(t)$ in the Hamiltonian $\hat{H}(t) = \hat{H}_0 + v(t)\hat{V}$ by its average

$$\int_0^1 \mathrm{d}z\, v(t_0 + z\Delta t) \tag{F.8}$$

over the interval $[t_0, t_0+\Delta t]$. Since in this case the time dependence of $\hat{H}$ is skipped, the differential equation (F.3) is simply solved by the exponential (F.7). Notice that the first mean-value theorem for integration states that a time $\tilde{t} \in [t_0, t_0+\Delta t]$ exists such that

$$v(\tilde{t}) = \int_0^1 \mathrm{d}z\, v(t_0 + z\Delta t)\ . \tag{F.9}$$

This means that the propagation from the initial time t_0 to the time $t_0+\Delta t$ using the approximation $\hat{U}_e(t_0+\Delta t, t_0)$ corresponds to the action of the Hamiltonian $\hat{H} = \hat{H}(\tilde{t})$ *frozen* at some particular time $\tilde{t}$ within the considered interval $[t_0, t_0+\Delta t]$.[3]

A second approximation is involved in the computation of integral (F.8). In this work, its numerical evaluation is performed by using the Simpson formula (95)

$$v(\tilde{t}) \;=\; \int_0^1 \mathrm{d}z\, v(t_0+z\Delta t) \;=\; \frac{1}{6}\left[v(t_0) + 4v\left(t_0+\frac{\Delta t}{2}\right) + v(t_0+\Delta t)\right] + O(\Delta t^4)\ . \tag{F.10}$$

In other words, the integral (F.8) is replaced by

$$v_s \;=\; \frac{1}{6}\left[v(t_0) + 4v\left(t_0+\frac{\Delta t}{2}\right) + v(t_0+\Delta t)\right]\ . \tag{F.11}$$

[1] We shall see later in Eq. (F.35) that $\hat{U}_e(t_0+\Delta t, t_0)$ is exact even up to the order Δt^2.

[2] Actually, Eq. (F.7) follows from the fact that the time ordering has been neglected. In fact, there are $\nu!$ different and exclusive ways of ordering ν time variables $s_1, \ldots s_\nu$. Therefore, the multiple integrals in Eq. (F.5) can be simplified to

$$\begin{aligned}
&\int_{t_0}^{t} \mathrm{d}s_1 \int_{t_0}^{s_1} \mathrm{d}s_2 \ldots \int_{t_0}^{s_{\nu-1}} \mathrm{d}s_\nu\, \hat{H}(s_1)\,\hat{H}(s_2)\ldots\hat{H}(s_\nu) \\
=&\frac{1}{\nu!}\int_{t_0}^{t} \mathrm{d}s_1 \int_{t_0}^{t} \mathrm{d}s_2 \ldots \int_{t_0}^{t} \mathrm{d}s_\nu\, \hat{H}(s_1)\,\hat{H}(s_2)\ldots\hat{H}(s_\nu) \\
=&\frac{1}{\nu!}\left[\int_{t_0}^{t} \mathrm{d}s\, \hat{H}(s)\right]^\nu\ .
\end{aligned}$$

Then, inserting this expression into the Dyson series yields the approximation (F.7).

[3] Notice that the implicit equation (F.9) can in principle be used to determine $\tilde{t}$. However, an explicit value for $\tilde{t}$ is not important, since only $v(\tilde{t})$ enters in the approximation (F.7).

This implies the approximation

$$\hat{U}_s(t_0 + \Delta t, t_0) \, = \exp\left(-\frac{i}{\hbar}\Delta t \, \hat{H}_s\right) \tag{F.12}$$

to the time-evolution operator, where

$$\hat{H}_s \, = \, \hat{H}_0 + v_s \, \hat{V} \tag{F.13}$$

is the corresponding approximation to the Hamiltonian. Importantly, within each considered time interval $[t_0 \, , \, t_0 + \Delta t]$ the Hamiltonian $\hat{H}_s$ does not depend on the time. The straightforward way to perform the time propagation

$$|\, \Psi(t_0 + \Delta t) \,\rangle \, = \, \hat{U}_s(t_0 + \Delta t, t_0) \, |\, \Psi(t_0) \,\rangle \tag{F.14}$$

would be to diagonalize the Hamiltonian $\hat{H}_s$ and to decompose the initial state $|\, \Psi(t_0) \,\rangle$ into its spectral parts $|\, \nu \,\rangle$. The time-evolution operator acts on them as

$$\exp\left(-\frac{i}{\hbar}\Delta t \, \hat{H}_s\right) |\, \nu \,\rangle \, = \, e^{-\frac{i}{\hbar}\Delta t E_\nu} |\, \nu \,\rangle \, , \tag{F.15}$$

where E_ν denotes the eigenenergy corresponding to the stationary state $|\, \nu \,\rangle$. However, as discussed in Section E.1, in most of the systems considered in the present work the dimension of the Hilbert space renders a full diagonalization of $\hat{H}_s$ impossible. Therefore, methods of further approximation are inevitable. We have chosen the SILP method (83). The basic idea of this approach is to represent the time-evolution operator

$$\hat{U}_s(t_0 + \Delta t, t_0) = \exp\left(-\frac{i}{\hbar}\Delta t \, \hat{H}_s\right) \tag{F.16}$$

in some polynomial of the Hamiltonian $\hat{H}_s$. To this aim, $\hat{H}_s$ is projected onto the Krylov subspace $K^N_{\Psi(t_0)}$ generated by the states

$$\left\{ |\, \Psi(t_0) \,\rangle, \, \hat{H}_s \, |\, \Psi(t_0) \,\rangle, \, ... \, , \, \hat{H}_s^{N-1} \, |\, \Psi(t_0) \,\rangle \right\} \, . \tag{F.17}$$

Notice that the Krylov space is tailored to include that portion of the Hilbert space that the wave function $|\, \Psi(t_0) \,\rangle$ explores in the near future $[t_0, t_0 + \Delta t]$. Let $\hat{H}_N$ denote the Hamiltonian $\hat{H}_s$ projected onto $K^N_{\Psi(t_0)}$. Then, $\hat{H}_N$ satisfies

$$\hat{H}_N^j |\, \Psi(t_0) \,\rangle \, = \, \hat{H}_s^j |\, \Psi(t_0) \,\rangle \tag{F.18}$$

for all $j < N$. By using the standard Lanczos basis (see Section E.1), the projected $N \times N$ Hamilton matrix H_N becomes tridiagonal and symmetric. The diagonalization of H_N yields

$$S_N^\dagger H_N S_N = D_N \tag{F.19}$$

with a unitary $N \times N$ matrix S_N and a $N \times N$ diagonal matrix D_N. Then, the approximation $| \Psi^{\mathrm{L}}(t_0 + \Delta t) \rangle$ to the propagated wave function reads

$$\begin{aligned} | \Psi^{\mathrm{L}}(t_0 + \Delta t) \rangle \; &= \; \exp\left(-\frac{i}{\hbar} \Delta t \, \hat{H}_N \right) \, | \Psi(t_0) \rangle \\ &= \; S_N \, \exp\left(-\frac{i}{\hbar} \Delta t \, D_N \right) \, S_N^\dagger \, | \Psi(t_0) \rangle \; . \end{aligned} \tag{F.20}$$

The corresponding approximation $\hat{U}^{\mathrm{L}}$ to the time-evolution operator is given by

$$\hat{U}^{\mathrm{L}}(t_0 + \Delta t, t_0) \; = \; \exp\left(-\frac{i}{\hbar} \Delta t \, \hat{H}_N \right) \; = \; S_N \, \exp\left(-\frac{i}{\hbar} \Delta t \, D_N \right) \, S_N^\dagger \; . \tag{F.21}$$

Notice that in each iteration $K^N_{\Psi(t)}$ is updatet, i.e., a new Krylov subspace is generated with the current state $| \Psi(t) \rangle$. This implies that in each time step from t to $t + \Delta t$, the matrices D_N and S_N involved in the Lanczos propagator $\hat{U}^{\mathrm{L}}(t + \Delta t, t)$ are also determined anew.

We shall see in the following Section that the SILP method becomes particularly efficient in practice if small Krylov spaces $K^N_{\Psi(t)}$ are generated and used for very short time steps Δt. According to this we have chosen a dimension $N = 4$ and a time step $\Delta t = 0.002$ fs in order to perform the dynamical simulations described in Chapter 5. We have verified that further increasing these numerical parameters does not improve the accuracy of the resulting time evolution of many-body states.[1] The mathematical foundation of using short time steps Δt and small Krylov space dimensions N is given in the following Section, where the accuracy of the Lanczos time-propagation $\hat{U}^{\mathrm{L}}$ is assessed as a function of Δt.

In this context, it is important to recall that the Lanczos approximation $\hat{U}^{\mathrm{L}}$ to the time-evolution operator comprises essentially two approximations: First, mapping the relevant physics onto optimally chosen subspaces by means of the Krylov expansion, and second, freezing the time dependence of the external field $v(t)$ in each considered

[1] Actually, the absorbed laser energy ΔE per atom has been considered as the criterion for appropriate parameters N and Δt. We have found that increasing these parameters beyond $N = 4$ and $\Delta t = 0.002$ fs yields only very small modifications not exceeding the sixth significant digit of ΔE.

time interval $[t\,,\,t+\Delta t]$. The latter, i.e., freezing of v, is equivalent to the application of electric fields, which are stepwise constant in time. It is clear that none of these approximations introduces any bias toward spin relaxation. Moreover, they do not violate any conservation laws of the model. In particular, the properties of the hopping integrals resulting from the lattice symmetry, the conservation of the total atomic angular momentum $\vec{J}_j = \vec{L}_j + \vec{S}_j$ in every spin-orbit coupling transition, and the optical selection rules for electric-dipole transitions, are not affected at all. For these reasons, the Lanczos propagation method certainly represents an unbiased sound numerical approach to investigate the physics of magnetization dynamics.

F.2 Assessing the accuracy of Lanczos propagations

In order to justify the application of the SILP method, it is necessary to assess the accuracy of the Lanczos approximation $\hat{U}^{\mathrm{L}}$ [see Eq. (F.21)] to the time-evolution operator, particularly in the limit of small time steps Δt. The error between propagation with $\hat{U}^{\mathrm{L}}$ and propagation with the exact operator $\hat{U}$ has various origins: freezing the time dependence of $\hat{H}$ within short time intervals $[t_0, t_0 + \Delta t]$, the numerical evaluation of integral (F.8), the Lanczos propagation method within reduced Krylov subspaces, and general numerical errors such as rounding errors. The first three of them are associated to the approximations $\hat{U}_e$, $\hat{U}_s$ and $\hat{U}^{\mathrm{L}}$ as given by Eqs. (F.7), (F.12) and (F.21). It is the purpose of this Section to demonstrate that with decreasing Δt these first three origins of error very rapidly decrease, and thus to demonstrate the high accuracy of the SILP method in the limit $\Delta t \to 0$. To this aim, we consider separately the associated approximations $\hat{U}_e$, $\hat{U}_s$ and $\hat{U}^{\mathrm{L}}$ to the time evolution. In particular, we want to determine the order (with respect to Δt) of the errors introduced by them.

As a first step, let us consider the *local error* after a single iteration. Its upper bound will be involved afterwards in the estimation of the error after multiple time steps. We assume $|\,\Psi(t_0)\,\rangle$ to be the exact solution at the initial time t_0. Then, the

local error at time $t_0 + \Delta t$ can be decomposed into three parts:

$$\begin{aligned}
\epsilon_{\text{local}} &= \Big\| \Big(\hat{U}(t_0+\Delta t, t_0) \, - \, \hat{U}^{\text{L}}(t_0+\Delta t, t_0) \Big) \, | \, \Psi(t_0) \, \rangle \Big\|_2 \\
&\leq \Big\| \Big(\hat{U}(t_0+\Delta t, t_0) \, - \, \hat{U}_e(t_0+\Delta t, t_0) \Big) \, | \, \Psi(t_0) \, \rangle \Big\|_2 \\
&\quad + \Big\| \Big(\hat{U}_e(t_0+\Delta t, t_0) \, - \, \hat{U}_s(t_0+\Delta t, t_0) \Big) \, | \, \Psi(t_0) \, \rangle \Big\|_2 \\
&\quad + \Big\| \Big(\hat{U}_s(t_0+\Delta t, t_0) \, - \, \hat{U}^{\text{L}}(t_0+\Delta t, t_0) \Big) \, | \, \Psi(t_0) \, \rangle \Big\|_2 \\
&= \epsilon_e + \epsilon_s + \epsilon_{\text{L}} \ ,
\end{aligned} \tag{F.22}$$

where the norm $\|.\|_2$ is as usually defined by $\big\| | \, \Psi \, \rangle \big\|_2 = \sqrt{\langle \, \Psi \, | \, \Psi \, \rangle}$. Each of these three contributions is associated to the three steps of approximation described in the previous Section F.1.

In order to give an upper bound for the first error contribution ϵ_e in Eq. (F.22), let us decompose the Dyson series (F.5) in its various orders ν. The zeroth order ($\nu = 0$) is simply given by the identity

$$\hat{U}^{(0)}(t_0+\Delta t, t_0) = 1 \ , \tag{F.23}$$

and the first order reads

$$\begin{aligned}
\hat{U}^{(1)}(t_0+\Delta t, t_0) \, &= \, -\frac{i}{\hbar} \int_{t_0}^{t_0+\Delta t} \mathrm{d}s_1 \, \hat{H}(s_1) \\
&= \, -\frac{i}{\hbar} \Delta t \left(\hat{H}_0 + \hat{V} \int_0^1 \mathrm{d}z \, v(t_0 + z\Delta t) \right) \ .
\end{aligned} \tag{F.24}$$

Similarly, the second-order contribution to $\hat{U}(t_0+\Delta t, t_0)$ can be written as

$$\begin{aligned}
\hat{U}^{(2)}(t_0+\Delta t, t_0) = &- \frac{1}{\hbar^2} \int_{t_0}^{t_0+\Delta t} \mathrm{d}s_1 \int_{t_0}^{s_1} \mathrm{d}s_2 \, \hat{H}(s_1) \, \hat{H}(s_2) \\
= &- \frac{\Delta t^2}{2\hbar^2} \hat{H}_0^2 - \frac{\Delta t^2}{\hbar^2} \hat{V}^2 \underbrace{\int_0^1 \mathrm{d}z_1 \int_0^{z_1} \mathrm{d}z_2 \, v(t_0 + z_1 \Delta t) \, v(t_0 + z_2 \Delta t)}_{I_1} \\
&- \frac{\Delta t^2}{\hbar^2} \hat{H}_0 \hat{V} \underbrace{\int_0^1 \mathrm{d}z_1 \int_0^{z_1} \mathrm{d}z_2 \, v(t_0 + z_2 \Delta t)}_{I_2} \\
&- \frac{\Delta t^2}{\hbar^2} \underbrace{\hat{V}\hat{H}_0}_{\hat{H}_0 \hat{V} + [\hat{V}, \hat{H}_0]} \int_0^1 \mathrm{d}z_1 \, v(t_0 + z_1 \Delta t) \underbrace{\int_0^{z_1} \mathrm{d}z_2}_{z_1} \ .
\end{aligned} \tag{F.25}$$

In order to simplify this expression, the two integrals I_1 and I_2 are considered in more detail:

$$\begin{aligned} I_1 &= \int_0^1 \mathrm{d}z_1 \int_0^{z_1} \mathrm{d}z_2\, v(t_0 + z_1\Delta t)\, v(t_0 + z_2\Delta t) \\ &= \frac{1}{2} \int_0^1 \mathrm{d}z_1 \int_0^{z_1} \mathrm{d}z_2\, v(t_0 + z_1\Delta t)\, v(t_0 + z_2\Delta t) \\ &\quad + \frac{1}{2} \underbrace{\int_0^1 \mathrm{d}z_2 \int_0^{z_2} \mathrm{d}z_1\, v(t_0 + z_2\Delta t)\, v(t_0 + z_1\Delta t)}_{\int_0^1 \mathrm{d}z_1 \int_{z_1}^1 \mathrm{d}z_2\, v(t_0+z_1\Delta t)\, v(t_0+z_2\Delta t)} \\ &= \frac{1}{2} \left(\int_0^1 \mathrm{d}z\, v(t_0 + z\Delta t) \right)^2 \end{aligned} \tag{F.26}$$

and

$$\begin{aligned} I_2 &= \int_0^1 \mathrm{d}z_1 \int_0^{z_1} \mathrm{d}z_2\, v(t_0 + z_2\Delta t) \\ &= \int_0^1 \mathrm{d}z_2\, v(t_0 + z_2\Delta t) \int_{z_2}^1 \mathrm{d}z_1 \\ &= \int_0^1 \mathrm{d}z\, v(t_0 + z\Delta t) \cdot (1 - z)\ . \end{aligned} \tag{F.27}$$

One therefore obtains

$$\begin{aligned} \hat{U}^{(2)}(t_0 + \Delta t, t_0) &= -\frac{\Delta t^2}{2\hbar^2} \left(\hat{H}_0^2 + \hat{V}^2 \left[\int_0^1 \mathrm{d}z\, v(t_0 + z\Delta t) \right]^2 \right) \\ &\quad - \frac{\Delta t^2}{\hbar^2} \hat{H}_0 \hat{V} \int_0^1 \mathrm{d}z\, v(t_0 + z\Delta t) \\ &\quad - \frac{\Delta t^2}{\hbar^2} [\hat{V},\, \hat{H}_0] \underbrace{\int_0^1 \mathrm{d}z\, z\, v(t_0 + z\Delta t)}_{I_3}\ . \end{aligned} \tag{F.28}$$

The function $v(t_0+z\Delta t)$ within the last integral I_3 can be expanded into a Taylor series around an arbitrary $\tilde{z} \in [0, 1]$. We choose $\tilde{z}$ such that it corresponds to the particular time $\tilde{t}$ satisfying Eq. (F.9), i.e., such that $t_0 + \tilde{z}\Delta t = \tilde{t}$. Then,

$$\begin{aligned} I_3 &= \int_0^1 \mathrm{d}z\, z \left[v(\tilde{t}) + \frac{\mathrm{d}v}{\mathrm{d}t}(\tilde{t})\, \Delta t\, (z - \tilde{z}) + O(\Delta t^2) \right] \\ &= \frac{1}{2} v(\tilde{t}) + \frac{\Delta t}{6} \frac{\mathrm{d}v}{\mathrm{d}t}(\tilde{t})\, (2 - 3\tilde{z}) + O(\Delta t^2)\ . \end{aligned} \tag{F.29}$$

Finally, using Eq. (F.9) the second-order contribution reads

$$\begin{aligned}\hat{U}^{(2)}(t_0+\Delta t,t_0) &= -\frac{\Delta t^2}{2\hbar^2}\left(\hat{H}_0^2 + \hat{V}^2\,v(\tilde{t})^2 + 2\hat{H}_0\,\hat{V}\,v(\tilde{t}) + [\hat{V},\,\hat{H}_0]\,v(\tilde{t})\right)\\ &\quad -\frac{\Delta t^3}{6\hbar^2}\,[\hat{V},\,\hat{H}_0]\,\frac{\mathrm{d}v}{\mathrm{d}t}(\tilde{t})\,(2-3\tilde{z}) + O(\Delta t^4)\\ &= -\frac{\Delta t^2}{2\hbar^2}\left(\hat{H}_0 + v(\tilde{t})\,\hat{V}\right)^2\\ &\quad -\frac{\Delta t^3}{6\hbar^2}\,[\hat{V},\,\hat{H}_0]\,\frac{\mathrm{d}v}{\mathrm{d}t}(\tilde{t})\,(2-3\tilde{z}) + O(\Delta t^4)\,.\end{aligned} \tag{F.30}$$

The third-order term $\hat{U}^{(3)}$ is given by

$$\begin{aligned}\hat{U}^{(3)}(t_0+\Delta t,t_0) &= \left(-\frac{i}{\hbar}\right)^3\int_{t_0}^{t_0+\Delta t}\mathrm{d}s_1\int_{t_0}^{s_1}\mathrm{d}s_2\int_{t_0}^{s_2}\mathrm{d}s_3\,\hat{H}(s_1)\,\hat{H}(s_2)\,\hat{H}(s_3)\\ &= \left(-\frac{i}{\hbar}\Delta t\right)^3\int_0^1\mathrm{d}z_1\int_0^{z_1}\mathrm{d}z_2\int_0^{z_2}\mathrm{d}z_3\,\left(\hat{H}_0+v(t_0+z_1\Delta t)\,\hat{V}\right)\times\\ &\quad\times\left(\hat{H}_0+v(t_0+z_2\Delta t)\,\hat{V}\right)\left(\hat{H}_0+v(t_0+z_3\Delta t)\,\hat{V}\right)\\ &= \left(-\frac{i}{\hbar}\Delta t\right)^3\int_0^1\mathrm{d}z_1\int_0^{z_1}\mathrm{d}z_2\int_0^{z_2}\mathrm{d}z_3\,\left(\hat{H}_0+v(\tilde{t})\,\hat{V}\right)^3 + O(\Delta t^4)\\ &= \frac{1}{6}\left(-\frac{i}{\hbar}\Delta t\right)^3\left(\hat{H}_0+v(\tilde{t})\,\hat{V}\right)^3 + O(\Delta t^4)\,.\end{aligned} \tag{F.31}$$

Notice that in the third equation we have used the expansion

$$v(t_0+z\Delta t) = v(t_0+\tilde{z}\Delta t) + \frac{\mathrm{d}v}{\mathrm{d}t}(t_0+\tilde{z}\Delta t)\,\Delta t\,(z-\tilde{z}) + O(\Delta t^2) \tag{F.32}$$

of the field amplitude v around $\tilde{z}$ for $z\in[0,1]$.

Combining Eqs. (F.23), (F.24), (F.30) and (F.31), one obtains the exact time-evolution operator in orders of Δt:

$$\begin{aligned}\hat{U}(t_0+\Delta t,t_0) &= \hat{U}^{(0)}(t_0+\Delta t,t_0) + \hat{U}^{(1)}(t_0+\Delta t,t_0)\\ &\quad + \hat{U}^{(2)}(t_0+\Delta t,t_0) + \hat{U}^{(3)}(t_0+\Delta t,t_0) + \ldots\\ &= 1 - \frac{i}{\hbar}\Delta t\left(\hat{H}_0+v(\tilde{t})\,\hat{V}\right) + \frac{1}{2}\left(-\frac{i}{\hbar}\Delta t\right)^2\left(\hat{H}_0+v(\tilde{t})\,\hat{V}\right)^2\\ &\quad + \frac{1}{6}\left(-\frac{i}{\hbar}\Delta t\right)^3\left(\hat{H}_0+v(\tilde{t})\,\hat{V}\right)^3\\ &\quad - \frac{\Delta t^3}{6\hbar^2}\,[\hat{V},\,\hat{H}_0]\,\frac{\mathrm{d}v}{\mathrm{d}t}(\tilde{t})\,(2-3\tilde{z}) + O(\Delta t^4)\,.\end{aligned} \tag{F.33}$$

Let us recall that the approximated time-evolution operator $\hat{U}_e$ resulting from freezing the time dependence of $\hat{H}$ [see Eq. (F.7)] reads

$$\hat{U}_e(t_0+\Delta t,t_0) \,=\, \exp\left[-\frac{i}{\hbar}\Delta t\,\left(\hat{H}_0+v(\tilde{t})\,\hat{V}\right)\right]\,. \tag{F.34}$$

Therefore, this approximation introduces the error

$$\hat{U}_e(t_0+\Delta t,t_0)\,-\,\hat{U}(t_0+\Delta t,t_0)\,=\,\frac{\Delta t^3}{6\hbar^2}\,[\hat{V},\,\hat{H}_0]\,\frac{\mathrm{d}v}{\mathrm{d}t}(\tilde{t})\,(2-3\tilde{z})\,+\,O(\Delta t^4)\,. \tag{F.35}$$

The corresponding *local error* ϵ_e at time $t=t_0+\Delta t$ is thus constrained by

$$\epsilon_e\,=\,\left\|\left(\hat{U}(t_0+\Delta t,t_0)\,-\,\hat{U}_e(t_0+\Delta t,t_0)\right)|\,\Psi(t_0)\,\rangle\right\|_2\,\leq\,B_e\,\Delta t^3\,+\,O(\Delta t^4)\,. \tag{F.36}$$

Here, the parameter

$$B_e\,=\,\frac{1}{3\hbar^2}\left\|[\hat{V},\,\hat{H}_0]\right\|_\infty\left\|\frac{\mathrm{d}v}{\mathrm{d}t}\right\|_{\infty,[t_0,t_0+\Delta t]} \tag{F.37}$$

describes the behavior of the error ϵ_e for small Δt, where

$$\left\|[\hat{V},\,\hat{H}_0]\right\|_\infty\,=\,\max_{\text{eigenvalues }\eta\text{ of }[\hat{V},\hat{H}_0]}|\eta| \tag{F.38}$$

and

$$\left\|\frac{\mathrm{d}v}{\mathrm{d}t}\right\|_{\infty,[t_0,t_0+\Delta t]}\,=\,\max_{s\in[t_0,t_0+\Delta t]}\left|\frac{\mathrm{d}v}{\mathrm{d}t}(s)\right|\,. \tag{F.39}$$

The second error contribution ϵ_s in Eq. (F.22) is given by the difference between $\hat{U}_e$ and the approximation $\hat{U}_s$ [see Eq. (F.12)], where $\hat{U}_s$ has been obtained by applying the Simpson formula for the numerical evaluation of integral (F.8). By means of Eqs. (F.10) and (F.11), this difference $\hat{U}_e-\hat{U}_s$ can be estimated as

$$\hat{U}_e(t_0+\Delta t,t_0)\,-\,\hat{U}_s(t_0+\Delta t,t_0)\,=\,e^{-\frac{i}{\hbar}\Delta t\left(\hat{H}_0+v(\tilde{t})\hat{V}\right)}\,-\,e^{-\frac{i}{\hbar}\Delta t\left(\hat{H}_0+v_s\hat{V}\right)}\,=\,O(\Delta t^5)\,. \tag{F.40}$$

Consequently,

$$\epsilon_s\,=\,\left\|\left(\hat{U}_e(t_0+\Delta t,t_0)\,-\,\hat{U}_s(t_0+\Delta t,t_0)\right)|\,\Psi(t_0)\,\rangle\right\|_2\,=\,O(\Delta t^5)\,. \tag{F.41}$$

Thus, ϵ_s can be neglected in comparison with ϵ_e which is proportional to Δt^3 [see Eq. (F.36)].

The third error contribution ϵ_{L} in Eq. (F.22) is given by the error between the propagation (F.12) and the Lanczos procedure (F.20). In order to estimate ϵ_{L}, let us

expand the exponentials (i.e., the corresponding time-evolution operators) into Taylor series:

$$\begin{aligned}
&\hat{U}_s(t_0+\Delta t,t_0)\,|\,\Psi(t_0)\,\rangle \;-\; \hat{U}^{\mathrm{L}}(t_0+\Delta t,t_0)\,|\,\Psi(t_0)\,\rangle \\
&\quad= \exp\left(-\frac{i}{\hbar}\Delta t\,\hat{H}_s\right)\,|\,\Psi(t_0)\,\rangle \;-\; \exp\left(-\frac{i}{\hbar}\Delta t\,\hat{H}_N\right)\,|\,\Psi(t_0)\,\rangle \\
&\quad= \sum_{j=0}^{\infty}\frac{1}{j!}\left(-\frac{i}{\hbar}\Delta t\right)^j\,\left(\hat{H}_s^j-\hat{H}_N^j\right)\,|\,\Psi(t_0)\,\rangle \\
&\quad= \sum_{j=0}^{N-1}\frac{1}{j!}\left(-\frac{i}{\hbar}\Delta t\right)^j\,\left(\underbrace{\hat{H}_s^j}_{\hat{H}_N^j}-\hat{H}_N^j\right)\,|\,\Psi(t_0)\,\rangle \\
&\qquad+\sum_{j=N}^{\infty}\frac{1}{j!}\left(-\frac{i}{\hbar}\Delta t\right)^j\,\left(\hat{H}_s^j-\hat{H}_N^j\right)\,|\,\Psi(t_0)\,\rangle \\
&\quad= \sum_{j=N}^{\infty}\frac{1}{j!}\left(-\frac{i}{\hbar}\Delta t\right)^j\,\left(\hat{H}_s^{j-N+1}-\hat{H}_N^{j-N+1}\right)\,\hat{H}_s^{N-1}\,|\,\Psi(t_0)\,\rangle\;.
\end{aligned} \tag{F.42}$$

Therefore, the local error ϵ_{L} is bounded as

$$\begin{aligned}
\epsilon_{\mathrm{L}} \;&=\; \left\|\left(\hat{U}_s(t_0+\Delta t,t_0)\;-\;\hat{U}^{\mathrm{L}}(t_0+\Delta t,t_0)\right)\,|\,\Psi(t_0)\,\rangle\right\|_2 \\
&\leq\; B_{\mathrm{L}}\,\Delta t^N\;+\;O(\Delta t^{N+1})\;,
\end{aligned} \tag{F.43}$$

where

$$B_{\mathrm{L}} \;=\; \frac{1}{N!\,\hbar^N}\left\|\hat{H}_s\right\|_\infty^{N-1}\,\left(\left\|\hat{H}_s\right\|_\infty+\left\|\hat{H}_N\right\|_\infty\right)\;. \tag{F.44}$$

Finally, the combined *local error* (F.22) can be written in the form

$$\begin{aligned}
\epsilon_{\mathrm{local}} \;&\leq\; \epsilon_e+\epsilon_s+\epsilon_{\mathrm{L}}+\epsilon_{\mathrm{rounding}} \\
&\leq\; B_e\Delta t^3\;+O(\Delta t^4)\;+\;B_{\mathrm{L}}\Delta t^N\;+\;O(\Delta t^{N+1})\;+\;\epsilon_{\mathrm{rounding}}\;.
\end{aligned} \tag{F.45}$$

Notice that in comparison with Eq. (F.22) we have now additionally included a rounding error $\epsilon_{\mathrm{rounding}}$ which may occur in numerical computation.

Next, we compute the error introduced by the Lanczos propagation method at times later than the initial time t_0. For this purpose, let us recall that usually at some given time t_p the propagated approximation $|\,\Psi^{\mathrm{L}}(t_p)\,\rangle$ already differs from the exact solution $|\,\Psi(t_p)\,\rangle$ at that time. Then, the *local error propagation* —obtained by propagating both $|\,\Psi^{\mathrm{L}}(t_p)\,\rangle$ and $|\,\Psi(t_p)\,\rangle$ with the approximated time-evolution operator $\hat{U}^{\mathrm{L}}$— is

given by

$$\begin{aligned}
&\left\| \hat{U}^{\mathrm{L}}(t_p + \Delta t, t_p) \,|\, \Psi^{\mathrm{L}}(t_p) \,\rangle \,-\, \hat{U}^{\mathrm{L}}(t_p + \Delta t, t_p) \,|\, \Psi(t_p) \,\rangle \right\|_2 \\
&= \Big\| \underbrace{\hat{U}^{\mathrm{L}}(t_p + \Delta t, t_p)}_{\text{unitary}} \left(|\, \Psi^{\mathrm{L}}(t_p) \,\rangle \,-\, |\, \Psi(t_p) \,\rangle \right) \Big\|_2 \\
&= \left\| |\, \Psi^{\mathrm{L}}(t_p) \,\rangle \,-\, |\, \Psi(t_p) \,\rangle \right\|_2 .
\end{aligned} \tag{F.46}$$

This allows us to compute the *cumulative error* between the propagated approximation $|\, \Psi^{\mathrm{L}}(t_p + \Delta t) \,\rangle$ and the exact solution $|\, \Psi(t_p + \Delta t) \,\rangle$ at time $t_p + \Delta t$:

$$\begin{aligned}
&\left\| |\, \Psi^{\mathrm{L}}(t_p + \Delta t) \,\rangle \,-\, |\, \Psi(t_p + \Delta t) \,\rangle \right\|_2 \\
&\leq \left\| \hat{U}^{\mathrm{L}}(t_p + \Delta t, t_p) \,|\, \Psi^{\mathrm{L}}(t_p) \,\rangle \,-\, \hat{U}^{\mathrm{L}}(t_p + \Delta t, t_p) \,|\, \Psi(t_p) \,\rangle \right\|_2 \\
&\quad + \left\| \hat{U}^{\mathrm{L}}(t_p + \Delta t, t_p) \,|\, \Psi(t_p) \,\rangle \,-\, \hat{U}(t_p + \Delta t, t_p) \,|\, \Psi(t_p) \,\rangle \right\|_2 \\
&\leq \left\| |\, \Psi^{\mathrm{L}}(t_p) \,\rangle \,-\, |\, \Psi(t_p) \,\rangle \right\|_2 \,+\, \epsilon_{\mathrm{local}} .
\end{aligned} \tag{F.47}$$

So far, we have only considered infinitesimal time steps Δt. Now, we want to estimate the error at arbitrary times $t_j = t_0 + j\Delta t$, provided that at time t_0 the initial state used for the approximative propagation $\hat{U}^{\mathrm{L}}$ is exact, i.e., $|\, \Psi^{\mathrm{L}}(t_0) \,\rangle = |\, \Psi(t_0) \,\rangle$. Then, Eq. (F.47) yields for the first time step t_1:

$$\left\| |\, \Psi^{\mathrm{L}}(t_1) \,\rangle \,-\, |\, \Psi(t_1) \,\rangle \right\|_2 \,\leq\, \epsilon_{\mathrm{local}} . \tag{F.48}$$

For the time t_2 one similarly obtains

$$\left\| |\, \Psi^{\mathrm{L}}(t_2) \,\rangle \,-\, |\, \Psi(t_2) \,\rangle \right\|_2 \,\leq\, \left\| |\, \Psi^{\mathrm{L}}(t_1) \,\rangle \,-\, |\, \Psi(t_1) \,\rangle \right\|_2 \,+\, \epsilon_{\mathrm{local}} \,\leq\, 2\,\epsilon_{\mathrm{local}} . \tag{F.49}$$

Finally, induction yields the estimation

$$\left\| |\, \Psi^{\mathrm{L}}(t_j) \,\rangle \,-\, |\, \Psi(t_j) \,\rangle \right\|_2 \,\leq\, j\,\epsilon_{\mathrm{local}} \tag{F.50}$$

for all $j \in \mathbb{N}$. For a particular finite time $t = t_\nu = t_0 + \nu\Delta t$, one finds $\nu = (t - t_0)/\Delta t$ and, therefore, the *total error* at time $t > t_0$ can be estimated as

$$\begin{aligned}
\left\| |\, \Psi^{\mathrm{L}}(t) \,\rangle \,-\, |\, \Psi(t) \,\rangle \right\|_2 \,&\leq\, \frac{t - t_0}{\Delta t}\,\epsilon_{\mathrm{local}} \\
&\leq\, (t - t_0) \left(B_e \Delta t^2 \,+\, B_{\mathrm{L}} \Delta t^{N-1} \,+\, \frac{\epsilon_{\mathrm{rounding}}}{\Delta t} \right) \\
&\quad +\, O(\Delta t^3) \,+\, O(\Delta t^N) .
\end{aligned} \tag{F.51}$$

The contributions $B_e\,\Delta t^2$ and $O(\Delta t^3)$ are related to the time dependence of the Hamiltonian. If $\hat{H}$ is independent of time, then these terms disappear and the dominant part in the *total error* is given by $B_{\mathrm{L}}\,\Delta t^{N-1}$. The latter originates from the finite Krylov spaces used in the SILP-diagonalization method. The last term $\epsilon_{\mathrm{rounding}}/\Delta t$ is given by the machine accuracy. If one neglects $\epsilon_{\mathrm{rounding}}$ and assumes a time-dependent Hamiltonian $\hat{H}(t)$, then the *total error* in the Lanczos propagation method is proportional to Δt^2 for short time steps Δt. In this case, increasing the subspace dimension N does not significantly improve the accuracy. In conclusion, these considerations justify the application of the SILP method and the use of very short time steps Δt and small Krylov subspace sizes N.

References

[1] E. Beaurepaire, J.-C. Merle, A. Daunois, and J.-Y. Bigot, *Ultrafast Spin Dynamics in Ferromagnetic Nickel*, Phys. Rev. Lett. **76**, 4250 (1996). 1, 2, 5, 6, 9, 11, 12, 33, 86

[2] J. Hohlfeld, E. Matthias, R. Knorren, and K. H. Bennemann, *Nonequilibrium Magnetization Dynamics of Nickel*, Phys. Rev. Lett. **78**, 4861 (1997). 2, 6, 9, 33, 86

[3] A. Scholl, L. Baumgarten, R. Jacquemin, and W. Eberhardt, *Ultrafast Spin Dynamics of Ferromagnetic Thin Films Observed by fs Spin-Resolved Two-Photon Photoemission*, Phys. Rev. Lett. **79**, 5146 (1997). 2, 33

[4] J. Güdde, U. Conrad, V. Jähnke, J. Hohlfeld, and E. Matthias, *Magnetization dynamics of Ni and Co films on Cu(001) and of bulk nickel surfaces*, Phys. Rev. B **59**, (R)6608 (1999). 2

[5] B. Koopmans, M. van Kampen, J. T. Kohlhepp, and W. J. M. de Jonge, *Ultrafast Magneto-Optics in Nickel: Magnetism or Optics?*, Phys. Rev. Lett. **85**, 844 (2000). 2, 86

[6] B. Koopmans, M. van Kampen, and W. J. M. de Jonge, *Experimental access to femtosecond spin dynamics*, J. Phys.: Condens. Matter **15**, S723 (2003). 2, 6, 7, 9, 13

[7] H.-S. Rhie, H. A. Dürr, and W. Eberhardt, *Femtosecond Electron and Spin Dynamics in Ni/W(110) Films*, Phys. Rev. Lett. **90**, 247201 (2003). 2, 6, 7, 13, 33, 86, 107

[8] C. Stamm, T. Kachel, N. Pontius, R. Mitzner, T. Quast, K. Holldack, S. Khan, C. Lupulescu, E. F. Aziz, M. Wietstruk, H. A. Dürr, and W. Eberhardt, *Femtosecond modification of electron localization and transfer of angular momentum in nickel*, Nature Mat. **6**, 740 (2007). 2, 3, 8, 14, 86

[9] J.-Y. Bigot, M. Vomir, and E. Beaurepaire, *Coherent ultrafast magnetism induced by femtosecond laser pulses*, Nature Phys. **5**, 515 (2009). 2, 5, 13, 86

[10] C. Stamm, N. Pontius, T. Kachel, M. Wietstruk, and H. A. Dürr, *Femtosecond x-ray absorption spectroscopy of spin and orbital angular momentum in photoexcited Ni films during ultrafast demagnetization*, Phys. Rev. B **81**, 104425 (2010). 2, 3, 86

[11] M. Cinchetti, M. Sánchez Albaneda, D. Hoffmann, T. Roth, J.-P. Wüstenberg, M. Krauß, O. Andreyev, H. C. Schneider, M. Bauer, and M. Aeschlimann, *Spin-Flip Processes and Ultrafast Magnetization Dynamics in Co: Unifying the Microscopic and Macroscopic View of Femtosecond Magnetism*, Phys. Rev. Lett. **97**, 177201 (2006). 2, 7, 86

[12] E. Carpene, E. Mancini, C. Dallera, M. Brenna, E. Puppin, and S. De Silvestri, *Dynamics of electron-magnon interaction and ultrafast demagnetization in thin iron films*, Phys. Rev. B **78**, 174422 (2008). 2, 8, 86

[13] J.-Y. Bigot, E. Beaurepaire, L. Guidoni, and J.-C. Merle, *Magnetization Dynamics on the Femtosecond Time-scale in Metallic Ferromagnets*, in *Magnetism: Molecules to Materials III*, edited by J. S. Miller and M. Drillon (Wiley-VCH Verlag, Weinheim, 2002). 5, 6, 7, 9

[14] G. Grosso and G. P. Parravicini, *Solid State Physics* (Academic Press, San Diego, 2003). 6

[15] G. P. Zhang and W. Hübner, *Laser-Induced Ultrafast Demagnetization in Ferromagnetic Metals*, Phys. Rev. Lett. **85**, 3025 (2000). 6, 12

[16] W. Nolting, and A. Ramakanth, *Quantum Theory of Magnetism* (Springer, Berlin, 2009). 7, 45, 65

[17] F. Bloch, *Zur Theorie des Ferromagnetismus*, Z. Phys. **61**, 206 (1930). 7

[18] B. Koopmans, H. H. J. E. Kicken, M. van Kampen, and W. J. M. de Jonge, *Microscopic model for femtosecond magnetization dynamics*,

J. Magn. Magn. Mater. **286**, 271 (2005). 7, 13, 14, 44

[19] B. Koopmans, J. J. M. Ruigrok, F. Dalla Longa, and W. J. M. de Jonge, *Unifying Ultrafast Magnetization Dynamics*, Phys. Rev. Lett. **95**, 267207 (2005). 7, 13, 14, 44

[20] D. Steiauf and M. Fähnle, *Elliott-Yafet mechanism and the discussion of femtosecond magnetization dynamics*, Phys. Rev. B **79**, 140401 (2009). 8, 14, 15, 17, 18, 37, 44

[21] D. Steiauf, C. Illg, and M. Fähnle, *Extension of Yafets theory of spin relaxation to ferromagnets*, J. Magn. Magn. Mat. **322**, L5 (2010). 8, 14, 17, 18, 37, 44

[22] M. Fähnle and C. Illg, *Electron theory of fast and ultrafast dissipative magnetization dynamics*, J. Phys.: Condens. Matter **23**, 493201 (2011). 8, 14, 15, 17, 37

[23] B. Koopmans, G. Malinowski, F. Dalla Longa, D. Steiauf, M. Fähnle, T. Roth, M. Cinchetti, and M. Aeschlimann, *Explaining the paradoxical diversity of ultrafast laser-induced demagnetization*, Nature Mat. **9**, 259 (2010). 8, 10, 14, 33

[24] A. Kirilyuk, A. V. Kimel, and T. Rasing, *Ultrafast optical manipulation of magnetic order*, Rev. Mod. Phys. **82**, 2731 (2010). 10, 13

[25] A. Melnikov, U. Bovensiepen, I. Radu, O. Krupin, K. Starke, E. Matthias, and M. Wolf, *Picosecond magnetization dynamics of the Gd(0001) surface*, J. Magn. Magn. Mat. **272**, 1001 (2004). 10, 14

[26] M. Lisowski, P. A. Loukakos, A. Melnikov, I. Radu, L. Ungureanu, M. Wolf, and U. Bovensiepen, *Femtosecond Electron and Spin Dynamics in Gd(0001) Studied by Time-Resolved Photoemission and Magneto-optics*, Phys. Rev. Lett. **95**, 137402 (2005). 10, 14

[27] U. Bovensiepen, *Coherent and incoherent excitations of the Gd(0001) surface on ultrafast timescales*, J. Phys.: Condens. Matter **19**, 083201 (2007). 10

[28] A. Melnikov, H. Prima-Garcia, M. Lisowski, T. Gießel, R. Weber, R. Schmidt, C. Gahl, N. M. Bulgakova, U. Bovensiepen, and M. Weinelt, *Nonequilibrium Magnetization Dynamics of Gadolinium Studied by Magnetic Linear Dichroism in Time-Resolved* $4f$ *Core-Level Photoemission*, Phys. Rev. Lett. **100**, 107202 (2008). 10

[29] M. Wietstruk, A. Melnikov, C. Stamm, T. Kachel, N. Pontius, M. Sultan, C. Gahl, M. Weinelt, H. A. Dürr, and U. Bovensiepen, *Hot-Electron-Driven Enhancement of Spin-Lattice Coupling in Gd and Tb* $4f$ *Ferromagnets Observed by Femtosecond X-Ray Magnetic Circular Dichroism*, Phys. Rev. Lett. **106**, 127401 (2011). 10

[30] S. Mathias, C. La-O-Vorakiat, P. Grychtol, P. Granitzka, E. Turgut, J. M. Shaw, R. Adam, H. T. Nembach, M. E. Siemens, S. Eich, C. M. Schneider, T. J. Silva, M. Aeschlimann, M. M. Murnane, and H. C. Kapteyn, *Probing the timescale of the exchange interaction in a ferromagnetic alloy*, Proc. Natl. Acad. Sci. USA **109**, 4792 (2012). 11

[31] I. Radu, C. Stamm, N. Pontius, T. Kachel, P. Ramm, J.-U. Thiele, H. A. Dürr, and C. H. Back, *Laser-induced generation and quenching of magnetization on FeRh studied with time-resolved x-ray magnetic circular dichroism*, Phys. Rev. B **81**, 104415 (2010). 11

[32] C. D. Stanciu, F. Hansteen, A. V. Kimel, A. Kirilyuk, A. Tsukamoto, A. Itoh, and Th. Rasing, *All-Optical Magnetic Recording with Circularly Polarized Light*, Phys. Rev. Lett. **99**, 047601 (2007). 11

[33] I. Radu, K. Vahaplar, C. Stamm, T. Kachel, N. Pontius, H. A. Dürr, T. A. Ostler, J. Barker, R. F. L. Evans, R. W. Chantrell, A. Tsukamoto, A. Itoh, A. Kirilyuk, Th. Rasing, and A. V. Kimel, *Transient ferromagnetic-like state mediating ultrafast reversal of antiferromagnetically coupled spins*, Nature **472**, 205 (2011). 11

[34] J. H. Mentink, J. Hellsvik, D. V. Afanasiev, B. A. Ivanov, A. Kirilyuk, A. V. Kimel, O. Eriksson, M. I. Katsnelson, and Th. Rasing, *Ultrafast Spin Dynamics in Multisublattice Magnets*, Phys. Rev. Lett. **108**, 057202 (2012). 11

[35] A. R. Khorsand, M. Savoini, A. Kirilyuk, A. V. Kimel, A. Tsukamoto, A. Itoh, and Th. Rasing, *Role of Magnetic Circular Dichroism in All-Optical Magnetic Recording*, Phys. Rev. Lett. **108**, 127205 (2012). 11

[36] T. A. Ostler, J. Barker, R. F. L. Evans, R. W. Chantrell, U. Atxitia, O. Chubykalo-Fesenko, S. El Moussaoui, L. Le Guyader, E. Mengotti, L. J. Heyderman, F. Nolting, A. Tsukamoto, A. Itoh, D. Afanasiev, B. A. Ivanov, A. M. Kalashnikova, K. Vahaplar, J. Mentink, A. Kirilyuk, Th. Rasing, and A. V. Kimel, *Ultrafast heating as a sufficient stimulus for magnetization reversal in a ferrimagnet*, Nature comm. **3**, 666 (2012). 11

[37] L. Le Guyader, S. El Moussaoui, M. Buzzi, R. V. Chopdekar, L. J. Heyderman, A. Tsukamoto, A. Itoh, A. Kirilyuk, Th. Rasing, A. V. Kimel, and F. Nolting, *Demonstration of laser induced magnetization reversal in GdFeCo nanostructures*, Appl. Phys. Lett. **101**, 022410 (2012). 11

[38] A. V. Kimel, A. Kirilyuk, A. Tsvetkov, R. V. Pisarev, and Th. Rasing, *Laser-induced ultrafast spin reorientation in the antiferromagnet $TmFeO_3$*, Nature **429**, 850 (2004). 11

[39] A. V. Kimel, A. Kirilyuk, P. A. Usachev, R. V. Pisarev, A. M. Balbashov, and Th. Rasing, *Ultrafast non-thermal control of magnetization by instantaneous photomagnetic pulses*, Nature **435**, 655 (2005). 11

[40] J. A. de Jong, A. V. Kimel, R. V. Pisarev, A. Kirilyuk, and Th. Rasing, *Laser-induced ultrafast spin dynamics in $ErFeO_3$*, Phys. Rev. B **84**, 104421 (2011). 11

[41] R. J. Elliott, *Theory of the Effect of Spin-Orbit Coupling on Magnetic Resonance in Some Semiconductors*, Phys. Rev. **96**, 266 (1954). 13

[42] Y. Yafet, *g Factors and Spin-Lattice Relaxation of Conduction Electrons*, in *Solid State Physics Vol. 14*, edited by F. Seitz and D. Turnbull (Academic Press, New York, 1963). 13

[43] K. Carva, M. Battiato, and P. M. Oppeneer, *Ab Initio Investigation of the Elliott-Yafet Electron-Phonon Mechanism in Laser-Induced Ultrafast Demagnetization*, Phys. Rev. Lett. **107**, 207201 (2011). 15

[44] M. Battiato, K. Carva, and P. M. Oppeneer, *Superdiffusive Spin Transport as a Mechanism of Ultrafast Demagnetization*, Phys. Rev. Lett. **105**, 027203 (2010). 15

[45] A. J. Schellekens, W. Verhoeven, T. N. Vader, and B. Koopmans, *Investigating the contribution of superdiffusive transport to ultrafast demagnetization of ferromagnetic thin films*, Appl. Phys. Lett. **102**, 252408 (2013). 15, 54

[46] N. Kazantseva, D. Hinzke, U. Nowak, R. W. Chantrell, and O. Chubykalo-Fesenko, *Atomistic models of ultrafast reversal*, phys. stat. sol. (b) **244**, 4389 (2007). 16

[47] N. Kazantseva, U. Nowak, R. W. Chantrell, J. Hohlfeld, and A. Rebei, *Slow recovery of the magnetisation after a sub-picosecond heat pulse*, Europhys. Lett. **81**, 27004 (2008). 16

[48] U. Atxitia, O. Chubykalo-Fesenko, N. Kazantseva, D. Hinzke, U. Nowak, and R. W. Chantrell, *Micromagnetic modeling of laser-induced magnetization dynamics using the Landau-Lifshitz-Bloch equation*, Appl. Phys. Lett. **91**, 232507 (2007). 16

[49] U. Atxitia, O. Chubykalo-Fesenko, J. Walowski, A. Mann, and M. Münzenberg, *Evidence for thermal mechanisms in laser-induced femtosecond spin dynamics*, Phys. Rev. B **81**, 174401 (2010). 16

[50] U. Atxitia and O. Chubykalo-Fesenko, *Ultrafast magnetization dynamics rates within the Landau-Lifshitz-Bloch model*, Phys. Rev. B **84**, 144414 (2011). 16

[51] W. Töws and G. M. Pastor, *Theoretical study of the temperature dependence of the magnon dispersion relation in transition-metal wires and monolayers*, Phys. Rev. B **86**, 054443 (2012). 20

[52] P. Stampfli and K. H. Bennemann, *Theory for the instability of the diamond structure of Si, Ge, and C induced by a dense electron-hole plasma*, Phys. Rev. B **42**, 7163 (1990). 20

[53] P. Stampfli and K. H. Bennemann, *Dynamical theory of the laser-induced lattice instability of silicon*, Phys. Rev. B **46**, 10686 (1992). 20

[54] M. Saubanère, M. Tanveer, P. Ruiz-Díaz, and G. M. Pastor, *First principles theoretical study of complex magnetic order in transition-metal nanowires*, Phys. Stat. Sol. B **247**, 2610 (2010). 21, 31

[55] M. Tanveer, P. Ruiz-Díaz, and G. M. Pastor, *Environment-dependent noncollinear magnetic orders and spin-wave spectra of Fe chains and stripes*, Phys. Rev. B **87**, 075426 (2013). 21, 31

[56] S. V. Halilov, A. Y. Perlov, P. M. Oppeneer, and H. Eschrig, *Magnon spectrum and related finite-temperature magnetic properties: A first-principle approach*, Europhys. Lett. **39**, 91 (1997). 22

[57] S. V. Halilov, H. Eschrig, A. Y. Perlov, and P. M. Oppeneer, *Adiabatic spin dynamics from spin-density-functional theory: Application to Fe, Co, and Ni*, Phys. Rev. B **58**, 293 (1998). 22

[58] P. Hohenberg and W. Kohn, *Inhomogeneous Electron Gas*, Phys. Rev. **136**, B864 (1964). 23, 127

[59] W. Kohn and L. J. Sham, *Self-Consistent Equations Including Exchange and Correlation Effects*, Phys. Rev. **140**, A1133 (1965). 23, 25, 127

[60] R. G. Parr and W. Yang, *Density-Functional Theory of Atoms and Molecules* (Oxford University Press, Oxford, 1989). 24

[61] R. M. Dreizler and E. K. U. Gross, *Density Functional Theory* (Springer, Berlin, 1990). 24

[62] N. D. Mermin, *Thermal Properties of the Inhomogeneous Electron Gas*, Phys. Rev. **137**, A1441 (1965). 24

[63] J. F. Janak, *Proof that $\partial E/\partial n_i = \varepsilon$ in density-functional theory*, Phys. Rev. B **18**, 7165 (1978). 24

[64] G. Kresse and J. Furthmüller, *Efficient iterative schemes for ab initio total-energy calculations using a plane-wave basis set*, Phys. Rev. B **54**, 11169 (1996). 25, 127

[65] G. Kresse and D. Joubert, *From ultrasoft pseudopotentials to the projector augmented-wave method*, Phys. Rev. B **59**, 1758 (1999). 25, 127

[66] P. Blaha, K. Schwarz, P. Sorantin, and S. B. Trickey, *Full-potential, linearized augmented plane wave programs for crystalline systems*, Comput. Phys. Commun. **59**, 399 (1990). 25

[67] K. Schwarz and P. Blaha, *Solid state calculations using WIEN2k*, Comput. Mater. Science **28**, 259 (2003). 25

[68] J. C. Tung and G. Y. Guo, *Ab initio studies of spin-spiral waves and exchange interactions in 3d transition metal atomic chains*, Phys. Rev. B **83**, 144403 (2011). 31

[69] L. D. Landau and E. M. Lifshitz, *Quantum Mechanics: Non-relativistic Theory* (Elsevier Butterworth-Heinemann, Oxford, 1981). 42, 46, 50, 51, 99

[70] C. S. Wang and J. Callaway, *Energy bands in ferromagnetic nickel*, Phys. Rev. B **15**, 298 (1977). 45

[71] J. C. Slater and G. F. Koster, *Simplified LCAO Method for the Periodic Potential Problem*, Phys. Rev. **94**, 1498 (1954). 46, 131, 134

[72] W. A. Harrison, *Electronic Structure and the Properties of Solids* (Dover Pubn Inc, Dover, 1989). 46

[73] A. Messiah, *Quantum Mechanics Volume II* (Elsevier Science B.V., Amsterdam, 1981). 49, 141, 143

[74] P. Bruno, *Magnetismus von Festkörpern und Grenzflächen* (KFA, Jülich, 1993), Chapter 24. 52, 64

[75] R. H. Victora and L. M. Falicov, *Exact Solution of a Four-Site d-Electron Problem: The Nickel-Metal Photoemission Spectrum*, Phys. Rev. Lett. **55**, 1140 (1985). 62, 65

[76] D. A. Papaconstantopoulos, *Handbook of the band structure of elemental solids* (Plenum Press, New York, 1986). 62

[77] S. Hüfner and G. K. Wertheim, *Multielectron effects in the XPS spectra of Nickel*, Physics Letters **51A**, 299 (1975). 65

[78] W. Eberhardt and E. W. Plummer, *Angle-resolved photoemission determination of the band structure and multielectron excitations in Ni*, Phys. Rev. B **21**, 3245 (1980). 65

[79] L. A. Feldkamp and L. C. Davis, *X-ray photoemission spectra of core levels in Ni metal*, Phys. Rev. B **22**, 3644 (1980). 65

[80] B. N. Parlett, *The Symmetric Eigenvalue Problem* (Prentice-Hall, Englewood Cliffs, 1980). 68, 146, 148

[81] R. A. Guirado-López, J. Dorantes-Dávila, and G. M. Pastor, *Orbital Magnetism in Transition-Metal Clusters: From Hunds Rules to Bulk Quenching*, Phys. Rev. Lett. **90**, 226402 (2003). 77

[82] M. Aichhorn, M. Daghofer, H. G. Evertz, and W. von der Linden, *Low-temperature Lanczos method for strongly correlated systems*, Phys. Rev. B **67**, 161103 (2003). 80, 149

[83] D. J. Tannor, *Introduction to Quantum Mechanics: A time-Dependent Perspective* (University Science Books, Sausalito, California, 2007). 87, 155, 158

[84] Y. Wang and J. P. Perdew, *Correlation hole of the spin-polarized electron gas, with exact small-wave-vector and high-density scaling*, Phys. Rev. B **44**, 13298 (1991). 127

[85] J. P. Perdew and Y. Wang, *Accurate and simple analytic representation of the electron-gas correlation energy*, Phys. Rev. B **45**, 13244 (1992). 127

[86] J. P. Perdew, J. A. Chevary, S. H. Vosko, K. A. Jackson, M. R. Pederson, D. J. Singh, and C. Fiolhais, *Atoms, molecules, solids, and surfaces: Applications of the generalized gradient approximation for exchange and correlation*, Phys. Rev. B **46**, 6671 (1992). 127

[87] P. E. Blöchl, *Projector augmented-wave method*, Phys. Rev. B **50**, 17953 (1994). 127

[88] D. Hobbs, G. Kresse, and J. Hafner, *Fully unconstrained noncollinear magnetism within the projector augmented-wave method*, Phys. Rev. B **62**, 11556 (2000). 128

[89] W. Kohn, *Density Functional and Density Matrix Method Scaling Linearly with the Number of Atoms*, Phys. Rev. Lett. **76**, 3168 (1996). 128

[90] P. D. Haynes and M. C. Payne, *Corrected penalty-functional method for linear-scaling calculations within density-functional theory*, Phys. Rev. B **59**, 12173 (1999). 128

[91] P. H. Dederichs, S. Blügel, R. Zeller, and H. Akai, *Ground States of Constrained Systems: Application to Cerium Impurities*, Phys. Rev. Lett. **53**, 2512 (1984). 128

[92] H. J. Monkhorst and J. D. Pack, *Special points for Brillouin-zone integrations*, Phys. Rev. B **13**, 5188 (1976). 128

[93] V. Heine, *s–d Interaction in Transition Metals*, Phys. Rev. **153**, 673 (1967). 131

[94] V. L. Moruzzi and P. M. Marcus, *Magnetism in bcc 3d transition metals: Onset and approach to the Hunds-rule limit*, Phys. Rev. B **38**, 1613 (1988). 131

[95] M. Hanke-Bourgeois, *Grundlagen der Numerischen Mathematik und des Wissenschaftlichen Rechnens* (Teubner, Wiesbaden, 2006). 146, 157